frontiers | Research Topics

Rising stars in nutrition and food science technology: Application of emerging technologies in the food industry, 2nd Edition

Edited by
Debao Niu, Zhi-Hong Zhang and Zhi-Wei Liu

Published in
Frontiers in Nutrition

ISSN 1664-8714
ISBN 978-2-8325-2921-8
DOI 10.3389/978-2-8325-2921-8

About Frontiers

Frontiers is more than just an open access publisher of scholarly articles: it is a pioneering approach to the world of academia, radically improving the way scholarly research is managed. The grand vision of Frontiers is a world where all people have an equal opportunity to seek, share and generate knowledge. Frontiers provides immediate and permanent online open access to all its publications, but this alone is not enough to realize our grand goals.

Frontiers journal series

The Frontiers journal series is a multi-tier and interdisciplinary set of open-access, online journals, promising a paradigm shift from the current review, selection and dissemination processes in academic publishing. All Frontiers journals are driven by researchers for researchers; therefore, they constitute a service to the scholarly community. At the same time, the *Frontiers journal series* operates on a revolutionary invention, the tiered publishing system, initially addressing specific communities of scholars, and gradually climbing up to broader public understanding, thus serving the interests of the lay society, too.

Dedication to quality

Each Frontiers article is a landmark of the highest quality, thanks to genuinely collaborative interactions between authors and review editors, who include some of the world's best academicians. Research must be certified by peers before entering a stream of knowledge that may eventually reach the public - and shape society; therefore, Frontiers only applies the most rigorous and unbiased reviews. Frontiers revolutionizes research publishing by freely delivering the most outstanding research, evaluated with no bias from both the academic and social point of view. By applying the most advanced information technologies, Frontiers is catapulting scholarly publishing into a new generation.

What are Frontiers Research Topics?

Frontiers Research Topics are very popular trademarks of the *Frontiers journals series*: they are collections of at least ten articles, all centered on a particular subject. With their unique mix of varied contributions from Original Research to Review Articles, Frontiers Research Topics unify the most influential researchers, the latest key findings and historical advances in a hot research area.

Find out more on how to host your own Frontiers Research Topic or contribute to one as an author by contacting the Frontiers editorial office: frontiersin.org/about/contact

Rising stars in nutrition and food science technology: Application of emerging technologies in the food industry, 2nd Edition

Topic editors

Debao Niu — Guangxi University, China

Zhi-Hong Zhang — Jiangsu University, China

Zhi-Wei Liu — Hunan Agricultural University, China

Citation

Niu, D., Zhang, Z.-H., Liu, Z.-W., eds. (2023). *Rising stars in nutrition and food science technology: Application of emerging technologies in the food industry, 2nd Edition*. Lausanne: Frontiers Media SA. doi: 10.3389/978-2-8325-2921-8

Publisher's note: In this 2nd edition, the following article has been added: Zhang Z-H, Liu Z-W and Niu D (2023) Editorial: Rising stars in nutrition and food science technology: application of emerging technologies in the food industry. *Front. Nutr.* 10:1225703. doi: 10.3389/fnut.2023.1225703

Table of contents

frontiers | Frontiers in Nutrition

TYPE Editorial
PUBLISHED 19 June 2023
DOI 10.3389/fnut.2023.1225703

OPEN ACCESS

EDITED AND REVIEWED BY
Elena Ibañez,
Spanish National Research Council (CSIC), Spain

*CORRESPONDENCE
Debao Niu
✉ happyndb@gxu.edu.cn

RECEIVED 19 May 2023
ACCEPTED 08 June 2023
PUBLISHED 19 June 2023

CITATION
Zhang Z-H, Liu Z-W and Niu D (2023) Editorial: Rising stars in nutrition and food science technology: application of emerging technologies in the food industry.
Front. Nutr. 10:1225703.
doi: 10.3389/fnut.2023.1225703

Editorial: Rising stars in nutrition and food science technology: application of emerging technologies in the food industry

Zhi-Hong Zhang[1], Zhi-Wei Liu[2] and Debao Niu[3]*

[1]School of Food and Biological Engineering, Jiangsu University, Zhenjiang, China, [2]College of Food Science and Technology, Hunan Agricultural University, Changsha, China, [3]College of Light Industry and Food Engineering, Guangxi University, Nanning, China

KEYWORDS

emerging technology, biological activity, food preservative, food industry, non-thermal processing

Editorial on the Research Topic
Rising stars in nutrition and food science technology: application of emerging technologies in the food industry

Food is essential, relating to human living and health. At present, the shortage of natural resources and environmental pressures are prominent factors in the food industry. Moreover, the demand for high-quality and natural food without chemical preservatives has been growing in recent years. In this context, the food industry faces enormous challenges and food production technologies that ensure safety and quality have become a top priority for the food industry globally. With the development of science and technology, a series of new technologies in the fields of modern nutrition, biology, optoelectronics, electromagnetism, machinery, program control, materials, and other scientific fields are widely used in scientific research and various processing links of the food industry. This can effectively improve the utilization rate of food resources and the degree of value-added processing, lead to the sustainable development of the food industry, and increase production to meet the population's growing material and nutritional needs.

In this Research Topic, the effects of emerging technologies in the food industry on food quality, microbial safety, and nutrition are summarized. Furthermore, the articles included in this RT evaluate the potential applications of these technologies in the food industry and consider current consumer demand for future food products, allowing for a deep understanding of the theory and development of these emerging technologies and how they will affect the food industry in the future.

Chinese grain vinegar is a popular daily condiment, which is produced by a solid-state fermentation style in open and non-sterile environmental conditions. In this production style, there are many shortcomings, such as the inconsistency of quality between different batches, the low production efficiency, and the low degree of mechanization. Therefore, an update to fermentation devices has been the development direction for Chinese grain vinegar in recent years. Wang W. et al. reported a solid-state fermentation technology based on a self-designed rotary drum bioreactor to study the changes in vinegar quality indexes and microbial dynamics. Results showed that the vinegar flavor changed due to the acetic acid bacteria increasing by 60% compared to the control. Moreover, the relationship between

bacterial dynamics and metabolite changes in acetic acid fermentation of vinegar production was established, which can help bioreactor optimization and expand the production scale to reach industrialization.

In recent years, natural antimicrobial agents have been rapidly developed due to an increase in health and safety awareness. Antimicrobial peptides (AMPs), a class of natural antimicrobial agents that are small molecular peptides (<100 amino acid) with antimicrobial activity and are non-toxic to humans, can be widely applied in the food industry instead of artificial synthetic preservatives. In their research article, Wang Z. et al. selected one lactic acid bacterium (named L. *plantarum* W3-2) producing bacteriocin (plantaricin W3-2) among 2,000 plant-derived strains by agar well diffusion method. The authors observed that plantaricin W3-2 showed good thermal and pH stability and broad-spectrum antimicrobial activity. Therefore, the authors suggested that this new bacteriocin is expected to become a food preservative.

In food processing, a large amount of processing waste can be produced, which could pollute the environment. Therefore, the comprehensive utilization of agricultural and food by-products is a research hotspot. Sugarcane bagasse is one of the major by-products of sugar mills. Due to the high concentration of lignin, the application of sugarcane bagasse has been limited. In their research article, Luo et al. improved the utilization rate of bagasse by applying optimal alkaline hydrogen peroxide treatment conditions (AHP). Moreover, the physicochemical properties of bagasse insoluble dietary fiber (BIDF) produced by AHP were significantly improved, such as water holding capacity, oil holding capacity, and bile salt adsorption capacity. Therefore, the authors suggested that BIDF could be used in the food industry. In another research article, Tian et al. reported that camellia shells (CSs) were used for camellia oil decolorization. The new decolorizer of the porous activated carbon-based CS was prepared by the pyrolysis plus acid (H_3PO_4), named CS-based p-doped porous activated carbon (CSHAC). Results showed that the adsorption efficiency of CSHAC for carotenoids was increased by 9.5%−29.5% compared to commercial decolorizers. Moreover, by analyzing the adsorption processing of carotenoids of camelia oil by CSHAC, the study showed that the adsorption property was complex adsorption, and the chemical adsorption was mainly through the adsorption process.

It is known that the maturity degree of a plant could influence the composition of chemical compounds of plant products, such as fruits, vegetables, and seeds. In their research article, Cai et al. determined the effect of different maturity stages of Noni (*Morinda citrifolia* L.) on the quality parameters of Noni polysaccharides (NP). Results showed that stages 4 and 5 have good extraction efficiency and bioactivity properties of NP, such as DPPH and ABTS free radical scavenging capacity. Therefore, the authors suggested that stages 4 and 5 could be the ideal extraction stages for obtaining high-quality Noni polysaccharides.

Compared to the traditional thermal processing technology, the non-thermal treatment technology has some advantages, such as mild treatment conditions, low-temperature rise (<10°C), and a short treatment period. Therefore, non-thermal technology is widely studied in food sterilization to obtain good-quality food products. Wang L.-H. et al. investigated the effects of dielectric barrier discharge-air cold plasma (DBD-ACP, 15–35 kV, 2–12 min) on the quality of foxtail millets (FM). Results showed that the color of FM can be changed, and the activity of lipoxygenase and lipase was significantly decreased induced by DBD-ACP. Moreover, in the optimal treatment condition, the quality of FM was better than the control in the storage period. Therefore, the authors suggested that DBD-ACP can be an underlying approach for the storage of foxtail millets.

Due to some limitations, such as bad flavor and taste, low stability and solubility, etc., some food raw materials with nutritious value cannot be applied on a large scale in the food industry. Therefore, pretreatment is an effective method to improve their application value and health attributes. Zhang et al. studied the effect of phytochemical properties and health benefits of Tartary buckwheat flour by extrusion treatment. Results showed that pre-gelatinization of Tartary buckwheat flour by extrusion treatment can improve the antioxidant capacity, α-glucosidase inhibitory activity, and relatively mild α-amylase inhibitory activity, which suggests that it could be used as an ideal functional food resource. In another study, Ashraf et al. observed that curcumin derived from fresh rhizomes (*Curcuma longa*) by conventional (CSE) and supercritical fluid (SFE) extractions was microencapsulated using a mixture of gelatin and maltodextrin. Results showed that microencapsulation of Curcuma has better bioavailability due to its sufficient gastrointestinal residence period and stability in the digestive tract, compared to turmeric powder. Moreover, Yu et al. conducted a study to overcome astaxanthin (AST)'s serious limitations of poor water solubility and structural stability. The carrier-free astaxanthin nanoparticles (AST-NPs) were prepared, and physicochemical properties and bioactivity capacity were determined. Results showed that AST-NPs have a high loading capacity (94.57 ± 0.7%), a small average size (74.29 ± 7.92 nm), and better antioxidant activity compared to free AST. Therefore, the authors suggested that AST-NPs can become novel functional foods.

To improve the flavor and stabilize the quality of fermented food, such as fermented tea, cheese, and fermented condiment, it is necessary to study the relationship between microbial species changes and flavor ingredients during the fermentation process. In their research article, Ma et al. studied the relationship between the changes in microbial communities and volatile components of fermented minced peppers (FMP). Results showed that 17 genera were core functional microorganisms of FMP by high-throughput sequencing. Meanwhile, 64 volatile compounds were detected by GC-MS of FMP. Moreover, *Cladosporium* and *Hansenpora* were, respectively, significantly correlated with the formation of nine and six volatiles, which could guide the industrial production of FMP with unique flavors and consistent quality.

Author contributions

Z-HZ: writing—original draft and writing—review and editing. Z-WL: writing—review and editing. DN: investigation and writing–review and editing. All authors contributed to the article and approved the submitted version.

Funding

This research was funded by the National Natural Science Foundation of China (grant numbers 32101893 and 32102133), the Natural Science Foundation of Guangxi Province (grant number 2021JJA130374), and the Science and Technology Plan Project of Guangxi Province (grant number 2022AC21255).

Conflict of interest

The authors declare that the research was conducted in the absence of any commercial or financial relationships that could be construed as a potential conflict of interest.

Publisher's note

All claims expressed in this article are solely those of the authors and do not necessarily represent those of their affiliated organizations, or those of the publisher, the editors and the reviewers. Any product that may be evaluated in this article, or claim that may be made by its manufacturer, is not guaranteed or endorsed by the publisher.

frontiers | Frontiers in Nutrition

TYPE Original Research
PUBLISHED 15 September 2022
DOI 10.3389/fnut.2022.1012901

OPEN ACCESS

EDITED BY
Debao Niu,
Guangxi University, China

REVIEWED BY
Suyun Lin,
Jiangxi Agricultural University, China
Ibrahim Khalifa,
Huazhong Agricultural University, China

*CORRESPONDENCE
Yanyan Huang
huang_yanyan@fosu.edu.cn
Xin-An Zeng
xazeng@scut.edu.cn

SPECIALTY SECTION
This article was submitted to Nutrition and Food Science Technology, a section of the journal Frontiers in Nutrition

RECEIVED 06 August 2022
ACCEPTED 15 August 2022
PUBLISHED 15 September 2022

CITATION
Wang L-H, Chen L, Zhao S, Huang Y, Zeng X-A and Aadil RM (2022) Inactivation efficacy and mechanisms of atmospheric cold plasma on *Alicyclobacillus acidoterrestris*: Insight into the influence of growth temperature on survival. *Front. Nutr.* 9:1012901. doi: 10.3389/fnut.2022.1012901

Inactivation efficacy and mechanisms of atmospheric cold plasma on *Alicyclobacillus acidoterrestris*: Insight into the influence of growth temperature on survival

Lang-Hong Wang[1,2], Lin Chen[2], Siqi Zhao[3], Yanyan Huang[1]*, Xin-An Zeng[1]* and Rana Muhammad Aadil[4]

[1]School of Food Science and Engineering, Guangdong Provincial Key Laboratory of Intelligent Food Manufacturing, Foshan University, Foshan, China, [2]College of Food Science and Technology and College of Life Sciences, Northwest University, Xi'an, China, [3]School of Food Science and Engineering, South China University of Technology, Guangzhou, China, [4]National Institute of Food Science and Technology, University of Agriculture, Faisalabad, Pakistan

The bactericidal effect of dielectric barrier discharge-atmospheric cold plasma (DBD-ACP, 20, and 30 kV) against *Alicyclobacillus acidoterrestris* on the saline solution and apple juice was investigated. Results show that DBD-ACP is effective for the inactivation of *A. acidoterrestris* by causing significant changes in cell membrane permeability and bacterial morphology. The effect of culture temperatures on the resistance of *A. acidoterrestris* to DBD-ACP was also studied. *A. acidoterrestris* cells grown at 25°C had the lowest resistance but it was gradually increased as the culture temperature was increased (25–45°C) ($p < 0.05$). Moreover, results from Fourier transform infrared spectroscopy (FT-IR) and Gas Chromatography-Mass Spectrometer (GC-MS) analysis showed that the increase in the culture temperature can gradually cause the decreased level of cyclohexaneundecanoic acid in the cell membrane of *A. acidoterrestris* ($p < 0.05$). In contrast, cyclopentaneundecanoic acid, palmitic acid, and stearic acid showed an increasing trend in which the fluidity of the bacterial cell membrane decreased. This study shows a specific correlation between the resistance of *A. acidoterrestris* and the fatty acid composition of the cell membrane to DBD-ACP.

KEYWORDS

***Alicyclobacillus acidoterrestris*, cold plasma, scanning electron microscopy, FT-IR, GC-MS**

Introduction

Alicyclobacillus acidoterrestris is a kind of spore-producing acidophilic heat-resistant bacteria. Many studies have shown that this bacterium is one of the main reasons for causing the spoilage of various fruit juices such as apple juice, orange juice, and grape juice (1–3). The fruit juice contaminated with *A. acidoterrestris* did not show obvious

rancidity or swelling at the initial stage. However, if its metabolites, (2, 6-dibromophenol, and 2, 6-dibromophenol) produced by *A. acidoterrestris* cells can cause quality issues by increasing turbidity as well as formation of white precipitates in the juice. These losses can cause problems for fruit juices by causing huge financial losses (4). Keeping in mind the potential risk to the quality of fruit and its beverages, *A. acidoterrestris* has been proposed as a reference microorganism for quality control in the juice industry. Heat pasteurization is the most common method in fruit juice processing. However, due to the acidophilic and heat-resistant characteristics of *A. acidoterrestris* cells, it is difficult to inactivate by heat pasteurization. Moreover, thermal processing could easily cause flavor components and heat-sensitive nutrients such as vitamins that significantly damage fruit juice (5). Therefore, *A. acidoterrestris* is an actual problem that urgently needs to be solved in fruit juice processing. It is essential to seek a safe, reliable, and effective means to kill *A. acidoterrestris* with less influence on fruit juice components.

Nonthermal plasma technology is an aggregate formed by atoms, electrons, charged particles, free radicals, and ultraviolet photons generated by ionized or partially ionized gases (6–8). Cold plasm can inactivate various microbial vegetative cells in food at low temperatures (generally lower than 40°C) and short time, but it has little effect on the quality of the food itself. So it has been considered as a potential technology for sterilization of various types of food (9). Studies have shown that many factors including gas composition, voltage and treatment time, and food characteristics affect the efficiency of cold plasma sterilization. Additionally, the inherent characteristics, including cell structure and intrinsic protective mechanisms of microorganisms and environmental factors, are also essential factors (10, 11). Temperature and pH are two of the common factors that can induce changes in the resistance of bacteria to decontamination processing, including plasma, which in turn affects sterilization efficiency (7, 12–14). However, from the results reported so far, the studies about temperature-mediated bacterial tolerance to plasma are obscure and insufficient (14, 15). Because of the potential hazard of *A. acidoterrestris* in the juice industry, it is of great significance to fully understand the bactericidal effect and influencing factors of non-thermal plasma on *A. acidoterrestris* to promote the application of this technology in juice sterilization. Therefore, this work is mainly aimed to investigate the bactericidal effect and mechanism for the inactivation of *A. acidoterrestris* cells by dielectric barrier discharge-atmospheric cold plasma (DBD-ACP). The changes in cell membrane permeability and morphology of *A. acidoterrestris* cells before and after DBD-ACP treatment were evaluated by an inverted fluorescence microscope, intracellular leakage contents, and scanning electron microscope. The effects of growth temperatures on the resistance of *A. acidoterrestris* cells to DBD-ACP were also studied based on cell membrane fluidity and membrane fatty acid composition from Fourier transform infrared spectroscopy (FT-IR) and gas-mass spectrometry. This work is expected to provide insight into the inactivation properties, mechanism, and resistance under various growth temperatures of *A. acidoterrestris* cells induced by DBD-ACP.

Materials and methods

Bacterial cultures

The bacterial strain of *A. acidoterrestris* ATCC 49025 was purchased as a lyophilized culture from the Microbial Culture Collection Center of Guangdong Institute of Microbiology (Guangzhou, China). *A. acidoterrestris* cells were revived by transferring the lyophilized culture to an AAM liquid medium (pH 4.0, per liter of deionized water containing 0.2 g ammonia sulfate, 0.25 g calcium chloride, 0.5 g magnesium sulfate, 2.0 g yeast extract, 5.0 g glucose, and 3.0 g monopotassium phosphate) and incubated overnight at 45°C in a shaker (200 rpm). A loopful of the culture of *A. acidoterrestris* cells suspension was inoculated onto cooled AAM agar medium and incubated at 45°C for 36 h. Then a single colony was transferred to a 500 mL-conical flask containing 200 mL of sterile AAM liquid medium and incubated to a late log phase of growth at 45°C. Pre-cultured *A. acidoterrestris* cells were transferred to a fresh AAM liquid medium (200 mL, OD 600 nm ≈ 0.10) for incubation at 25, 35, 45 and 55 °C.

DBD-plasma treatment

The cultured *A. acidoterrestris* was harvested by centrifugation at 4,000 × g for 10 min at 4°C. The collected pellet was washed with sterile water thrice and resuspended into sterilized saline water or apple juice (JinLiuYuan, not from concentration). It was prepared to be treated with DBD-ACP (CTP-2000K plasma equipment, equipped with DBD-50 reactor, Nanjing Suman Co., Ltd. Nanjing, China) at 20 kV and 30 kV for 0, 0.5, 1.0, 1.5 and 2.0 min, where the distance between the upper plate and liquid surface was 4 mm, and the frequency was 1.0 kHz. The treated bacterial solution was serially diluted, and the spread plate was counted, and cultured at 45°C for 36–48.0 h to detect the total number of colonies (CFU/mL). The lethality was analyzed according to the change in the number of colonies before (N_0) and after (N) DBD-ACP treatment. Each treatment was repeated three times and the experimental results were averaged.

Cell membrane permeability of *A. Acidoterrestris*

A. acidoterrestris cells were subjected to DBD-ACP treatment under 30 kV for 0, 0.5, 1.0 and 2.0 min. After DBD-ACP treatment, 10 μL of *A. acidoterrestris* cells

suspension was added to 990 μL of sterilized saline water containing 3.0 μL of propidium iodide (PI, 1 mg mL^{-1}, Beijing Soleibao Technology Co., Ltd., Beijing, China) and incubated darkly at room temperature for 20 min. The red fluorescence of *A. acidoterrestris* cells from PI staining was observed by an inverted fluorescence microscope (Nikon Eclipse Ti2-A, Nikon Instruments Co. LTD., Tokyo, Japan). Additionally, membrane permeabilization was also evaluated by measuring the leakage of nucleic acids including DNA and RNA, and proteins from *A. acidoterrestris* cells using a NanoDrop spectrophotometer (ND-2000, Thermo Fisher Scientific, Massachusetts, USA) to record the absorbance at 260 nm and 280 nm according to the method reported by Cai et al. (16).

Scanning electron microscopy

Bacterial sample preparation for morphological observation was carried out regarding the previous method (17). *A. acidoterrestris* cells were collected by centrifuging at 4,000 × *g* for 5.0 min and then treated with 2.5% (v/v) glutaraldehyde in PBS buffer were stored overnight at 4°C. After centrifugation, the bacterial samples were dehydrated by gradient using 30–100% ethanol solution. The dehydrated cells were treated with tert-butanol twice. The samples were dropped on silver paper for vacuum freeze-drying, and the morphological changes of *A. acidoterrestris* cells could be observed after spraying gold.

Cell membrane fatty acid extraction and analysis

Fatty acid composition of *A. acidoterrestris* cells was detected using the method previously reported by Pan et al. (18). After membrane fatty acid extraction and methylation, the fatty acid profiles were detected by gas chromatography-mass spectrometry (GC-MS) (8890B—7000D, Agilent Technologies, Palo Alto, California, USA) by matching the mass spectra with the mass spectral library 2016 of the National Institute of Standards and Technology (NIST, Gaithersburg, Maryland, USA) and the retention times in the bacterial acid methyl ester (BAME) mix solution (analytical standard, Sigma-Supelco, Bellefonte, PA, USA).

Fourier transform infrared spectroscopy analysis

The lyophilized *A. acidoterrestris* cells were analyzed by infrared spectrum on Bruker Vetex70 FT-IR spectrometer (Bruker, Germany). The spectrum collection range was 600–4,000 cm^{-1} and the resolution was 4 cm^{-1}. The spectral data is smoothed, normalized and converted to a second derivative to improve peak resolution using the Savtitzky-Golay algorithm (19).

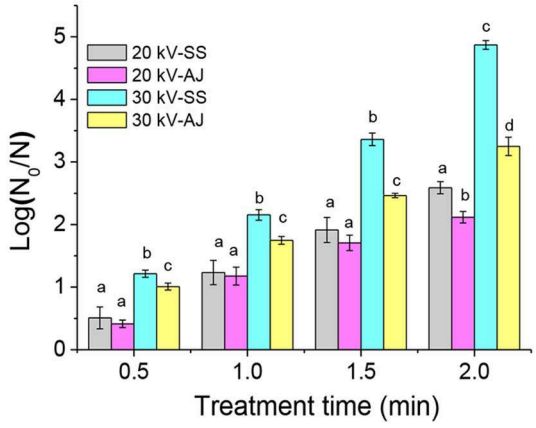

FIGURE 1
Inactivation of *A. acidoterrestris* by DBD-plasma at 20 kV and 30 kV on apple juice (AJ) and 0.85% sterile saline solution (SS). Different letters (a–d) on the top of the bars denote significant differences ($p < 0.05$).

Statistical analyses

Statistical analysis was performed using OriginPro 8.0 (Origin Lab, Northampton, MA, USA) in triplicate with three independent experiments and results expressed as means ± SD. Analysis of variance (ANOVA) followed by Tukey's test was carried out using SPSS 22.0 software (IBM, NY, USA), and values were considered significantly different if $p < 0.05$.

Results and discussion

Inactivation of *A. Acidoterrestris* cells by DBD-ACP

The inactivation efficacy of DBD-ACP under various treatment voltage and time against *A. acidoterrestris* cells in 0.85% sterile saline solution and apple juice is shown in Figure 1. For *A. acidoterrestris* cells in 0.85% sterile saline solution, 0.5 and 1.2-log reductions occurred for the exposure of DBD-ACP at 20 kV for 0.5 and 1 min and increased to approximately 1.9- and 2.5-log reductions for 1.5 and 2 min. Comparatively, DBD-ACP exhibited a much stronger bactericidal effect on *A. acidoterrestris* cells at 30 kV, which induces the bacterial populations was inactivated by approximately 1.2, 2.1, 3.4 and 4.9-log reductions with the same treatment time.

A similar trend of DBD-ACP inactivation was detected for *A. acidoterrestris* cells in apple juice. However, DBD-ACP has

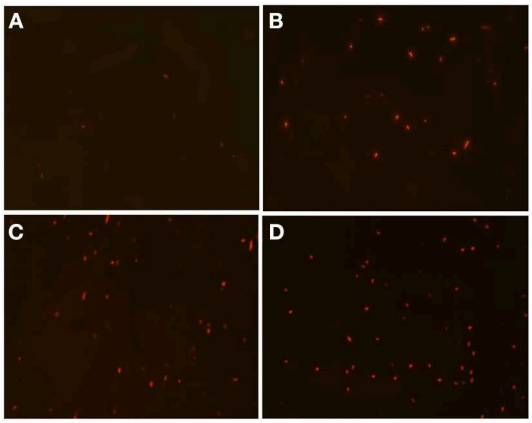

FIGURE 2
The PI staining *A. acidoterrestris* cells treated by DBD-plasma at 30 kV for 0 **(A)**, 0.5 min **(B)**, 1.0 min **(C),** and 2.0 min **(D)**, respectively.

a relatively lower inactivation against *A. acidoterrestris* cells in apple juice than in sterile saline solution. A similar work conducted by Mahnot et al. (20), found that *S. enterica serovar Typhimurium* in distilled water and the inactivation (>5 log-reduction) was observed much higher than in other simulating tender coconut water. Moreover, they also suggested that the presence of phosphate and Mg^{2+} ions reduced the inactivation of *S. enterica serovar Typhimurium*. Therefore, it could be inferred that the presence of nutrients and ions in apple juice may help to repair and recover *A. acidoterrestris* cells after DBD-ACP treatment.

Membrane permeability of *A. Acidoterrestris* cells

The cell membrane permeability of *A. acidoterrestris* cells after DBD-ACP treatment was observed by staining with PI, which incorporates genomic DNA by emitting red fluorescence if the bacterial cell membrane is permeable (21). As shown in Figure 2A, *A. acidoterrestris* cells without DBD-ACP treatment did not show much red fluorescence. Whereas the DBD-ACP treated *A. acidoterrestris* was stained with PI to emit higher degrees of red fluorescence with increasing time (Figures 2B–D). These results indicated that the plasma-treated *A. acidoterrestris* cell membrane was damaged, resulting in an increased permeability.

The cell membrane permeability induced by DBD-ACP may increase the leakage of cytoplasmic contents, including nucleic acids and proteins. Thus, the leakage of cytoplasmic contents of *A. acidoterrestris* cells was further determined in this study. The results of protein leakage of the DBD-ACP treated and untreated bacteria are shown in Figure 3A. The protein content in the untreated bacteria group was about 0.25 mg/L. However, this leakage of protein increases to 1.61 and 2.72 mg/L after being treated by DBD-ACP at 20 and 30 kV for 2.0 min. The nucleic acid concentration of *A. acidoterrestris* cells with or without DBD-ACP treatment presented a similar behavior (Figure 3B). As compared to untreated cells, the nucleic acid concentration was increased from 4.12 and 3.98 ng/μL to 34.31 and 50.42 ng/μL for *A. acidoterrestris* cells treated by DBD-ACP at 20 and 30 kV for 2.0 min, respectively. These results were consistent with the results obtained by PI staining with an inverted fluorescence microscope. Qian et al. (2022) found that the leakage of nucleic acids and proteins of *L. monocytogenes* and *S. enteritidis* induced reached the maximum content by cold plasma at 90 and 150 s, respectively (22). Olatunde et al. (23) reported a loss in cell membrane integrity of bacteria, including *L. monocytogenes*, *S. aureus*, *P. aeruginosa*, *E. coli,* and *V. parahaemolyticus*, which was measured by the increased conductivity and DNA content in supernatant induced by DBD-ACP treatment. In conclusion, the changes in membrane permeability that causes the formation of reversible permeabilization in bacterial cells were responsible for the lethal damage of *A. acidoterrestris* after DBD-ACP treatment.

Morphological changes of *A. Acidoterrestris* cells induced by DBD-ACP

Figures 4A–D show the cell morphological changes of *A. acidoterrestris* cells before and after DBD-ACP treatment at the voltage of 30 kV for 0.5, 1.0 and 2.0 min. Results showed that the untreated *A. acidoterrestris* cells showed a short rod-like shape with a smooth surface, while the DBD-ACP treated cells showed wrinkles, shrinkage, and deformation on the surface. These results suggested that *A. acidoterrestris* cells exhibit significant changes in their morphology with the increasing treatment. Such cell morphological deformations have been observed in *E. coli*, *L. monocytogenes*, and *S. enteritidis* after cold plasma treatment (24–26). Thus, it could be inferred that the lethal effect of *A. acidoterrestris* cell could be attributed to its destructive effects on the bacterial membrane with the leakage of cytoplasmic components by reactive oxygen species (ROS), particularly O_3 and atomic oxygen generated during the processing of DBD-ACP treatment.

Effect of growth temperature on the resistance of *A. Acidoterrestris* to DBD-ACP

The temperature, pH, and other growth conditions play a vital role in bacterial resistance against inactivation technologies

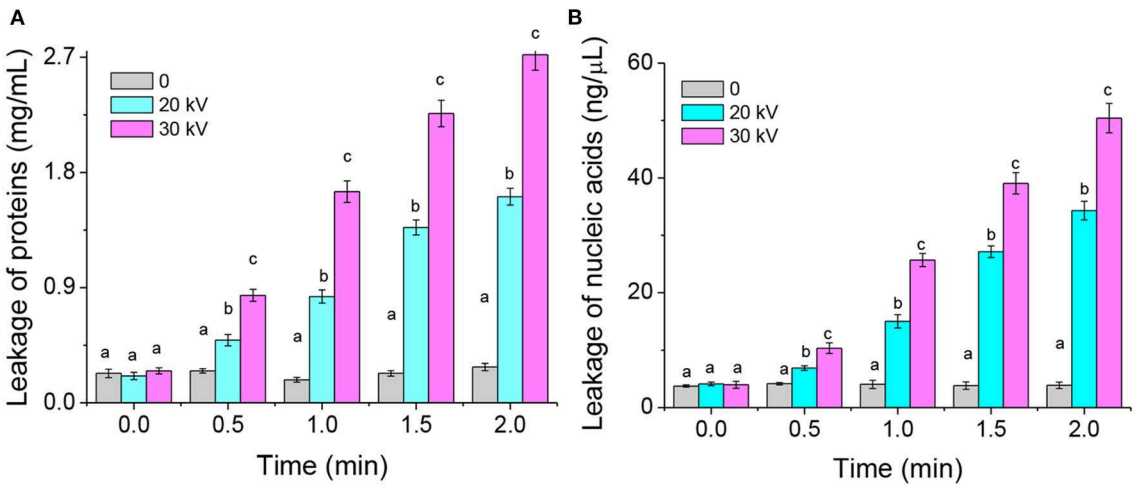

FIGURE 3
Leakage of proteins **(A)** and nucleic acids **(B)** from *A. acidoterrestris* cells induced by DBD-ACP. Different letters (a-d) on the top of the bars denote significant differences ($p < 0.05$).

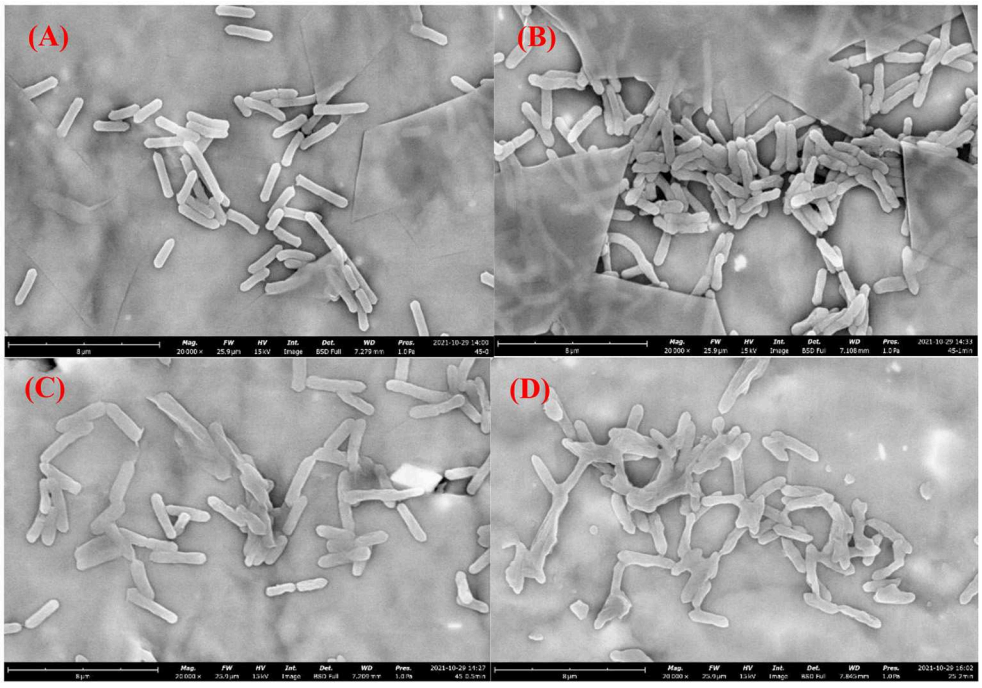

FIGURE 4
Morphological images of *Alicyclobacillus acidoterrestris* cells growth at 45°C exposure to DBD-plasma at 30 kV for 0 **(A)**, 0.5 **(B)**, 1.0 **(C)** and 2.0 min **(D)**, respectively.

such as thermal, acidic, high-pressure, and pulsed electric field treatments. After being grown at 25, 35, 45, and 55°C to the late-logarithmic phase, *A. acidoterrestris* cells were collected and re-suspended on different systems (sterilized saline solution and apple juice) for DBD-ACP treatment. As shown in Figure 5, the inactivation of *A. acidoterrestris* cells increases with the increasing treatment voltage and time. On the sterilized saline solution, the inactivation levels of *A. acidoterrestris* cells cultivated at 25°C that increased from 1.8 to 3.8 log-reduction and from 1.9 to 6.7 log-reduction for DBD-ACP at 20 kV and

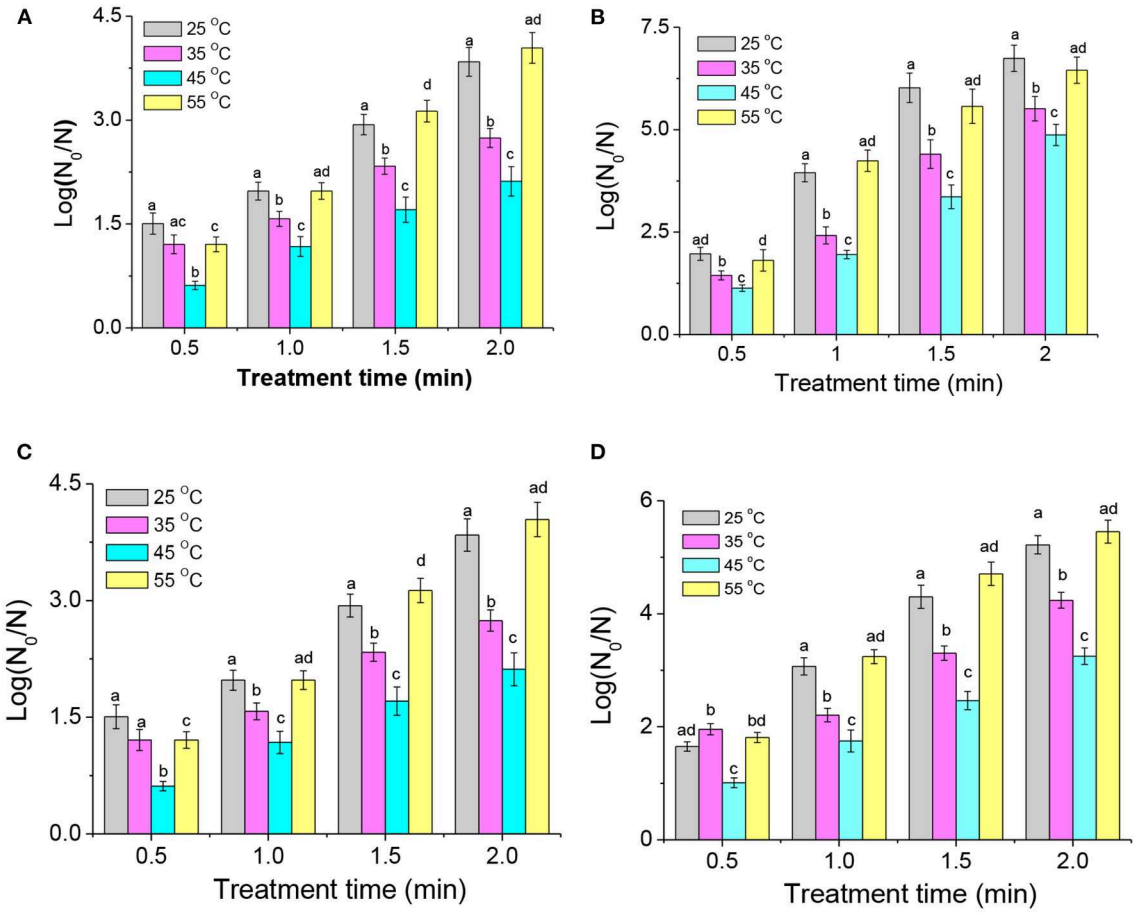

FIGURE 5
The effect of growth temperatures on the resistance of *A. acidoterrestris* cells on the sterile saline solution to DBA-ACP under 20 kV **(A)** and 30 kV **(B)**, and apple juice with 20 kV **(C)** and 30 kV **(D)** for different treatment times. Different letters (a–d) on the top of the bars denote significant differences ($p < 0.05$).

30 kV with treatment time from 0.5 to 2.0 min. Bacterial cells at different growth temperatures exhibited different resistance to DBD-ACP treatment. Among them, *A. acidoterrestris* cells grown at 45°C were found to be the most resistant, followed by at 35°C. Interestingly, the resistance of *A. acidoterrestris* cells at 25 and 55°C were similar ($p > 0.05$), and more sensitive to DBD-ACP than at 45 and 35°C no matter on the sterilized saline solution (Figures 5A,B) and apple juice (Figures 5C,D).

For the sterilized saline solution, DBD-ACP treatment at the voltage of 20 kV with 1.0 min resulted in a 2.3 and 2.4 log-reduction ($p>0.05$) of *A. acidoterrestris* cultivated at 25 and 55°C, respectively. In contrast, the degree of inactivation of *A. acidoterrestris* was significantly lower by 1.6 log-reduction and (1.0 logs) ($p < 0.05$) for being cultivated at 35°C and 45°C, respectively. As the treatment time increased to 2.0 min, the inactivation of *A. acidoterrestris* cultured at different temperatures increased significantly. However, the inactivation behavior of *A. acidoterrestris* by DBD-ACP treatment was still similar. Specifically, the inactivation of *A. acidoterrestris* grown at 55°C was the highest that reaching to 5.3 log-reduction after DBD-ACP treatment, followed by *A. acidoterrestris* cultured at 25°C (4.8 log-reductions), and the inactivation rate was significantly decreased to 3.4 and 2.6 log-reduction for cells grown at 35 and 45°C, respectively ($p < 0.05$). Additionally, when the treatment voltage was 30 kV with the same treatment time of 2.0 min (Figure 5B), then the inactivation of *A. acidoterrestris* cultured at 25 and 55°C reached 6.7 and 6.4 log-reduction, respectively. The amount of inactivation at 35 and 45°C was significantly reduced ($p < 0.05$) to 5.5 and 4.9 log-reduction, respectively. The effect of growth temperatures on *A. acidoterrestris* cells exposed to DBD-ACP treatment with apple juice has similar results. For example, *A. acidoterrestris* cells grown at 25 and 55°C, DBD-ACP induced 5.2 and 5.4 log-reductions at 30 kV for 2 min, while *A. acidoterrestris* cells cultivated at 35 and 45°C resulted in 4.2 and 3.2 log reductions of viability, respectively. These results suggest that the resistance of *A. acidoterrestris* to DBD-ACP gradually increased with the increase of culture temperature in the range of 25 ∼ 45°C expect 55°C. The above results concerning the effect of growth temperature on plasma inactivation are

inconsistent with the resistance data reported by Pan et al. (27) revealing that the inactivation of *L. monocytogenes* cultivated at 10°C was found to be the most resistant to plasma exposure. Additionally, Fernandez et al. (15) found that the effect of growth temperatures (20, 25, 37, and 45°C) on the inactivation efficiency of *Salmonella enterica serovar Typhimurium* by cold plasma was insignificant (15). This inconsistency may be due to the different bacteria owning various adaptive mechanisms to temperature, resulting in different consequences regarding the effect of growth temperature on the resistance to DBD-ACP. However, the present study was similar to the literature showing that bacteria such as *E. coli*, *L. monocytogenes,* and *S. aureus* inoculated at low cultured temperatures showed high sentences to thermal or some nonthermal processing techniques including pulsed electrical field, high-pressure processing and atmosphere uniform glow discharge plasma (13, 14, 28). For example, Kayes et al. (14) found that *E. coli*, *S. aureus*, and *B. subtilis* cultured at 35°C were more tolerant to air plasma than bacteria cultured at 10°C (14).

Analysis of the cell membrane fluidity

The distinct difference in resistance to DBD-ACP may be responsible for the alterations of cell membrane fluidity and fatty acid composition of *A. acidoterrestris* at the different growth temperatures. The cellular membrane is one of the main targets being attacked by ROS and free radicals induced by cold plasma. As membrane fluidity is distinctive for the exchange of nutrients, ions, and regulatory molecules of cells, which directly affects the permeation of ROS into bacterial cells (7, 29). Therefore, the membrane fluidity was worth investigating.

FT-IR is a sensitive, non-destructive technique commonly used to detect changes in bacterial cell composition (30, 31). In Figure 6A, the FT-IR spectra of *A. acidoterrestris* cultured at different temperatures showed some typical characteristic peaks: 1,070 cm^{-1} and 1,234 cm^{-1} are typical P = O asymmetric and symmetric stretching vibration peaks, representing the main chain of nucleic acid and phosphodiester, respectively; while 1,399 cm^{-1} is the asymmetric and symmetric deformation of CH_3– and CH_2– of the protein; 1,542 cm^{-1} is the N-H characteristic vibration peak of protein amide II band; 1,655 cm^{-1} is the absorption peak near 1 is mainly the vibration peak of protein amide I, which is assigned to C=O stretching vibration; 2,928 cm^{-1} is the asymmetric stretching vibration peak of ω-cyclic fatty acid acyl chain υsCH_2–. The above results in agreement with the previous study (32), indicating that the basic structure of the bacteria cultured at different temperatures is consistent. The differences in the infrared spectra exhibited by *A. acidoterrestris* at different temperatures are not noticeable.

To further study the changes in fatty acid and fluidity of the cell membrane of *A. acidoterrestris* at different temperatures. In this study, the 2,800 ∼ 3,000 cm^{-1} infrared spectral data were processed by the second derivative to enhance spectral resolution. It can be seen from Figure 6B that the spectra of this band at different culture temperatures show specific differences, indicating that different culture temperatures have certain effects on the composition of fatty acids in the cell membrane of *A. acidoterrestris*. According to the asymmetric stretching vibration of ω-cyclic fatty acid acyl chain υsCH_2– near 2,928 cm^{-1}, the changes in cell membrane fluidity at different temperatures were analyzed, and it was found that when the culture temperature increased from 25 to 55°C, the peak frequency from 2,927 cm^{-1} drops to 2,923 cm^{-1}. Previous studies suggested that the peak frequency of fatty acid acyl chain υsCH_2- is related to cell membrane fluidity. It is generally believed that the larger the value, the greater the fluidity of the cell membrane, and *vice versa* (19). Thus, it can be inferred that the membrane fluidity of *A. acidoterrestris* cells decreased gradually with the increase in culture temperature.

Membranes fatty acid analysis of *A. Acidoterrestris* Cells

Previously, studies have shown that bacteria at different temperatures and pH alter membrane fatty acid composition in order to maintain a proper cell membrane fluidity and to ensure the normal functioning of membrane physiology (33, 34). For example, the saturated fatty acid content in *Shewanella putrefaciens* cell decreased with the decrease of incubation temperature (30, 10 and 4°C), while the content of palmitoleic acid (C16:1), lauric acid (C12:0), and myristic acid (C14:0) increased (33). Similarly, *E. coli* cells were apt to increase the proportions of saturated fatty acids at the expense of unsaturated fatty acids, as reported by Liu et al. (28), who found that the proportion of unsaturated fatty acids decreased from 51.63 to 29.58% as the growth temperature increased from 15 to 45°C. In a recent study, *A. acidoterrestris* was found to increase the level of cyclic fatty acids with the expense of saturated fatty acids to improve the acid-tolerance capability (3).

The membrane fatty acid composition of the cell of *A. acidoterrestris* cultured at different temperatures is shown in Table 1. There are five main types of fatty acids detected, namely myristic acid (C14:0), palmitic acid (C16:0), stearic acid (C18:0), cyclohexaneundecanoic acid (ω-cyclohexyl C17:0) and cyclopentanetridecanoic acid (ω-cyclopentane C18:0), which has good consistency with the results obtained by Zhao et al. (3). In this study, *A. acidoterrestris* as an acidophilic heat-resistant bacterium and ω-cyclohexyl C17:0 and ω-cyclopentane C18:0 accounted for more than 80%, which is good in consistence with previous studies that ω-cyclic fatty acids appear in the cell membrane of acidophilic, heat-resistant bacteria, in which the proportion could reach 60 to 90% (35, 36). The fatty acid components including C16:0, C18:0, ω-cyclohexyl C17:0, and ω-cyclopentane C18:0 showed a significant change under various

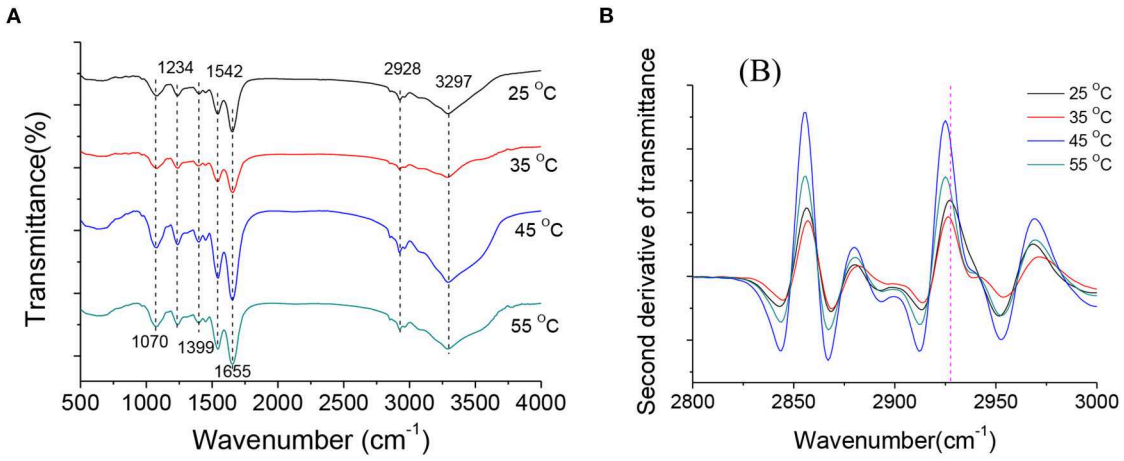

FIGURE 6
Raw FT-IR spectra of *A. acidoterrestris* at late log phase under different growth temperatures **(A)** and calculated second derivatives of FT-IR spectra in the spectral range of 2,800–3,000 cm^{-1} **(B)**.

TABLE 1 The proportions of primary membrane fatty acid composition of *A. acidoterrestris* under different growth temperatures.

Fatty acid composition (%)	Growth temperature			
	25°C	35°C	45°C	55°C
C14:0	1.21 ± 0.05a	1.27 ± 0.07a	1.23 ± 0.12a	0.66 ± 0.09a
C16:0	4.36 ± 0.52a	5.79 ± 0.84b	8.19 ± 0.98c	11.35 ± 1.49d
C18:0	2.42 ± 0.49a	3.61 ± 0.33b	4.53 ± 0.88bc	5.85 ± 1.48c
ω-cyclohexyl C17:0	81.09 ± 1.23a	72.37 ± 1.63b	59.23 ± 1.53c	49.86 ± 1.83d
ω-cyclopentane C18:0	10.83 ± 1.53a	16.94 ± 1.81b	26.81 ± 1.47c	32.21 ± 1.86d
SFAs	7.99 ± 1.06a	10.67 ± 1.24ab	13.95 ± 1.98c	17.86 ± 3.06d
CFAs	91.92 ± 2.76a	89.31 ± 3.44ab	86.04 ± 3.0b	82.07 ± 3.69bc

Values followed by a different letter (a–d) in the same line are significantly different ($p < 0.05$).

culture temperatures. Among them, the relative content of ω-cyclohexyl C17:0 was the highest when the culture temperature was 25°C, accounting for 81.9%. With the increase in culture temperature (35-55°C), the proportion of ω-cyclohexyl C17:0 was gradually decreased, accounting for 72.37, 59.23, and 49.86%, respectively ($p < 0.05$). In contrast, the level of ω-cyclopentane C18:0 showed an upward trend, increasing from 10.83 to 32.21% with an increased temperature of 25 to 55°C, respectively. In a study, as compared with straight-chain fatty acids, cyclic fatty acids can reduce the *trans-gauche* isomerization of lipid chains, thereby increasing the order degree of lipid chains and the area of lipid layers, and reducing the fluidity of cell membranes (37, 38). However, a study has shown that the loose packing of ω-alicyclic fatty acids in the cell membrane is in the disorder of lipid tails increasing membrane fluidity, and the larger the ring size (3- to 7-membered cycloalkyl) in ω-alicyclic fatty acids, the disorder degree is greater (36). On the other hand, the relative proportion of C16:0 and C18:0 also increased, i.e., from 4.36, 2.43% at 25°C and to 11.35 and 5.85%, at 55°C. Generally, straight-chain fatty acids, including C16:0 and C18:0 are neatly arranged in the cell membrane, and the stacking is good and tight. Therefore, the higher the proportion of straight-chain fatty acids in the cell membrane, the lower the fluidity of the cell membrane (17, 39, 40). Thus, it could be inferred that the decreased cell membrane fluidity with the increased culture temperature of *A. acidoterrestris* cells are the results of an increase of C16:0, C18:0, and ω-cyclopentane C18:0.

Implication for the resistance of *A. Acidoterrestris* cells with membrane fatty acid profile

The stacked loose ω-alicyclic fatty acids can protect acidophilus from high temperature and low pH conditions by forming a dynamic barrier that restricts lipid diffusion and H^+ transmembrane diffusion (36). However, different from the mechanism of high temperature and low acid action, various reactive oxygen species and reactive nitrogen components such as ozone, hydroxyl radicals, and singlet oxygen radicals generated by plasma treatment, which will damage the function of fatty acids, induce lipids, especially the peroxidation of unsaturated fatty acids even destroys the cell membrane and leads to cell lysis and bacterial death (25, 41). In addition, the free radicals generated by plasma treatment can also cross the cell membrane and enter the cytoplasm to attack the biological macromolecules such as nucleic acids

(25). In this study, *A. acidoterrestris* as an acidophilic heat-resistant bacteria, and ω-cyclohexyl C17:0 and ω-cyclopentane C18:0 accounted for more than 80%. With the increase in culture temperature (25–55°C), the total content of straight-chain fatty acids in the cell membrane of *A. acidoterrestris* increased gradually from 8.0 to 17.86% ($p<0.05$). In contrast, the content of cyclic fatty acids decreased from 92.92 to 82.07%. It can be inferred that loosely stacked ω-alicyclic fatty acids (especially ω-cyclohexyl C17:0) may be more conducive to the accumulation of oxygen free radicals and other reactive components in the cell membrane, that not only cause damage to the cell membrane but also increases oxygen free radicals and other components entry and cause cell death. In contrast, the well-arranged, packed, tight straight-chained fatty acids may prevent the entry of these harmful substances to a certain extent. Therefore, the decrease of cyclic fatty acid content and the increase of straight-chain fatty acids caused by the increase in culture temperature may be the reason for the increase in plasma tolerance of *A. acidoterrestris* in the culture temperature range of 25 to 45°C. It is worth mentioning that the content of straight-chain fatty acids in the cell membrane of *A. acidoterrestris* was the highest when cultured at 55°C, but these cells are highly sensitive to DBD-ACP treatment. These results may be related to the aerobic metabolism of *A. acidoterrestris* was improved at higher temperatures (55°C). Reportedly, the generation of intracellular reactive oxygen species by aerobic metabolism was increased with environment temperature (42). Therefore, it could speculate that a growth temperature of 55°C might cause remarkable effects on the plasma-mediated accumulated abundance of intracellular ROS inducing bacteria to be more sensitive to DBD-ACP treatment (7, 43).

Conclusions

The inactivation of DBD-ACP on *A. acidoterrestris* and effects of growth temperatures on their resistance was investigated. Results show that DBD-ACP is effective in the inactivation of *A. acidoterrestris* by causing a significant increase in cell membrane permeability with leakage of cytoplasmic contents and changes in bacterial morphology. *A. acidoterrestris* cells at different growth temperatures (25, 35 45 and 55°C) exhibited different resistance to DBD-ACP treatment. *A. acidoterrestris* cells grown at 45°C were found to be the most resistant, followed by at 35°C, 25°C and 55°C. The growth temperatures of *A. acidoterrestris* induced noticeable modifications of membrane fatty acid profile and fluidity during cultivation. For example, the most abundant fatty acids, i.e. ω-cyclohexyl C17:0 and ω-cyclopentane C18:0, changed from 81.09% to 49.86% and 10.83% to 32.21% at the growth temperatures of 25 to 55°C. Growth temperature-mediated alterations in fatty acid profile and membrane fluidity of *A. acidoterrestris* were associated with its viability to DBD plasma exposure and a significant increase in resistance with increased growth temperatures from 25 to 45°C. It is worth mentioning that *A. acidoterrestris* cells grown at 55°C are highly sensitive to DBD-ACP treatment. These results may be related to the growth temperature of 55°C causing remarkable effects on the plasma-mediated accumulated abundance of intracellular ROS inducing bacteria to be more sensitive to DBD-ACP treatment. In conclusion, this study demonstrated DBD-ACP is a promising technology in inactivating *A. acidoterrestris*, but it is worth noting growth temperature plays a role in the resistance of *A. acidoterrestris* to DBD-ACP, suggesting a potential way to improve the sterilization efficiency in practical application by adjusting the preconditioning temperature. However, more investigations are still needed to further understand how *A. acidoterrestris* regulate membrane fatty acid and fluidity based on the genetics and metabolomics in response to various temperature.

Data availability statement

The original contributions presented in the study are included in the article/supplementary material, further inquiries can be directed to the corresponding authors.

Author contributions

L-HW: conceptualization, methodology, software, investigation, and writing—original draft. LC: methodology, validation, formal analysis, visualization, and data curation. SZ and RA: writing—review & editing. YH: resources, methodology, and supervision. X-AZ: resources, writing—review & editing, supervision, and data curation. All authors contributed to the article and approved the submitted version.

Funding

Support for this research by the Project of Science and Technology Department of Shaanxi Province (2021JQ-448), the Key Laboratory Project of Guangdong Province (2022B1212010015), and the National Natural Science Foundation of China (3210160758) are all gratefully acknowledged.

Conflict of interest

The authors declare that the research was conducted in the absence of any commercial or financial relationships that could be construed as a potential conflict of interest.

Publisher's note

References

1. Van Luong TS, Moir C, Chandry PS, Pinfold T, Olivier S, Broussolle V, et al. Combined high pressure and heat treatment effectively disintegrates spore membranes and inactivates Alicyclobacillus acidoterrestris spores in acidic fruit juice beverage. *Innovative Food Sci Emerg Technol.* (2020) 66:102523. doi: 10.1016/j.ifset.2020.102523

2. Feng X, He C, Jiao L, Liang X, Zhao R, Guo Y. Analysis of differential expression proteins reveals the key pathway in response to heat stress in Alicyclobacillus acidoterrestris DSM 3922T. *Food Microbiol.* (2019) 80:77–84. doi: 10.1016/j.fm.2019.01.003

3. Zhao N, Zhang J, Qi Y, Xu J, Wei X, Fan M. New insights into thermo-acidophilic properties of Alicyclobacillus acidoterrestris after acid adaptation. *Food Microbiol.* (2021) 94:103657. doi: 10.1016/j.fm.2020.103657

4. Pornpukdeewattana S, Jindaprasert A, Massa S. Alicyclobacillus spoilage and control-a review. *Crit Rev Food Sci Nutr.* (2020) 60:108–22. doi: 10.1080/10408398.2018.1516190

5. Guo L, Azam SR, Guo Y, Liu D, Ma H. Germicidal efficacy of the pulsed magnetic field against pathogens and spoilage microorganisms in food processing: an overview. *Food Control.* (2021) 136:108496. doi: 10.1016/j.foodcont.2021.108496

6. Roobab U, Chacha JS, Abida A, Rashid S, Muhammad Madni G, Lorenzo J M, et al. Emerging trends for nonthermal decontamination of raw and processed meat: ozonation, high-hydrostatic pressure and cold plasma. *Foods.* (2022) 11:2173. doi: 10.3390/foods11152173

7. Asghar A, Rashid MH, Ahmed W, Roobab U. Inam-ur-Raheem M, Shahid A, et al. An in-depth review of novel cold plasma technology for fresh-cut produce. *J Food Process Pres.* (2022) 7:e16560. doi: 10.1111/jfpp.16560

8. Mahnot NK, Mahanta CL, Farkas BE, Keener KM, Misra N. Atmospheric cold plasma inactivation of Escherichia coli and Listeria monocytogenes in tender coconut water: Inoculation and accelerated shelf-life studies. *Food Control.* (2019) 106:106678. doi: 10.1016/j.foodcont.2019.06.004

9. Charoux CM, Free L, Hinds LM, Vijayaraghavan RK, Daniels S, O'Donnell CP, et al. Effect of non-thermal plasma technology on microbial inactivation and total phenolic content of a model liquid food system and black pepper grains. *LWT-Food Sci Technol.* (2020) 118:108716. doi: 10.1016/j.lwt.2019.108716

10. Umair M, Jabbar S, Ayub Z, Aadil RM, Abid M, Zhang J, et al. Recent advances in plasma technology: Influence of atmospheric cold plasma on spore inactivation. *Food Rev Int.* (2021) 1:1–23. doi: 10.1080/87559129.2021.1888972

11. Liao X, Liu D, Xiang Q, Ahn J, Chen S, Ye X, et al. Inactivation mechanisms of non-thermal plasma on microbes: a review. *Food Control.* (2017) 75:83–91. doi: 10.1016/j.foodcont.2016.12.021

12. Wang LH, Wang MS, Zeng XA, Liu ZW. Temperature-mediated variations in cellular membrane fatty acid composition of Staphylococcus aureus in resistance to pulsed electric fields. *Biochim Biophys Acta, Biomembr.* (2016) 1858:1791–800. doi: 10.1016/j.bbamem.2016.05.003

13. Hayman MM, Anantheswaran RC, Knabel SJ. The effects of growth temperature and growth phase on the inactivation of Listeria monocytogenes in whole milk subject to high pressure processing. *Int J Food Microbiol.* (2007) 115:220–6. doi: 10.1016/j.ijfoodmicro.2006.10.019

14. Kayes MM, Critzer FJ, Kelly-Wintenberg K, Roth JR, Montie TC, Golden DA. Inactivation of foodborne pathogens using a one atmosphere uniform glow discharge plasma. *Foodborne Pathog Dis.* (2007) 4:50–9. doi: 10.1089/fpd.2006.62

15. Fernandez A, Noriega E, Thompson A. Inactivation of Salmonella enterica serovar Typhimurium on fresh produce by cold atmospheric gas plasma technology. *Food Microbiol.* (2013) 33:24–9. doi: 10.1016/j.fm.2012.08.007

16. Cai R, Zhang M, Cui L, Yuan Y, Yang Y, Wang Z, et al. Antibacterial activity and mechanism of thymol against Alicyclobacillus acidoterrestris vegetative cells and spores. *LWT-Food Sci Technol.* (2019) 105:377–84. doi: 10.1016/j.lwt.2019.01.066

17. Wang L-H, Wen Q-H, Zeng X-A, Han Z, Brennan CS. Influence of naringenin adaptation and shock on resistance of Staphylococcus aureus and Escherichia coli to pulsed electric fields. *LWT-Food Sci Technol.* (2019) 107:308–17. doi: 10.1016/j.lwt.2019.03.029

18. Pang D, Huang Z, Li Q, Wang E, Liao S, Li E, et al. Antibacterial Mechanism of Cinnamaldehyde: modulation of biosynthesis of Phosphatidylethanolamine and Phosphatidylglycerol in *Staphylococcus aureus* and *Escherichia coli*. *J Agric Food Chem.* (2021) 69:13628–36. doi: 10.1021/acs.jafc.1c04977

19. Alvarez-Ordóñez A, Halisch J, Prieto M. Changes in Fourier transform infrared spectra of Salmonella enterica serovars Typhimurium and Enteritidis after adaptation to stressful growth conditions. *Int J Food Microbiol.* (2010) 142:97–105. doi: 10.1016/j.ijfoodmicro.2010.06.008

20. Mahnot NK, Mahanta CL, Keener KM, Misra N. Strategy to achieve a 5-log Salmonella inactivation in tender coconut water using high voltage atmospheric cold plasma (HVACP). *Food Chem.* (2019) 284:303–11. doi: 10.1016/j.foodchem.2019.01.084

21. Wang L-H, Pyatkovskyy T, Yousef A, Zeng X-A, Sastry SK. Mechanism of *Bacillus subtilis* spore inactivation induced by moderate electric fields. *Innovative Food Sci Emerg Technol.* (2020) 62:102349. doi: 10.1016/j.ifset.2020.102349

22. Qian J, Ma L, Yan W, Zhuang H, Huang M, Zhang J, et al. Inactivation kinetics and cell envelope damages of foodborne pathogens Listeria monocytogenes and Salmonella Enteritidis treated with cold plasma. *Food Microbiol.* (2022) 101:103891. doi: 10.1016/j.fm.2021.103891

23. Olatunde OO, Benjakul S, Vongkamjan K. Dielectric barrier discharge cold atmospheric plasma: bacterial inactivation mechanism. *J Food Saf.* (2019) 39:12705. doi: 10.1111/jfs.12705

24. Ziuzina D, Patil S, Cullen PJ, Keener K, Bourke P. Atmospheric cold plasma inactivation of Escherichia coli, Salmonella enterica serovar Typhimurium and Listeria monocytogenes inoculated on fresh produce. *Food Microbiol.* (2014) 42:109–16. doi: 10.1016/j.fm.2014.02.007

25. Jin T, Dai C, Xu Y, Chen Y, Xu Q, Wu Z. Applying cold atmospheric plasma to preserve the postharvest qualities of winter jujube (Zizyphus jujuba Mill. cv. Dongzao) during cold storage. *Front Nutr.* (2022) 9:934841. doi: 10.3389/fnut.2022.934841

26. Bourke P, Ziuzina D, Han L, Cullen P, Gilmore BF. Microbiological interactions with cold plasma. *J Appl Microbiol.* (2017) 123:308–24. doi: 10.1111/jam.13429

27. Pan Y-Y, Zhang Y, Cheng J-H, Sun D-W. Inactivation of Listeria monocytogenes at various growth temperatures by ultrasound pretreatment and cold plasma. *LWT-Food Sci Technol.* (2020) 118:108635. doi: 10.1016/j.lwt.2019.108635

28. Liu Z-W, Zeng X-A, Ngadi M, Han Z. Effect of cell membrane fatty acid composition of Escherichia coli on the resistance to pulsed electric field (PEF) treatment. *LWT-Food Sci Technol.* (2017) 76:18–25. doi: 10.1016/j.lwt.2016.10.019

29. Hong S-H, Szili EJ, Jenkins ATA, Short RD. Ionized gas (plasma) delivery of reactive oxygen species (ROS) into artificial cells. *J Phys D: Appl Phys.* (2014) 47:362001. doi: 10.1088/0022-3727/47/36/362001

30. Al-Holy MA, Lin M, Cavinato AG, Rasco BA. The use of Fourier transform infrared spectroscopy to differentiate *Escherichia coli* O157: H7 from other bacteria inoculated into apple juice. *Food Microbiol.* (2006) 23:162–8. doi: 10.1016/j.fm.2005.01.017

31. Campos J, Sousa C, Mourão J, Lopes J, Antunes P, Peixe L. Discrimination of non-typhoid Salmonella serogroups and serotypes by Fourier Transform Infrared Spectroscopy: A comprehensive analysis. *Int J Food Microbiol.* (2018) 285:34–41. doi: 10.1016/j.ijfoodmicro.2018.07.005

32. Al-Qadiri HM, Lin M, Cavinato AG, Rasco BA. Fourier transform infrared spectroscopy, detection and identification of *Escherichia coli* O157: H7 and Alicyclobacillus strains in apple juice. *Int J Food Microbiol.* (2006) 111:73–80. doi: 10.1016/j.ijfoodmicro.2006.05.004

33. Yang S-P, Xie J, Cheng Y, Zhang Z, Zhao Y, Qian Y-F. Response of Shewanella putrefaciens to low temperature regulated by membrane fluidity and fatty acid metabolism. *LWT-Food Sci Technol.* (2020) 117:108638. doi: 10.1016/j.lwt.2019.108638

34. Cebrián G, Condón S, Mañas P. Heat resistance, membrane fluidity and sublethal damage in *Staphylococcus aureus* cells grown at different temperatures. *Int J Food Microbiol.* (2019) 289:49–56. doi: 10.1016/j.ijfoodmicro.2018.09.002

35. Huertas J-P, Ros-Chumillas M, Garre A, Fernández PS, Aznar A, Iguaz A, et al. Impact of heating rates on alicyclobacillus acidoterrestris heat resistance under non-isothermal treatments and use of mathematical modelling to optimize orange juice processing. *Foods.* (2021) 10:1496. doi: 10.3390/foods10071496

36. Poger D, Mark AE. Effect of ring size in ω-alicyclic fatty acids on the structural and dynamical properties associated with fluidity in lipid bilayers. *Langmuir.* (2015) 31:11574–82. doi: 10.1021/acs.langmuir.5b02635

37. Oshima M, Ariga T. Omega-cyclohexyl fatty acids in acidophilic thermophilic bacteria. Studies on their presence, structure, and biosynthesis using precursors labeled with stable isotopes and radioisotopes. *J Biol Chem.* (1975) 250:63–78. doi: 10.1016/S0021-9258(19)41026-0

38. Kannenberg E, Blume A, Poralla K. Properties of ω-cyclohexane fatty acids in membranes. *FEBS Lett.* (1984) 172:331–44. doi: 10.1016/0014-5793(84)81151-5

39. Najjar MB, Chikindas M, Montville TJ. Changes in Listeria monocytogenes membrane fluidity in response to temperature stress. *Appl Environ Microbiol.* (2007) 73:6429–35. doi: 10.1128/AEM.00980-07

40. Boudjemaa R, Cabriel C, Dubois-Brissonnet F, Bourg N, Dupuis G, Gruss A, et al. Impact of bacterial membrane fatty acid composition on the failure of daptomycin to kill Staphylococcus aureus. *Antimicrob Agents Chemother.* (2018) 62:e00023–18. doi: 10.1128/AAC.00023-18

41. Korachi M, Gurol C, Aslan N. Atmospheric plasma discharge sterilization effects on whole cell fatty acid profiles of *Escherichia coli* and *Staphylococcus aureus*. *J Electrostat.* (2010) 68:508–12. doi: 10.1016/j.elstat.2010.06.014

42. Schulte PM. The effects of temperature on aerobic metabolism: towards a mechanistic understanding of the responses of ectotherms to a changing environment. *J Exp Biol.* (2015) 218:1856–66. doi: 10.1242/jeb.118851

43. Ma R, Feng H, Liang Y, Zhang Q, Tian Y, Su B, et al. An atmospheric-pressure cold plasma leads to apoptosis in *Saccharomyces cerevisiae* by accumulating intracellular reactive oxygen species and calcium. *J Phys D: Appl Phys.* (2013) 46:285401. doi: 10.1088/0022-3727/46/28/285401

frontiers | Frontiers in Nutrition

TYPE Original Research
PUBLISHED 28 September 2022
DOI 10.3389/fnut.2022.1022323

OPEN ACCESS

EDITED BY
Zhi-Hong Zhang,
Jiangsu University, China

REVIEWED BY
Rana Muhammad Aadil,
University of Agriculture,
Faisalabad, Pakistan
Xiangrui Yang,
Xiangya Hospital, Central South
University, China
Qiang Xia,
Ningbo University, China

*CORRESPONDENCE
Xiao Dong Chen
xdchen@mail.suda.edu.cn
Xuehui Hong
hongxu@xmu.edu.cn
Zhongquan Qi
zqqi@xmu.edu.cn

†These authors have contributed equally to this work

SPECIALTY SECTION
This article was submitted to Nutrition and Food Science Technology, a section of the journal Frontiers in Nutrition

RECEIVED 18 August 2022
ACCEPTED 06 September 2022
PUBLISHED 28 September 2022

CITATION
Yu F, Chen J, Wei Z, Zhu P, Qing Q, Li B, Chen H, Lin W, Yang H, Qi Z, Hong X and Chen XD (2022) Preparation of carrier-free astaxanthin nanoparticles with improved antioxidant capacity. *Front. Nutr.* 9:1022323. doi: 10.3389/fnut.2022.1022323

Preparation of carrier-free astaxanthin nanoparticles with improved antioxidant capacity

Fei Yu[1†], Jiaxin Chen[1†], Zizhan Wei[1†], Pingchuan Zhu[2†], Qing Qing[1], Bangda Li[1], Huimin Chen[1], Weiying Lin[3], Hua Yang[1], Zhongquan Qi[1,4*], Xuehui Hong[5*] and Xiao Dong Chen[6*]

[1]Medical College, Guangxi University, Nanning, China, [2]State Key Laboratory for Conservation and Utilization of Subtropical Agro-Bioresources, College of Life Science and Technology, Guangxi University, Nanning, China, [3]Guangxi Key Laboratory of Electrochemical Energy Materials, School of Chemistry and Chemical Engineering, Institute of Optical Materials and Chemical Biology, Guangxi University, Nanning, China, [4]The Fourth People's Hospital of Nanning, Nanning, China, [5]Department of Gastrointestinal Surgery, Zhongshan Hospital of Xiamen University, Xiamen, China, [6]Suzhou Key Lab of Green Chemical Engineering, School of Chemical and Environmental Engineering, College of Chemistry, Chemical Engineering and Materials Science, Soochow University, Suzhou, China

Astaxanthin (AST), a red pigment of the carotenoids, has various advantageous biological activities. Nevertheless, the wide application of AST is restricted due to its poor water solubility and highly unsaturated structure. To overcome these limitations, carrier-free astaxanthin nanoparticles (AST-NPs) were fabricated through the anti-solvent precipitation method. The AST-NPs had a small particle size, negative zeta potential and high loading capacity. Analysis of DSC and XRD demonstrated that amorphous AST existed in AST-NPs. In comparison with free AST, AST-NPs displayed enhanced stability during storage. Besides, it also showed outstanding stability when exposed to UV light. Furthermore, the antioxidant capacity of AST-NPs was significantly increased. *In vitro* release study showed that AST-NPs significantly delayed the release of AST in the releasing medium. These findings indicated that AST-NPs would be an ideal formulation for AST, which could contribute to the development of novel functional foods.

KEYWORDS

astaxanthin, carrier-free, antioxidant, food industry, nanoparticles

Introduction

Astaxanthin (AST) is a lipid-soluble and red keto-carotenoid that has been separated from sundry microorganisms, phytoplankton, marine animals and seafood (1–4). It is commonly applied in the food, beverages, aquaculture, cosmetics and pharmaceutical industries due to its excellent antioxidant activity (5). Massive studies have demonstrated that the antioxidant activity of AST is 10 times higher than β-carotene and 100 times more powerful than vitamin E (6, 7). However, AST is highly unsaturated and decomposes easily when exposed to light, heat and oxygen during storage. In addition, its poor water solubility, pungent odor and instability have hampered its wide application in human nutrition (8).

Different methods have been explored to solve these issues, such as β-cyclodextrin complexes, liposomes and polymeric nanospheres (9). For example, the stability of AST was significantly improved when using MCC and CMC-Na as wall materials (10). AST nano-dispersion was prepared using WPI and PWP through an emulsification-evaporation technique and showed increased bioavailability (11). Besides, it has been reported that the antioxidant capacity of AST-nanodispersions was much greater than that of free AST (12, 13). Nevertheless, these preparation process usually require some chemical cross-linking agent (aldehydes), which may have certain security concerns (14). Furthermore, the design and synthesis of multi-component delivery systems are usually time-consuming and complicated. To avoid possible toxicity from carriers or problems related to biodegradation, carrier-free drug delivery systems (DDS) have been recently developed (15, 16). The nanostructures of carrier-free DDS were aggregated by pure drugs and could maximize the loading capacity of hydrophobic drug molecules. Meanwhile, many carrier-free nanoparticles were successfully prepared by anti-solvent method (17). These carrier-free DDS are speculated to self-assemble *via* hydrophobic interactions (π-π stacking) or hydrogen bonds in the structures of the molecules. On this basis, we wondered whether the carrier-free AST nanoparticles could also be designed.

The aim of our study was to fabricate carrier-free astaxanthin nanoparticles (AST-NPs) through the anti-solvent precipitation method (Figure 1). The physicochemical properties of AST-NPs were systematically measured. Meanwhile, the photostability and storage stability of AST-NPs were also determined to study the potential of industrial application. Additionally, XRD and DSC were used to assess the crystalline nature and thermal property of AST-NPs, respectively. Finally, the *in vitro* release behavior of AST-NPs as well as its antioxidant activity was also evaluated. These results indicated that AST-NPs could simultaneously improve the stability and antioxidant capacity of AST, which would extend the use of lipophilic nutraceuticals (AST) in foods.

Abbreviations: AST, Astaxanthin; CMC-Na, Carboxymethyl cellulose sodium; MCC, Microcrystalline cellulose; WPI, Whey protein isolation; PWP, Polymerized whey protein; PVP, Poly-vinylpyrrolidone; DLS, Dynamic light scattering; PDI, Polydispersity index; mPEG-DSPE, 1,2-distearoyl-sn-glycero-3-phosphoethanolamine-N-[methoxy(polyethyleneglycol)]; DSC, Differential scanning calorimetry; XRD, X-ray diffraction; TEM, Transmission electron microscopy; SEM, Scanning electron microscopy; LC, Loading capacity; ABTS, 2, 2′-azino-bis (3-ethylbenzothiazoline-6-sulfonic acid).

Materials and methods

Materials

Astaxanthin (AST) (pure > 97%) was bought from Aladdin Industrial Corporation (Shanghai, China). ABTS and potassium persulfate were purchased from Shanghai Macklin Biochemical Co., Ltd. (Shanghai, China). All other solvents including dimethyl sulfoxide (DMSO) and ethanol were supplied by Sinopharm Chemical Reagent Co., Ltd (Shanghai, China).

Preparation

AST-NPs were fabricated by the anti-solvent method. AST-DMSO solution was obtained by dissolving AST in DMSO through sonication treatment for 1 min. 250 μL of AST-DMSO solution was dropwise injected into 10 mL of DI water and then mPEG-DSPE was added under stirring condition. Finally, the AST-NPs were fabricated after being stirred for 2 h at 40 °C.

Characterization of AST-NPs

The mean particle size of AST-NPs was determined by DLS. The morphology of AST-NPs was examined by TEM (HT-7700, Hitachi High-Technologies Corporation, Japan). 200 μL of sample was dropped to a copper gird, which was dried by a filter paper. The samples were subjected to TEM after drying. The surface morphology of AST-NPs was also examined under a SEM (Hitachi, SU8220, Japan). The gold spray treatment was carried out on samples before measurement.

Loading capacity

The UV-Vis spectroscopy was used to determine LC of AST-NPs. Briefly, the AST-NPs were transferred into a centrifuge tube and then centrifuged. The precipitation was collected and mixed with DMSO-water solution. The absorbance of samples was determined by a UV-Vis spectrophotometer to calculate the concentration of AST. A standard calibration curve of AST in DMSO-water solution was previously obtained: $Y = 0.1834X - 0.009$ ($R^2 = 0.9996$), where Y and X refer to the absorbance and concentration of AST, respectively. Finally, LC was investigated according to the following equation:

$$LC\ (\%) = \frac{Total\ AST - free\ AST}{Total\ amount\ of\ nanoparticles} \times 100\% \quad (1)$$

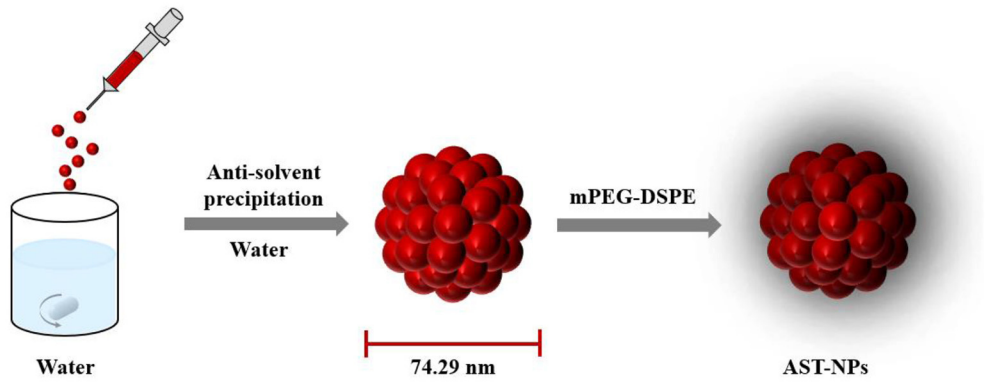

FIGURE 1
Schematic illustration of the AST-NPs.

XRD patterns

The XRD patterns of AST, mPEG-DSPE and AST-NPs powders were recorded using an X-ray diffractometer (Rigaku D/MAX 2500V). The XRD patterns were recorded from 5 to 60° at a speed of 10 °/min.

DSC measurements

The measurement of DSC (STA 449 F3, NETZSCH) was carried out to characterize the thermal property of samples. Briefly, the sample was placed in a sealed aluminum pan. The DSC curves were scanned from 50 to 300 °C.

Storage stability

The samples of free AST and AST-NPs were transferred to the transparent tube and then stored at room temperature in a light-proof cabinet for 72 h to investigate the stability behavior.

Photostability study

The photostability of AST-NPs was assessed by the UV-Vis spectroscopy. In brief, the samples were transferred to transparent container and then exposed to UV light for 70 min. The samples were collected at certain times (0, 10, 20, 30, 40, 50, 60 and 70 min). The retention rate of AST was calculated:

$$Retention\ rate\ of\ AST\ (\%) = \frac{A}{A_0} \times 100\% \quad (2)$$

where A and A_0 represent the absorbance at different time points and the initial absorbance of AST, respectively.

In vitro release study

The release rate of AST-NPs *in vitro* was studied by the dialysis method. The samples of free AST and AST-NPs were poured inside dialysis bags, respectively. Then, the dialysis bags were placed into PBS buffer with Tween-80 (0.1%) and kept under 100 rpm for 240 min in a constant temperature incubator shaker (MQT-60, Shanghai Minquan Instrument Co., LTD). At pre-determined intervals (30, 60, 90, 120, 150, 180, 210 and 240 min), 4 mL of sample inside the dialysis bags was collected. The absorbance of each sample was determined to estimate the percentage of the released drug.

Antioxidant activity

ABTS stock solution and potassium persulfate solution were mixed in equal volumes. ABTS working solution can be obtained by diluting with ethanol. Then, 3 mL of ABTS working solution was mixed with an equal volume of sample solution for 10 min. All of the samples at 734 nm were determined by a UV-Vis spectrophotometer.

Results and discussion

Preparation and characterization of AST-NPs

As depicted in Figure 2A, the obtained AST-NPs presented a nearly monodisperse particle size distribution with a mean diameter of 74.29 ± 7.92 nm (PDI = 0.130 ± 0.012). In this study, the zeta potential of AST-NPs was −14.4 ± 2.96 mV, which was responsible for the stability of the nanoparticles. In addition, an obvious Tyndall effect could be observed *via* a laser (Figure 2B), which suggested the formation of

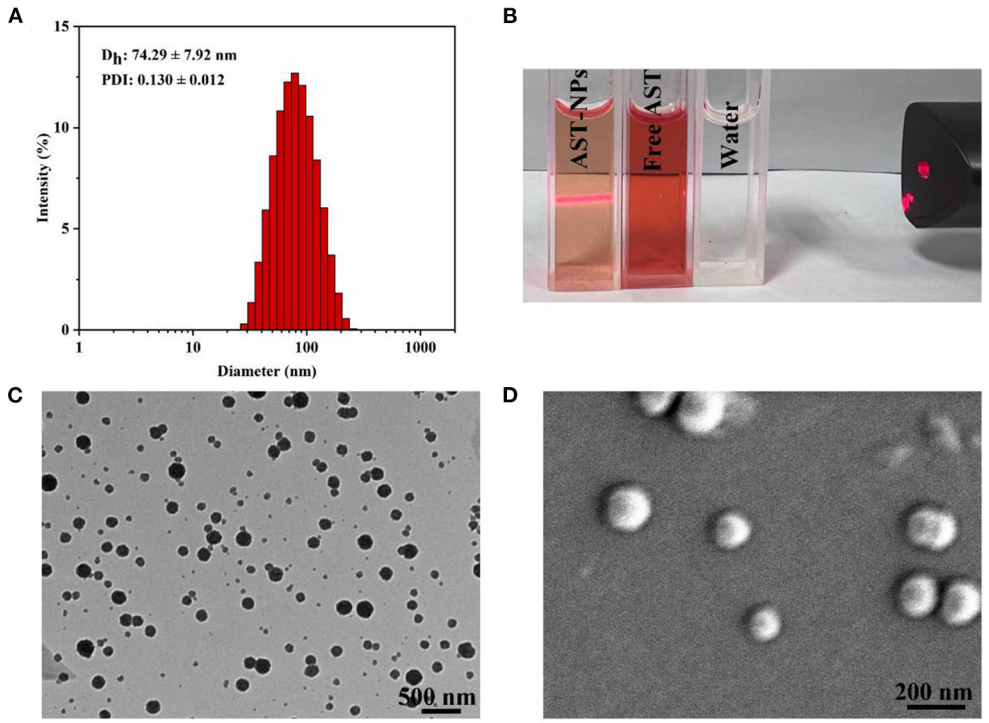

FIGURE 2
(A) Particle size and PDI of AST-NPs. **(B)** Tyndall effect of AST-NPs. **(C)** TEM image and **(D)** SEM image of AST-NPs.

nanoparticles (18). The morphological characteristics of the AST-NPs were investigated by TEM and SEM. The TEM image displayed uniformly dispersed AST-NPs with spherical structure (Figure 2C) and the SEM photo also showed that the nanoparticles were well-dispersed without any aggregation (Figure 2D). The LC (94.57 ± 0.70%) of AST-NPs was significantly improved than that of other carrier-based DDS (mostly <10%). This phenomenon might be attributed to that the stable interaction forces could be formed between AST molecules without the help of any carrier.

XRD analysis

The stability and solubility of functional components are related to their crystalline state (19). XRD measurements were performed on free AST, mPEG-DSPE and AST-NPs to obtain information about the crystalline state (Figure 3). Generally, the more peaks in XRD patterns of samples mean the higher degree of structural crystallites (20). The XRD pattern of free AST indicated multiple distinct characteristic peaks at 11.1, 13.7, 16.38, 18.36, 20.52 and 25.6°, which were related to its crystalline nature (21). By contrast, these sharp peaks in the diffractogram of AST-NPs were disappeared. This phenomenon indicated that the AST was embedded in the nanoparticles and transformed the crystal form into an amorphous form. Typically, the modification of a crystalline nature through nano-dimension can be an ideal way for elevating the solvability of drugs, which may be advantageous for the application of AST (19).

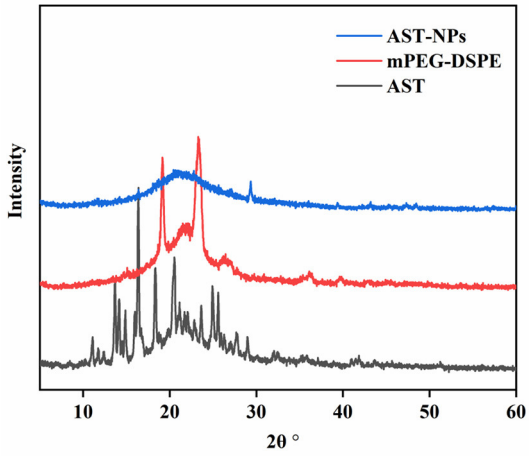

FIGURE 3
XRD patterns of AST-NPs, mPEG-DSPE and free AST.

DSC analysis

DSC analysis could qualitatively reflect changes in physical state of drugs, relying on the changes of endothermic peaks (22). DSC thermograms of free AST, mPEG-DSPE and AST-NPs were shown in Figure 4. The free AST exhibited an endothermic peak near 218 °C corresponding to its melting point, which showed that AST was present in a crystal form (23). However, the melting endothermic peak of AST was not visible in the DSC spectrum of AST-NPs, which indicated that the AST was in an amorphous form rather than in a crystalline form. In addition, it also indicated that the AST was successfully encapsulated into AST-NPs. Unlike crystalline AST, the dissolution of amorphous AST required less energy to diffuse, making it have better solubility (24). These results were consistent with the findings of XRD analysis.

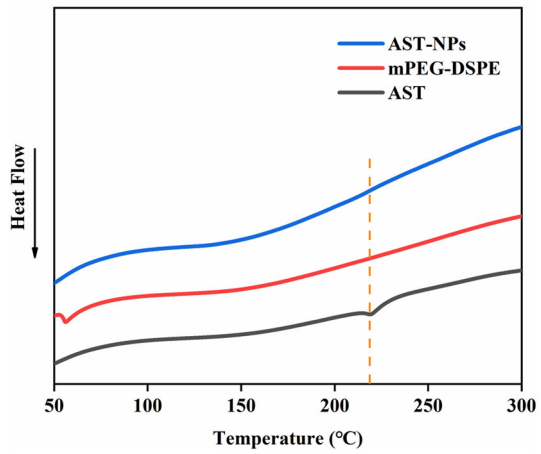

FIGURE 4
DSC thermograms of AST-NPs, mPEG-DSPE and free AST.

Storage stability

For AST-NPs, it is important that they have excellent stability during storage time (25). For this reason, we recorded the changes in the physical properties of the AST-NPs dispersion over time and compared them to the aqueous solution of free AST. Obvious differences between free AST and AST-NPs in anti-aggregation ability were observed after the storage for 72 h at room temperature in the dark. Specially, as shown in Figures 5A–D, no obvious visual differences were observed in the nano-dispersion (72 h). In contrast, visual observations of free AST indicated the formation of sediment at the bottom of the test tubes over time, which suggested that free AST molecules aggregated during storage. Meanwhile, the appearance and turbidity of the AST-NPs dispersion remained relatively unchanged after being stored at 25 °C for 36 h. In fact, only slight color fading and a small amount of sediment were observed after 72 h. This could be attributed to the high hydrophilicity and favorable charge characteristics, which could protect AST-NPs against aggregation during storage.

Photostability assay

Photochemical degradation of AST could lead to its loss of biological activity (26). The photostability of free AST or AST-NPs was investigated by exposing them to UV light. As can be seen in Figure 6, comparing to free AST, AST-NPs were more stable against UV light due to the physical barrier of nanoparticles. On the contrary, the degradation of free AST varied linearly when it was continuously exposed to UV light. It should be noted that, following with illumination, the retention rate of AST in all samples was decreased. After the first 30 min of UV treatment, 87.30 ± 5.74% of AST-NPs suspension was unchanged. At the same time, 64.87 ± 5.18% of free AST was retained. After the whole lighting period of 70 min, the retention rate of free AST was 35.07 ± 2.20%. In contrast, 84.23 ±

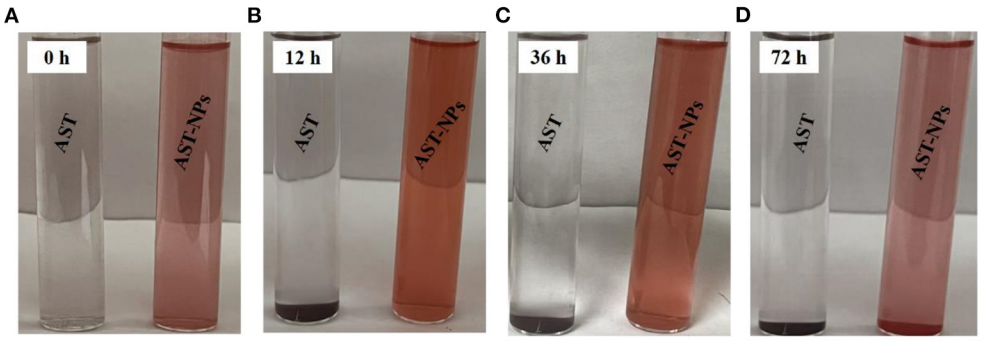

FIGURE 5
The visual appearances of free AST and AST-NPs at 25°C at different time points.

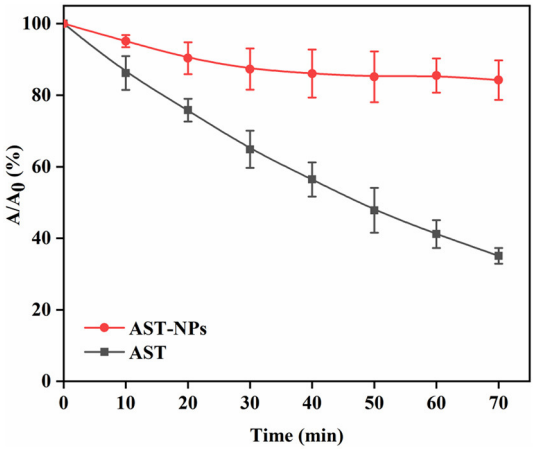

FIGURE 6
Retention rate of AST-NPs and free AST under UV light.

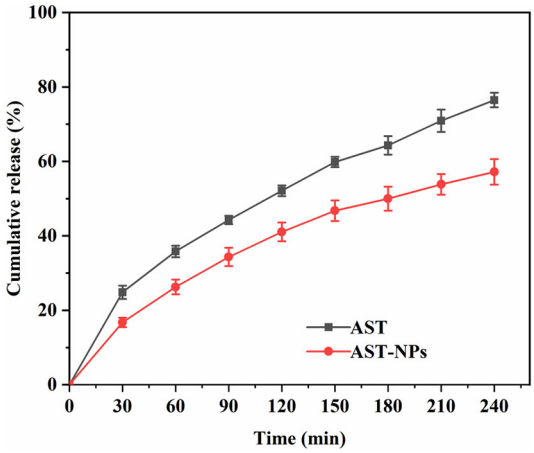

FIGURE 7
In vitro release profiles of free AST and AST-NPs.

5.53% of AST-NPs survived due to the protective effect from UV light afforded by encapsulation. The observation suggested that AST-NPs considerably improved the photostability of AST, which would be constructive to the application of AST in the food industry.

Release property of AST-NPs

An ideal drug delivery system should release the drug in a controlled way as well as possess excellent loading capability (27). Figure 7 depicted *in vitro* release profiles of free AST and AST-NPs. For AST-NPs, a burst release was presented within 30 min in PBS buffer, which might be due to the loss of weakly adsorbed AST molecules on or near the surface of the AST-NPs. After the burst release, the drug release of AST-NPs was slowed down. At 240 min, the release of free AST was 76.48 ± 1.96% whereas the drug release of AST-NPs was 57.20 ± 3.44%. Compared with free AST, the release rate of AST-NPs decreased significantly, which indicated that the AST-NPs achieved controlled release effect. This phenomenon could be attributed to the fact that various non-covalent interactions were existed between AST molecules. The slow and steady release of AST-NPs is essential for providing the body with a continuous supply of AST (28). These results indicated that AST-NPs would be an effective delivery system for AST.

Antioxidant activity

The high antioxidant activity of AST has been reported owing to the keto groups and hydroxyl groups in the β-ionone ring (29). One of the convenient ways to evaluate the antioxidant

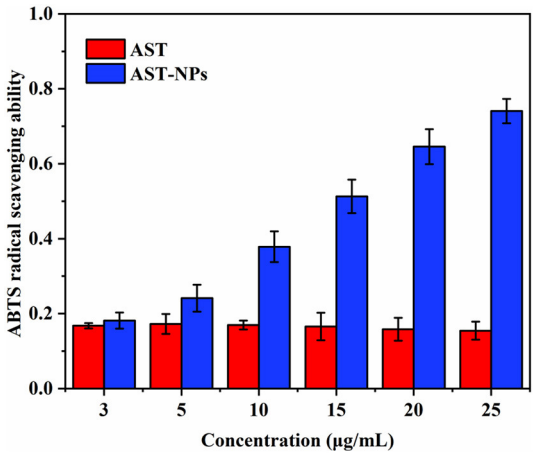

FIGURE 8
ABTS radical scavenging ability of free AST and AST-NPs.

activity is to react the AST with ABTS radical (30, 31). The ABTS radical scavenging rate of free AST and AST-NPs was shown in Figure 8. For all samples of AST-NPs, with the increasing of the concentrations, the ABTS scavenging effect increased in a concentration-dependent manner. As a lipophilic compound, the free AST showed relatively low scavenging activity at a wide range of concentrations (3–25 μg/mL) due to its poor solubility (32). At the concentration of 25 μg/mL, the ABTS radical scavenging activity of free AST was 15.45 ± 2.40%. In contrast, the ABTS radical scavenging activity of AST-NPs at equal concentration was 74.07 ± 3.26%, which indicated that the AST-NPs could lead to the increased ABTS radical scavenging activity. The reason for the enhancement of antioxidant activity of AST-NPs may be due to its improved

dispersibility, which increased the amount of AST molecules to interact with ABTS radical. Therefore, the AST-NPs would be an efficient way to improve the antioxidant capacity of AST.

Conclusion

In summary, the AST-NPs were successfully fabricated through the anti-solvent precipitation method. The obtained AST-NPs exhibited extremely high loading capacity (94.57 ± 0.70%), small average size (74.29 ± 7.92 nm) and uniform morphology. The AST-NPs increased the solubility of AST in water and improved its physicochemical properties. The AST-NPs, as a delivery system for AST, not only exhibited excellent ABTS radical scavenging activity but also had a relatively sustained release effect in the releasing medium. This study proved the feasibility of AST-NPs as a delivery system. Therefore, the AST-NPs would provide a new sight for the development of functional foods.

Data availability statement

The original contributions presented in the study are included in the article/supplementary material, further inquiries can be directed to the corresponding authors.

Author contributions

FY and JC: methodology, investigation, and data collection. PZ, WL, and HY: provided assistance in the use of the instrument. ZW: data analysis and writing-original draft. QQ, HC, and BL: critical revision and editing of the manuscript. FY, ZQ, XH, and XDC: conceptualization, review, and funding acquisition. All authors contributed to the article and approved the submitted version.

Funding

This work was supported by the National Natural Science Foundation of China (82003300, 81771721, 81971505, 21877048, 22077048, and 21672083), the National Key R&D Program of China (2018YFA0108304), the Natural Science Foundation of Guangxi Province (2020GXNSFBA297131, AD21220026, 2021GXNSFDA075003, and AD21220061), and the start-up grant from Guangxi University (A3370051003 and A3040051003).

Conflict of interest

The authors declare that the research was conducted in the absence of any commercial or financial relationships that could be construed as a potential conflict of interest.

Publisher's note

All claims expressed in this article are solely those of the authors and do not necessarily represent those of their affiliated organizations, or those of the publisher, the editors and the reviewers. Any product that may be evaluated in this article, or claim that may be made by its manufacturer, is not guaranteed or endorsed by the publisher.

References

1. Zhao T, Yan X, Sun L, Yang T, Hu X, He Z, et al. Research progress on extraction, biological activities and delivery systems of natural astaxanthin. *Trends Food Sci Tech.* (2019) 91:354–61. doi: 10.1016/j.tifs.2019.07.014

2. Liu Z-W, Zeng X-A, Cheng J-H, Liu D-B, Aadil RM. The efficiency and comparison of novel techniques for cell wall disruption in astaxanthin extraction from Haematococcus pluvialis. *Int J Food Sci Tech.* (2018) 53:2212–9. doi: 10.1111/ijfs.13810

3. Liu Z-W, Yue Z, Zeng X-A, Cheng J-H, Aadil RM. Ionic liquid as an effective solvent for cell wall deconstructing through astaxanthin extraction from Haematococcus pluvialis. *Int J Food Sci Tech.* (2019) 54:583–90. doi: 10.1111/ijfs.14030

4. Liu Z-W, Zhou Y-X, Wang L-H, Ye Z, Liu L-J, Cheng J-H, et al. Multi-spectroscopies and molecular docking insights into the interaction mechanism and antioxidant activity of astaxanthin and β-lactoglobulin nanodispersions. *Food Hydrocoll.* (2021) 117:106739. doi: 10.1016/j.foodhyd.2021.106739

5. Yu BS, Lee SY, Sim SJ. Effective contamination control strategies facilitating axenic cultivation of Haematococcus pluvialis: risks and challenges. *Bioresour Technol.* (2022) 344:126289. doi: 10.1016/j.biortech.2021.126289

6. Fakhri S, Abbaszadeh F, Dargahi L, Jorjani M. Astaxanthin: a mechanistic review on its biological activities and health benefits. *Pharmacol Res.* (2018) 136:1–20. doi: 10.1016/j.phrs.2018.08.012

7. Ren Y, Deng J, Huang J, Wu Z, Yi L, Bi Y, et al. Using green alga Haematococcus pluvialis for astaxanthin and lipid co-production: advances and outlook. *Bioresour Technol.* (2021) 340:125736. doi: 10.1016/j.biortech.2021.125736

8. Martinez-Delgado AA, Khandual S, Villanueva-Rodriguez SJ. Chemical stability of astaxanthin integrated into a food matrix: effects of food processing and methods for preservation. *Food Chem.* (2017) 225:23–30. doi: 10.1016/j.foodchem.2016.11.092

9. Wang S, Lu Y, Ouyang XK, Ling J. Fabrication of soy protein isolate/cellulose nanocrystal composite nanoparticles for curcumin delivery. *Int J Biol Macromol.* (2020) 165:1468–74. doi: 10.1016/j.ijbiomac.2020.10.046

10. Feng Z-Z, Li M-Y, Wang Y-T, Zhu M-J. Astaxanthin from Phaffia rhodozyma: Microencapsulation with carboxymethyl cellulose sodium and microcrystalline cellulose and effects of microencapsulated astaxanthin on yogurt properties. *LWT.* (2018) 96:152–60. doi: 10.1016/j.lwt.2018.04.084

11. Shen X, Zhao C, Lu J, Guo M. Physicochemical properties of whey-protein-stabilized astaxanthin nanodispersion and its transport via a caco-2 monolayer. *J Agric Food Chem.* (2018) 66:1472–8. doi: 10.1021/acs.jafc.7b05284

12. Wu C, Sun J, Jiang H, Li Y, Pang J. Construction of carboxymethyl konjac glucomannan/chitosan complex nanogels as potential delivery vehicles for curcumin. *Food Chem.* (2021) 362:130242. doi: 10.1016/j.foodchem.2021.130242

13. Kaga K, Honda M, Adachi T, Honjo M, Wahyudiono, Kanda H, et al. Nanoparticle formation of PVP/astaxanthin inclusion complex by solution-enhanced dispersion by supercritical fluids (SEDS): effect of PVP and astaxanthin Z-isomer content. *J Supercrit Fluid.* (2018) 136:44–51. doi: 10.1016/j.supflu.2018.02.008

14. Deka SR, Yadav S, Kumar D, Garg S, Mahato M, Sharma AK. Self-assembled dehydropeptide nano carriers for delivery of ornidazole and curcumin. *Colloids Surf B.* (2017) 155:332–40. doi: 10.1016/j.colsurfb.2017.04.036

15. Zhang J, Li S, An FF, Liu J, Jin S, Zhang JC, et al. Self-carried curcumin nanoparticles for in vitro and in vivo cancer therapy with real-time monitoring of drug release. *Nanoscale.* (2015) 7:13503–10. doi: 10.1039/C5NR03259H

16. Ao M, Yu F, Li Y, Zhong M, Tang Y, Yang H, et al. Carrier-free nanoparticles of camptothecin prodrug for chemo-photothermal therapy: the making, in vitro and in vivo testing. *J Nanobiotechnology.* (2021) 19:350. doi: 10.1186/s12951-021-01093-y

17. Zhao Y, Zhao Y, Ma Q, Zhang H, Liu Y, Hong J, et al. Novel carrier-free nanoparticles composed of 7-ethyl-10-hydroxycamptothecin and chlorin e6: self-assembly mechanism investigation and *in vitro*/*in vivo* evaluation. *Colloids Surf B.* (2020) 188:110722. doi: 10.1016/j.colsurfb.2019.110722

18. Hao T, Wang K, Zhang S, Yang S, Wang P, Gao F, et al. Preparation, characterization, antioxidant evaluation of new curcumin derivatives and effects of forming HSA-bound nanoparticles on the stability and activity. *Eur J Med Chem.* (2020) 207:112798. doi: 10.1016/j.ejmech.2020.112798

19. Ghobadi-Oghaz N, Asoodeh A, Mohammadi M. Fabrication, characterization and in vitro cell exposure study of zein-chitosan nanoparticles for co-delivery of curcumin and berberine. *Int J Biol Macromol.* (2022) 204:576–86. doi: 10.1016/j.ijbiomac.2022.02.041

20. Anarjan N, Tan CP, Nehdi IA, Ling TC. Colloidal astaxanthin: preparation, characterisation and bioavailability evaluation. *Food Chem.* (2012) 135:1303–9. doi: 10.1016/j.foodchem.2012.05.091

21. Yuan Y, Ma M, Zhang S, Wang D, Xu Y. pH-driven self-assembly of alcohol-free curcumin-loaded propylene glycol alginate nanoparticles. *Int J Biol Macromol.* (2022) 195:302–8. doi: 10.1016/j.ijbiomac.2021.12.025

22. Feng S, Sun Y, Wang D, Sun P, Shao P. Effect of adjusting pH and chondroitin sulfate on the formation of curcumin-zein nanoparticles: synthesis, characterization and morphology. *Carbohydr Polym.* (2020) 250:116970. doi: 10.1016/j.carbpol.2020.116970

23. Song R, Qi Y, Jia Z, Liu X, Wei R. Astaxanthin-loaded zein/calcium alginate composite microparticles: characterization, molecular interaction and release kinetics in fatty food simulant system. *LWT.* (2020) 134:110146. doi: 10.1016/j.lwt.2020.110146

24. Liu C, Xu B, McClements DJ, Xu X, Cui S, Gao L, et al. Properties of curcumin-loaded zein-tea saponin nanoparticles prepared by antisolvent co-precipitation and precipitation. *Food Chem.* (2022) 391:133224. doi: 10.1016/j.foodchem.2022.133224

25. Sorasitthiyanukarn FN, Muangnoi C, Rojsitthisak P, Rojsitthisak P. Chitosan oligosaccharide/alginate nanoparticles as an effective carrier for astaxanthin with improving stability, *in vitro* oral bioaccessibility, and bioavailability. *Food Hydrocoll.* (2022) 124:107246. doi: 10.1016/j.foodhyd.2021.107246

26. Peng S, Zhou L, Cai Q, Zou L, Liu C, Liu W, et al. Utilization of biopolymers to stabilize curcumin nanoparticles prepared by the pH-shift method: caseinate, whey protein, soy protein and gum Arabic. *Food Hydrocoll.* (2020) 107:105963. doi: 10.1016/j.foodhyd.2020.105963

27. Shakeri M, Razavi SH, Shakeri S. Carvacrol and astaxanthin co-entrapment in beeswax solid lipid nanoparticles as an efficient nano-system with dual antioxidant and anti-biofilm activities. *LWT.* (2019) 107:280–90. doi: 10.1016/j.lwt.2019.03.031

28. Yang J, Zhou Q, Huang Z, Gu Z, Cheng L, Qiu L, et al. Mechanisms of *in vitro* controlled release of astaxanthin from starch-based double emulsion carriers. *Food Hydrocoll.* (2021) 119:106837. doi: 10.1016/j.foodhyd.2021.106837

29. Liu Q, Sun Y, Cui Q, Cheng J, Killpartrik A, Kemp AH, et al. Characterization, antioxidant capacity, and bioaccessibility of coenzyme Q10 loaded whey protein nanoparticles. *LWT.* (2022) 160:113258. doi: 10.1016/j.lwt.2022.113258

30. Hu Q, Hu S, Fleming E, Lee JY, Luo Y. Chitosan-caseinate-dextran ternary complex nanoparticles for potential oral delivery of astaxanthin with significantly improved bioactivity. *Int J Biol Macromol.* (2020) 151:747–56. doi: 10.1016/j.ijbiomac.2020.02.170

31. Rodriguez-Ruiz V, Salatti-Dorado JA, Barzegari A, Nicolas-Boluda A, Houaoui A, Caballo C, et al. Astaxanthin-loaded nanostructured lipid carriers for preservation of antioxidant activity. *Molecules.* (2018) 23:2601. doi: 10.3390/molecules23102601

32. Tirado DF, Palazzo I, Scognamiglio M, Calvo L, Della Porta G, Reverchon E. Astaxanthin encapsulation in ethyl cellulose carriers by continuous supercritical emulsions extraction: a study on particle size, encapsulation efficiency, release profile and antioxidant activity. *J Supercrit Fluid.* (2019) 150:128–36. doi: 10.1016/j.supflu.2019.04.017

frontiers | Frontiers in Nutrition

TYPE Original Research
PUBLISHED 06 October 2022
DOI 10.3389/fnut.2022.1026890

OPEN ACCESS

EDITED BY
Debao Niu,
Guangxi University, China

REVIEWED BY
Ayesha Murtaza,
University of Central Punjab, Pakistan
Muhammad Tayyab Rashid,
Henan University of Technology, China
Xing Xie,
Jiangxi Normal University, China

*CORRESPONDENCE
Iahtisham-Ul-Haq
iahtisham@fccollege.edu.pk
Alexandru Vasile Rusu
rusu_alexandru@hotmail.com
Monica Trif
monica_trif@hotmail.com

SPECIALTY SECTION
This article was submitted to Nutrition and Food Science Technology, a section of the journal Frontiers in Nutrition

RECEIVED 24 August 2022
ACCEPTED 16 September 2022
PUBLISHED 06 October 2022

CITATION
Ashraf H, Butt MS, Iahtisham-Ul-Haq, Nadeem M, Aadil RM, Rusu AV and Trif M (2022) Microencapsulated curcumin from *Curcuma longa* modulates diet-induced hypercholesterolemia in Sprague Dawley rats. *Front. Nutr.* 9:1026890. doi: 10.3389/fnut.2022.1026890

Microencapsulated curcumin from *Curcuma longa* modulates diet-induced hypercholesterolemia in Sprague Dawley rats

Humaira Ashraf[1], Masood Sadiq Butt[2], Iahtisham-Ul-Haq[3]*, Muhammad Nadeem[4], Rana Muhammad Aadil[2], Alexandru Vasile Rusu[5,6]* and Monica Trif[7]*

[1]Department of Food Science and Technology, Jinnah University for Women, Karachi, Pakistan, [2]National Institute of Food Science and Technology, University of Agriculture, Faisalabad, Pakistan, [3]Kauser Abdulla Malik School of Life Sciences, Forman Christian College (A Chartered University), Lahore, Pakistan, [4]Institute of Human Nutrition and Dietetics, Gulab Devi Educational Complex, Lahore, Pakistan, [5]Life Science Institute, University of Agricultural Sciences and Veterinary Medicine Cluj-Napoca, Cluj-Napoca, Romania, [6]Faculty of Animal Science and Biotechnology, University of Agricultural Sciences and Veterinary Medicine Cluj-Napoca, Cluj-Napoca, Romania, [7]Department of Food Research, Centre for Innovative Process Engineering (Centiv) GmbH, Syke, Germany

Hypercholesterolemia is one of the major causes of cardiovascular ailments. The study has been conducted on the hypothesis that hypercholesterolemia can be modulated by microencapsulated curcumin due to its enhanced bioavailability. In this context, curcumin obtained from fresh rhizomes of *Curcuma longa* by conventional (CSE) and supercritical fluid (SFE) extractions, has been successfully microencapsulated using a mixture of gelatin and maltodextrin. The microencapsulated curcumin $_{CSE\ \&SFE}$, has been added as supplemented diet and has been resulted in maximum plasma concentration of curcumin at 100 min as 529.31 ± 8.73 and 405.23 ± 7.12 μg/mL, respectively compared to non-encapsulated turmeric powder used as control. During the bio evaluation trial, turmeric powder (3%), microencapsulated curcumin$_{CSE}$ (1%) and microencapsulated curcumin$_{SFE}$ (0.5%) were provided to designate rat groups categorized by normal; N_1, N_2, and N_3 and hypercholesterolemic; H_1, H_2, and H_3 conditions, respectively. The incorporation of microencapsulated curcumin$_{SFE}$ in the supplemented diet caused a reduction in serum cholesterol, low density lipoprotein (LDL) and triglycerides, athrogenic index (AI) and cardiac risk ration (CRR) as 5.42 and 12.81%, 7.25 and 15.42%, 3.17 and 9.38%, 15.38 and 29.28%, and 10.98 19.38% in normo- and hypercholesterolemic rat groups. Additionally, high-density lipoprotein (HDL) and anti-atherogenic index (AAI) indicated a significant increase in all treated rat groups. Conclusively, the inclusion of turmeric and curcumin microencapsulates in the dietary module has been proven effective to alleviate hyperlipidemia. Therefore, the present study is proven that curcumin absorption *via* the gastrointestinal tract and its stability

toward metabolization in the body increased *via* microencapsulation using maltodextrin and gelatin. Microencapsulated curcumin reaches the target site *via* oral administration because of sufficient gastrointestinal residence period and stability in the digestive tract.

KEYWORDS

curcumin, atherogenic index, microencapsulation, maltodextrin, gelatin, cholesterol, bioavailability, supercritical fluid extraction

Introduction

Globally, the incidence of cardiovascular diseases (CVDs) is escalating owing to poor living patterns and unwise food choices. Furthermore, hyperlipidemia is amongst the leading causes of CVDs, characterized by increased cholesterol and triglyceride levels. Cholesterol is one of the lipophilic compounds that is circulated by chylomicron, low-density lipoproteins (LDL), very low-density lipoproteins (vLDL) and HDL as carriers (1, 2). A progression of LDL oxidation, which is lethal to endothelial cells, can be caused by poor eating habits over an extended period. In this way the oxidative balance of the body is disturbed, further resulting in plaque formation in blood vessels by oxidizing lipoproteins (3).

Plants have always been a part of traditional health treatments since antiquity around the globe (4, 5). Isolated bioactive molecules from spices may serve as preliminary materials for diet-based therapies. Amongst, curcumin is the principal turmeric bioactive moiety and accounts for 75–80% of total curcuminoids. Curcuminoids are secondary plant constituents that are extracted from the rhizome of various Curcuma species. It is aryl-C7-aryl, exhibiting a diarylheptanoid structure responsible for the orange-red shade of turmeric (6, 7). Unfortunately, the bioavailability of curcumin is a challenge as a merely insignificant fraction of curcumin reaches the target site *via* oral administration because of insufficient gastrointestinal residence period, low absorption through the intestinal wall and instability in the acidic environment of digestive tract (8). The reseason behind its limited stability is rapid convertion into ferulic acid and vanillin by intestinal enzymes and conjugation with glucuronide and sulfate in hepatic cells, thus lowering systemic concentration (9, 10). To extract the maximum therapeutic outputs from curcumin, it is necessary to enhance the bioavailability of this bioactive compound. Purposely, various techniques have been tested to enhance the bioavailability of curcumin with improved food applications. A variety of methods are available to increase the bioavailability, e.g., the addition of piperine, micellation of curcuminoids or nanotechnological methods. Among all of these, curcumin encapsulation at micro-level using lyophilization is gaining more popularity due to its suitability for heat sensitive biomolecules and versatility for utilizing various coating materials composed of sugars, proteins, lipids, gums, native and modified polysaccharides and synthetic polymers whilst considering the compatibility with the core ingredient i.e., curcumin. In this context, foregoing explorations on coating of micro/nano-food particles with compatible material have assured high encapsulating efficiency and shelf life of bioactive compounds. Furthermore, the absorption and stability of curcumin against metabolization *via* gastrointestinal tract may be improved (11).

Numerous epidemiological studies provide convincing evidence regarding the use of curcumin to prevent coronary diseases (8, 12). Earlier literature revealed that curcumin blocks the aggregation of platelets and improves erythrocyte fragility, which are important factors in the pathogenesis of heart attack and arteriosclerosis. Moreover, the administration of curcumin through a daily diet tends to enhance the activity of hepatic acyl-CoA that hinders excessive fat accumulation in adipose tissues and the liver (13). Turmeric possesses hepatoprotective properties due to its cholesterol-lowering effects. It was confirmed by research outcomes of Elahi (14) on rat models concluding that curcumin intakes decreases the absorption of saturated fat by rapidly eliminating bile hence lowering the risk of heart diseases.

The mechanistic approach related to curcumin revealed the regulatory effect on the activity of hepatic cholesterol 7-α-hydroxylase thus normalizing the biosynthesis of bile acids. Since no drug is deprived of any side effects, it is therefore recommended to attenuate hypercholesterolemia using diet-based therapies having no or low toxic effects as compared to pharmaceuticals. It is interesting to know that curcumin down-regulates gene expression for 3-hydroxy-3-methyl-glutaryl-co-enzyme A reductase (HMGR) through transcriptional inhibition. The major objective of cholesterol management is to attenuate serum LDL levels (15). The proposed mechanism described that curcumin decreases the level of Apo-B lipoprotein in serum from hepatocytes. Apo-B lipoprotein is involved in LDL transfer to extrahepatic cells at a 1:1 ratio (one Apo-B lipoprotein can bind one LDL). Moreover, regulating HDL to manage hyperlipidemia is considered good as it sets back the transport of cholesterol to the liver for the removal of triglycerides (TG) and cholesterol bodies along with bile acid (16). Unfortunately, there is a lack of

sufficient data regarding the use of microencapsulated curcumin isolated using a supercritical fluid extraction system and conventional solvent, i.e., ethanol in comparison with turmeric to address dyslipidemia. In this study, it has been expected that due to microencapsulated curcumin, which has a higher bioavailability than turmeric, it could be possible to reduce diet-induced hypercholesterolemia. As a result, the current research was designed to investigate the hypocholesterolemic potential of turmeric and microencapsulated curcumin obtained from dried rhizomes of *Curcuma longa* by conventional (CSE) and supercritical fluid extracts (SFE) using male rats in a diet module.

Materials and methods

Fresh rhizomes of turmeric (Kasur) were procured from Ayub Agriculture Research Institute, Faisalabad, Pakistan. Analytical and HPLC grade reagents and standards were purchased from Merck (Merck KGaA, Darmstadt, Germany) and Sigma-Aldrich (Sigma-Aldrich Tokyo, Japan). For an efficacy study, Male Sprague Dawley rats were acquired and housed in the Animal Room of NIFSAT. For biological assays, diagnostic kits were purchased from Sigma-Aldrich, Bioassay (Bioassays Chemical Co. Germany) and Cayman Chemicals (Cayman Europe, Estonia).

Extraction of curcumin

Fresh rhizomes of *Curcuma longa* (turmeric variety: Kasur) were purchased from Ayub Agriculture Research Institute (AARI), Faisalabad, Pakistan. The turmeric was then cleaned, and adherent soil or other matter was separated followed by dehydrating it at 60°C in a lab-scale dehydrator. The dried turmeric was ground to a fine powder and kept in an airtight glass container till further utilization. Curcumin from dehydrated turmeric powder was isolated using two different protocols. Firstly, aqueous ethanol (50% v/v) was used to extract curcumin from turmeric powder by agitation at a constant temperature of 50°C for 65 min following the prescribed procedures of Kulkarni et al. (17). Afterward, Rotary Evaporator (Eyela, Japan) was used to concentrate the filtered ensuing curcumin extract and termed conventional solvent extract ($curcumin_{CSE}$) containing 31.48 ± 1.35 mg/g of curcumin in it. Secondly, SFE of dried turmeric powder was obtained using CO_2 as supercritical fluid through supercritical fluid extraction (SFT-150) system. The sample was placed in an extraction vessel and CO_2 was introduced to the vessel and a stay time of 150 min was given (18). After completion of the cycle, the extracted curcumin is recovered in a glass vial. This curcumin extract was encoded as SFE ($curcumin_{SFE}$) containing 52.41 ± 2.38 mg/g of curcumin in it (19).

Microencapsulation of curcumin

Curcumin was encapsulated using homogenous emulsions comprised of maltodextrin (20 g) and gelatin (6 g) per 100 g solution. For this purpose, gelatin was dissolved in warm distilled water and mixed with maltodextrin solution. Afterward, turmeric extracts were added at a concentration of 10% depending on the weight of encapsulating material. The mixture was homogenized for 10 min at 3,500 rpm. The prepared emulsions were kept at −35°C for 24 h following lyophilization at −30°C according to the prescribed method of Malacrida and Telis (11). The resultant material was finely ground and stored for evaluation trial.

Bioavailability of curcumin

The study was approved by the Directorate of Graduate Studies, UAF (No. DGS/474-79) after ensuring the standards for handling and care of laboratory animals from the Departmental Bioethics Committee. To access the bioavailability of encapsulated curcumin, already acclimatized (23 ± 2°C temperature, 55 ± 5% relative humidity and 12 h light/dark cycle for 1 week before study) male Sprague Dawley rats (n = 10 per group; power analysis) were randomly distributed into three groups. The turmeric powder (3%) enriched diet was orally administrated to the G_0 group whereas, G_1 and G_2 were provided with microencapsulated $curcumin_{CSE}$ (1%) and microencapsulated $curcumin_{SFE}$ (0.5%) enriched diets, respectively. To quantify the curcumin content in plasma, samples were collected at time intervals of 50, 100, 150, and 200 min (20).

Bioevaluation trial for a hypolipidemic effect

Male Sprague Dawley rats were used and National Research Council's Guide for the Care and Use of Laboratory Animals were followed during the entire study. The efficacy trial was performed to test the therapeutic potential of curcumin-supplemented diets against hypercholesterolemia. The rats were acclimatized for a week by feeding on a control diet alongside controlling temperature (23 ± 2°C) and relative humidity (55 ± 5%) and then randomly assigned to different groups as illustrated in **Table 1**.

A Bioevaluation trial (60 days) was conducted on normal and hypercholesterolemic rats where hypercholesterolemia was induced by administrating a high cholesterol diet to the rats. Each rat group (n = 10) was given the respective dietary module during the whole trial (**Table 2**). In this connection, N_1 and H_1 were reared on turmeric powder @ 3% enriched diet, whilst N_2 and H_2 were provided with microencapsulated $curcumin_{CSE}$

TABLE 1 Bioefficacy plan.

Groups	Description
N_0	Normal rats reared on a normal diet
N_1	Normal rats reared on a turmeric powder containing diet
N_2	Normal rats reared on Microencapsulated $curcumin_{CSE}$ containing diet
N_3	Normal rats reared on Microencapsulated $curcumins_{FE}$ containing diet
H_0	Hypercholesterolemic rats reared on a normal diet
H_1	Hypercholesterolemic rats reared on a turmeric powder containing diet
H_2	Hypercholesterolemic rats reared on Microencapsulated $curcumin_{CSE}$ containing diet
H_3	Hypercholesterolemic rats reared on Microencapsulated $curcumins_{FE}$ containing diet

CSE, Conventional solvent extract; SFE, Supercritical fluid extract.

@ 1% enriched diet. The rats in N_3 and H_3 were fed on a 0.5% microencapsulated $curcumins_{FE}$ enriched diet whereas, N_0 (negative control) and H_0 (positive control) were used as reference controls. At the end of the trial, blood samples of overnight fasted rats were collected and centrifuged (4,000 rpm for 6 min) for collection of sera *via* centrifuge machine. The collected sera were subjected to assessment of various lipidemic biomarkers using Microlab 300, Merck, Germany. Furthermore, lipidemic ratios were also calculated to assess the risk index for cardiac diseases.

Serum lipid profile

Serum lipid profiles including total cholesterol (TC), LDL, HDL, and TG were measured following respective protocols. Sera cholesterol and LDL were estimated by CHOD–PAP method and TG were estimated by GPO–PAP method as described by Kim et al. (21). HDL in sera was measured by the Cholesterol Precipitant procedure as described by Alshatwi et al. (22). However, VLDL and non-HDL levels in sera were calculated using Friedewald expression. Moreover, Atherogenic Index (AI), HDL to TC ratio (HTR%), Cardiac Risk Ratio (CRR) and Anti-Atherogenic Index (AAI) were computed using the expressions mentioned by Ashfaq et al. (23).

Statistical analyses

One-way Analysis of Variance (ANOVA) was used to determine the level of significance using Cohort version 6.1. The P-value < 0.05 was considered a significant effects. Furthermore, Tukey's Honest Significant Difference (HSD) test was used for *post hoc* comparison of the means. All the results are then expressed as mean ± SD.

Results

Bioavailability of curcumin

Data obtained for curcumin bioavailability in plasma samples of rats were statistically analyzed. Due to the influence of treatments and time intervals, there was a considerable fluctuation in curcumin content in rat plasma (Figure 1). The maximum value (C_{max}) for curcumin (529.31 ± 8.73 μg/mL) was observed for the rat group (G_2) that was provided with a microencapsulated $curcumins_{FE}$ enriched diet with a maximum time (T_{max}) of 100 min that decreases to 462.98 ± 7.25 and 385.76 ± 5.01 μg/mL at 150 and 200 min, respectively (Figure 1). For the G_1 group rats fed on a microencapsulated $curcumin_{CSE}$ enriched diet, the recorded values for curcumin in rat's plasma were 223.51 ± 3.76, 405.23 ± 7.12, 319.57 ± 6.41, and 237.49 ± 4.25 μg/mL at 50, 100, 150, and 200 min, respectively. However, curcumin concentration decreased

TABLE 2 Diet composition for different rat groups.

Ingredients	Quantities (g/1,000 g)							
	N_0	N_1	N_2	N_3	H_0	H_1	H_2	H_3
Flour	812	782	802	807	769.6	739.6	759.6	764.6
Corn oil	90	90	90	90	120	120	120	120
Casein	50	50	50	50	50	50	50	50
Minerals	30	30	30	30	30	30	30	30
Vitamin	10	10	10	10	10	10	10	10
Bran	8	8	8	8	5	5	5	5
Cholesterol	–	–	–	–	15	15	15	15
Choline	–	–	–	–	0.4	0.4	0.4	0.4
Turmeric powder	–	30	–	–	–	30	–	–
$Microencapsulated\ curcumin_{CSE}$	–	–	10	–	–	–	10	–
$Microencapsulated\ curcumins_{FE}$	–	–	–	5	–	–	–	5

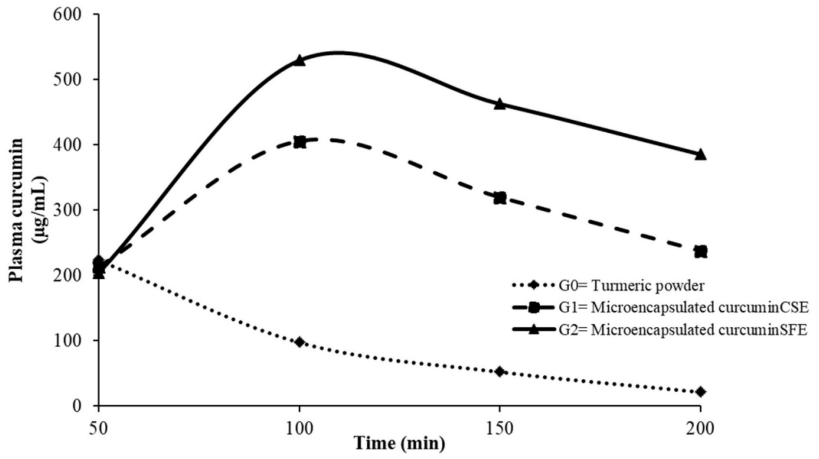

FIGURE 1
Curcumin concentration (μg/mL) in rat plasma at different time intervals.

TABLE 3 Serum lipid profile of rats treated with different curcumin-enriched diets.

Groups	High density lipoproteins (mg/dL)	Low density lipoproteins (mg/dL)	Triglycerides (mg/dL)	Total cholesterol (mg/dL)	Very low density lipoprotein (mg/dL)	Non-high density lipoprotein (mg/dL)
N_0	34.87 ± 1.25^{c}	31.73 ± 1.30^{d}	64.31 ± 2.18^{d}	80.22 ± 2.72^{d}	12.86 ± 0.23^{c}	45.35 ± 1.76^{d}
N_1	35.42 ± 1.31^{c}	30.98 ± 1.16^{de}	63.08 ± 2.45^{d}	78.34 ± 2.89^{d}	12.61 ± 0.45^{c}	42.92 ± 0.97^{de}
N_2	35.89 ± 1.56^{c}	29.77 ± 1.03^{e}	62.59 ± 2.39^{de}	76.85 ± 3.18^{de}	12.51 ± 0.19^{c}	40.96 ± 1.41^{e}
N_3	36.01 ± 1.72^{c}	29.23 ± 0.99^{d}	62.27 ± 1.92^{e}	75.87 ± 3.41^{e}	12.45 ± 0.57^{c}	39.86 ± 2.12^{e}
H_0	59.30 ± 2.07^{b}	58.15 ± 2.26^{a}	97.02 ± 4.36^{a}	142.56 ± 6.42^{a}	19.40 ± 0.71^{a}	83.26 ± 2.78^{a}
H_1	60.55 ± 2.24^{ab}	52.41 ± 1.61^{b}	91.69 ± 3.32^{b}	130.12 ± 4.70^{b}	18.33 ± 0.62^{ab}	69.57 ± 3.09^{b}
H_2	61.48 ± 2.26^{a}	50.14 ± 2.06^{bc}	89.53 ± 3.60^{bc}	127.53 ± 4.97^{bc}	17.90 ± 0.49^{b}	66.05 ± 1.82^{bc}
H_3	62.31 ± 2.04^{a}	$49.18 \pm 1.87b^{c}$	87.91 ± 3.52^{c}	124.29 ± 5.09^{c}	17.58 ± 0.33^{b}	61.98 ± 1.95^{c}

Data values represent mean ± SD ($n = 10$); means carrying different superscripted letters in a column differ significantly ($P < 0.05$).

rapidly from 205.45 ± 3.84–21.29 ± 0.14 μg/mL in plasma of rat group (G_0) fed on a diet containing turmeric powder from 50 to 200 min, respectively. The trends observed in these results showed that the bioavailability of curcumin is enhanced using microencapsulation which is one of the limiting factors in the effectiveness of curcumin's medicinal worth.

Cholesterol

The data for the serum lipid profile of male Sprague Dawley rats after a 60-day feed model trial is depicted in Table 3. The statistical analysis of the pooled data regarding TC in normal and high cholesterol diet-induced hypercholesterolemic rat groups depicted significant differences ($P < 0.05$) among treated groups for 2 months of study. It was observed that in the normal group TC decreased in rat groups fed on a diet containing turmeric powder, microencapsulated $curcumin_{CSE}$ and microencapsulated $curcumin_{SFE}$, respectively as compared to rats treated with a normal diet. On the other side, the TC of rats (H_0) fed with a diet containing high cholesterol increased by 43.72% in contrast to its normal counterpart (N_0). These outcomes showed that the cholesterol administration in the daily diet caused lipid metabolic dysfunction, ultimately endorsing hyperlipidemia. However, variations in dietary patterns of rat groups by the inclusion of turmeric powder, $curcumin_{CSE}$ and $curcumin_{SFE}$ microencapsulated alleviated total sera cholesterol as signified in H_1 (7.32%), H_2 (10.54%) and H_3 (12.81%) groups, respectively. The current findings show that supplementing the diets with curcumin microencapsulated lowers circulating lipids, alleviating the negative effects of treated rats' hypercholesterolemia.

High-density lipoprotein

The means relating to HDL expounded significant differences ($P < 0.05$) for normal as well as hyper cholesterolemic rat groups (Table 3). The diet-induced

hypercholesterolemic rat group reared on a regular diet (H_0) illustrated a marked reduction in HDL level as compared to its negative control group (N_0) illuminated the highly damaging impact of high cholesterol diet on lipidemic biomarkers, HDL. Nonetheless, it is unusual to mention that a diet containing turmeric powder (H_1), nutraceutical microencapsulated-curcumin$_{CSE}$ (H_2) and –curcumin$_{SFE}$ (H_3) restored the HDL cholesterol more significantly than H_0. However, a comparative study for normal and hypercholesterolemic rats showed that differences in sera HDL cholesterol were statistically similar in normal rats although marginally better HDL levels were recorded in N_1, N_2, and N_3 rats treated with relevant turmeric powder and curcumin microencapsulated than N_0 indicating a positive effect of turmeric polyphenol curcumin that helps to maintain the needed level of good cholesterol, which prevents plaque development in the body's systemic blood circulation.

Low-density lipoprotein

The statistical data regarding LDL cholesterol in normal rats depicted a higher level of LDL in sera of control rats (N_0) than turmeric powder, nutraceutical microencapsulated-curcumin$_{SFE}$ (N_2) and –curcumin$_{CSE}$ (N_1) treated rats. Furthermore, remarkable differences ($P < 0.05$) were recorded related to LDL cholesterol among the groups of hyperlipidemic rat models. The highest LDL value was noted in the positive control group (H_0) of hypercholesterolemic rats. The cholesterol feeding throughout the experimental period disturbed lipid metabolism in rats thus elevating serum LDL cholesterol. Nonetheless, the provision of curcumin-based diet to hypercholesterolemic rats was proven effective to manage lipid-related anomalies by suppressing the elevated LDL level as illustrated by their mean values relating to H_1, H_2, and H_3. Compared to H_0, a significant 15.42, 13.77, and 9.86% reduction in LDL levels of H_1, H_2 and H_3 groups correspondingly were observed validating the therapeutic potential of a turmeric polyphenol enriched diet. In a nutshell, diet containing a variety of turmeric bioactives could be beneficial in reducing a variety of lifestyle-related discrepancies associated with serum lipid abnormalities.

Very low-density lipoprotein

From the results, it is obvious that rats depending on a high cholesterol diet in group H_0 got higher (33.71%) VLDL cholesterol than that of N_0 thus, demonstrating the adverse impact of high cholesterol on balanced lipidemic parameters as about 50% of a VLDL particle is composed of TG. N_1, N_2 and N_3 were statistically alike when compared to N_0, whereas, significant variations ($P < 0.05$) were specified compared to H_0, H_1, H_2, and H_3. However, in terms of VLDL, when compared to H_0, supplementation of turmeric powder, nutraceutical curcumin isolated using conventional solvent and supercritical fluid in the dietary module of H_1, H_2, and H_3 rats' groups managed to lower VLDL cholesterol by 5.52, 7.73, and 9.38%, correspondingly highlighting protective effects of curcumin-based diet (Table 3).

Non-high-density lipoprotein

The data for normal and diet-induced hypercholesterolemic rat groups (Table 3) elucidated the significant efficacy of the study of microencapsulated curcumin in reducing serum non-High-density lipoprotein (n-HDL) levels for all treated groups. Administration of turmeric powder (H_1), microencapsulated-curcumin$_{CSE}$ (H_2) and –curcumin$_{SFE}$ (H_3) showed a significant impact on n-HDL indicating modulatory effect of turmeric bioactive compound, i.e., curcumin on the major lipoproteins linked with a higher risk of cardiovascular disease. When compared to H_0, diet modification by using turmeric for H_1, H_2, and H_3 lowered n-HDL by 16.44, 20.67, and 25.56%, correspondingly. Similarly, the normal counterparts of H_1, H_2, and H_3, that is, N_1, N_2, and N_3 groups also presented significantly lower n-HDL levels.

Triglycerides

Triacylglycerols are a major element of chylomicron and may act as energy substrates for hepatic and peripheral tissues, chiefly, muscles. The pooled means (Table 3) revealed an obvious trend in which TG in the serum of three test groups (N_1, N_2, and N_3) was lower than the rat group fed a normal diet (N_0). However, triglyceride level of hyperlipidemic rat groups reared on diet containing turmeric powder (H_1), microencapsulated-curcumin$_{CSE}$ (H_2) and –curcumin$_{SFE}$ (H_3) was dramatically lower than that of H_0 ($P < 0.05$). The momentous decline was observed in H_3 (9.38%) followed by H_2 (7.72%) and H_1 (5.49%), respectively as referred from H_0. It indicated that Curcumin-rich diets reduce the negative effects of high cholesterol consumption on lipid profiles.

Lipidemic ratios

In terms of lipidemic ratios, the rats in the H_0 group had a significantly higher AI ($P < 0.05$) than rats in the N_0 group due to high cholesterol in their diet. There was a significant difference between H0 and the other study groups (Table 4). The variations in this parameter among groups were attributed to the provision of curcumin-enriched diets that normalized the atherogenic index; a novel indicator involved in dyslipidemia by normalizing HDL levels. It caused an 18.57, 23.57, and 29.28%

reduction in the AI in H_1, H_2, and H_3, respectively than H_0. The alike trend was observed for other study groups relying on a normal diet. In contradiction, the AAI of all rat groups increased momentously as compared to their control groups N_0 and H_0 due to the positive effect of curcumin on good cholesterol (HDL) in sera. The risk of cardiac arrest due to plaque formation in arteries is increased by elevation in LDL serum cholesterol, hence increasing the CRR.

According to statistical inferences for CRR (**Table 4**), turmeric and curcumin inclusion isolated by conventional ethanol and super-critical fluid in daily intakes of different rat groups had a significant effect on CRR value. The rat groups N_1, N_2, and N_3 are at lower cardiac risk in comparison to N_0. Likewise, the higher cardiac risk was recorded in H_0 that was remarkably lower for rat groups feeding on turmeric powder (H_1) and curcumin$_{CSE}$ (H_2) and curcumin$_{SFE}$ (H_3) microencapsulated containing diet proving its prophylactic role against elevated lipid biomarkers (LDL, VLDL, and TG). It is also noteworthy, that turmeric and its bioactive; curcumin significantly improves the HTR (%) by upgrading the level of HDL cholesterol in normal (N_1, N_2, and N_3) and high cholesterol (H_1, H_2, and H_3) treated rat groups as compared to negative (N_0) and positive (H_0) controls during 2-month efficacy trial.

Discussion

Nowadays, increased reliance on hypercaloric foods, poor dietary habits and a deskbound lifestyle are the dominant factors throughout the world, ultimately responsible for the escalated prevalence of lifestyle-related disorders such as hyperlipidemia, coronary complications, etc. To cope with this scenario, consumers have been curious about healthy food options to ensure disease prevention beyond basic nutrition. Accordingly, bioactive plant ingredients have captured the attention of health-conscious consumers owing to their acceptability, low cost and safe nature (24). Numerous evidence have enlightened the affirmative participation of spices in improving physiological functionality (25, 26). In this regard, turmeric has gained great attention due to its antioxidant potential, which is primarily attributed to curcumin. Considering the aforementioned facts, the purpose of this study was to evaluate the nutraceutical value of locally cultivated turmeric against high serum cholesterol levels caused by diet (27). To secure these health benefits, it is noteworthy to select optimum extraction modes (conventional and non-conventional techniques), solvent (polar and non-polar), extraction parameters (temperature, pH and time) to isolate curmin from parent plant; turmeric. A study relating to aforementioned parameters was conducted (19). They concluded that green extraction technologies (SFE) should be employed to isolate and purify heat labile food components as compared to conventional extraction tools. Additionally, the low stability and escalated intestinal metabolism of curcumin during first pass metabolism have limited its therapeutic value against various maladies. However, encapsulating the core material in bio-stable matrices improves its bioavailability in systemic circulation. In pharmacokinetic study, Takahashi et al. (28) determined the impact of lecithin liposome as coating material to modulate curcumin release at targeted tissues in rats. Accordingly, 319.2 μg/mL was recorded at 120 min in rat plasma receiving Liposome Encapsulated Curcumin (LEC) as compared to group fed on free curcumin with maximum concentration (C_{max}) of 34.6 μg/mL at T_{max} 30 min. It was studied that ingestion of turmeric biomolecule "curcumin" decreases the absorption of high cholesterol diet by rapidly eliminating bile hence lowering the risk of heart diseases (14).

The result of this research supported the modulatory effect of turmeric and microencapsulated curcumin against hyperlipidemia. The outcomes of the research firmly supported the established hypothesis for the research and concluded that microencapsulated curcumin modulates diet-induced hypercholesterolemia due to its higher bioavailability in contrast to turmeric powder. As it was observed that curcumin encapsulated in maltodextrin and gelatin is less susceptible to degradation into metabolites and conjugation. The graphical representation for microencapsulated curcumin availability in

TABLE 4 Lipidemic ratio of rats treated with different curcumin-enriched diets.

Groups	AI	Cardiac risk ratio (CRR)	HDL:TC ratio (HTR%)	AAI
N_0	1.30 ± 0.02^{b}	0.91 ± 0.03^{b}	43.47 ± 1.72^{bc}	0.77 ± 0.01^{bc}
N_1	1.21 ± 0.01^{bc}	0.87 ± 0.02^{bc}	45.21 ± 1.37^{b}	0.83 ± 0.04^{b}
N_2	1.14 ± 0.05^{b}	0.83 ± 0.01^{c}	46.70 ± 0.79^{b}	0.88 ± 0.01^{c}
N_3	1.10 ± 0.02^{bc}	0.81 ± 0.01^{cd}	47.46 ± 2.45^{ab}	0.90 ± 0.03^{ab}
H_0	1.40 ± 0.03^{a}	0.98 ± 0.07^{a}	41.60 ± 1.98^{c}	0.71 ± 0.02^{c}
H_1	1.14 ± 0.01^{b}	0.87 ± 0.04^{bc}	46.53 ± 2.13^{b}	$0.87 \pm 0.04b^{c}$
H_2	1.07 ± 0.06^{bc}	0.82 ± 0.02^{c}	48.20 ± 1.56^{ab}	0.93 ± 0.06^{b}
H_3	0.99 ± 0.02^{c}	0.79 ± 0.05^{d}	50.13 ± 0.66^{a}	1.01 ± 0.05^{a}

Data values represent mean ± SD (n = 10); means carrying different superscripted letters in a column differ significantly ($P < 0.05$).

rat plasma has confirmed its maximum retention at 100 min as compared to turmeric powder. Another important parameter of the study was green extraction technology, i.e., supercritical fluid extraction used for improved curcumin yield extraction and eco-friendly compared to the conventional extraction method. It is worth noting that the efficacy of biomolecules can be improved by employing novel extraction tools in conjunction with various combinations of bio-stable matrices.

Diet-induced hypercholesterolemia in model feed trials has been used as a routine approach to check the effects of functional compounds against dyslipidemia (23). The results of our study are quite in line with the previous reports. One of the mechanistic approaches behind the hypocholesterolemic potential of turmeric bioactive is to modulate liver X receptor-α, i.e., nuclear receptor protein that regulates macrophage formation and transcriptional factors ultimately maintaining lipid homeostasis (29). It has been reported that the consumption of a high-fat diet (HFD) caused deposition of inflammatory cells, lipid infiltration and localization of Intercellular Adhesion Molecule-1 (ICAM-1) and Vascular Cell Adhesion Molecule-1 (VCAM-1), which are key indicators of coronary heart diseases. However, administration of curcumin did not show any mark of ICAM-1 and VCAM-1 adhesion molecules in the aortic arch of rats fed on high cholesterol diet (16, 30, 31). Later on, Mahmoud et al. (32) investigated the prophylactic effects of curcumin against the hyperlipidemia induced by feeding rats on a HFD. The data proved that curcumin modulates hepatic lipid levels. Accordingly, curcumin may decrease circulatory lipids by hindering adipocytes' fatty acid synthase (FAS), consequently inhibiting the hepatic lipid accumulation due to suppression in transport of lipid to the liver.

Another theory behind the lipid-lowering capacity of curcumin is the activation of peroxisome proliferator-activated receptor-α (PPAR-α) that accelerates the gene regulating cholesterol transport and fatty acid oxidation thus lowering hepatic cholesterol (33). Curcumin can maintain a balance between β-lipoprotein and α-lipoprotein, which are imperative for the structural and functional integrity of both LDL and HDL, respectively (1).

HDL is necessary to clear TG and cholesterol esters from plasma to be secreted in bile. Curcumin improves HDL levels by reducing the transfer of cholesteryl esters from HDL to LDL (16) thus improving the atherogenic index. In the limelight of another theory, high apolipoprotein A, i.e., precursor of HDL leads to elevated oxido-resistant lipoprotein resultantly, improving the AAI. In this context, curcumin up-regulates the level of apolipoprotein A and acetyltransferase that are involved in cholesterol transport to the liver (34, 35). It is concluded from the aforesaid discussion that turmeric is helpful against cardiovascular complications owing to its positive impact on HDL levels.

Oxidation of LDLs is of prime importance for the progression of arteriosclerosis, which damages the inner lining of endothelial cells. In this connection, curcumin provides cellular integrity and blocks platelet aggregation and peroxidation of lipids thus minimizing the chances of plaque formation in arteries (3, 36). An array of evidence exposed an inverse relation between curcumin consumption and lipid irregularities as it scavenges free radicals and reverses LDL oxidation hindering the formation of foam cells and its deposition in aortic arteries alongside improvement in HDL further coupled with its hypocholesterolemic potential (37). Curcumin directly interacts with hepatic cells for the translation of mRNA that encodes to increase LDL receptors on liver cells. As a result of the increase in LDL receptors, liver cells may sweep up the body's greater levels of LDL (14). In the current study, the provision of curcumin-based diet to hypercholesterolemic rats was proven to be effective in managing lipid-related abnormalities by suppressing the elevated LDL levels. It can be summarized that turmeric-supplemented foods are useful in alleviating a variety of lifestyle-related ailments.

Hyperlipidemia interrupts the redox balance and leads to irregular and uncontrolled release of free radicals ensuring accelerated atherogenic cases by developing a state of oxidative stress (38). But in the current scenario, the AI was significantly decreased due to the provision of curcumin, which depicts the hypocholesterolemic potential of curcumin. Therefore, a diet containing turmeric, and especially curcumin is valuable to attenuate the risk indices for cardiac ailments by elevating HDL and reducing LDL.

The current findings are consistent with the findings of Chandrakala and Tekulapally (39) who investigated the hypolipidemic effect of turmeric curcumin to alleviate the negative effects of hypercholesterolemia. They reported that both turmeric and curcumin decreased TC, TG, and LDL along with simultaneous increment in HDL concerning control. However, curcumin depicted a more pronounced effect on lipid profile than that turmeric. Another approach elucidated that curcumin upregulates cholesterol-7α-hydroxylase in the hypercholesterolemic rats *via* nuclear receptor liver X receptor (LXR), i.e., responsible for the catabolism of cholesterol in bile acid. Thus, the hypocholesterolemia potential of curcumin is attributed to increased excretion of cholesterol and bile acid from the body *via* feces which reduces cholesterol reabsorption from dietary sources. Moreover, curcumin intakes regulate AMP-dependent kinase and peroxisome proliferator regulated receptors, engaged in the catabolism of adipocytes present in subcutaneous layer (32, 40). Recently, Iwueke et al. (41) have proven that a daily intake of turmeric powder (200 mg/kg) considerably lowers the TC and TG levels in sera. Another meta-analysis conducted on patient with metabolic disorder, Type II diabetes mellitus showed beneficial effect on lipid parameters on relying on diet

supplemented with curcumin (42). The previous literature showed that consumption of high fat diet caused deposition of inflammatory cells, lipid infiltration and localization of Intercellular Adhesion Molecule-1 (ICAM-1) and Vascular Cell Adhesion Molecule-1 (VCAM-1) that are key indicators of coronary heart diseases. However, curcumin significantly reduced ICAM-1 and VCAM-1 adhesion molecules in aortic arch of rats fed on high cholesterol diet (16). Another theory behind lipid lowering capacity of curcumin is the activation of PPAR-α (peroxisome proliferator activated receptor-α) that accelerates the gene regulating cholesterol transport and fatty acid oxidation thus lowers the hepatic cholesterol. Although, the benefits of turmeric and its biologically active constituent curcumin for the treatment of hyperlipidemia have been discussed in depth. However, further research on genetic aspects of the modulatory effects and the underlying mechanisms of microencapsulated curcumin are yet to be uncovered so that a successful nutraceutical or dietary regimen can be recommended for humans.

Conclusion

Microencapsulation helps to incorporate sensitive ingredients into foods, food supplements or pharmaceuticals. This study showed that curcumin absorption *via* the gastrointestinal tract and the stability toward metabolization in the body can be increased *via* microencapsulation using maltodextrin and gelatin. In this way, microencapsulated active ingredients can be released with a delay without catabolizing and being conjugated in first pass, thus increase gastric tolerance compared to conventional forms such as rapidly disintegrating tablets. Furthermore, the current research has provided evidence that turmeric has nutraceutical worth to alleviate hyperlipidemia. A diet containing turmeric or curcumin can modulate lipid profile markers. In this context, microencapsulated curcumin showed a remarkable regulatory impact on total cholesterol, LDL and TG along with improvement in HDL of treated rat groups. It was noticed that turmeric powder, microencapsulated-curcumin$_{CSE}$ and –curcumin$_{SFE}$ are more effective and biologically active in delivering the therapeutic effects in the hyperlipidemic state than that in normocholesterolemic conditions. Thereby, it is concluded that the use of microencapsulated curcumin could be a sustainable strategy to alleviate cardiovascular complications *via* dietary therapies. Nonetheless, there are research gaps regarding the histopathological study of blood vessels under normal and hypercholesterolemic conditions. Future research into microencapsulated curcumin as a lipid-modulating agent is therefore required to be explored. This will involve evaluating cholesterol deposition in blood vessels using histopathological, immunohistochemical, and genomic indicators, and especially correlating the findings with human study.

Data availability statement

The original contributions presented in this study are included in the article/supplementary material, further inquiries can be directed to the corresponding author/s.

Ethics statement

The animal study was reviewed and approved by the Directorate of Graduate Studies, UAF (No. DGS/474-79) after ensuring the standards for handling and care of laboratory animals from the Departmental Bioethics Committee.

Author contributions

HA conceptualized, designed and conducted the research experiments. MB co-conceptualized and provided technical assistance in designing the research. I-U-H, HA, and MN analyzed the results, drafted the manuscript, and wrote the original draft. RA and MT technically modified the manuscript concerning data visualization, language and editing. AR, I-U-H, RA, and MT contributed to the review and editing. All authors approved the final version of this manuscript.

Funding

The authors are thankful to Higher Education Commission, Pakistan for supporting the first authors *via* funding to conduct this research. Supported by a grant from the Romanian National Authority for Scientific Research and Innovation, CNCS—UEFISCDI, project nos. PN-III-P2-2.1-PED-2019-1723 and PFE 14, within PNCDI III.

Acknowledgments

We are thankful to the Functional and Nutraceutical Food Research Section at the National Institute of Food Science and Technology, University of Agriculture, Faisalabad, Pakistan for providing support during the conduct of this research.

Conflict of interest

Author MT was employed by Centiv.

The remaining authors declare that the research was conducted in the absence of any commercial or financial relationships that could be construed as a potential conflict of interest.

Publisher's note

References

1. Yang Q, Cogswell ME, Flanders WD, Hong Y, Zhang Z, Loustalot F, et al. Trends in cardiovascular health metrics and associations with all-cause and CVD mortality among US adults. *JAMA.* (2012) 307:1273–83. doi: 10.1001/jama.2012.339

2. Yao YS, Li TD, Zeng ZH. Mechanisms underlying direct actions of hyperlipidemia on myocardium: an updated review. *Lipids Health Dis.* (2020) 19:23. doi: 10.1186/s12944-019-1171-8

3. Bengmark S. Control of systemic inflammation and chronic disease–the use of turmeric and curcumenoids. In: Mine Y, Miyashita K, Shahidi F editors. *Nutrigenomics and Proteomics in Health and Disease: Food Factors and Gene Interactions.* Hoboken, NJ: Wiley-Blackwell (2009). p. 161–80. doi: 10.1002/9780813807263.ch12

4. Anwar R, Rabail R, Rakha A, Bryla M, Roszko M, Aadil RM, et al. Delving the role of caralluma fimbriata: an edible wild plant to mitigate the biomarkers of metabolic syndrome. *Oxid Med Cell Longev.* (2022) 2022:5720372. doi: 10.1155/2022/5720372

5. Rehman A, Jafari SM, Tong Q, Riaz T, Assadpour E, Aadil RM, et al. Drug nanodelivery systems based on natural polysaccharides against different diseases. *Adv Colloid Interface Sci.* (2020) 284:102251. doi: 10.1016/j.cis.2020.102251

6. Alberti Á, Riethmüller E, Béni S. Characterization of diarylheptanoids: an emerging class of bioactive natural products. *J Pharm Biomed Anal.* (2018) 147:13–34. doi: 10.1016/j.jpba.2017.08.051

7. Anamika B. Extraction of curcumin. *IOSR J Environ Sci Toxicol Food Technol.* (2012) 1:1–16. doi: 10.9790/2402-0130116

8. Fang Z, Bhandari B. Encapsulation of polyphenols–a review. *Trends Food Sci Technol.* (2010) 21:510–23. doi: 10.1016/j.tifs.2010.08.003

9. Anand P, Kunnumakkara AB, Newman RA, Aggarwal BB. Bioavailability of curcumin: problems and promises. *Mol Pharm.* (2007) 4:807–18. doi: 10.1021/mp700113r

10. Prasad S, Gupta SC, Tyagi AK, Aggarwal BB. Curcumin, a component of golden spice: from bedside to bench and back. *Biotechnol Adv.* (2014) 32:1053–64. doi: 10.1016/j.biotechadv.2014.04.004

11. Malacrida, C, Telis V. Effect of different ratios of maltodextrin/gelatin and ultrasound in the microencapsulation efficiency of turmeric oleoresin. *11th International Congress on Engineering and Food*. Athens: Elsevier Procedia (2011).

12. Noureddin SA, El-Shishtawy RM, Al-Footy KO. Curcumin analogues and their hybrid molecules as multifunctional drugs. *Eur J Med Chem.* (2019) 182:111631. doi: 10.1016/j.ejmech.2019.111631

13. Xia Z-H, Chen WB, Shi L, Jiang X, Li K, Wang YX, et al. The underlying mechanisms of curcumin inhibition of hyperglycemia and hyperlipidemia in rats fed a high-fat diet combined with STZ treatment. *Molecules.* (2020) 25:271. doi: 10.3390/molecules25020271

14. Elahi RK. Preventive effects of turmeric (*Curcuma longa* Linn.) powder on hepatic steatosis in the rats fed with high fat diet. *Life Sci J.* (2012) 9:5462–8.

15. Ilic D, Misso M. Lycopene for the prevention and treatment of benign prostatic hyperplasia and prostate cancer: a systematic review. *Maturitas.* (2012) 72:269–76. doi: 10.1016/j.maturitas.2012.04.014

16. Shin SK, Ha TY, McGregor RA, Choi MS. Long-term curcumin administration protects against atherosclerosis *via* hepatic regulation of lipoprotein cholesterol metabolism. *Mol Nutr Food Res.* (2011) 55:1829–40. doi: 10.1002/mnfr.201100440

17. Kulkarni S, Maske KN, Budre MP, Mahajan R. Extraction and purification of curcuminoids from Turmeric (*Curcuma longa* L.). *Int J Pharmacol Pharm Technol.* (2012) 1:81–4.

18. Wakte PS, Sachin BS, Patil AA, Mohato DM, Band TH, Shinde DB. Optimization of microwave, ultra-sonic and supercritical carbon dioxide assisted extraction techniques for curcumin from *Curcuma longa*. *Separat Purificat Technol.* (2011) 79:50–5. doi: 10.1016/j.seppur.2011.03.010

19. Ashraf H, Butt MS, Asghar A, Shahid M. Comparative study of conventional solvent and supercritical fluid extracts of turmeric using high performance liquid chromatography. *Pakistan J Agric Sci.* (2016) 53:941–6. doi: 10.21162/PAKJAS/16.5361

20. Xie X, Tao Q, Zou Y, Zhang F, Guo M, Wang Y, et al. PLGA nanoparticles improve the oral bioavailability of curcumin in rats: characterizations and mechanisms. *J Agric Food Chem.* (2011) 59:9280–9. doi: 10.1021/jf202135j

21. Kim JY, Paik JK, Kim OY, Park HW, Lee JH, Jang Y, et al. Effects of lycopene supplementation on oxidative stress and markers of endothelial function in healthy men. *Atherosclerosis.* (2011) 215:189–95. doi: 10.1016/j.atherosclerosis.2010.11.036

22. Alshatwi AA, Al Obaaid MA, Al Sedairy SA, Al-Assaf AH, Zhang JJ, Lei KY. Tomato powder is more protective than lycopene supplement against lipid peroxidation in rats. *Nutr Res.* (2010) 30:66–73. doi: 10.1016/j.nutres.2009.12.002

23. Ashfaq F, Butt MS, Bilal A, Tehseen S, Hafiz S. Bioefficacy of red cabbage against hypercholesterolemic diet mediated oxidative stress. *Clin Phytosci.* (2019) 5:1–9. doi: 10.1186/s40816-019-0126-y

24. Daliri EB-M, Lee BH. Current trends and future perspectives on functional foods and nutraceuticals. In: Liong MT editor. *Beneficial Microorganisms in Food and Nutraceuticals*. Cham: Springer (2015). p. 221–44. doi: 10.1007/978-3-319-23177-8_10

25. Al-Saud NBS. Impact of curcumin treatment on diabetic albino rats. *Saudi J Biol Sci.* (2020) 27:689–94. doi: 10.1016/j.sjbs.2019.11.037

26. Urala N, Lähteenmäki L. Consumers' changing attitudes towards functional foods. *Food Qual Prefer.* (2007) 18:1–12. doi: 10.1016/j.foodqual.2005.06.007

27. Singletary K. Turmeric: potential health benefits. *Nutr Today.* (2020) 55:45–56. doi: 10.1097/NT.0000000000000392

28. Takahashi M, Uechi S, Takara K, Asikin Y, Wada K. Evaluation of an oral carrier system in rats: bioavailability and antioxidant properties of liposome-encapsulated curcumin. *J Agric Food Chem.* (2009) 57:9141–6. doi: 10.1021/jf9013923

29. Singh V, Rana M, Jain M, Singh N, Naqvi A, Malasoni R, et al. Curcuma oil attenuates accelerated atherosclerosis and macrophage foam-cell formation by modulating genes involved in plaque stability, lipid homeostasis and inflammation. *Br J Nutr.* (2015) 113:100–13. doi: 10.1017/S0007114514003195

30. Uchendu IK, Ekeigwe IB, Nnedu EB. Antidyslipidaemic and cardioprotective effects of turmeric (*Curcuma longa*) in rat fed a high cholesterol diet. *J Drug Delivery Ther.* (2020) 10(1-Suppl.):178–81. doi: 10.22270/jddt.v10i1-s.3869

31. Ghelani H, Razmovski-Naumovski V, Chang D, Nammi S. Chronic treatment of curcumin improves hepatic lipid metabolism and alleviates the renal damage in adenine-induced chronic kidney disease in sprague-dawley rats. *BMC Nephrol.* (2019) 20:431. doi: 10.1186/s12882-019-1621-6

32. Mahmoud AA, Abdelrahman A, Abd el Aziz HO. Protective effect of curcumin on the liver of high fat diet-fed rats. *Gene Rep.* (2018) 11:18–22. doi: 10.1016/j.genrep.2018.01.004

33. Al-Nazawi M, El-Bahr S. Hypolipidemic and hypocholestrolemic effect of medicinal plant. *J Animal Veter Adv.* (2012) 11:2013–9. doi: 10.3923/javaa.2012.2013.2019

34. Zimetti F, Adorni MP, Marsillach J, Marchi C, Trentini A, Valacchi G, et al. Connection between the altered HDL antioxidant and anti-inflammatory properties and the risk to develop Alzheimer's disease: a narrative review. *Oxid Med Cell Longev.* (2021) 2021:6695796. doi: 10.1155/2021/6695796

35. Hussein SA, Azab ME-S, El-Shall SK. Protective effect of curcumin on antioxidant defense system and oxidative stress in liver tissue of iron overloading rats. *Asian J Clin Nutr.* (2014) 6:1–17. doi: 10.3923/ajcn.2014.1.17

36. Pourbagher-Shahri AM, Farkhondeh T, Ashrafizadeh M, Talebi M, Samargahndian S. Curcumin and cardiovascular diseases: focus on cellular targets and cascades. *Biomed Pharm.* (2021) 136:111214. doi: 10.1016/j.biopha.2020.111214

37. Bahorun T, Luximon-Ramma A, Neergheen-Bhujun VS, Gunness TK, Googoolye K, Auger C, et al. The effect of black tea on risk factors of cardiovascular disease in a normal population. *Prev Med.* (2012) 54:S98–102. doi: 10.1016/j.ypmed.2011.12.009

38. Kim M, Kim Y. Hypocholesterolemic effects of curcumin *via* up-regulation of cholesterol 7a-hydroxylase in rats fed a high fat diet. *Nutr Res Practice.* (2010) 4:191–5. doi: 10.4162/nrp.2010.4.3.191

39. Chandrakala MP, Tekulapally K. An evaluation of hypolipidemic effect of curcumin: a double blind, placebo controlled, randomized trial. *Int J Phytother Res.* (2014) 4:20–6.

40. El-Bahr S, Al-Azraqi A. Effects of dietary supplementation of turmeric (*Curcuma longa*) and black cumin seed (*Nigella sativa*) in streptozotocin induced diabetic rats. *Int J Biochem Res Rev.* (2014) 4:481–92. doi: 10.9734/IJBCRR/2014/11120

41. Iwueke A, Madu W, Chukwu E. Turmeric powder gavage improves lipid profile of albino rats. *J Complement Alternat Med Res.* (2020) 9:42–6. doi: 10.9734/jocamr/2020/v11i330189

42. Tian J, Feng B, Tian Z. The effect of curcumin on lipid profile and glycemic status of patients with type 2 diabetes mellitus: a systematic review and meta-analysis. *Evid Based Complement Alternat Med.* (2022) 2022:8278744. doi: 10.1155/2022/8278744

frontiers | Frontiers in Nutrition

TYPE Original Research
PUBLISHED 20 October 2022
DOI 10.3389/fnut.2022.1041608

OPEN ACCESS

EDITED BY
Debao Niu,
Guangxi University, China

REVIEWED BY
Xuebo Song,
University of Florida, United States
Hangjun Chen,
Zhejiang Academy of Agricultural Sciences, China
Tao Xiong,
Nanchang University, China

*CORRESPONDENCE
Lingyan Zhao
lyzhaohnau@hunau.edu.cn
Fangming Deng
fmdenghnau@sina.com

SPECIALTY SECTION
This article was submitted to Nutrition and Food Science Technology, a section of the journal Frontiers in Nutrition

RECEIVED 11 September 2022
ACCEPTED 03 October 2022
PUBLISHED 20 October 2022

CITATION
Ma D, Li Y, Chen C, Fan S, Zhou Y, Deng F and Zhao L (2022) Microbial succession and its correlation with the dynamics of volatile compounds involved in fermented minced peppers.
Front. Nutr. 9:1041608.
doi: 10.3389/fnut.2022.1041608

Microbial succession and its correlation with the dynamics of volatile compounds involved in fermented minced peppers

Ding Ma[1], Yong Li[2], Chengcheng Chen[3], Shichao Fan[4], Yi Zhou[5], Fangming Deng[1]* and Lingyan Zhao[1]*

[1]College of Food Science and Technology, Hunan Agricultural University, Changsha, China, [2]Department of Human Nutrition, Food and Animal Sciences, University of Hawai'i at Mānoa, Honolulu, HI, United States, [3]Hunan Guotai Foods Co., Ltd., Yueyang, China, [4]Junjie Food Technology Co., Ltd., Shaoyang, China, [5]Lameizi Foodstuff Co., Ltd., Yiyang, China

Fermented minced peppers are a traditional fermented food that has a unique flavor due to various microbial communities involved in fermentation. Understanding the changes in microbial communities and volatile components of fermented minced peppers is particularly important to unveil the formation of unique flavor of fermented peppers. In this study, the microbial communities and volatile compounds in fermented minced pepper was analyzed by high-throughput sequencing and GC-MS, as well as their underlying correlations were also established. Results indicated that 17 genera were identified as dominant microorganisms in the fermentation of minced pepper, accompanied by the detection of 64 volatile compounds. Further hierarchical clustering analysis (HCA) displayed that dynamic change of volatile metabolites were involved in the fermentation process, where alkane volatile components were mainly generated in the early stage (3–5 days), and alcohols volatile components were in the middle stage (7–17 days), while ester volatile components were mainly produced in both the early stage (3–5 days) and last stage (17–20 days). Bidirectional orthogonal partial least squares (O2PLS) analysis revealed that 11 genera were core functional microorganisms of fermented minced pepper. *Cladosporium* and *Hansenpora* were significantly correlated with the formation of 9 and 6 volatiles, respectively. These findings provide new insights into aroma profile variation of fermented minced peppers and underlying mechanism of characteristic aroma formation during fermentation.

KEYWORDS

fermented minced pepper, natural fermentation, microbial diversity, volatile components, correlation analysis

Introduction

Fermented minced pepper, a traditional fermented vegetable in the southern region of China, is widely consumed due to its nutritional and sensory properties (1). Aroma is one of the key criteria to evaluate the quality of fermented minced peppers, together with its appearance and taste. Alcohol, ester, and ketone compounds are regarded as the critical components in fermented peppers, which determine its special favor (2, 3). Numerous factors contribute to the quality of fermented peppers, such as biological origin, substrate conditions, microbial composition, and processing methods. Specifically, the composition of used substrates and fermentative microorganisms are the main factors (4). During the natural fermentation, microorganisms play a critical role in generating special flavor characteristics of fermented peppers *via* complex physiochemical reaction of secondary metabolites (5, 6).

In recent years, large numbers studies have been conducted to dig out the underlying mechanism and correlation between microorganisms and aroma and sensory characteristics of fermented food, such as Fu brick tea, cheese, and fermented bamboo shoots, etc. Li et al. (7) has explored the key aroma compounds and microorganisms, and the relationship between volatiles, sensory descriptors and microorganisms of Fu brick tea during processing, and found *Aspergillus*, *Candida*, *Debaryomyces*, *Penicillium*, *Unclassified_k_Fungi*, *Unclassified_o_Saccharomycetales* genera six fungal genera were identified as core functional microorganisms associated with volatile metabolism (7). Zheng et al. (8) identified eight bacterial genera and seven fungal genera was the core microbiota for flavor production of cheese (8). Guan et al. (9) found that *Lactobacillus*, *Clostridium*, *Enterobacter,* and *Akebia* play a crucial role in the formation of the unique flavor formation of suansun by investigating the dynamics of physicochemical parameters, flavor compounds and microbial communities during the natural production of sour bamboo shoots (9). Nature microbial community determines the formation of volatile components of fermented peppers and the quality of product (10). To standardize fermentation and avoid undesirable substance of fermented peppers, it is urgent to apply pure starter cultures instead of traditional natural fermentation. Therefore, it is vital to elucidate the key microbial community in traditional fermented peppers in China, which determine favor aroma and desirable properties of fermented peppers. So far most of the studies have mainly focused on the composition of volatile compounds in traditional Chinese fermented minced peppers or the differential volatile compounds between raw material and finished products. However, the information of the correlation between microbial diversity and flavor profile of fermented minced pepper was still insufficient.

In this study, fermented minced pepper was studied to (a) investigate the bacterial and fungal community during the fermentation process using a high-throughput sequencing method, (b) monitor the changes in volatile flavor components during fermentation using gas chromatography-mass spectrometry, and (c) assess the correlation between volatile flavors and microbial communities during fermentation using bidirectional orthogonal partial least squares (O2PLS) regression. Those findings were valuable for gaining insight into the mechanisms of aroma formation in fermented minced pepper, and improving the quality of fermented minced peppers with desirable sensory properties.

Materials and methods

Preparation of fermented minced pepper

Fresh *Capsicum annuum* L. Var. *Dactylus* M were cleaned, minced, salted with 8% (w/w) salt, placed in 24 sterile pickle jars with the same mass, covered, sealed with water, and fermented in a 20°C incubator. To study the changes in microbial diversity during fermentation, three Mason jars were removed at the same time on days 3, 5, 7, 9, 11, 14, 17, and 20 of fermentation for aseptic sampling. For sampling, 100 g of each product was transferred into tubes. minced pepper samples were labeled as 3, 5, 7, 9, 11, 14, 17, and 20 days, and stored at −80°C. Fresh minced pepper was labeled as 0 days.

DNA extraction, amplification, and sequencing

Total DNA was extracted from all samples with an E.Z.N.A Soil DNA kit (OMEGA, Bio-Tek, USA), according to the manufacturer's instructions, and stored at −20°C. We used the universal forward primer 27 F (5′-AGAGTTTGATCCTGGCTCAG-3′) and the reverse primer 533 R (5′-TTACCGCGGCTGCTGGCAC-3′) to amplify the V1–V3 region of bacterial 16S rDNA gene. We used a broadly conserved primer set (ITS1 and ITS4) to amplify the ITS region of fungal ITS rDNA. The 454 Life Sciences primer B sequence was found within the forward primer ITS1 (5′-TCCGTAGGTGAACCTGCGG-3′), while the 454 Life Sciences primer A sequence was found within the reverse primer ITS4 (5′-TCCTCCGCTTATTGATATGC-3′). Each PCR product was tagged using a specific 10-nt barcode. The PCR reactions (20 μL) were performed using 5 μM of reverse and forward primers, 10 ng of template DNA, 2 μL of 2.5 mM dNTPs, and 2 μL of 5 × fast Pfu master mix. Thermal cycling was performed as follows: initial denaturation for 2 min at 95°C, 30 cycles of denaturation for 30 s at 95°C, annealing for 30 s at 55°C, and extension for 30 s at 72°C. The final extension was performed at 72°C for 5 min. The replicated PCR products were mixed in a PCR tube, visualized on a 2.0% agarose

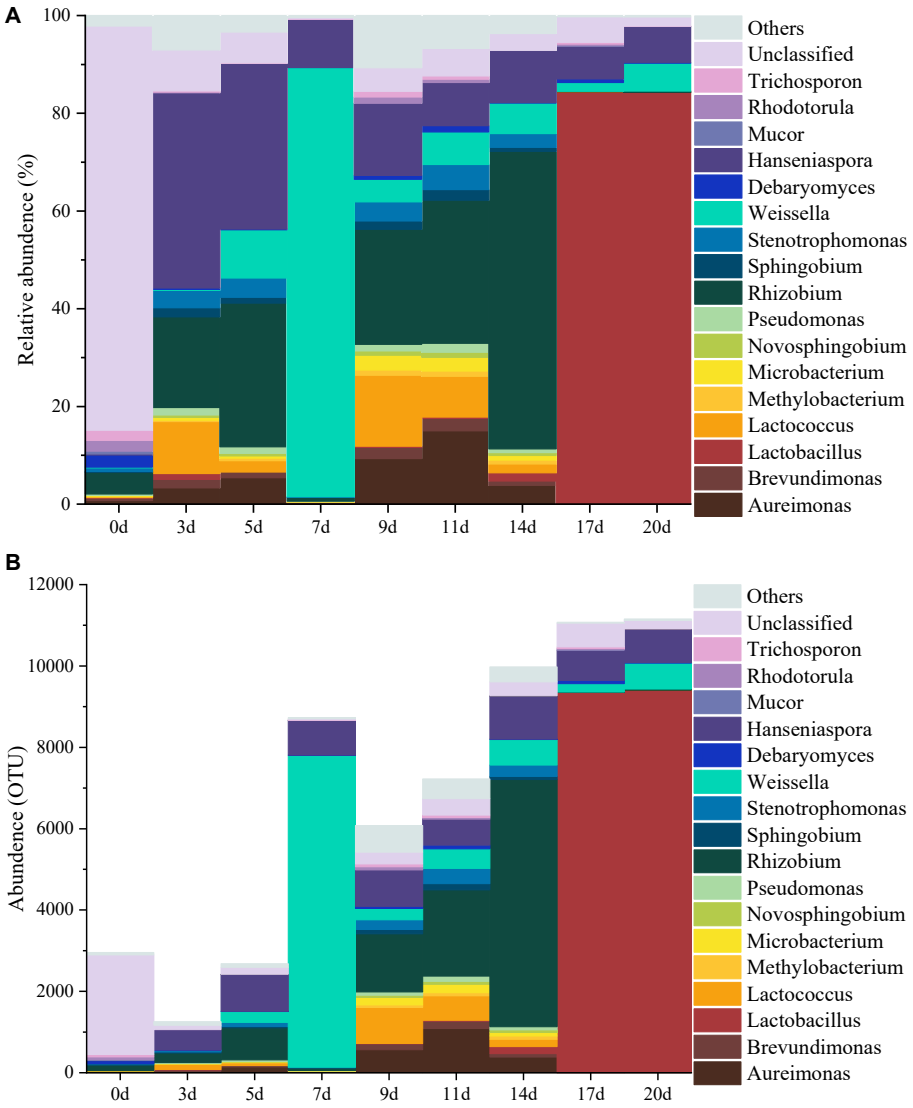

FIGURE 1
Dynamics of the relative abundance **(A)** and abundance **(B)** of microorganisms at the genus level during the production of fermented minced peppers.

gel, and purified with an AxyPrep DNA Gel Extraction Kit (AXYGEN), according to the manufacturer's instructions. Prior to sequencing the PCR product, its DNA concentration was analyzed with a QuantiFluor-ST (Promega, USA) and its quality was determined with an Agilent 2100 bioanalyzer (Agilent, USA). The resulting amplicons from each reaction mix were then mixed, in equimolar proportions, based on their concentrations. Emulsion PCR was then performed to produce the amplicon libraries, according to the methods used by 454 Life Sciences. A 454/Roche A sequencing primer kit was used on a Roche Genome Sequencer GS FLX Titanium platform at Shanghai Majorbio Bio-Pharm Technology Co., Ltd., (Shanghai, China) to carry out the pyrosequencing of the amplicons.

Bioinformatics analyses

QIIME (Version 1.17[1]) was used to process the resulting raw DNA sequences, while the standard barcodes and primer sets were not included. We trimmed all sequences with quality scores that were lower than 20, while those sequences with lengths less than 200 bp, or which possess ambiguous or homologous base scores less than 6, were removed. We denoised the pyrosequencing data, identified the chimera, and used UCHIME (Version 4.2.40[2]) to remove them from the datasets.

1 http://qiime.org/
2 https://www.drive5.com/usearch/manual/uchime_algo.html

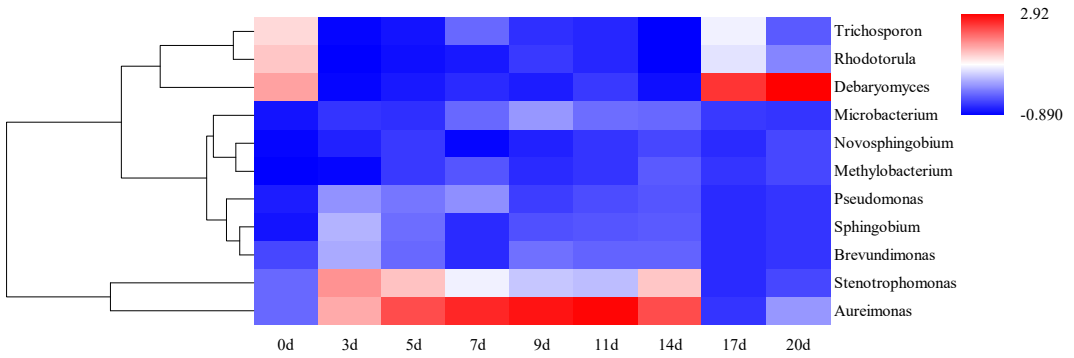

FIGURE 2
Hierarchical clustering analysis (HCA) of microbial abundance during the production of fermented minced peppers. The colors corresponded to normalized mean levels from low (blue) to high (red).

Once the low-quality sequences were removed, the sequences of suitable quality were grouped into operational taxonomic units (OTUs) using USEARCH (Version 6.1[3]) and 0.97 cut-off settings. The Ribosomal Database Project (RDP) classifier and NCBI Taxonomy Browser were used to sort the taxonomic classifications of the resulting sequences.

Extraction of volatile components from minced peppers

The headspace solid-phase microextraction (HS-SPME) method was employed to extract the volatile compounds from the minced pepper samples. The volatile components were analyzed according to the methods previously described (2). Samples (30 g each) were blended with 30 ml of distilled water, and 2 g of the sample was immediately transferred into a 15 ml SPME vial (Supelco, Bellefonte, PA, USA) followed by addition of 50 μL 2-octanol (10^{-6} mol/L) in methanol as an internal standard. After sample preparation, each vial was placed in a water bath at 70°C for 15 min with agitation to reach an equilibrium state. Subsequently, a fiber coated with 50/30 μm DVB/CAR/PDMS (Supelco, Bellefonte, PA, USA) was injected into the vial for 30 min to absorb volatile compounds.

Determination of volatile components using GC–MS

GC-MS analysis was carried out using a Shimadzu GC-2010 gas chromatograph connected to a QP2010 mass spectrometry system (Shimadzu Corp., Kyoto, Japan). A DB-Wax fused silica capillary column (30 m long × 0.25 mm internal diameter × 0.25 μm film thickness) was used with helium as the carrier gas at a constant flow rate of 1 ml/min. The heating gradient program was 40°C for 2 min, followed by increasing at 4°C/min to 80°C and remaining for 1 min. Thereafter, the temperature was raised to 240°C at 3.5°C/min and held on this stage for 4 min. Helium (purity 99.999%) carrier gas flow was at a constant pressure of 2 psi. All mass spectra were acquired in the electron impact (EI) mode (70 eV ionization energy, source temperature 225°C). EI mass spectra ranged from 30 to 550 a.m.u. Volatile compounds were identified by comparing the mass spectra of the samples with the data system (NIST 08 and WILEY 05). Quantitative results were calculated from the peak areas of the GC-MS chromatograms.

Statistical analysis

The samples were analyzed in triplicate to generate results in the physicochemical analyses. Significant differences were determined using a one-way ANOVA in SPSS 20.0 (International Business Machines Corp., USA). The line graph was created using OriginPro 2019 (OriginLab Corp., USA). To study the dynamic succession of microbial communities, hierarchical clustering analysis (HCA), principal component analysis (PCA), and Spearman's correlation coefficient calculations were performed using OriginPro 2019 (OriginLab, Inc., USA). The heatmaps and stacked histogram of the relative abundance of microbes at the genus level were created using OriginPro 2019 (OriginLab Corp., USA). O2PLS modeling was used to outline the relationship between the microbiota and volatile components assessed in this study. This consisted of a simultaneous projection of both the X and Y matrices on low-dimension hyper planes. The R^2 (close to 1) and Q^2 (> 0.4) are both necessary conditions for producing an optimal model and indicate suitable predictive ability. The O2PLS of the multivariate analysis was performed using SIMCA 14.1 (Umetrics, Sweden), while the visualized network planning

3 http://drive5.com/usearch/

10.3389/fnut.2022.1041608

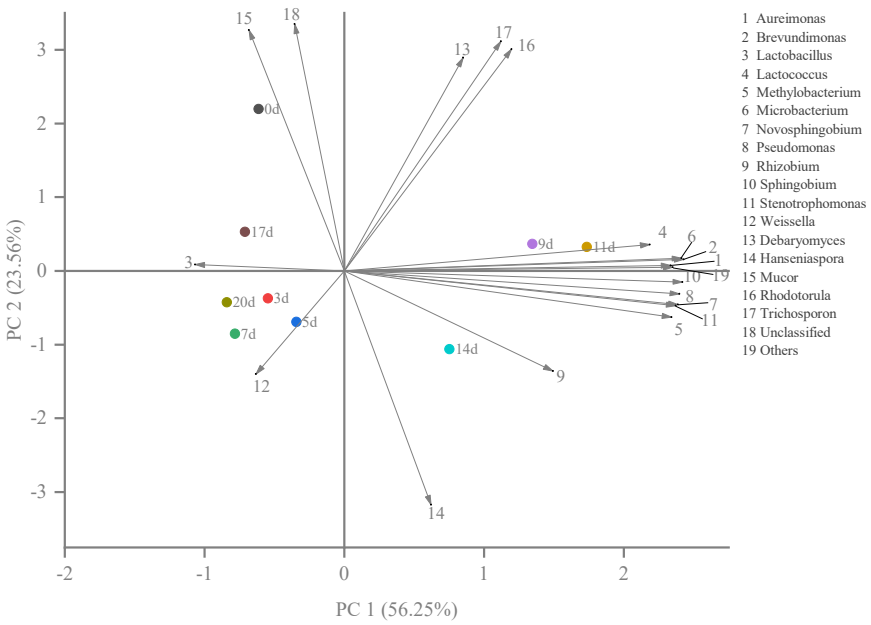

FIGURE 3
The results of principal component analysis (PCA) showed the correlation between microorganisms and fermentation time during the production of fermented minced peppers.

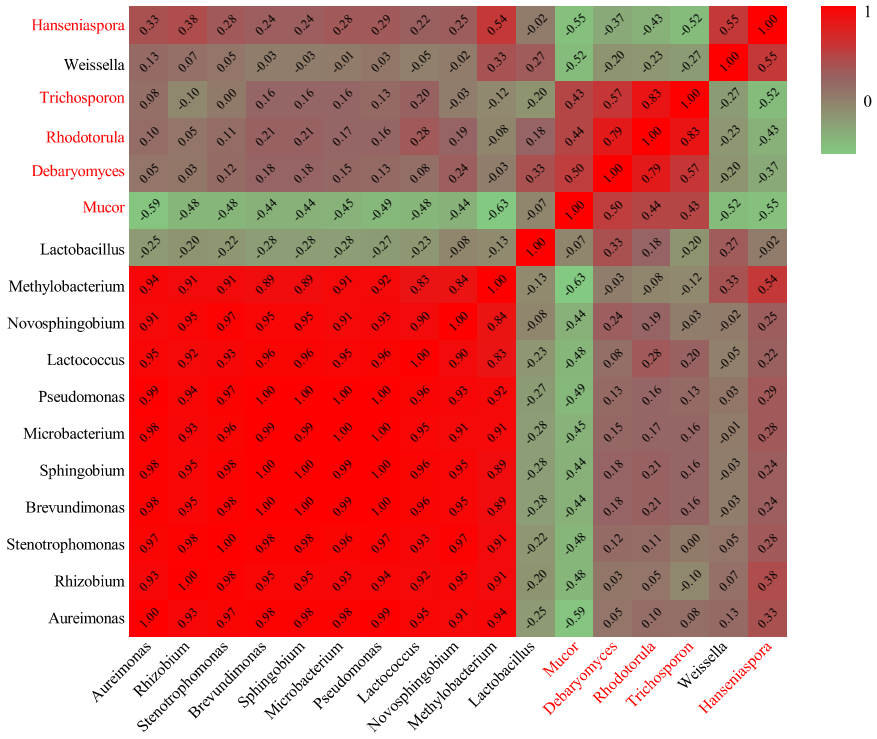

FIGURE 4
Heatmap of Spearman rank correlation between microorganisms during the production of fermented minced peppers. Black letters are bacteria. Red letters are fungi.

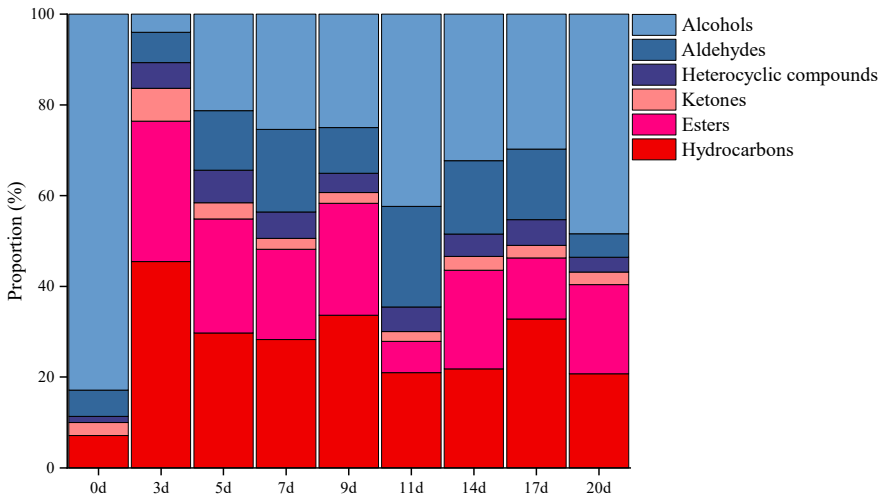

FIGURE 5
Dynamics of the relative proportion of volatiles during the production of fermented minced peppers.

of the Pearson correlation coefficient was conducted using Cytoscape 3.8.2.

Results and discussion

Dynamics and succession of the microbial community

A total of 104,784 16S rDNA and 10,781 ITS rDNA valid reads were generated from nine fermented minced pepper samples, with a total of 3,844 and 967 OTUs for bacteria and fungi, respectively, at an identity level of 97%. As showed in **Supplementary Figures 1, 2**, Shannon and Simpson diversity index analysis indicated that bacterial diversity in fermented minced pepper was initially increased with fermentation time, and reached maximum at the 9 days. Subsequently, decreased as fermentation prolonged (**Supplementary Figure 1**). On the other hand, fungal diversity was most abundant in initial time and gradually decreased from 0 to 7 days as fermentation proceeded (**Supplementary Figure 2**). Additionally, a rapid increase of Chao1 and ACE index was observed from 7 to 9 days. Subsequently, there were decreased from 14 to 17 days, implying that the abundance of fungal species fluctuated during the fermentation.

The top 1% of the abundance were used as the main species to study the dynamics of the microbial community during the fermentation of minced peppers. As depicted in **Figures 1A,B**. Dynamic changes of microbial communities were occurred as fermentation time proceeded. The dominant microorganisms including 12 bacterial and five fungal genera were identified. Initially, the original microbial community in unfermented minced pepper mainly consisted of *Rhizobium* (4%), *Debaryomyces* (2%), *Rhodotorula* (2%), *Trichosporon* (2%), unclassified (83%), and other (2%). During fermentation, the relative abundance of *Rhizobium* was higher at 3–5 days and 9–14 days (13–61%), reached maximum at 14 days. *Hanseniaspora* was the microorganism relatively stable in abundance during minced pepper fermentation. Its growth rate was most rapid during the fermentation from 0 to 3 days, and 40% relative abundance was achieved at 3 days. *Weissella* and *Lactobacillus* were the most abundant microorganisms in relative abundance at 7 days (88%) and 17–20 days (84%), respectively (**Figure 1A**). Similar results were obtained by the dynamics of microbial genus level abundance during the production of fermented minced peppers (**Figure 1B**).

Hierarchical clustering analysis and heat map were used to explore similar growth trends in different microorganisms during fermentation (**Figure 2**). *Aureimonas* and *Stenotrophomonas*, *Pseudomonas* and *Sphingobium*, *Methylobacterium* and *Novosphingobium*, and *Rhodotorula* and *Trichosporon* displayed similar growth trends during minced pepper fermentation. The variation of microorganisms with fermentation time during minced pepper fermentation was further analyzed by PCA (**Figure 3**). *Aureimonas* and *Lactococcus* were the main genera in the early fermentation process and were highly correlated with 9 and 11 days. While *Rhizobium* was associated highly with 14 days, *Weisseria* was found to be strongly associated with 5 and 7 days, and *Lactobacillus* was shown to be correlated highly with 17 and 20 days. This result suggests that microorganisms become dominant at different stages of fermentation as they evolve and compete, leading to large variations in microbial abundance and diversity at each fermentation time. Co-occurrence/exclusion analysis is an effective method to elucidate

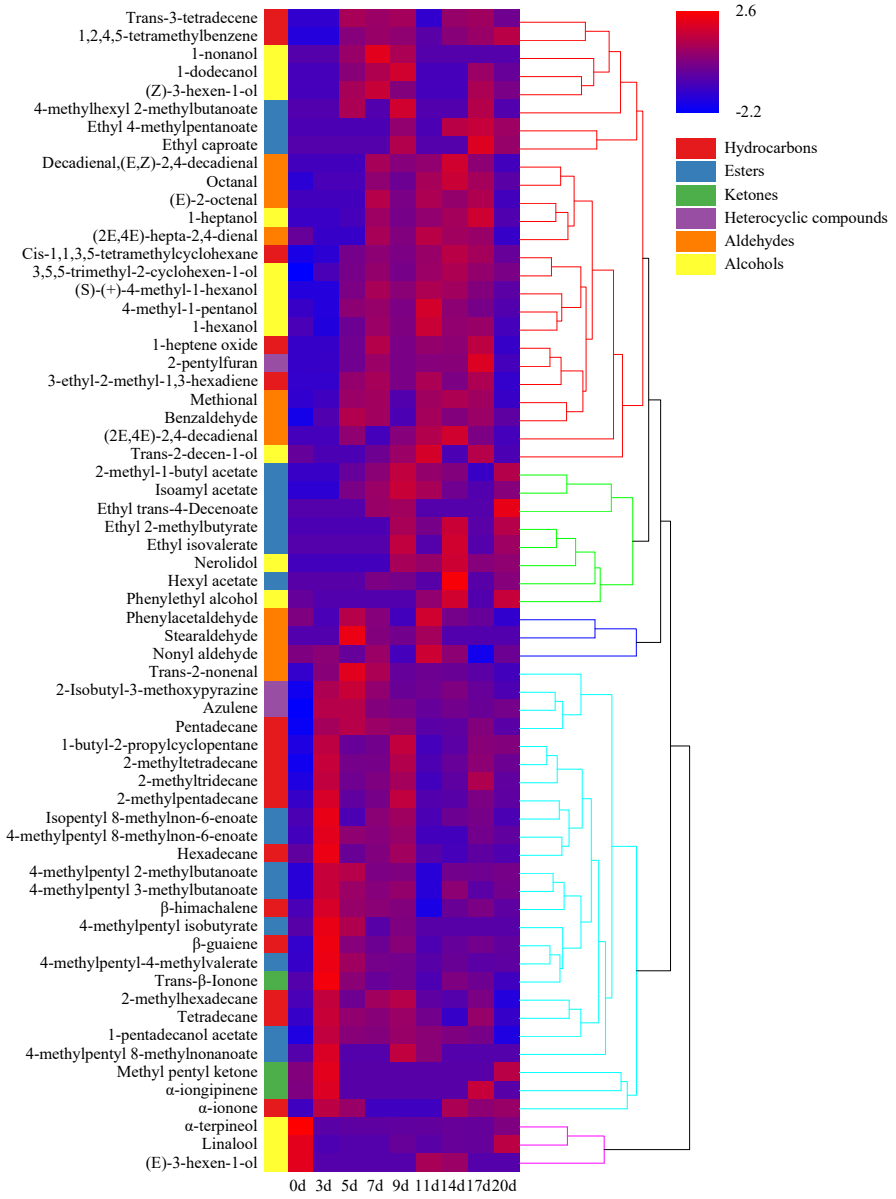

FIGURE 6
Hierarchical clustering analysis (HCA) of volatile components during the production of fermented minced peppers. The colors corresponded to normalized mean levels from low (blue) to high (red).

correlations in complex microbial communities (11, 12). The interactions between microorganisms during minced pepper fermentation were shown in **Figure 4**. Positive correlations were found between bacteria such as *Aureimonas*, *Rhizobium*, *Stenotrophomonas*, *Brevundimonas*, and *Methylobacterium*. While *Lactobacillus* as a bacterium was negatively correlated with most bacteria. For fungal community, positive correlations were found between *Mucor*, *Debaryomyces*, *Rhodotorula,* and *Trichosporon*. *Hanseniaspora*, as a fungus, was negatively correlated with these fungi. In addition, *Mucor* was negatively correlated with all bacteria. No significant correlations were found between *Debaryomyces*, *Rhodotorula*, *Trichosporon,* and *Hanseniaspora* and bacteria.

Indeed, several of the detected genera had previously been detected in dairy products, fermented vegetables, meat, and wine, and may contribute to the formation of nutrients and the unique flavors of fermented foods. *Lactobacillus* plays an important role in the fermentation of many foods, such as dairy products, vegetables, meat, and wine (13). Lactic acid fermentation positively affects the flavor and nutritional content of foods by producing organic acids, bacteriocins and volatile compounds, and contributes to improved sensory

and quality safety of foods. *Weissella* is one of the common microorganisms used in the preparation of cheese and fermented vegetables. Several studies have demonstrated the antimicrobial ability of compounds produced by *Weissella* against the growth of Gram-positive and Gram-negative bacteria as inhibitors of phytopathogenic and deteriorating fungal and bacterial growth of fruits and vegetables (14, 15). In addition, some endophytic fungi in peppers play certain roles during fermentation. *Hanseniaspora* are endophytic fungi whose abundance is maintained during fermentation; however, their metabolites may have biological activity. For example, the yeast *Hanseniaspora*, isolated from grapes and grape juice, helps to shorten the fermentation time and reduce the ethanol content of the fermentation product, and increases the total polyphenol and flavonoid content of the wine giving it a higher antioxidant potential (16, 17). *Debaryomyces* is the main yeast used in fermented meat products such as dry fermented sausages. Several studies have demonstrated that *Debaryomyces* contributes to food maturation and aroma presentation, and to the formation of flavor substances such as esters (18, 19). The ability of these detected microorganisms to produce specific flavor compounds has not been systematically investigated. This lack of research has resulted in a lack of development potential for improving existing fermented minced pepper products or developing new products.

Volatile components change during the pepper fermentation

The volatile components in minced pepper during fermentation were analyzed and quantified by GC-MS. A total of 64 volatile compounds including 17 esters, 14 alcohols, 11 aldehydes, 3 ketones, 16 hydrocarbons, and 3 heterocyclic compounds were identified (**Figure 5**). Among them, alcohols volatiles were the most abundant, accounted for 4.01–48.43% of the identified volatiles, and followed by hydrocarbons (20.76–45.50%), esters (6.92–30.91%), aldehydes (5.14–22.18%), ketones (2.14–7.25%), and heterocyclic compounds (3.26–7.15%). The alcohol volatile component was highest in unfermented minced pepper (0 days), accounting for 82.87% of the volatile component. As fermentation proceed, the content of alcohols decreased by 34.4%. Previous studies have shown that the significant decrease in alcohol content is partly due to the high volatility of these compounds, leading to their volatilization during fermentation (20). Also, the content of esters and hydrocarbons increased by 19.60 and 13.66%, respectively. This could be caused by microbial metabolism during the fermentation of minced peppers. In addition, the levels of aldehydes, ketones and heterocyclic compounds containing volatiles fluctuated during the manufacturing process, but no significant differences were observed.

Hierarchical clustering analysis classified the volatile components of minced pepper fermentation process into five categories according to their contents at different fermentation times. And heat map analysis showed the changes of different volatile components during minced pepper fermentation (**Figure 6**). During fermentation, 11 alkanes, 7 esters, 3 ketones, and 2 heterocyclic compounds were found to be higher in 5 days, 8 alcohols, 6 hydrocarbons, 5 aldehydes, and 3 esters in 5–17 days, and 8 esters and 2 alcohols in 17–20 days. These results implied that volatile components of alkanes were mainly produced in the early stage (3–5 days) of fermentation process. Alcohols were mainly generated in the middle stage (5–17 days), while the esters were mainly formed in the early stage (3–5 days) and the late stage (17–20 days). It is noteworthy that some esters were produced late in the minced pepper fermentation processes, which may be due to the fact that esters are synthesized by enzymatic esterification reactions of microorganisms with alcohols and acids as substrates (21). Esters have a sweet or fruity taste and can enhance the flavor of fermented foods by reducing the intensity of unpleasant odors (22). It was found that the concentration of most esters increased significantly after fermentation. Among them, 4-methylpentyl 2-methylbutanoate and 4-methylpentyl 3-methylbutanoate were found to be the most abundant esters in fermented minced pepper. They have an euryhaline herbal odor and a faint waxy odor, respectively (23). Alcohol volatiles have higher gas thresholds than ester volatiles and usually produce fruity and irritating odors, as well as being important precursors to esters (24). Among all alcohols detected in fermented minced pepper, linalool was the most abundant, which has a transient floral and herbal aroma, was detected in large amounts in both unfermented minced peppers, with a gradual increase in content during fermentation. Those results were in accordance with the studies conducted by (2, 25). Linalool which is a key odorant in fermented peppers was derived from glycosides by the action of microbial glycosidases during the fermentation process (26, 27). In addition, β-guaiene was found to be the most abundant terpene volatile component, and this compound contributes significantly to woody flavor and is thought to enhance flavor quality (28). Previous findings have indicated that the content of certain volatiles changes considerably during the fermentation of peppers inoculated with autotrophic or xenobiotic microorganisms (29). Therefore, these changes in volatiles may be related to the metabolism of microorganisms during the fermentation process.

Correlation between microbiota and volatile components

Further studies to unveil the underlying correlation between microorganisms and volatiles during the fermentation was conducted. Results of O2PLS model displayed that in

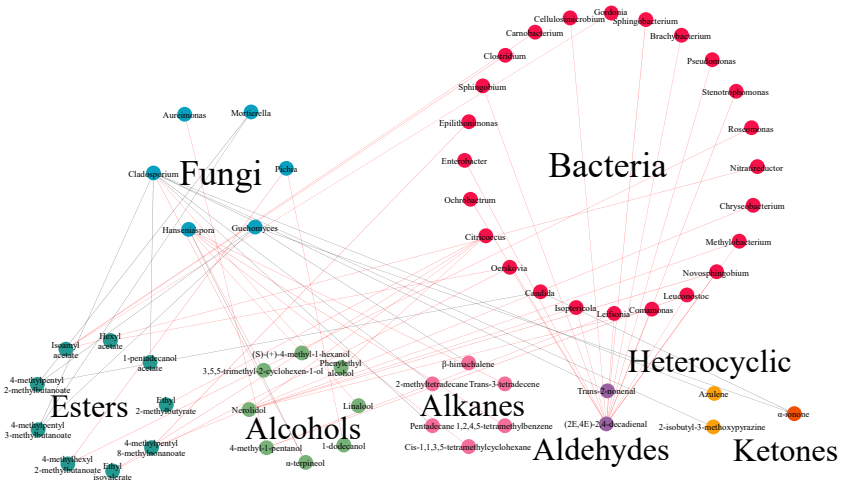

FIGURE 7
Analyses of correlation between microbiota and volatile components by bidirectional orthogonal partial least squares (O2PLS) modeling during the production of fermented minced peppers. Correlation network between microorganisms and volatile components during fermentation. Red lines indicate positive correlations. Gray lines indicate negative correlations.

fermented minced pepper, there were 45 independent variables X, including 41 genera of bacteria and 4 genera of fungi. And 64 dependent variables Y, with R^2 (0.939) and Q^2 (0.405). The correlation index between microorganisms (X) and volatile compounds (Y) was investigate by O2PLS analysis with Pearson's correlation method (**Supplementary Table 1**). And it was visualized in **Figure 7**. There were 30 genera of microorganisms (24 bacteria and 6 fungi) and 28 volatile components in network. *Cladosporium* was correlated with 9 volatile components ($|\rho| > 0.7$). But it mere positively related with alcohols. The highest correlation ($\rho = 0.902$) was with linalool. Similarly, *Hanseniaspora* was correlated with six volatile components ($|\rho| > 0.7$), including 3 hydrocarbons and 3 alcohols, and only negatively correlated with α-terpineol ($\rho = -0.80846$). *Citricoccus* was correlated with 4 volatile components ($|\rho| > 0.7$), including 2 alcohols and 2 esters, and all were positively correlated. In addition, the results showed that a few microbial genera were negatively correlated with volatile components. For example, *Cladosporium* and *Mortierella* showed negative correlations with the differences of seven and two volatile components, respectively. This phenomenon may be due to the decrease in competitiveness between these microorganisms during the fermentation process (30). Furthermore, the selection of core functional microorganisms correlated with flavor from species-rich communities is challenging and requires consideration of both dominance and functionality. To identify the core functional microorganisms in the fermentation process of minced peppers, three criteria were considered: (a) VIP value ≥ 1; (b) correlation coefficient ≥ 0.7; (c) number of microbes highly correlated ($|\rho| \geq 0.7$) with chemical compounds ≥ 1 (10) (**Supplementary Table 1**). Based on these criteria, 11 genera were identified in fermented minced pepper, including *Candida*, *Citricoccus*, *Cladosporium*, *Epilithonimonas*, *Guehomyces*, *Hanseniaspora*, *Mortierella*, *Nitratireductor,* *Ochrobactrum*, *Oerskovia,* and *Pichia*.

Correlation analysis predicted the relationship between volatile components and microorganisms. In fact, several studies have demonstrated the correlation between microbiota and flavor. *Hanseniaspora* has an important role as a non-Saccharomyces yeasts in the production of aromatic compounds such as esters, higher alcohols, acids, and monoterpenes (31, 32). It has been shown that *H. guilliermondii* produces β-phenylethyl acetate and ethyl acetate (16, 33). *Pichia* can produce flavor substances such as phenylethanol, 2-methylbutyric acid, 3-methylbutyric acid, and ethyl linoleate (34). A significant inverse relationship between acetyl ester hydrolase activity and acetate production was found in *Pichia kudriavzevii* 129 (35). *Candida* was considered important in fermentation because of its ester production capacity, where *Candida antarctica* lipase B (Calb) was found to catalyze the synthesis of several spice esters, including ethyl acetate, isoamyl acetate, *cis*-3-hexenyl acetate, geranyl acetate, ethyl butyrate, isoamyl butyrate, and *cis*-3-hexenyl butyrate (36–38). *Cladosporium* was reported to bioconvert limonene to α-pinoresinol (39, 40). Thus, these core microorganisms may come together to form a core microbiota that contributes to the production of certain key metabolites during the production of fermented minced pepper. Further studies should focus on the mechanisms of volatile component production by functional microorganisms. Meanwhile, the specific expression of related genes during fermentation requires subsequent meta-analysis to monitor how the metabolism of microorganisms affects the formation of key odorants.

Conclusion

In this study, changes in the main volatile components and the dynamics of the microbial community and the relationships between them were elucidated. The succession and competition of microorganisms during the fermentation process resulted in large differences in microbial abundance and diversity at different fermentation times. A total of 11 microbial genera, including *Candida*, *Citricoccus*, *Cladosporium*, *Epilithonimonas*, *Guehomyces*, *Hanseniaspora*, *Mortierella*, *Nitratireductor, Ochrobactrum*, *Oerskovia,* and *Pichia* were identified as core functional microorganisms. They promoted the production of 14 volatile components such as nerolidol, ethyl isovalerate, 4-methylhexyl 2-methylbutanoate and linalool, which are responsible for providing important fruit or floral aromas to fermented minced peppers. These findings have contributed to the elucidation of the potential role of specific bacterial genera in the formation of specific flavors during fermented minced pepper production, and have helped in the development of fermented minced pepper starter cultures with unique flavors and consistent quality.

Data availability statement

The original contributions presented in this study are included in the article/**Supplementary material**, further inquiries can be directed to the corresponding authors.

Author contributions

FD and LZ designed the work. DM performed the experimental work and prepared the initial draft of manuscript. YL analyzed the data. CC, SF, and YZ critically revised the manuscript. All authors contributed to the article and approved the submitted version.

Funding

This research was funded by the National Natural Science Foundation of China (Project No. 31401675), the Hunan Provincial Department of Science and Technology Support Program (Project Nos. 2015NK3011 and 2016NK2110), the Double first-class construction project of Hunan Agricultural University (Project No. SYL201802006), and the National Modern Agricultural Industrial Technology System (Project No. CARS-24-E-02).

Conflict of interest

Author CC was employed by Hunan Guotai Foods Co., Ltd. Author SF was employed by Junjie Food Technology Co., Ltd. Author YZ was employed by Lameizi Foodstuff Co., Ltd.

The remaining authors declare that the research was conducted in the absence of any commercial or financial relationships that could be construed as a potential conflict of interest.

Publisher's note

Supplementary material

The Supplementary Material for this article can be found online at: https://www.frontiersin.org/articles/10.3389/fnut.2022.1041608/full#supplementary-material

References

1. Li J, Zhao F, Liu H, Li R, Wang Y, Liao X. Fermented minced pepper by high pressure processing, high pressure processing with mild temperature and thermal pasteurization. *Innov Food Sci Emerg Technol.* (2016) 36:34–41. doi: 10.1016/j.ifset.2016.05.012

2. Wang J, Wang R, Xiao Q, Liu C, Deng F, Zhou H. Spme/Gc-Ms characterization of volatile compounds of Chinese traditional-chopped pepper during fermentation. *Int J Food Propert.* (2019) 22:1863–72. doi: 10.1080/10942912.2019.1684320

3. Chen Y, Xu H, Ding S, Zhou H, Qin D, Deng F, et al. Changes in volatile compounds of fermented minced pepper during natural and inoculated fermentation process based on headspace-gas chromatography-ion mobility spectrometry. *Food Sci Nutr.* (2020) 8:3362–79. doi: 10.1002/fsn3.1616

4. Sharma R, Garg P, Kumar P, Bhatia SK, Kulshrestha S. Microbial fermentation and its role in quality improvement of fermented foods. *Fermentation.* (2020) 6:106. doi: 10.3390/fermentation6040106

5. Zhang L, Xiang W-L, Zeng Z-S, Yu S, Chen Z-W, Li M-Y, et al. Separation, identification and direct vat set (Dvs) development of bacteria from fermented chili pepper. *Food Sci.* (2013) 34:242–7. doi: 10.7506/spkx1002-6630-201321049

6. Luo F-L, Xia Y-B, Ouyang J-X, Wang Y, Xia X-F. Changes in tasty materials during fermentation of chopped chili. *Food Sci.* (2013) 34:21–4.

7. Li Q, Li Y, Luo Y, Xiao L, Wang K, Huang J, et al. Characterization of the key aroma compounds and microorganisms during the manufacturing process of Fu brick tea. *LWT.* (2020) 127:109355. doi: 10.1016/j.lwt.2020.109355

8. Zheng X, Liu F, Shi X, Wang B, Li K, Li B, et al. Dynamic correlations between microbiota succession and flavor development involved in the ripening of Kazak artisanal cheese. *Food Res Int.* (2018) 105:733–42. doi: 10.1016/j.foodres.2017.12.007

9. Guan Q, Huang T, Peng F, Huang J, Liu Z, Peng Z, et al. The microbial succession and their correlation with the dynamics of flavor compounds involved in the natural fermentation of Suansun, a traditional Chinese fermented bamboo shoots. *Food Res Int.* (2022) 157:111216. doi: 10.1016/j.foodres.2022.111216

10. Li Z, Dong L, Jeon J, Kwon SY, Zhao C, Baek H-H. Characterization and evaluation of aroma quality in Doubanjiang, a Chinese traditional fermented red pepper paste, using aroma extract dilution analysis and a sensory profile. *Molecules.* (2019) 24:3107. doi: 10.3390/molecules24173107

11. Chen Y, Li P, He W, Liao L, Xia B, Jiang L, et al. Analysis of microbial community and the characterization of *Aspergillus flavus* in Liuyang Douchi during fermentation. *LWT.* (2022) 154:112567. doi: 10.1016/j.lwt.2021.112567

12. Huang Z-R, Guo W-L, Zhou W-B, Li L, Xu J-X, Hong J-L, et al. Microbial communities and volatile metabolites in different traditional fermentation starters used for Hong Qu glutinous rice wine. *Food Res Int.* (2019) 121:593–603. doi: 10.1016/j.foodres.2018.12.024

13. Seddik HA, Bendali F, Gancel F, Fliss I, Spano G, Drider D. *Lactobacillus plantarum* and its probiotic and food potentialities. *Probiot Antimicrob Proteins.* (2017) 9:111–22. doi: 10.1007/s12602-017-9264-z

14. Yu H-S, Lee N-K, Choi A-J, Choe J-S, Bae CH, Paik H-D. Antagonistic and antioxidant effect of probiotic *Weissella cibaria* Jw15. *Food Sci Biotechnol.* (2019) 28:851–5. doi: 10.1007/s10068-018-0519-6

15. Kariyawasam K, Jeewanthi R, Lee N-K, Paik H-D. Characterization of cottage cheese using *Weissella cibaria* D30: physicochemical, antioxidant, and antilisterial properties. *J Dairy Sci.* (2019) 102:3887–93. doi: 10.3168/jds.2018-15360

16. Martin, V, Valera MJ, Medina K, Dellacassa E, Schneider R, Boido E, et al. Application of *Hanseniaspora vineae* to improve white wine quality. *White Wine Technol.* (2022) 9:99–115. doi: 10.1016/B978-0-12-823497-6.00004-1

17. Zhao Y-S, Eweys AS, Zhang J-Y, Zhu Y, Bai J, Darwesh OM, et al. Fermentation affects the antioxidant activity of plant-based food material through the release and production of bioactive components. *Antioxidants.* (2021) 10:2004. doi: 10.3390/antiox10122004

18. Perea-Sanz L, López-Díez JJ, Belloch C, Flores M. Counteracting the effect of reducing nitrate/nitrite levels on dry fermented sausage aroma by *Debaryomyces hansenii* inoculation. *Meat Sci.* (2020) 164:108103. doi: 10.1016/j.meatsci.2020.108103

19. Murgia MA, Marongiu A, Aponte M, Blaiotta G, Deiana P, Mangia NP. Impact of a selected debaryomyces hansenii strain's inoculation on the quality of Sardinian fermented sausages. *Food Res Int.* (2019) 121:144–50. doi: 10.1016/j.foodres.2019.03.042

20. Li Z, Feng C, Luo X, Yao H, Zhang D, Zhang T. Revealing the influence of microbiota on the quality of Pu-Erh tea during fermentation process by shotgun metagenomic and metabolomic analysis. *Food Microbiol.* (2018) 76:405–15. doi: 10.1016/j.fm.2018.07.001

21. Kruis AJ, Bohnenkamp AC, Patinios C, van Nuland YM, Levisson M, Mars AE, et al. Microbial production of short and medium chain esters: enzymes, pathways, and applications. *Biotechnol Adv.* (2019) 37:107407. doi: 10.1016/j.biotechadv.2019.06.006

22. Xu Y, Zhao J, Liu X, Zhang C, Zhao Z, Li X, et al. Flavor mystery of Chinese traditional fermented Baijiu: the great contribution of ester compounds. *Food Chem.* (2022) 369:130920. doi: 10.1016/j.foodchem.2021.130920

23. Garruti DS, Mesquita WDS, Magalhães HCR, Araújo ÍMDS, Pereira RDCA. Odor-contributing volatile compounds of a new Brazilian Tabasco Pepper cultivar analyzed by Hs-Spme-Gc-Ms and Hs-Spme-Gc-O/Fid. *Food Sci Technol.* (2021) 41:696–701. doi: 10.1590/fst.18020

24. Wei Y, Zou W, Shen CH, Yang JG. Basic flavor types and component characteristics of Chinese traditional liquors: a review. *J Food Sci.* (2020) 85:4096–107. doi: 10.1111/1750-3841.15536

25. Xu X, Wu B, Zhao W, Pang X, Lao F, Liao X, et al. Correlation between autochthonous microbial communities and key odorants during the fermentation of red pepper (*Capsicum annuum* L.). *Food Microbiol.* (2020) 91:103510. doi: 10.1016/j.fm.2020.103510

26. Wang R, Sun J, Lassabliere B, Yu B, Liu SQ. B-Glucosidase activity of cyberlindnera (Williopsis) Saturnus Var. Mrakii Ncyc 2251 and its fermentation effect on green tea aroma compounds. *LWT.* (2021) 151:112184. doi: 10.1016/j.lwt.2021.112184

27. Zhang Q, Zhang F, Gong C, Tan X, Ren Y, Yao K, et al. Physicochemical, microbial, and aroma characteristics of Chinese pickled red peppers (*Capsicum annuum*) with and without biofilm. *RSC Adv.* (2020) 10:6609–17. doi: 10.1039/D0RA00490A

28. Lv H-P, Zhong Q-S, Lin Z, Wang L, Tan J-F, Guo L. Aroma characterisation of Pu-Erh tea using headspace-solid phase microextraction combined with Gc/Ms and Gc–olfactometry. *Food Chem.* (2012) 130:1074–81. doi: 10.1016/j.foodchem.2011.07.135

29. Lee SM, Lee JY, Cho YJ, Kim MS, Kim YS. Determination of volatiles and carotenoid degradation compounds in red pepper fermented by *Lactobacillus parabuchneri*. *J Food Sci.* (2018) 83:2083–91. doi: 10.1111/1750-3841.14221

30. Laranjo M, Potes ME, Elias M. Role of starter cultures on the safety of fermented meat products. *Front Microbiol.* (2019) 10:853. doi: 10.3389/fmicb.2019.00853

31. Zhang B, Liu H, Xue J, Tang C, Duan C, Yan G. Use of *Torulaspora delbrueckii* and *Hanseniaspora vineae* co-fermentation with saccharomyces cerevisiae to improve aroma profiles and safety quality of petit manseng wines. *LWT.* (2022) 161:113360. doi: 10.1016/j.lwt.2022.113360

32. Wei R-T, Chen N, Ding Y-T, Wang L, Liu Y-H, Gao F-F, et al. Correlations between microbiota with physicochemical properties and volatile compounds during the spontaneous fermentation of cabernet sauvignon (*Vitis vinifera* L.) wine. *LWT.* (2022) 163:113529. doi: 10.1016/j.lwt.2022.113529

33. Dellacassa E, Trenchs O, Fariña L, Debernardis F, Perez G, Boido E, et al. Pineapple (*Ananas comosus* L. Merr.) wine production in Angola: characterisation of volatile aroma compounds and yeast native flora. *Int J Food Microbiol.* (2017) 241:161–7. doi: 10.1016/j.ijfoodmicro.2016.10.014

34. Chen Z, Yan Q, Jiang Z, Liu Y, Li Y. High-level expression of a novel A-galactosidase gene from *Rhizomucor miehei* in *Pichia pastoris* and characterization of the recombinant enyzme. *Protein Express Purif.* (2015) 110:107–14. doi: 10.1016/j.pep.2015.02.015

35. Van Rijswijck IM, Kruis AJ, Wolkers–Rooijackers JC, Abee T, Smid EJ. Acetate-ester hydrolase activity for screening of the variation in acetate ester yield of *Cyberlindnera fabianii*, *Pichia kudriavzevii* and *Saccharomyces cerevisiae*. *LWT.* (2019) 104:8–15. doi: 10.1016/j.lwt.2019.01.019

36. Jin Z, Ntwali J, Han S-Y, Zheng S-P, Lin Y. Production of flavor esters catalyzed by Calb-displaying *Pichia pastoris* whole-cells in a batch reactor. *J Biotechnol.* (2012) 159:108–14. doi: 10.1016/j.jbiotec.2012.02.013

37. Bayramoglu G, Celikbicak O, Kilic M, Arica MY. Immobilization of *Candida rugosa* lipase on magnetic chitosan beads and application in flavor esters synthesis. *Food Chem.* (2022) 366:130699. doi: 10.1016/j.foodchem.2021.130699

38. Xue D, Yao D, You X, Gong C. Green synthesis of the flavor esters with a marine *Candida parapsilosis* esterase expressed in *Saccharomyces cerevisiae*. *Indian J Microbiol.* (2020) 60:175–81. doi: 10.1007/s12088-020-00856-9

39. Malik T, Rawat S. Biotechnological interventions for production of flavour and fragrance compounds. In: Venkatramanan V, Shah S, Prasad R editors. *Sustainable Bioeconomy*. Singapore: Springer (2021). p. 131–70.

40. Sales A, Felipe LDO, Bicas JL. Production, properties, and applications of α-terpineol. *Food Bioprocess Technol.* (2020) 13:1261–79. doi: 10.1007/s11947-020-02461-6

frontiers | Frontiers in Nutrition

TYPE Original Research
PUBLISHED 09 November 2022
DOI 10.3389/fnut.2022.1052730

OPEN ACCESS

EDITED BY
Zhi-Hong Zhang,
Jiangsu University, China

REVIEWED BY
Xiaolong Ji,
Zhengzhou University of Light Industry, China
Chunsen Wu,
Yangzhou University, China

*CORRESPONDENCE
Yang Yao
yaoyang@caas.cn
Lizhen Zhang
lizhen@sxu.edu.cn
Peiyou Qin
qinpeiyou@caas.cn

†These authors have contributed equally to this work

SPECIALTY SECTION
This article was submitted to Nutrition and Food Science Technology, a section of the journal Frontiers in Nutrition

RECEIVED 24 September 2022
ACCEPTED 25 October 2022
PUBLISHED 09 November 2022

CITATION
Zhang Z, Fan X, Zou L, Xing B, Zhu M, Yang X, Ren G, Yao Y, Zhang L and Qin P (2022) Phytochemical properties and health benefits of pregelatinized Tartary buckwheat flour under different extrusion conditions.
Front. Nutr. 9:1052730.
doi: 10.3389/fnut.2022.1052730

Phytochemical properties and health benefits of pregelatinized Tartary buckwheat flour under different extrusion conditions

Zhuo Zhang[1,2†], Xin Fan[2†], Liang Zou[3], Bao Xing[1,2], Manli Zhu[1,2], Xiushi Yang[4], Guixing Ren[2,3], Yang Yao[2*], Lizhen Zhang[1*] and Peiyou Qin[2*]

[1]Key Laboratory of Chemical Biology and Molecular Engineering of Ministry of Education, School of Life Sciences, Shanxi University, Taiyuan, China, [2]Key Laboratory of Quality Evaluation and Nutrition Health of Agro-Products, Ministry of Agriculture and Rural Affairs, Institute of Crop Sciences, Chinese Academy of Agricultural Sciences, Beijing, China, [3]Key Laboratory of Coarse Cereal Processing, Ministry of Agriculture and Rural Affairs, Sichuan Engineering & Technology Research Center of Coarse Cereal Industrialization, School of Food and Biological Engineering, Chengdu University, Chengdu, China, [4]Institute of Bast Fiber Crops, Chinese Academy of Agricultural Sciences, Changsha, China

This work investigated the phytochemical properties and health benefits of Tartary buckwheat flour obtained with different extrusion conditions including high, medium, and low temperature. Extrusion significantly decreased the fat content and changed the original color of Tartary buckwheat flour. The contents of protein, total flavonoids, and D-*chiro*-inositol were affected by the extrusion temperature and moisture. Extrusion significantly decreased the total flavonoids and flavonoid glycosides contents, while it significantly increased aglycones. Compared to native Tartary buckwheat flour and pregelatinization Tartary buckwheat flour obtained with traditional extrusion processing technology, the pregelatinization Tartary buckwheat flour obtained with improved extrusion processing technology contained higher aglycones and lower flavonoid glycosides, which had stronger antioxidant capacity, α-glucosidase inhibitory activity and relatively mild α-amylase inhibitory activity. Correlation analysis proved that the aglycone content was positively correlated with antioxidant and α-glucosidase inhibitory activities. These findings indicate that the pregelatinization Tartary buckwheat flour obtained with improved extrusion processing technology could be used as an ideal functional food resource with antioxidant and anti-diabetic potential.

KEYWORDS

Tartary buckwheat, extrusion, flavonoids, antioxidant activity, α-glucosidase inhibitory activity, α-amylase inhibitory activity

Introduction

Tartary buckwheat [*Fagopyrum tataricum* (L.) Gaench], which is a species of buckwheat, has been cultivated since ancient times, and is currently distributed in Asia (especially in China), America, and Europe (1). As a pseudocereal, Tartary buckwheat has been receiving increasing attention as a potential functional ingredient or food that is rich in a range of nutrients including bioactive carbohydrates and proteins, polyphenols, phytosterols, flavonoids, D-*chiro*-inositol (DCI), vitamins, carotenoids, and minerals. These nutritious substances endow Tartary buckwheat with various health benefits such as antioxidant, anti-cancer, anti-diabetic, anti-hypertensive, cholesterol-lowering, and anti-inflammatory properties (2–4). Our previous study reported that flavonoids are the main phenolic secondary metabolites in Tartary buckwheat grain, and they are 10-fold higher than in common buckwheat (5). The flavonoids mainly include rutin, quercetin, and kaempferol and their glycoside forms, of which rutin is the most abundant in Tartary buckwheat (6–8). Moreover, Tartary buckwheat is an important natural source of DCI, which is a compound with an insulin-like bioactivity (9). Previous studies have indicated that DCI has a synergistic effect with phenolic compounds in the treatment of type II diabetes. Specifically, DCI mainly eliminates insulin resistance by enhancing the body's sensitivity to insulin, thereby regulating blood glucose (10, 11), and the phenolic compounds mainly control blood glucose by inhibiting the activity of α-glucosidase and α-amylase (12). However, strong α-amylase inhibitory activity can cause abnormal fermentation by bacteria in the colon, triggering a series of adverse reactions (such as diarrhea and flatulence). Therefore, the recommended way to control blood sugar is to have strong α-glucosidase inhibitory activity and relatively mild α-amylase inhibitory activity (13, 14).

Based on above nutritional and functional properties, many products related to Tartary buckwheat have been developed, such as noodles, tea, baked goods, and meal replacement powder (1). However, native Tartary buckwheat flour (NTBF) is gluten-free and cannot form an optimal network structure, which restricts the development of Tartary buckwheat products and their sensory quality (13, 15). Therefore, in order to increase the utility of Tartary buckwheat in the food processing industry, several processing technologies have been used to modify NTBF including high pressure (15), high hydrostatic pressure (16), fermentation (8, 17) and roasting, boiling, extrusion, and microwave treatment (3, 18). These treatment methods have been shown to change the phytochemical composition of Tartary buckwheat, thereby affecting its nutritional properties. Our previous research found that the rutin in Tartary buckwheat degraded into quercetin and rutinoside during processing (5). Although the high concentration of quercetin has stronger antioxidant and α-glucosidase inhibitory properties than rutin, it will produce a bitter taste and decrease the sensory quality (4, 8, 19). Therefore, antioxidant and α-glucosidase inhibition as well as the sensory qualities and levels of bitterness should always be taken into account when processing Tartary buckwheat foods. It has been confirmed that hydrothermal treatment of Tartary buckwheat at 100°C for 20 min can better maintain the rutin and quercetin content (17). To prevent rutin from degrading and thus reduce bitterness, Wu et al. found that superheated steam and saturated steam could efficiently inactivate rutin-degrading enzymes (RDEs) in Tartary buckwheat (20). High temperature wet heat treatment (cooking and extrusion) will inactivate most of the RDEs, while dry heat treatment has almost no effect on RDEs (21).

Among the processing methods considered above, extrusion cooking is a technology with high production efficiency, strong applicability, low cost, and energy consumption, and it has been widely used in the food industry (22, 23). Traditional extrusion processing technology (TEPT) is a continuous high-temperature short-term process that is frequently used to produce puffed food (23, 24). Nevertheless, previous studies have shown that TEPT significantly decreases antioxidant activity (AC) in buckwheat (25, 26). Recently, an improved extrusion processing technology (IEPT) was designed with a longer screw, lower speed, lower temperature, and higher pressure than TEPT (24). Buckwheat samples obtained with IEPT have shown a high retention rate of functional ingredients and desired physical properties (13).

At present, there is no systematic research on the changes to individual flavonoids, DCI, α-glucosidase, and α-amylase inhibitory activities in Tartary buckwheat, nor on the correlation between individual flavonoids and their biological functions after extrusion (TEPT and IEPT). Therefore, the aim of this study was to identify changes to phytochemical composition including nutritional substances, total and individual flavonoids, DCI, and color properties as well as the antioxidant, α-glucosidase, and α-amylase inhibitory activities in Tartary buckwheat samples after treatment with different extrusion conditions. A correlation analysis between individual flavonoids and their biological functions was also conducted in this study.

Materials and methods

Materials

Standard reagents (rutin, isoquercitrin, quercetin, and kaempferol), α-glucosidase (100 U), and p-nitrophenyl-a-D-glucopyranoside were purchased from the Yuan Ye Biological Technology Company (Shanghai, China); kaempferol-3-*O*-rutinoside and DNS reagent were purchased from Solarbio (Beijing, China); Trolox, a-amylase, 1,1-diphenyl-2-pic-rylhydrazyl (DPPH), 2,2'-azino-bis (3-ethylbenzothiazoline-6-sulphonic acid) (ABTS) and 2,4,6-tripyridyl-s-triazine (TPTZ) reagents were purchased from

Sigma-Aldrich (Shanghai, China). Acarbose, used as a positive control, was produced by Bayer HealthCare Company Co. Ltd. (Beijing, China). The other chemicals and reagents used in this study were of analytical grade.

Dehulling of Tartary buckwheat groats were performed in Chengdu University. Native Tartary buckwheat flour (NTBF) was obtained by grinding using an experimental mill (Glen Creston Ltd., Stanmore, England) and passed through a 60-mesh sieve.

Pre-gelatinization of Tartary buckwheat flour by different extrusion treatments

The Tartary buckwheat flour was extruded using a twin-screw extruder (Brabender KETSE 20/40, Duisburg, Germany) with a screw diameter of 20 mm, L/D ratio of 40:1 and die diameter of 1 mm. We used five of the six independent zones (we did not use the die) and controlled the temperature in the barrel in each. The samples were processed under different conditions as shown in **Table 1**. After extrusion, the samples were immediately oven-dried at 45°C for 24 h and then ground and sieved through 60 mesh to obtain pre-gelatinization of Tartary buckwheat flour (PTBF). All samples were stored at 4°C for further analysis. A total of 7 PTBF sample types were prepared and analyzed. They were denoted as TxMy, where x is the extrusion temperature at the fourth zone and y is the feed moisture content.

Chemical composition analysis

The compositions of Tartary buckwheat components including moisture, ash, protein, and fat were determined according to the methods of GB5009.3–2016, 5009.4–2016, 5009.5–2016, 5009.6–2016. The total starch content was determined by kit assays (Megazyme International Ireland Ltd., Wicklow, Ireland).

Color determination

The color parameters of the Tartary buckwheat samples were measured following the method of Xiao et al. (8) with slight modifications. The colorimeter was calibrated using a standard white plate. Thirty replicate measurements were performed before the color parameters were recorded. The total color difference (°E), which represents the color change between PTBF and NTBF, was calculated using the following formula:

$$\triangle E \sqrt{(L^* - L_0^*)^2 + (a^* - a_0^*)^2 + (b^* - b_0^*)^2} \quad (1)$$

where L^*_0, a^*_0, and b^*_0 are the color parameters of NTBF; L^*, a^*, and b^* are the color parameters of PTBF. L^* means lightness (0 for black and 100 for white), a^* is red (+) to green (−), and b^* is yellow (+) to blue (−).

Analysis of total flavonoids and individual flavonoid compounds

The total flavonoids and individual flavonoid compounds were extracted and determined according to a procedure described by our laboratory (5). The total flavonoids content (TFC) results were determined using the aluminum chloride colorimetric method and expressed as micrograms of rutin equivalent per gram of sample.

After the samples were passed through a 0.45 μm PEC syringe filter membrane (Jinteng, Tianjin, China), the individual flavonoid compounds including rutin, isoquercitrin, kaempferol-3-*O*-rutinoside, quercetin, and kaempferol were analyzed by an Alltech high performance liquid chromatography (HPLC) system (Alltech, Chicago, IL, USA) according to the method of Xiao et al. (8) with modifications. The analytical column was a PerkinElmer® column (250 mm × 4.6 mm, Sheiton, USA) and the wavelength of the UV detector was set at 375 nm. The mobile phase was 0.05% trifluoroacetic acid aqueous solution (A) and 100% acetonitrile (B). A gradient flow system was established as follows with a flow rate of 1 ml/min: 0–8 min, 28% B; 8–18 min, 28–50% B; 18–30 min, 50–100% B; 30–35 min, 100% B; 35–38 min, 100–28% B; and 38–45 min, 28% B. The column temperature was kept at 30°C and the injection volume was 20 μl.

Analysis of D-*chiro*-inositol

D-*chiro*-inositol in Tartary buckwheat samples was determined following the method established by our laboratory

TABLE 1 Conditions of different extrusion treatments.

Treatments	Moisture content (%)	Extrusion temperate (°C)	The feeding rate (g/min)	The screw speed (rpm)
TEPT	30	40/75/110/160/95	40	100
IEPT	30, 40, 60	40/60/75/100/85	10	30
	30, 40, 60	40/60/70/70/70	10	30

TEPT, traditional extrusion processing technology; IEPT, improved extrusion processing technology.

(27). Briefly, the sample (1 g) was mixed with 20 ml of 50% ethanol and incubated at room temperature for 30 min in a water bath with continuous shaking. The extract was passed through qualitative filter paper (Newstar, Hangzhou, China) and 1 ml of supernatant was transferred into a vial and oven-dried at 50°C. The dried extract was re-dissolved in 1 ml of methanol and passed through a 0.45 μm PEC syringe filter membrane (Jinteng, Tianjin, China) for immediate HPLC-ELSD (evaporative light scattering detector) analysis. A Prevail Carbohydrate ES 5u column (250 mm × 4.6 mm, Alltech, Chicago, IL, USA) was used. The injection volume was 10 μl. The mobile phase was 80% acetonitrile, the flow rate was set at 1 ml/min, and the eluant was sent to the ELSD (Alltech, Chicago, IL, USA). The temperature of the drift tube was set at 95°C, the nebulizing gas flow rate was 2.2 L/min, and the gain was 1.

Antioxidant activity

The antioxidant activity of the flavonoids extracts from different Tartary buckwheat samples was evaluated by the following three methods with different reaction mechanisms.

1,1-diphenyl-2-pic-rylhydrazyl radical scavenging capacity

1,1-diphenyl-2-pic-rylhydrazyl free radical scavenging capacity was determined following the method established by our laboratory (27). Sample solution (1 ml) was mixed with an equal volume of DPPH solution (0.4 mM) and incubated in darkness at room temperature for 20 min. The absorbance of the mixture was read at λ = 517 nm. Distilled water was used as a blank control. Trolox was measured at different concentrations (0–70 μg/ml) to produce a standard curve. The results were expressed as the Trolox equivalent concentration.

ABTS radical scavenging capacity

The ABTS activity was carried out as reported previously (27). Briefly, the ABTS stock solution was prepared by mixing equal volumes of ABTS preparation solution (7 mM) with potassium persulfate solution (2.45 mM) after incubation in the dark at room temperature for 16 h. The prepared solution was diluted with methanol until the absorbance was around 0.7 (±0.02) at λ = 734 nm. Next, the solution (20 μl) was mixed with 1,980 μl of ABTS working solution and incubated in darkness at room temperature for 6 min, and the absorbance was then determined at λ = 734 nm. Methanol was used as a blank control. Trolox was measured at different concentrations (10–100 μg/ml) to produce a standard curve. The results were expressed as the Trolox equivalent concentration.

Fe^{3+} reducing antioxidant power capacity

The Fe^{3+} reducing antioxidant power (FRAP) activity was performed according to the described method (8) with small modifications. The FRAP reagent was generated by mixing 300 mM sodium acetate buffer (pH 3.6), 10 mM TPTZ and 20 mM ferric chloride solution in 40 mM hydrochloric acid at a ratio of 10: 1: 1 (v/v/v). Sample solutions (200 μl) were mixed with 2 ml of FRAP reagent, and then incubated in a water bath at 37°C for 30 min. The absorbance was read at λ = 593 nm. Distilled water was used as a blank control. Trolox was measured at different concentrations (10–100 μg/ml) to produce a standard curve. The results were expressed as the Trolox equivalent concentration.

α-glucosidase inhibition study *in vitro*

The α-glucosidase inhibitory activity of flavonoids extracts isolated from Tartary buckwheat samples was assessed by using the method of Xiao et al. (8). Before the experiment, the α-glucosidase (0.2 U/ml) was prepared by mixing it with phosphate buffer solution (PBS, 0.1 M, pH 6.8), and the sample solution (50 μl) was then mixed with 120 μl of the α-glucosidase solution. After incubation at 37°C for 10 min, 120 μl 2.5 mM 4-nitrophenyl-α-D-gluco-pyranoside (pNPG) in PBS was added. Then the mixture was incubated at 37°C for 15 min and the reaction was terminated by adding 480 μl 0.2 M sodium carbonate. Finally, the absorbance was measured at λ = 405 nm. The PBSZZ and acarbose were used as a reagent blank and positive control, respectively. The α-glucosidase inhibitory activity was calculated using the following formula:

$$\text{Inhibition (\%)} = (A_0\text{-}A_1)/A_0 \times 100 \quad (2)$$

where A_0 and A_1 represent the absorbance of the control and the experimental samples, respectively.

The α-glucosidase inhibitory activities of samples were represented as half inhibition concentration (IC_{50}) values, meaning that 50% of α-glucosidase activity was inhibited at this concentration.

α−amylase inhibition study *in vitro*

The α-amylase inhibitory activity of flavonoids extracts isolated from Tartary buckwheat samples was conducted according to the method described by Ji et al. (28). Specifically, sample solutions (100 μl) of different concentrations were mixed with 100 μl of α-amylase solution (4.5 U/ml) dissolved in PBS. After incubation at 37°C for 10 min, 100 μl of 1% (m/v) soluble starch (Xilong Chemical Factory Co., Ltd., Shantou, China) in PBS was added to start the reaction and further incubated at 37°C for 5 min. Next, 750 μl of DNS reagent was added to terminate the reaction, and the mixture immediately heated in a boiling water bath for 10 min. Afterward, the reaction mixture was immediately cooled down to room temperature and diluted three times. The absorbance was measured at λ = 540 nm, and sodium citrate buffer and

acarbose were used as the reagent blank and positive control, respectively. The α-amylase inhibitory activity was calculated using equation (2). The α-amylase inhibitory abilities of the samples were shown as inhibiting percentages at 400 μg/ml, and the concentration of acarbose is 10 μ g/ml.

Statistical analysis

All analyses were carried out in triplicate; and the data are presented as mean ± standard deviation (SD). All the data were analyzed using SPSS 22.0. Analysis of variance (ANOVA) and Duncan's multiple range tests ($p < 0.05$) were used to express the statistical significance of differences. The correlation matrix analysis was analyzed with the Pearson correlation coefficient.

Results and discussion

Nutritional composition

The nutritional composition of NTBF and PTBF are shown in **Table 2**. The total starch content of NTBF was 77.26 g/100 g dry weight (DW), and had higher values than in our previous studies (5, 29). This was due to an improved kit assay (AOAC Method 996.11 with a slight modification) used in this study that employed a thermostable α-amylase that is active and stable at pH 5. This modification is known to give higher starch values than those obtained with AOAC Method 996.11 (30). After extrusion, the total starch content of PTBF slightly increased or decreased, and ranged from 75.61 to 79.30 g/100 g DW. Similar results were observed in barley (31). Compared to NTBF, the protein content of PTBF obtained with TEPT and T100My significantly decreased ($p < 0.05$), while it increased in the PTBF obtained with T70My ($p < 0.05$). Previous studies have indicated that extrusion could cause the loss of protein and amino acids (32, 33). A previous kinetic study on the loss of lysine and other amino acids during extrusion of maize grits showed that the first-order rate constants were dependent mainly on extrusion temperature and feed moisture, whereas screw speed had no influence (34). Liu et al. (24) also found that a significant increase ($p < 0.05$) in protein was observed in texturized rice after adding 4% rice bran prior to treatment with IEPT. However, further studies are required to elucidate the mechanism of the increase in protein with IEPT. Compared to NTBF, the PTBF samples have a lower level of fat, and there was no significant difference ($p > 0.05$) in the ash content. These results are in agreement with an earlier study on brown rice (35). The decrease in fat content may be attributed to the interaction between lipid and amylose during extrusion (35).

Color attributes

The color parameters (L^*, a^*, b^*, ΔE) are shown in **Table 3**. Different extrusion treatments had significant effects on the color parameters of Tartary buckwheat samples ($p < 0.05$), and the color manifestation is due to various mechanisms including non-enzymatic browning (such as Maillard reaction), pigment degradation and oxidation of ascorbic acid during the extrusion process (36, 37). NTBF was lighter than PTBF according to a decrease in the lightness (L^*) score, which is consistent with a previous study (3). The free amino group of the amino acid can react with reducing sugars to form Maillard browning products during extrusion (3). Similarly, the a^* scores of extruded samples significantly decreased ($p < 0.05$), except for T160M30 and T70M30. Conversely, the b^* scores were significantly increased by the extrusion process, which means the color of PTBF was yellower than NTBF. Similarly observations have been reported by previous work, and they were explained by pigment degradation and non-enzymic browning reactions (38). ΔE is used to evaluate the overall color change, and generally, when ΔE values exceed 5.0, it is considered to be significantly different from the color of the control (37). The ΔE values of PTBF ranged from 10.34 to 34.27 (**Table 3**), indicating that extrusion affected the overall color of Tartary buckwheat

TABLE 2 Concentrations of moisture, total starch, protein, fat, and ash contents of native and pregelatinized Tartary buckwheat flour (g/100 g dry weight).

Material	Moisture	Total starch	Protein	Fat	Ash
Native	10.98 ± 0.018b	77.26 ± 1.01b	11.47 ± 0.43cd	2.82 ± 0.08a	2.76 ± 0.19a
T160M30	5.92 ± 0.009g	79.09 ± 1.20a	10.95 ± 0.13f	0.85 ± 0.07d	2.76 ± 0.13a
T100M30	7.04 ± 0.033f	78.28 ± 0.33ab	11.11 ± 0.05ef	1.56 ± 0.12b	2.62 ± 0.28a
T100M40	7.40 ± 0.087e	79.30 ± 1.66a	11.43 ± 0.06de	1.49 ± 0.03b	2.66 ± 0.16a
T100M60	11.27 ± 0.119a	75.61 ± 0.25c	11.80 ± 0.13bc	1.07 ± 0.09c	2.66 ± 0.19a
T70M30	10.05 ± 0.058c	76.75 ± 0.51bc	11.98 ± 0.01b	0.52 ± 0.08e	2.62 ± 0.24a
T70M40	9.74 ± 0.047d	77.63 ± 0.39ab	12.07 ± 0.14b	1.00 ± 0.06c	2.63 ± 0.04a
T70M60	10.14 ± 0.059c	79.04 ± 0.67a	12.59 ± 0.27a	1.11 ± 0.11c	2.68 ± 0.27a

TxMy, x is the extrusion temperature at the fourth zone (°C) and y is the feed moisture content (%). The results were expressed as mean ± SD ($n = 3$) and different letters in the same column indicate significant differences ($p < 0.05$).

samples. Therefore, the extrusion process significantly changes the original color of Tartary buckwheat.

Extractable total flavonoids and individual flavonoid compounds

The contents of total flavonoids and individual flavonoid compounds are presented in Table 4. All the extrusion processes significantly decreased ($p < 0.05$) TFC and flavonoid glycosides (rutin, isoquercitrin, kaempferol-3-*O*-rutinoside), while they significantly increased aglycones (quercetin and kaempferol). Sun et al. also reported that the extruded buckwheat flours showed lower contents of total flavonoids and rutin, as well as higher levels of quercetin than native flours (3). This study found that TFC was mainly affected by extrusion temperature and feed moisture. The loss of total flavonoids decreased with increases in the moisture content under the same extrusion temperature. When the moisture content was the same, the TFC in T70My was higher than T100My, but lower than T160M30. Similar results were also obtained by Cheng et al. (13). The TFC mainly depends on changes in the five individual flavonoid compounds, as shown in Table 4. On the one hand, most of rutin, isoquercitrin, kaempferol-3-*O*-rutinoside in PTBF obtained with IEPT was degraded to quercetin and kaempferol by flavonol-3-glucosidase (f3g) (8). On the other hand, it has been reported that high temperature processes (for instance, steaming) could cause the destruction of flavonoid compounds (8). This study also indicated that the sums of individual flavonoids in the different flours all had varying degrees of decline under different extrusion conditions.

As shown in Table 4 and Figure 1, rutin had the highest retention rate at high temperature of 83.8% (15.42 mg/g DW). This result was in line with results obtained by Li et al. (21). This may be attributed to nearly complete denaturing of the rutin-degrading enzyme under high temperature conditions (8). For IEPT, when the temperature was kept constant and the feed moisture was increased from 30 to 60%, a significant ($p < 0.05$) increase was observed in flavonoid aglycones. The T70M60 sample had the highest proportion of aglycones (8.82 mg/g DW), while the glycosides are under the limit of detection. These results suggested that the moisture content of feed is an important factor for converting flavonoid glycosides to aglycones (especially quercetin). Additionally, moist heat is more destructive, and moisture produces a synergistic effect alongside high temperatures (22), which may be responsible for flavonoid glycoside degradation. Our previous study also reported that soak-treating Tartary

TABLE 3 The color properties of the native and pregelatinized Tartary buckwheat flour.

Material	L^*	a^*	b^*	ΔE
Native	79.92 ± 0.09a	0.18 ± 0.01c	20.06 ± 0.09f	–
T160M30	70.18 ± 0.10d	0.70 ± 0.01b	23.68 ± 0.59e	18.46 ± 0.50e
T100M30	75.15 ± 0.14c	−1.05 ± 0.04e	23.18 ± 0.34e	10.34 ± 0.34g
T100M40	75.44 ± 0.26c	−1.73 ± 0.02g	24.92 ± 0.03d	12.19 ± 0.33f
T100M60	66.39 ± 0.13f	−1.01 ± 0.02e	29.31 ± 0.38c	29.12 ± 0.49c
T70M30	64.57 ± 0.57g	2.26 ± 0.03a	29.56 ± 0.13c	32.22 ± 0.73b
T70M40	76.53 ± 0.12b	−0.88 ± 0.02d	30.59 ± 0.22b	19.69 ± 0.30d
T70M60	68.65 ± 0.09e	−1.23 ± 0.04f	35.71 ± 0.22a	34.27 ± 0.39a

TxMy, x is the extrusion temperature at the fourth zone (°C) and y is the feed moisture content (%). Data are expressed as means ± SD ($n = 30$) and different letters in the same column indicate significant differences ($p < 0.05$).

TABLE 4 Concentrations of total flavonoids, DCI, and individual flavonoids in native and pregelatinized Tartary buckwheat flour (mg/g dry weight).

Material	Total flavonoids	DCI	Rutin	Isoquercitrin	Kaempferol-3-*O*-rutinoside	Quercetin	Kaempferol
Native	19.93 ± 0.35a	1.71 ± 0.08b	18.40 ± 0.23a	0.052 ± 0.014a	1.50 ± 0.12a	0.07 ± 0.00f	0.12 ± 0.01f
T160M30	17.61 ± 0.00b	1.79 ± 0.10ab	15.42 ± 0.53b	0.058 ± 0.002a	1.18 ± 0.06b	0.18 ± 0.01e	0.24 ± 0.01e
T100M30	11.81 ± 0.82f	1.90 ± 0.10a	0.64 ± 0.06de	0.016 ± 0.001c	0.05 ± 0.00d	4.70 ± 0.03d	0.54 ± 0.02c
T100M40	13.53 ± 0.56e	1.67 ± 0.12b	0.83 ± 0.03d	0.001 ± 0.000d	0.07 ± 0.00d	5.75 ± 0.05c	0.56 ± 0.00c
T100M60	14.91 ± 0.02d	1.14 ± 0.09d	0.86 ± 0.03d	ND	0.07 ± 0.00d	7.96 ± 0.05a	0.64 ± 0.01a
T70M30	13.89 ± 0.46e	1.49 ± 0.05c	3.82 ± 0.11c	0.026 ± 0.002b	0.25 ± 0.01c	4.79 ± 0.03d	0.50 ± 0.01d
T70M40	15.56 ± 0.12d	1.24 ± 0.05d	0.36 ± 0.03ef	ND	ND	6.94 ± 0.18b	0.61 ± 0.01b
T70M60	16.67 ± 0.24c	1.11 ± 0.04d	ND	ND	ND	8.21 ± 0.05a	0.61 ± 0.00b

TxMy, x is the extrusion temperature at the fourth zone (°C) and y is the feed moisture content (%). DCI, D-*chiro*-Inositol; ND, not detected. The results were expressed as mean ± SD ($n = 3$) and different letters in the same column indicate significant differences ($p < 0.05$).

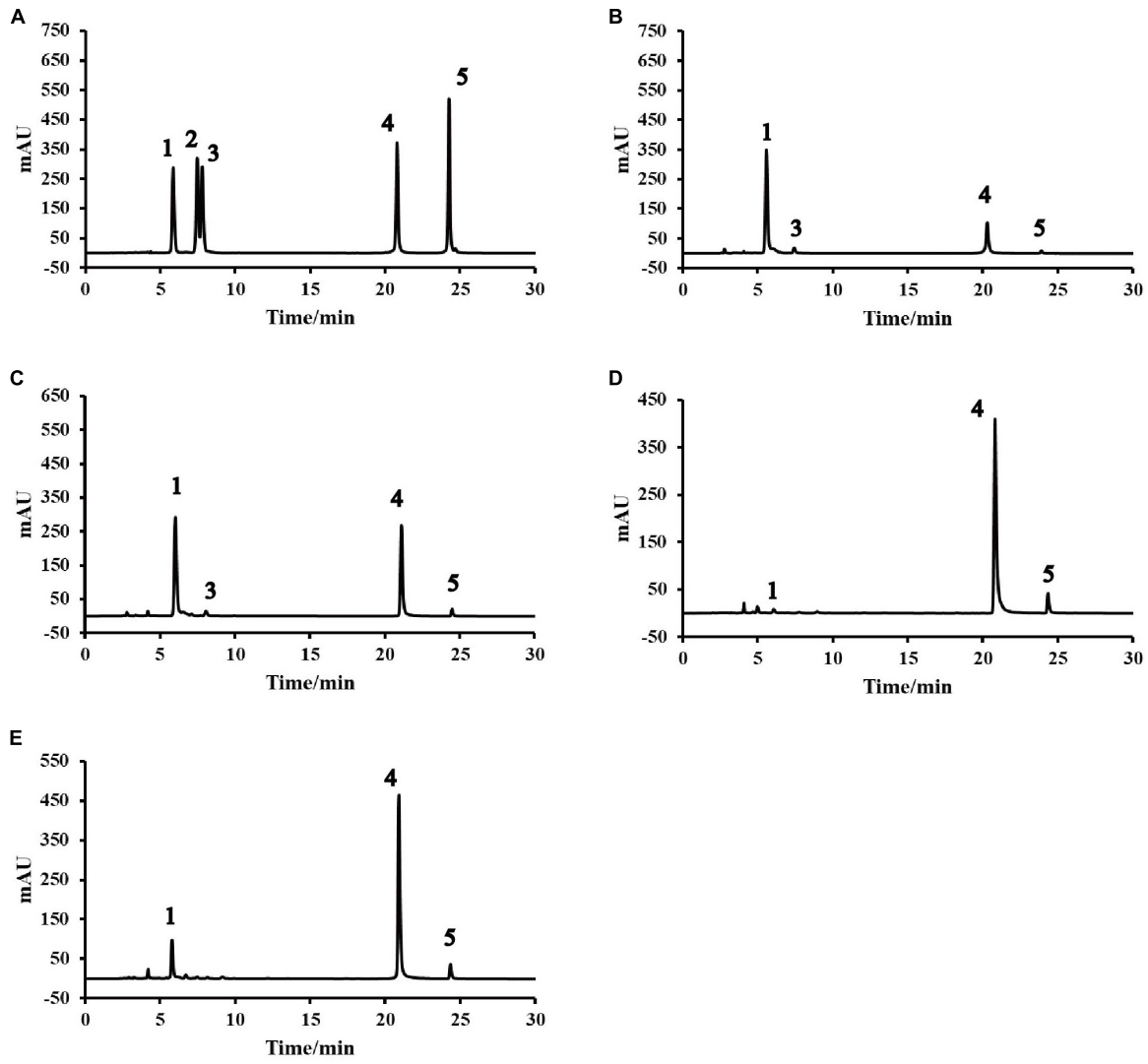

FIGURE 1
High performance liquid chromatography (HPLC) profiles of native and pregelatinized Tartary buckwheat flour: **(A)** Standards. **(B)** Native. **(C)** T160M30. **(D)** T100M30. **(E)** T70M30. (1) Rutin. (2) Isoquercitrin. (3) Kaempferol-3-*O*-rutinoside. (4) Quercetin. (5) Kaempferol. TxMy, x is the extrusion temperature at the fourth zone (°C) and y is the feed moisture content (%).

buckwheat seeds significantly decreased the rutin content, whereas it significantly increased the contents of quercetin and kaempferol (5). Li et al. found that 96.46% of the rutin in the Tartary buckwheat dough was degraded into quercetin when the Tartary buckwheat flour was mixed with 50% water for 1 min at room temperature (21). In addition, Suzuki et al. (38) and Xiao et al. (8) has proved that f3g is an important enzyme involved in the transformation of the flavonoid compounds. Based on the above results, we hypothesized that different extrusion conditions including feed moisture content, temperature, feed rate, and screw speed could affect the activity of f3g and lead to changes in flavonoid content and composition. Further mechanistic studies are needed to elucidate this hypothesis.

D-*chiro*-inositol content

Besides flavonoid compounds, changes in the DCI content of Tartary buckwheat samples obtained with different extrusion conditions was evaluated using a simple and rapid method based on HPLC linked to an evaporative light-scattering detector (HPLC-ELSD). As shown in **Table 4**, the DCI content in NTBF was 1.71 mg/g DW. For PTBF, the values of the DCI content ranged from 1.11 to 1.90 mg/g DW. Compared to NTBF, T100M30, and T160M30 samples had higher DCI levels (1.90 mg/g DW, $p < 0.05$; 1.79 mg/g DW, $p > 0.05$). Our previous study indicated that steaming buckwheat bran in an autoclave at 1.6 MPa and 120°C for 60 min could significantly enrich the DCI level in Tartary buckwheat bran extract from

0.03 to 0.22% (39). Similarly, Zielinski et al. (39) reported that baking at 220°C for 30 min significantly enhanced the DCI levels in buckwheat biscuits. Therefore, the likely explanation is that the high temperature and pressure caused by extrusion or other thermal processing technologies is able to disrupt galactosidic bonds and release the free form of DCI. Although other extrusion conditions (for instance T100M40, T100M60, and T70My) significantly decreased the DCI level ($p < 0.05$), the DCI level was still of the same order of magnitude (>1 mg/g DW). In addition, the mechanism of decrease was unclear.

Antioxidant activity

The AC of bioactive components was related to a variety of determination methods with different mechanisms, including hydrogen atom transfer (HAT), single electron transfer (ET), reducing power, and metal chelation (40). Pellegrini et al. (41) reported that ABTS radicals are suitable for water and organic phases, whereas DPPH radicals can only be used for organic phases. In addition, FRAP assay was used to determine the AC of hydrophilic antioxidants with ferric reducing potency at acidic pH but it has a low sensitivity toward antioxidants with thiol-group. Therefore, the approach of using only one detection method may underestimate AC values because antioxidant compounds are incompletely extracted.

Three different assays including DPPH, ABTS, and FRAP were employed to evaluate the AC of flavonoid extracts isolated from Tartary buckwheat samples in this study. As shown in **Figure 2A**, DPPH radical scavenging activity in NTBF was 1.74 mmol Trolox equivalent (TE)/g DW, which was significantly higher ($p < 0.05$) than in the T160M30 and T70M30 samples, and significantly lower than T70M60 ($p < 0.05$). Moreover, DPPH radical scavenging activity of T100My and T70M40 samples showed no significant differences from NTBF ($p > 0.05$). The results shown in **Figure 2B** suggested that PTBF (especially samples produced by IEPT) possessed significantly ($p < 0.05$) higher $ABTS^{+}$ radical-eliminating capacity than NTBF (1.66 mmol TE/g DW). In addition, the antioxidant capacity in PTBF determined with the ABTS assay was generally significantly higher than that determined with the DPPH assay, which is in agreement with previous studies (8, 40). This suggested the PTBF were rich in both lipophilic and hydrophilic radical scavengers. Similar results were observed in plant extracts (42). Compared to NTBF, the FRAP capacity of the T160M30 sample significantly decreased ($p < 0.05$), whereas PTBF obtained with IEPT showed a significant increase in the FRAP capacity ($p < 0.05$) (**Figure 2C**).

Combining the three detection methods above, these results confirmed that extrusion processes (especially samples produced by IEPT) significantly increased the AC ($p < 0.05$), Similar observations have also been reported in barley (22).

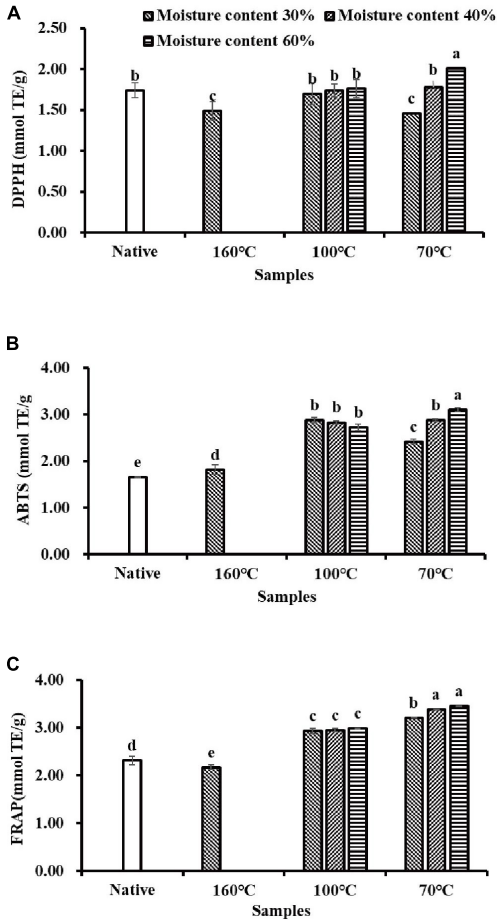

FIGURE 2
The antioxidant activities of flavonoids extracts isolated from native and pregelatinized Tartary buckwheat flour: **(A)** 1,1-diphenyl-2-pic-rylhydrazyl (DPPH) radical scavenging activity. **(B)** ABTS radical scavenging activity. **(C)** Ferric reducing antioxidant power (FRAP).

The antioxidant compounds in the flavonoid extracts were not only good reductants but also efficient radical scavengers (42). The AC was contrary to the trend in changes in the flavonoid content. On the one hand, many studies have indicated that quercetin and kaempferol contain immensely higher AC than their glycoside compounds (8, 43). As mentioned before, flavonoid glycosides (rutin, isoquercitrin, kaempferol-3-*O*-rutinoside) were transformed into these aglycones (quercetin, kaempferol) after extrusion (especially in IEPT). Consequently, the AC of PTBF obtained with IEPT was much higher than in the non-extrusion treatment and TEPT treatment. Previous workers have also noted that quercetin-3-glucoside exhibits lower antioxidant capacity and it was proposed that this phenomenon was mainly due to the substitution of sugar or alkoxy groups that hinder the hydroxyl group (44). On the other hand, another study reported that thermal processing can produce pigments due to Maillard browning, and that these pigments enhance the

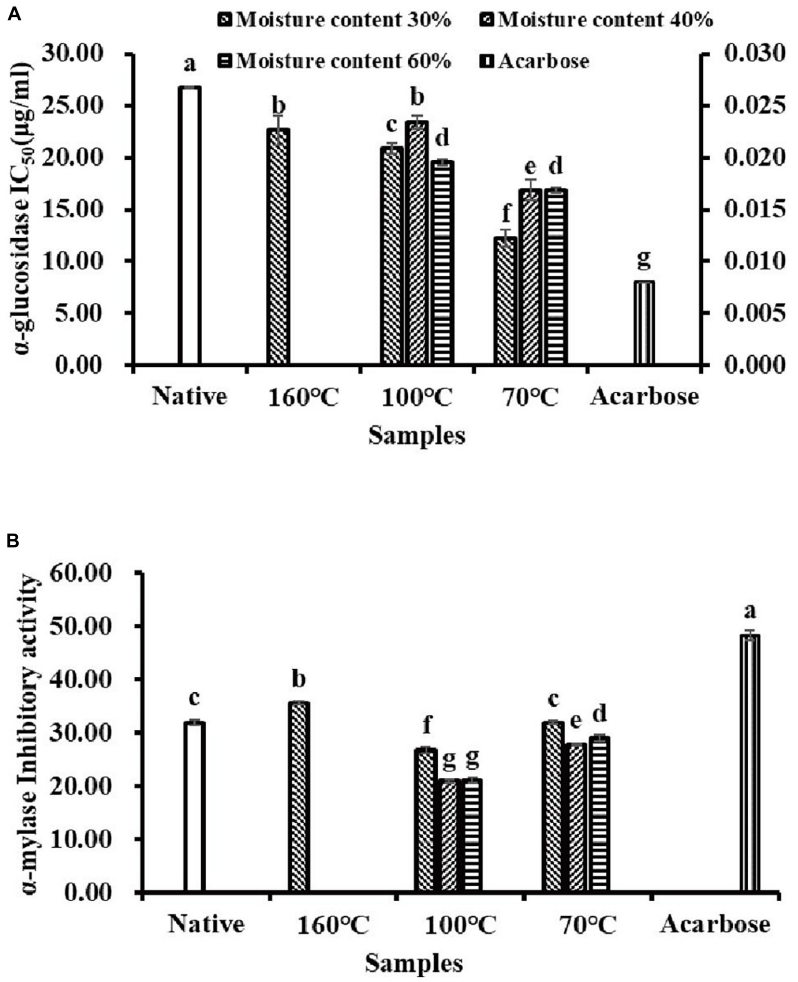

FIGURE 3
The α-glucosidase **(A)** and α-amylase **(B)** inhibitory activities of flavonoids extracts isolated from native and pregelatinized Tartary buckwheat flour.

antioxidant activity of the extrudate (22). To summarize, there are two possible explanations for improving the antioxidant activity: one was an alteration of the antioxidant profile and generation of more aglycones with stronger biological activities, and the other was due to contributions by the Maillard reaction.

α-glucosidase and α-amylase inhibitory activities

The inhibitory effects of flavonoid extracts from Tartary buckwheat samples on α-glucosidase and α-amylase activities were investigated *in vitro* (Figure 3). Calculation of the half inhibitory concentration (IC_{50}) of α-glucosidase was used to evaluate the inhibitory activity. As shown in Figure 3A, NTBF showed the lowest α-glucosidase inhibitory activity with the highest IC_{50} value (26.73 μg/ml). The α-glucosidase inhibitory activity of flavonoid extracts in PTBF was significantly enhanced by extrusion, with the IC_{50} values ranging from 12.23 to 23.45 μg/ml. As shown in Table 4, the flavonoid glycosides (rutin, isoquercitrin, kaempferol-3-*O*-rutinoside) were transformed into quercetin and kaempferol by extrusion, and especially IEPT. Similarly, previous studies have confirmed that the inhibitory activity of quercetin and kaempferol on α-glucosidase was superior to those of the glycoside derivatives (8, 19). Compared with individual flavonoids, Oboh et al. (44) found that the combination of quercetin and rutin had a synergistic effect on α-glucosidase inhibitory activity.

Not all TBF samples showed higher than 50% inactivation of the α-amylase enzyme within the concentration range studied. Therefore, the IC_{50} value for α-amylase inhibition could not be estimated in this study (Figure 3B). The α-amylase inhibitory activity significantly decreased ($p < 0.05$) under the extrusion processes, except for T160M30 and T70M30. Among the extrusion processes, the most α-amylase inhibitory activity was lost under T100My. It has been determined that individual

TABLE 5 Correlation between flavonoid compounds and color parameters, the activities of antioxidant, α-glucosidase, and α-amylase inhibitory.

	L^*	a^*	b^*	DPPH	ABTS	FRAP	α -glucosidase IC_{50} (μ g/ml)	α -amylase inhibitory activities (%)
Total flavonoids	0.318	0.130	−0.223	0.152	−0.544**	−0.663**	0.508*	0.528**
Rutin	0.305	0.486*	−0.661**	−0.362	−0.877**	−0.972**	0.584**	0.688**
Isoquercitrin	0.248	0.600**	−0.694**	−0.467*	−0.860**	−0.969**	0.493*	0.760**
Kaempferol-3-*O*-rutinoside	0.331	0.453*	−0.670**	−0.328	−0.881**	−0.979*	0.611**	0.660**
Quercetin	−0.386	−0.496*	0824**	0.509*	0.894**	0.944**	−0.581**	−0.681**
Kaempferol	−0.386	−0.480*	0.725**	0.379	0.865**	0.983**	−0.601**	−0.691**

Pearson correlation tests are performed to calculate the correlations between variables. * represents significant difference between data, $p < 0.05$; ** represents extremely significant difference between data, $p < 0.01$.

flavonoids (rutin, isoquercitrin, quercetin) play a major role in the inhibition of α-amylase (45). In addition, the complex produced by the combination of individual flavonoids and α-amylase could cause static quenching of α-amylase *via* non-radiation energy transfer and further inhibit the activity of α-amylase (45). Therefore, we deduced that the inhibitory effect of flavonoid extracts from Tartary buckwheat samples on α-amylase might be the result of the combined effect of multiple active ingredients.

The PTBF obtained with IEPT exhibited strong α-glucosidase inhibitory activity and mild α-amylase inhibitory activity in this study. In view of the fact that strong α-amylase inhibition could cause undesirable effects, such as diarrhea and flatulence (11, 12); PTBF can be used as an ideal α-amylase and α-glucosidase inhibitor and it has great potential in the development of anti-diabetic foods.

Pearson's correlations

The Pearson correlation coefficients for the relationship between flavonoid compounds and color parameters, the activities of antioxidant, α-glucosidase, and α-amylase inhibitory of different samples are shown in **Table 5**. The a^* scores significantly correlated with TFC, rutin, isoquercitrin, kaempferol-3-*O*-rutinoside, quercetin, and kaempferol levels (r = 0.486, 0.600, 0.453, −0.496, −0.480), whereas the b^* scores possessed the opposite tendency. This suggested that the a^* and b^* scores of different samples are closely related to the individual flavonoid compounds levels. In addition, the antioxidants (DPPH, ABTS, FRAP) significantly correlated with flavonoid levels in Tartary buckwheat samples. Specifically, the antioxidant activity was positively correlated with the levels of quercetin and kaempferol and negatively correlated with TFC, rutin, isoquercitrin, and kaempferol-3-*O*-rutinoside levels. The α-glucosidase inhibitory activity was positively correlated with the levels of quercetin and kaempferol, and negatively correlated with TFC, rutin, isoquercitrin and kaempferol-3-*O*-rutinoside levels, whereas the α-amylase inhibitory activity possessed the opposite tendency. Based on these results, we can conclude that the changes in flavonoid content and composition caused by extrusion have synergistic or antagonistic effects on the color parameters, the activities of antioxidant, α-glucosidase, and α-amylase inhibitory of different samples.

Conclusion

This work indicated that the type of extrusion treatment induces a significant effect on the phytochemical composition and color properties of Tartary buckwheat samples and strongly influences its antioxidant, α-glucosidase, and α-amylase inhibitory activities. Extrusion processes have a significant effect on the overall color of Tartary buckwheat samples. The contents of fat, total flavonoids, and flavonoid glycosides decreased upon extrusion, while the aglycone contents and the activities of antioxidant and α-glucosidase inhibition increased significantly. In particular, different aspects of the extrusion treatments (including the temperature and moisture properties) had different effects on the levels of protein and DCI, as well as α-amylase inhibitory activity. Overall, PTBF obtained with IEPT showed particularly high levels of aglycones, strong antioxidant and α-glucosidase inhibition and relatively mild α-amylase inhibitory activity. These findings indicate that PTBF obtained under IEPT could serve as an ideal functional food resource with antioxidant and anti-diabetic potential.

Data availability statement

The original contributions presented in the study are included in the article/supplementary material, further inquiries can be directed to the corresponding authors.

Author contributions

ZZ: investigation, data curation, and writing—original draft. XF: methodology and formal analysis. LZu: material and formal analysis. BX: software and formal analysis.

MZ: visualization. XY: writing—review and editing. GR: project administration. YY: methodology and writing—review and editing. LZa: supervision and resources. PQ: supervision, conceptualization, and funding acquisition. All authors contributed to the article and approved the submitted version.

Funding

This work was supported by grants from National Key R&D Program of China (Grant No. 2020YFD1001400) and the Agricultural Science and Technology Innovation Program of the Chinese Academy of Agricultural Sciences (Grant No. CAAS-ASTIP-2017-ICS).

Acknowledgments

We thank Chao Liu from Shanxi Agricultural University for his great help to preparation of PTBF samples. We are grateful to the support from all the team members and National Key R&D Program of China (Grant No. 2020YFD1001400) and the Agricultural Science and Technology Innovation Program of the Chinese Academy of Agricultural Sciences (Grant No. CAAS-ASTIP-2017-ICS).

Conflict of interest

The authors declare that the research was conducted in the absence of any commercial or financial relationships that could be construed as a potential conflict of interest.

Publisher's note

References

1. Zou, L, Wu D, Ren G, Hu Y, Peng L, Zhao J, et al. Bioactive compounds, health benefits, and industrial applications of Tartary buckwheat (*Fagopyrum tataricum*). *Crit Rev Food Sci.* (2021) 61:1–17. doi: 10.1080/10408398.2021.1952161

2. Ge RH, Wang H. Nutrient components and bioactive compounds in tartary buckwheat bran and flour as affected by thermal processing. *Int J Food Prop*. (2020) 23:127–37. doi: 10.1080/10942912.2020.1713151

3. Sun XJ, Li WH, Hu YY, Zhou XJ, Ji MY, Yu D, et al. Comparison of pregelatinization methods on physicochemical, functional and structural properties of tartary buckwheat flour and noodle quality. *J Cereal Sci.* (2018) 80:63–71. doi: 10.1016/j.jcs.2018.01.016

4. Zhu F. Chemical composition and health effects of Tartary buckwheat. *Food Chem.* (2016) 203:231–45. doi: 10.1016/j.foodchem.2016.02.050

5. Qin PY, Wu L, Yao Y, Ren GX. Changes in phytochemical compositions, antioxidant and alpha-glucosidase inhibitory activities during the processing of tartary buckwheat tea. *Food Res Int.* (2013) 50:562–7. doi: 10.1016/j.foodres.2011.03.028

6. Borovaya SA, Klykov AG. Some aspects of flavonoid biosynthesis and accumulation in buckwheat plants. *Plant Biotechnol Rep.* (2020) 14:213–25. doi: 10.1007/s11816-020-00614-9

7. Beitane I, Zemture GK, Sabovics M. Effect of germination and extrusion on the phenolic content and antioxidant activity of raw buckwheat (*Fagopyrum esculentum* Moench). *Agron Res.* (2018) 16:1331–40. doi: 10.15159/AR.18.005

8. Xiao Y, Yang C, Xu HN, Zhang J, Zhang LF. Study on the change of flavonoid glycosides to aglycones during the process of steamed bread containing tartary buckwheat flour and antioxidant, alpha-glucosidase inhibitory activities evaluation in vitro. *LWT Food Sci Technol.* (2021) 145:111527. doi: 10.1016/j.lwt.2021.111527

9. Yao Y, Shan F, Bian JS, Chen F, Wang MF, Ren GX. D-chiro-inositol-enriched tartary buckwheat bran extract lowers the blood glucose level in KK-A(y) mice. *J Agr Food Chem.* (2008) 56:10027–31. doi: 10.1021/jf801879m

10. Sensoy I, Rosen RT, Ho CT, Karwe MV. Effect of processing on buckwheat phenolics and antioxidant activity. *Food Chem.* (2006) 99:388–93. doi: 10.1016/j.foodchem.2005.08.007

11. Zhao J, He J, Dang Y, Cao J, Sun Y, Pan D. Ultrasound treatment on the structure of goose liver proteins and antioxidant activities of its enzymatic hydrolysate. *J Food Biochem.* (2020) 44:e13091. doi: 10.1111/jfbc.13091

12. Deng YT, Lin-Shiau SY, Shyur LF, Lin JK. Pu-erh tea polysaccharides decrease blood sugar by inhibition of alpha-glucosidase activity in vitro and in mice. *Food Funct.* (2015) 6:1539–46. doi: 10.1039/c4fo01025f

13. Cheng WW, Gao L, Wu D, Gao CC, Meng LH, Feng X, et al. Effect of improved extrusion cooking technology on structure, physiochemical and nutritional characteristics of physically modified buckwheat flour: its potential use as food ingredients. *LWT Food Sci Technol.* (2020) 133:109872. doi: 10.1016/j.lwt.2020.109872

14. Sun XY, Yu C, Fu MX, Wu D, Gao CC, Feng X, et al. Extruded whole buckwheat noodles: effects of processing variables on the degree of starch gelatinization, changes of nutritional components, cooking characteristics and in vitro starch digestibility. *Food Funct.* (2019) 10:6362–73. doi: 10.1039/c9fo01111k

15. Zhou ZK, Ren XC, Wang F, Li J, Si X, Cao R, et al. High pressure processing manipulated buckwheat antioxidant activity, anti-adipogenic properties and starch digestibility. *J Cereal Sci.* (2015) 66:31–6. doi: 10.1016/j.jcs.2015.09.002

16. Kim S, Yang SY, Chun HH, Bin Song K. High hydrostatic pressure processing for the preparation of buckwheat and tapioca starch films. *Food Hydrocolloid.* (2018) 81:71–6. doi: 10.1016/j.foodhyd.2018.02.039

17. Wang X, Fan D, Zhang TL. Effects of hydrothermal processing on rutin retention and physicochemical properties of Tartary buckwheat enriched dough and Chinese steamed bread. *Int J Food Sci Tech.* (2017) 52:2180–90. doi: 10.1111/ijfs.13497

18. Dziedzic K, Szwengiel A, Gorecka D, Rudzinska M, Korczak J, Walkowiak J. The effect of processing on the phytosterol content in buckwheat groats and by-products. *J Cereal Sci.* (2016) 69:25–31. doi: 10.1016/j.jcs.2016.02.003

19. Wang L, Luo Y, Wu YN, Liu Y, Wu ZQ. Fermentation and complex enzyme hydrolysis for improving the total soluble phenolic contents, flavonoid aglycones contents and bio-activities of guava leaves tea. *Food Chem.* (2018) 264:189–98. doi: 10.1016/j.foodchem.2018.05.035

20. Wu XJ, Fu GM, Li RY, Li Y, Dong B, Liu CM. Effect of thermal processing for rutin preservation on the properties of phenolics & starch in Tartary buckwheat achenes. *Int J Biol Macromol.* (2020) 164:1275–83. doi: 10.1016/j.ijbiomac.2020.07.135

21. Li D, Li XL, Ding XL, Park KH. A process for preventing enzymatic degradation of rutin in tartary buckwheat (*Fagopyrum tataricum* Gaertn) flour. *Food Sci Biotechnol.* (2008) 17:118–22.

22. Sharma P, Gujral HS, Singh B. Antioxidant activity of barley as affected by extrusion cooking. *Food Chem.* (2012) 131:1406–13. doi: 10.1016/j.foodchem.2011.10.009

23. Zhang M, Bai X, Zhang ZS. Extrusion process improves the functionality of soluble dietary fiber in oat bran. *J Cereal Sci.* (2011) 54:98–103. doi: 10.1016/j.jcs.2011.04.001

24. Liu CM, Zhang YJ, Liu W, Wan J, Wang WH, Wu L, et al. Preparation, physicochemical and texture properties of texturized rice produce by improved extrusion cooking technology. *J Cereal Sci.* (2011) 54:473–80. doi: 10.1016/j.jcs.2011.09.001

25. Zielinski H, Michalska A, Piskula MK, Kozlowska H. Antioxidants in thermally treated buckwheat groats. *Mol Nutr Food Res.* (2006) 50:824–32. doi: 10.1002/mnfr.200500258

26. Yang N, Ren GX. Determination of D-chiro-inositol in tartary buckwheat using high-performance liquid chromatography with an evaporative light-scattering detector. *J Agr Food Chem.* (2008) 56:757–60. doi: 10.1021/jf0717541

27. Yao Y, Yang XS, Tian J, Liu CY, Cheng XZ, Ren GX. Antioxidant and antidiabetic activities of black Mung bean (*Vigna radiata* L.). *J Agr Food Chem.* (2013) 61:8104–9. doi: 10.1021/jf401812z

28. Ji YL, Liu D, Jin Y, Zhao J, Zhao J, Li H, et al. In vitro and in vivo inhibitory effect of anthocyanin-rich bilberry extract on alpha-glucosidase and alpha-amylase. *Lwt-Food Sci Technol.* (2021) 145:111484. doi: 10.1016/j.lwt.2021.111484

29. Qin PY, Wang Q, Shan F, Hou ZH, Ren GX. Nutritional composition and flavonoids content of flour from different buckwheat cultivars. *Int J Food Sci Tech.* (2010) 45:951–8. doi: 10.1111/j.1365-2621.2010.02231.x

30. McCleary BV, Charmier LMJ, McKie VA. Measurement of starch: critical evaluation of current methodology. *Starch.* (2019) 71:1800146. doi: 10.1002/star.201800146

31. Østergård K, Björck I, Vainionpää J. Effects of extrusion cooking on starch and dietary fibre in barley. *Food Chem.* (1989) 34:215–27. doi: 10.1016/0308-8146(89)90142-8

32. Sobota A, Sykut-Domańska E, Rzedzicki Z. Effect of Extrusion-cooking process on the chemical composition of corn-wheat extrudates, with particular emphasis on dietary fibre fractions. *Pol J Food Nutr Sci.* (2010) 60:251–9.

33. Ilo S, Berghofer E. Kinetics of lysine and other amino acids loss during extrusion cooking of maize grits. *J Food Sci.* (2003) 68:496–502. doi: 10.1111/j.1365-2621.2003.tb05701.x

34. Wang L, Duan W, Zhou SM, Qian HF, Zhang H, Qi XG. Effects of extrusion conditions on the extrusion responses and the quality of brown rice pasta. *Food Chem.* (2016) 204:320–5. doi: 10.1016/j.foodchem.2016.02.053

35. Jozinovic A, Šubaric D, Ackar D, Babic J, Klaric I, Kopjar M, et al. Influence of buckwheat and chestnut flour addition on properties of corn extrudates. *Croatian J Food Sci Tech.* (2012) 4:26–33.

36. Lund MN, Ray CA. Control of Maillard reactions in foods: strategies and chemical mechanisms. *J Agr Food Chem.* (2017) 65:4537–52. doi: 10.1021/acs.jafc.7b00882

37. Lee J, Kang YR, Kim YJ, Chang YH. Effect of high pressure and treatment time on nutraceuticals and antioxidant properties of *Lonicera japonica* Thunb. *Innov Food Sci Emerg.* (2019) 54:243–51. doi: 10.1016/j.ifset.2019.05.005

38. Suzuki T, Honda Y, Funatsuki W, Nakatsuka K. Purification and characterization of flavonol 3-glucosidase, and its activity during ripening in tartary buckwheat seeds. *Plant Sci.* (2002) 163:417–23. doi: 10.1016/s0168-9452(02)00158-9

39. Zielinski H, Honke J, Baczek N, Majkowska A, Wronkowska M. Bioaccessibility of D-chiro-inositol from water biscuits formulated from buckwheat flours fermented by lactic acid bacteria and fungi. *LWT Food Sci Technol.* (2019) 106:37–43. doi: 10.1016/j.lwt.2019.02.065

40. Shahidi F, Zhong Y. Measurement of antioxidant activity. *J Funct Foods.* (2015) 18:757–81. doi: 10.1016/j.jff.2015.01.047

41. Pellegrini N, Serafini M, Colombi B, Del Rio D, Salvatore S, Bianchi M, et al. Total antioxidant capacity of plant foods, beverages and oils consumed in Italy assessed by three different in vitro assays. *J Nutr.* (2003) 133:2812–9. doi: 10.1093/jn/133.9.2812

42. Ng ZX, See AN. Effect of in vitro digestion on the total polyphenol and flavonoid, antioxidant activity and carbohydrate hydrolyzing enzymes inhibitory potential of selected functional plant-based foods. *J Food Process Preserv.* (2019) 43:e13903. doi: 10.1111/jfpp.13903

43. de Araujo M, Franco YEM, Alberto TG, Sobreiro MA, Conrado MA, Priolli DG, et al. Enzymatic de-glycosylation of rutin improves its antioxidant and antiproliferative activities. *Food Chem.* (2013) 141:266–73. doi: 10.1016/j.foodchem.2013.02.127

44. Oboh G, Ademosun AO, Ayeni PO, Omojokun OS, Bello F. Comparative effect of quercetin and rutin on α-amylase, α-glucosidase, and some pro-oxidant-induced lipid peroxidation in rat pancreas. *Comp Clin Pathol.* (2015) 24:1103–10. doi: 10.1007/s00580-014-2040-5

45. Li Y, Gao F, Gao F, Shan F, Bian J, Zhao C. Study on the interaction between 3 flavonoid compounds and alpha-amylase by fluorescence spectroscopy and enzymatic kinetics. *J Food Sci.* (2009) 74:C199–203. doi: 10.1111/j.1750-3841.2009.01080.x

frontiers | Frontiers in Nutrition

TYPE Original Research
PUBLISHED 16 November 2022
DOI 10.3389/fnut.2022.1058025

OPEN ACCESS

EDITED BY
Zhi-Hong Zhang,
Jiangsu University, China

REVIEWED BY
Qiang Xia,
Ningbo University, China
Jing-Kun Yan,
Dongguan University of Technology, China

*CORRESPONDENCE
Kai Li
gxlikai@gxu.edu.cn

SPECIALTY SECTION
This article was submitted to Nutrition and Food Science Technology, a section of the journal Frontiers in Nutrition

RECEIVED 30 September 2022
ACCEPTED 31 October 2022
PUBLISHED 16 November 2022

CITATION
Tian R, Liu Y, Cao D, Gai L, Du N, Yin J, Hu D, Lu H, Li W and Li K (2022) Preparation of highly efficient p-doped porous camellia shell-based activated carbon and its adsorption of carotenoids in camellia oil. *Front. Nutr.* 9:1058025. doi: 10.3389/fnut.2022.1058025

Preparation of highly efficient p-doped porous camellia shell-based activated carbon and its adsorption of carotenoids in camellia oil

Run Tian[1], Yang Liu[1], Danyu Cao[1], Lili Gai[1], Nan Du[1], Jiangyu Yin[1], Dongbin Hu[1], Haiqin Lu[1], Wen Li[2] and Kai Li[1,3]*

[1]College of Light Industry and Food Engineering, Guangxi University, Nanning, China, [2]Guangxi Key Laboratory of Chemistry and Engineering of Forest Products, School of Chemistry and Chemical Engineering, Guangxi University for Nationalities, Nanning, China, [3]Provincial and Ministerial Collaborative Innovation Center for Sugar Industry, Nanning, China

The vegetable oil industry is limited by the high cost of the refining process, and the camellia shells (CS) are beneficial to the development of the industry as a biomass raw material for camellia oil decolorization. In this study, CS-based p-doped porous activated carbon (CSHAC) obtained after the pyrolysis of H_3PO_4-laden CS-hydrochar (CSH) was used for the adsorption of carotenoids in camellia oil. The results showed that the adsorption efficiency of CSHAC for carotenoids was 96.5% compared to 67–87% for commercial decolorizers, and exhibited a fast adsorption rate (20 min). The results of adsorption isotherms indicated that the adsorption of carotenoids on CSHAC occurred through a multi-layer process. Furthermore, the analysis of adsorption kinetics showed that the adsorption of carotenoids by CSHAC was a complex process involving physical and chemical reactions, and chemisorption was the dominant kinetic mechanism. This superior performance of CSHAC in adsorbing carotenoids was attributed to its micro-mesoporous structure, hydrophobicity, and numerous active sites.

KEYWORDS

camellia oil, adsorption, activated carbon, interaction, mechanism

Introduction

Carotenoids are derivatives of 40-carbon isoprene, which can be derived from a variety of classes due to different substituents. Common carotenoids in vegetable oils are β-carotene and lutein, which appear yellow, orange, or red (1). Although carotenoids have health-benefiting antioxidant properties, they show pro-oxidant activity at high temperatures during vegetable oil refining process (2). Therefore, research on the removal of carotenoids is necessary for the subsequent processing of refined vegetable oils, to meet oil quality standards and to promote a healthy diet.

Activated clay and activated carbon have been utilized in oil decolorization (3). However, in the refining process, acid-activated activated clay catalyzes the oxidation of oil in oxygenated and high-temperature environment (4). In contrast, carbon materials are considered to be a better choice. However, the existing commercial activated carbon (CAC) is not satisfactory for the decolorization efficiency of vegetable oils, and the production of high-efficiency carbon materials requires expensive precursors and equipment. Biomass has attracted extensive research attention due to its distinctive advantages, including resource-rich, clean, and eco-friendly (5). Bamboos (6), peanut shells (7), rubber seed shells (8), and pinewoods (9) have been used to produce effective activated carbon, which is used as an adsorbent in many applications and can eliminate the waste of certain resources. However, detailed studies on the adsorption of carotenoids from vegetable oils by activated carbon are rare.

Hydrothermal carbonisation (HTC) refers to operation in a sealed reactor under mild subcritical reaction conditions below 250°C to promote the dissolution of lignocellulosic components into water (10). The HTC process produces hydrochar with a high aromatic structure and a high content of oxygen-containing functional groups (11). A study revealed that carotenoids were oxidized upon adsorption (12). Therefore, this process is capable of facilitating the removal of pigments. Increasing the micro-mesoporous structure, surface area, and active groups of carbon materials can also improve their adsorption efficiency (13). Bentonite clays with predominantly mesoporous structural characteristics have been fabricated, and the researchers believed that the average pore size of clay particles affected their oil-bleaching capacity (14). Another study investigated the bleaching capacity of activated animal bone with a surface area of 593.27 m^2/g on palm oil, but its efficiency at 120°C was only 75.14% (15). Some researchers studied the thermo-mechanical process of bleaching oil on adsorbents constituted of 5% activated carbon and 95% activated earth (16). However, the above studies of composite adsorbents did not fully demonstrate the mechanism of adsorption between all carbon-based adsorbents and pigments.

Camellia shells (CS) can be used as decolorizers for refined camellia oil. These shells have great potential for mass production, and comprehensive utilization of agricultural by-products can reduce industrial costs, which is conducive to increasing their economic added value. Moreover, considering the rich mesoporous structure of the shell, it is a promising material for the production of porous carbon. There is minimal research on the HTC method for yielding high-efficient activated carbon from CS as vegetable oil decolorizing agents. Although the effectiveness of single-step carbonisation is acceptable, HTC-assisted carbonisation has been investigated to optimize consumption of energy, as well as to biomass applications, since biomass has a high percentage of water. Therefore, pre-treatment with the HTC process before pyrolysis is expected to produce carbon materials with improved physicochemical performances.

In this study, p-doped porous activated carbon (CSHAC) with high specific surface area and ample surface groups was prepared from CS. The adsorption mechanisms of adsorbents for carotenoids of camellia oil were analyzed through adsorption kinetics, isotherms, and thermodynamics. This is the first report on CS as a precursor for the synthesis of p-doped porous carbon for removing carotenoids from vegetable oils, to the best of our knowledge. This work introduces a new type of biomass for rapid carotenoid adsorption. It can also provide a reference for decolorization mechanisms for vegetable oils.

Materials and methods

Chemicals and materials

Crude camellia oil was supplied by the Zhongzhou Company, China. Camellia shells were from Kaihua County, Quzhou City, Zhejiang Province, China. Camellia shells were pretreated by washing thoroughly with distilled water and drying in the sun for 8 h before being crushed and sieved with a 100 μm mesh in a stable arm crusher. Phosphoric acid (H_3PO_4, 85%) was purchased from Guangdong Guanghua Sci-Tech Co., Ltd. Commercial activated clay (CC) was purchased from Gongyi Runsen Water Treatment Materials Co., Ltd. Commercial activated carbon was purchased from Dongguan Hongsheng Activated Carbon Co., Ltd.

Preparation of CSHAC

CSHAC was obtained using the HTC method, then acidified with 20% H_3PO_4 and carbonized (17). The HTC method was performed in an autoclave reactor. First, 5 g of CS and 50 ml of distilled water were mixed well and sealed in a stainless steel sample reactor. The reactor was then heated at 200°C for 1 day. Next, the solid product, namely CS-hydrochar (CSH), was flushed with distilled water and whereafter dried at 105°C for 1 day. The process was continued by stirring CSH with 50 ml of 20% H_3PO_4 at ambient temperature for 5 min and drying at 105°C for 1 day. The dried products were then carbonized at 600°C at a heating rate of 5°C min^{-1} with a continuous N_2 flow for 3 h. The collected product was designated CSHAC after being rinsed with distilled water to remove excess acid and by-products up to pH 7.

Preparation of refined camellia oil

The refined camellia oil contained 35.2 mg/kg carotenoids, which was obtained by filtering the crude camellia oil through

a ceramic membrane with a pore size of 0.14 μm to remove possible suspended impurities.

Batch adsorption studies

Batch adsorption tests were performed to assess the performance of CSHAC for the adsorption of carotenoids. All the adsorption studies were performed in a temperature-controlled incubator shaker with consistent stirring (150 rpm) (ZQZY-85CN, Zhichu, China). A conical flask was used to place refined camellia oil during the experiments. The influences of important factors, for instance, sorbent material, sorbent dosage, temperature, and contact time on carotenoid adsorption were investigated. Each adsorption experiment was repeated thrice, and the results were averaged. After adsorption, the samples were split from the oil by transiting them through filter paper. Based on the British Standard Methods of Analysis (BS, 1993), the carotenoid concentrations of samples were determined at 454 nm with cyclohexane as the reference solution using a spectrophotometer (SP-752, Spectrum, China). The total carotenoid content was expressed as β-carotene equivalents. Later, 1 g of refined camellia oil was weighed, dissolved in cyclohexane, and diluted to a final volume of 100 ml. To acquire reliable results, the suspended impurities were filtered through the membrane (0.45 μm) and residual carotenoid concentrations were detected. The followings are the adsorption capacities of carotenoids on CSHAC at time $t(q_t)$ and equilibrium (q_e) and the carotenoid removal rate (R):

$$q_t = \frac{(C_0 - C_t) \times V}{m} \quad (1)$$

$$q_e = \frac{(C_0 - C_e) \times V}{m} \quad (2)$$

$$R = \frac{C_0 - C_t}{C_0} \times 100\% \quad (3)$$

where C_0 (mg/L), C_t (mg/L), and C_e (mg/L) show the concentrations of carotenoid at the original time, equilibrium, and time t, respectively; m (g) is the adsorbent dosage; V (L) is refined camellia oil volume.

Analysis

The N_2 adsorption-desorption analysis was determined by using the Brunauer–Emmett–Teller (BET; ASAP2460;

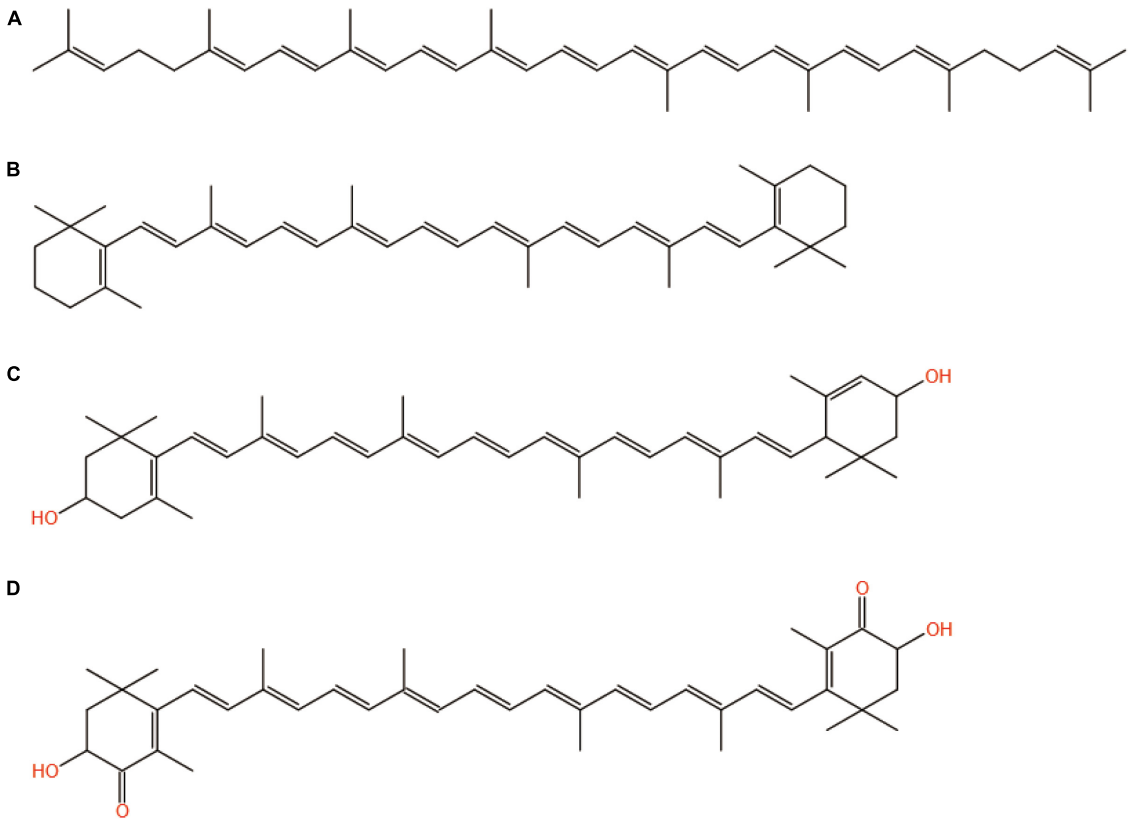

FIGURE 1
Structures of **(A)** lycopene, **(B)** β-carotene, **(C)** lutein, and **(D)** astaxanthin.

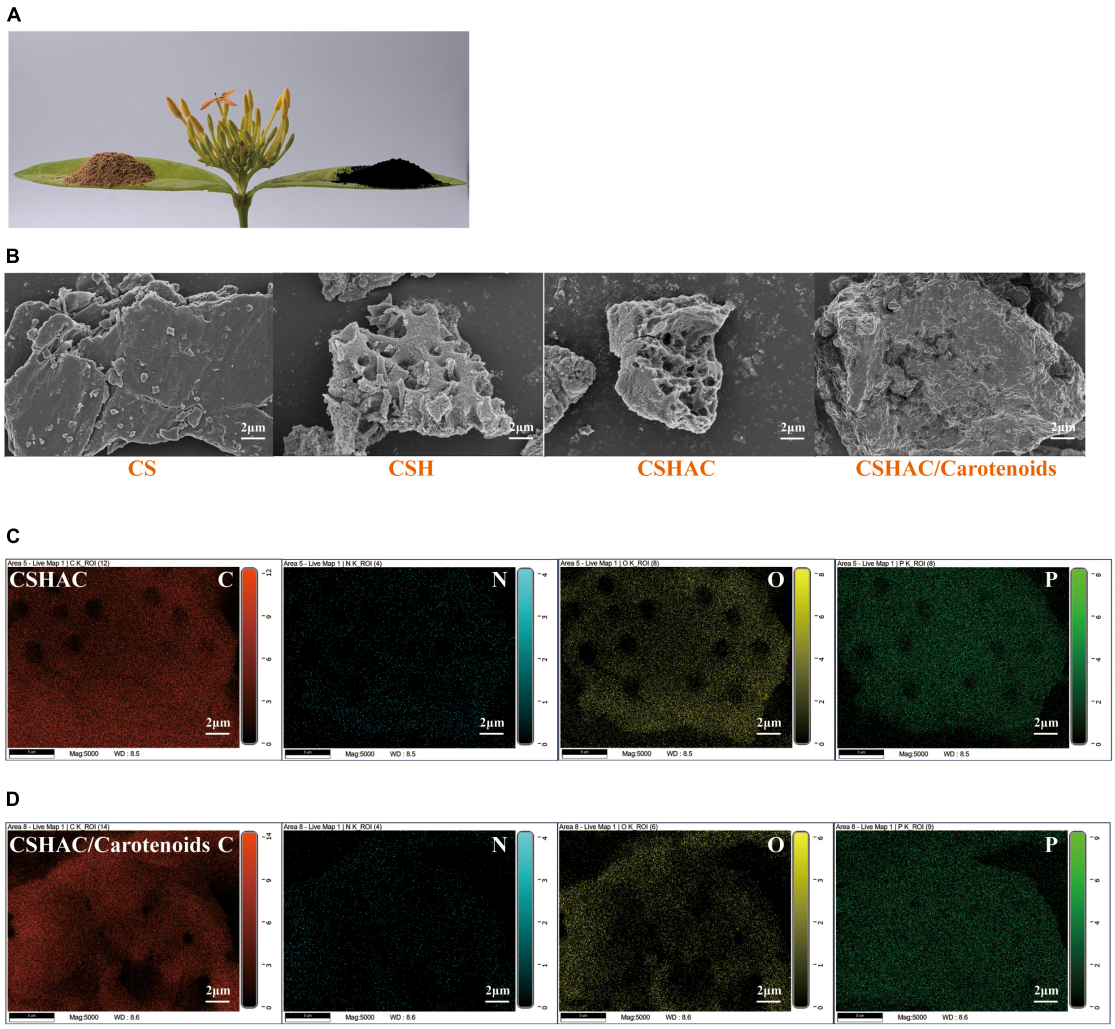

FIGURE 2
(A) Images of CS and CSHAC on *Ixora chinensis* leaves. **(B)** SEM images of CS, CSH, CSHAC, and CSHAC/carotenoids. EDX images of **(C)** CSHAC and **(D)** CSHAC/carotenoids.

Micromeritics, USA) equation. The surface features of samples were observed using scanning electron microscopy (SEM; Zeiss Gemini 300, Germany). The X-ray diffraction (XRD) patterns in the scanning range of 5–80° of the samples were measured using an X-ray diffractometer (SmartLab3KW, Rigaku, Japan). Raman spectroscopy was performed using a DORIBA Spectra instrument operating with a 532 nm green laser (Horiba LabRAM HR Evolution, Japan). The mapping images were provided with an X-ray spectrometer [energy-dispersive X-ray spectrometer (EDX); SMART, EDAX Inc., USA]. X-ray photoelectron spectrometry (XPS) was used to analyze compositions of sample surfaces (K-Alpha, Thermo Fisher Scientific, USA). Contact angles analysis of samples was obtained by using contact angle equipment (DSA100; KRUSS, Germany). Fourier transform infrared spectrometer (FTIR) was used to detect the functional groups of the samples (IRTracer-100, Shimadzu, Japan). An ultraviolet detector was used for identifying compounds at a wavelength of 454 nm. The free fatty acid contents of the samples were determined using the AOCS Official Method, C. (2017). 3d-63. Acid value fats and oils. The peroxide values of the samples were determined using the national standard (GB 5009.227–2016).

Results and discussion

Characterisation of CSHAC

Scanning electron microscopy-energy-dispersive X-ray spectrometer studies

The structures of the four common carotenoids were depicted in Figure 1. As depicted in Figure 2A, CS and CSHAC could be easily placed on the leaves of *Ixora chinensis*.

Unnoteworthy deformation of the leaf manifested that the density of prepared CSHAC did not change significantly compared with CS. Surface morphologies of CS, CSH, CSHAC, and CSHAC/carotenoids were characterized using SEM. Figure 2B exhibited the typical SEM images. The pristine CS exhibited a relatively smooth surface. In comparison, the

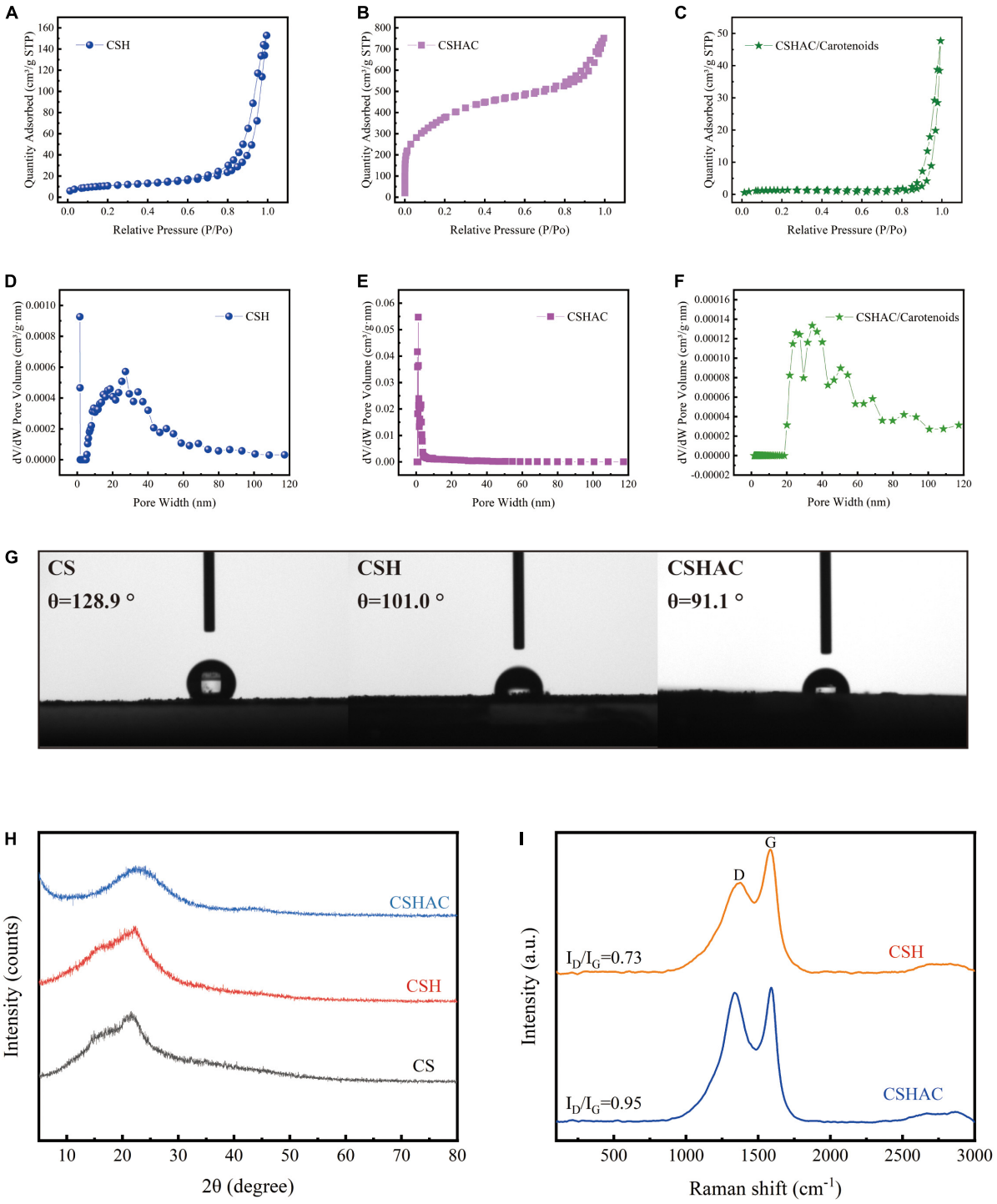

FIGURE 3
N_2 adsorption-desorption isotherms for **(A)** CS, **(B)** CSH, and **(C)** CSHAC. The pore size distribution curves of **(D)** CSH, **(E)** CSHAC, and **(F)** CSHAC/carotenoids. **(G)** Contact angles determined for CS, CSH, and CSHAC. **(H)** X-ray diffraction patterns of CS, CSH, and CSHAC. **(I)** Raman spectra of CSH and CSHAC.

HTC process developed some pore space with a multilevel layered structure on the CSH surface. CSHAC exhibited an abundant network-like porous structure that could expose more available active sites for the uptake of carotenoids during the adsorption process. The lignin skeleton was exposed during acidification and pyrolysis (18). The pore structure of CSHAC was well developed, forming delamination within the pore channel, and even causing surface etching of CSHAC. As depicted in Figure 2B, the morphology of CSHAC changed upon carotenoid adsorption. At the end of the adsorption process, the surface of CSHAC was wrapped with the refined camellia oil pigments, and the pore structure was no longer clearly and visibly exposed.

Figures 2C,D exhibited the EDX element mapping images for CSHAC and CSHAC/carotenoids. The EDX spectra of CSHAC were mainly composed of C, O, N, and P. It was evident that the P element were successfully doped into the carbon skeleton after biomass pyrolysis and evenly distributed on the CSHAC surface, which ensured that CSHAC had a high chemical reactivity for carotenoid adsorption. Compared with CSHAC, the C, N, and O contents of CSHAC/carotenoids were significantly different, revealing that the chemical composition of CSHAC changed after the carotenoid adsorption process.

Brunauer–Emmett–Teller analysis

The results of the N_2 adsorption-desorption isotherms investigation were exhibited in Figures 3A–F. It was evident in Figure 3A that the CSH adsorbent exhibited a typical type IV isotherm with an H_3 hysteresis loop, proving that the CSH process transformed the adsorbent into a mesoporous material with inter-granular voids or slit pores (IUPAC classification). The adsorption isotherms for CSHAC (Figure 3B) exhibited a sharp rise in the low relative pressure range ($p/p_0 < 0.1$) and represented a hysteresis loop at a relative pressure of 0.45, which indicated that the isotherms belonged to the combination of type I and type IV isotherms (19). Moreover, the hysteresis loop corresponded to the H_4 loop. These results implied that the prepared CSHAC was micro-mesoporous carbons (20). The isotherms exhibited an obvious upturn at p/p_0 higher than 0.95, indicating that the adsorbent contained macropores. These findings were consistent with the results of the SEM investigation and the reasons for the pore collapse of CSH and CSHAC proposed by the authors. As depicted in Figure 3C, the adsorption-desorption isotherm of CSHAC/carotenoids was a type IV isotherm of the H_3 hysteresis loop, proving that carotenoid adsorption changed the pore structure of the adsorbent. This might be related to the physical or chemical adsorption of carotenoids. The specific surface areas, total pore volumes, and average pore sizes of the samples were calculated (see Table 1 for details). The specific surface area and pore volume of CSHAC were significantly higher than those of CSH, demonstrating that CSHAC was well activated and could facilitate the capture of colorants from refined camellia oil. By comparing the difference in average pore sizes between CSHAC and CSH, we speculated that the pore size distributions of adsorbent might affect adsorption efficiency (13). The specific surface area and pore volume of CSHAC after adsorption were significantly lower than before, and the microporous structure disappeared, indicating that the pigments diffused through the pore surface and inside the pores. This finding also indicated that CSHAC exhibited good pore-mediated adsorption.

TABLE 1 Physicochemical properties of CS, CSH, CSHAC, and CSHAC/carotenoids.

Adsorbent	Specific surface area (m^2/g)	Pore volume (cm^3/g)			Average pore size (nm)
		Vtot	Vmic	Vmes	
CS	0.19	0.012	–	–	261
CSH	37.87	0.263	0.005	0.231	31
CSHAC	1,359.25	1.162	0.451	0.922	4.1
CSHAC/ Carotenoids	3.86	0.074	0.002	0.073	76

Vtot, total pore volume; Vmic, micropore volume; Vmes, mesopore volume.

Contact angle measurement

As shown in Figure 3G, a contact angle measurement apparatus was used for studying the hydrophilicities/hydrophobicities of CS, CSH, and CSHAC. The contact angle of the CS surface was 128.9°, which manifested hydrophobicity. After the HTC, acidification, and pyrolysis processes, the contact angles of the CSH (101.0°) and CSHAC (91.1°) surfaces were slightly lower than those of the CS surface. The decrease in hydrophobicity could be ascribed to an increase in the porosity and number of functional groups of CSH and CSHAC (21). The adsorption process proceeded in two steps (22). First, the adsorbate was transferred through the liquid film around the adsorbent. Second, the adsorbate diffused through the pores of the adsorbent and then adsorption took place in the active sites of the sorbent. The hydrophobicity of sorbent behaved a significant part in the sorption process (23). Under hydrophobic conditions, the diffusion rates through the liquid film and pore could be accelerated to achieve adsorption equilibrium (section "Effect of contact time"). Hence, high carotenoid removal and rapid adsorptive rates could be accomplished during the disposal of colorants in refined camellia oil.

X-ray diffraction analysis

The crystallinities of CS, CSH, and CSHAC were examined using XRD spectroscopy in the range of 5–80°. The results were shown in Figure 3H. Remarkably, the XRD patterns of the samples after one- and two-step processing exhibited XRD patterns similar to those of the raw material, indicating that their natural structure was preserved. Two broad peaks centered at approximately $2\theta = 23°$ and 43° corresponded to the diffraction

peaks of the (002) and (100) planes of the amorphous carbon material (24). The absence of a sharp peak from the pattern further signified that the activated carbon had a lower degree of graphitisation; at such a temperature, the graphitic structure had not developed (25). Compared the XRD patterns of CSHAC with CSH, it was distinct that the diffraction at (002) was less broad, which meant a higher degree of graphitisation. This might be the result of a complete reaction between H_3PO_4 and CSH at a high carbonization temperature. These results indicated that the characteristics of the high specific surface area and microporous structure of the adsorbent were closely related to the orientation of the graphite layer and the expansion and distribution of the carbon lattice (26).

Raman analysis

Raman analysis of carbon exhibited a further comprehension of the structural defects on the surface of the materials. **Figure 3I** depicted the results of the Raman analysis of the CSH and CSHAC samples. The Raman spectra for CSH showed two well-defined peaks at 1,383 cm $^{-1}$ (D peak) and 1,588 cm^{-1} (G peak), respectively (27). The peak at around 2,500–3,200 cm^{-1} was due to the existence of either the –OH group of carboxylic acid or disordered substances (28). The D peak indicated disorders in the graphitic structure of carbon materials, while the G peak represented the graphitic structure of carbon materials caused by the vibration of sp^2 hybrid carbon atoms in both rings and chains (29). The relative intensity ratio of the D peak to the G peak (ID/IG) was approximately 0.73. Furthermore, the Raman spectra of CSHAC exhibited an increased ID/IG ratio of 0.95, which obviously established the presence of more structural disorders in CSHAC. Acid treatment endowed CSHAC with more defective structures, and thus the increased number of active sites enhanced its adsorption capacity.

Fourier transform infrared spectrometer analysis

The FTIR spectra of CS, CSH, CSHAC, and CSHAC/carotenoids were depicted in **Figure 4C**. As the processing steps increased, the intensity of the absorption peak at 3,417 cm^{-1} decreased, which implied a decrease in the content of –OH (30). After the activation of CS at 600°C, the inter- and intra-molecular dehydration reactions of cellulose and hemi-cellulose were intense, and the hydroxyl group was released in the form of water. The higher the temperature, the more the hydroxyl groups were released, and the lower the intensity of their absorption peak in the infrared spectrum. The oxygen content decreased from 20.16 to 17.58% with the activation of the phosphoric acid solution (**Table 3**). This result was attributed to the dehydration of phosphoric acid, which could eliminate O and H from carbon. The $–CH_3$ and $–CH_2$ stretching vibrations of aliphatic hydrocarbons or cycloalkanes were observed near 2,933 cm^{-1} (31). The intensity of this absorption peak in the CSHAC spectrum was not significant when compared with that of CS, mainly because the sample underwent a demethylation reaction after activation at 600°C, producing H_2, CH_4, and C_2H_6 gases (32). The peak was found at 1,625 cm^{-1} (C=C stretching), which represented the possible aromatic skeleton in CSHAC and indicated that CSHAC had some hydrophobicity (20). This result was similar to the contact angle results (section "X-ray diffraction analysis"). The positions of C=C (shifted from 1,625 to 1,734 cm^{-1}) on CSHAC changed after carotenoid adsorption, which manifested that they might participate in carotenoid complexation. The 1,500–1,100 cm^{-1} bands were the absorption peaks of C-O-C, C-H, C-OH, and other stretching vibrations (33). The 1,039 cm^{-1} band corresponded to C-O stretching, and 977 cm^{-1} was the band between acid and carbon (33). This indicated that the P element doped into CSH might be combined with the C and O element. After the high-temperature treatment, some C-OH groups in the oil shell charcoal were broken, and the intensity of the absorption peaks was reduced. The results indicated that activation promoted the pyrolysis of $–CH_3$ and –OH, however, the oxygen-containing functional groups in the carbon materials were retained. The unsaturated aromatic units on carotenoids and the oxygen-containing functional groups on CSHAC exhibited significant electron absorption capacity and could be considered as π-electron acceptors, and hydroxyl and methyl groups could act as π-electron donors. The π–π interactions enhance the adsorption capacity of carotenoids on CSHAC.

X-ray photoelectron spectrometry analysis

The surface compositions of the CS, CSH, CSHAC, and CSHAC/carotenoids were analyzed using XPS. The results were shown in **Figure 4**. The survey spectra of all samples exhibited pronounced peaks of carbon and oxygen (**Figure 4F**). There were two other weak peaks at approximately 191.0 and 132.75 eV that were observed in the survey curves of both CSHAC and CSHAC/carotenoids, which corresponded to the binding energies of P2s and P2p spectra. These came from the H_3PO_4 activation process (20). The C1s spectra of CS and CSH were divided into three contributions: C-C/C=C, C-O, and C=O, whose predominant chemical states were C-C/C=C (**Figures 4A,D**) (34). Their percentages were ascertained on the strength of the depth profiles acquired using XPS. When compared with CS, CSH had a higher C-C/C=C content, indicating higher aromaticity. The O1s peak recorded for CS and CSH were split into two peaks at 532.75 (C-O/O-H) and 531.75 eV (C=O), respectively (**Figures 4B–E**) (14). The result of the O1s spectrum profile recorded for CSH suggested that the proportion of each component of CSH was different from that observed for CS due to reactions such as dehydration and decarboxylation.

The C1s spectra were recorded for CSHAC (**Figure 4G**). The peaks corresponded to C=O (289.02 eV), C-O/C-P (285.13 eV), and C-C/C=C (284.34 eV) of CSH, respectively (35). The presence of the peak at 284.34 eV (C-C/C=C) indicated

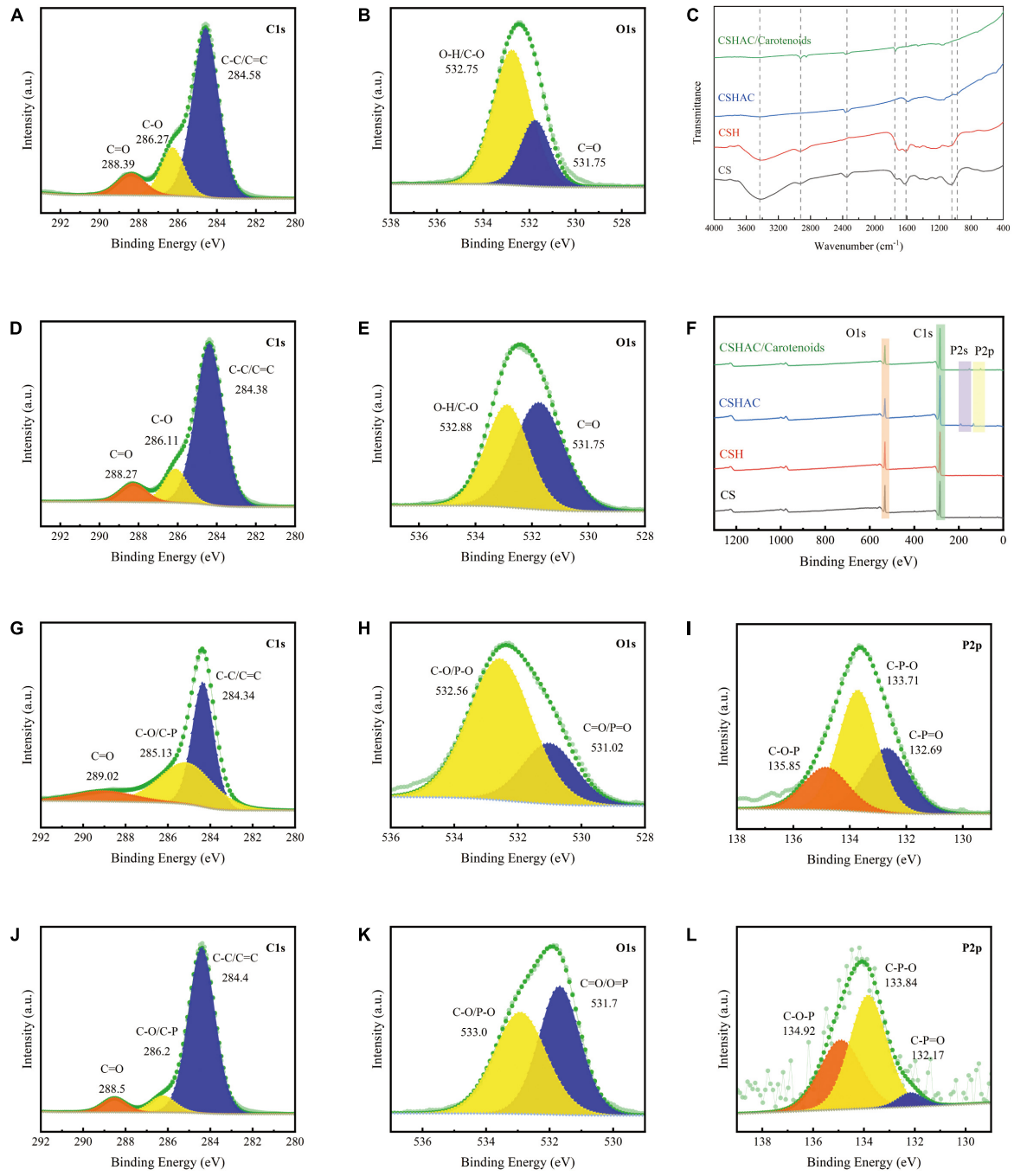

FIGURE 4
(A) C1s and **(B)** O1s spectra of CS. **(C)** FTIR spectra of CS, CSH, CSHAC, and CSHAC/carotenoids. **(D)** C1s and **(E)** O1s spectra of CSH. **(F)** XPS survey spectra of CS, CSH, CSHAC, and CSHAC/carotenoids. **(G)** C1s, **(H)** O1s, and **(I)** P2p spectra of CSHAC. **(J)** C1s, **(K)** O1s, and **(L)** P2p spectra of CSHAC/carotenoids.

that the CSHAC surface had a certain degree of aromatic structure. Theoretically, phosphoric acid activation of CSH led to oxidation and catalytic dehydration reactions, as confirmed by the increased molar percentages of C-O and C=O in the C1s spectra of CSHAC (Figures 4D,G). The O1s spectrum of CSHAC was depicted in Figure 4H. The peaks of C-O/P-O (532.56 eV) and C=O/P=O (531.06 eV) were ascribed to the CSH after acidification and carbonisation, respectively. As shown in Figure 4I, the P2p spectrum of CSHAC could be parsed into C-O-P, C-P-O, and C-P=O components at 135.85, 133.71, and 132.65 eV, respectively (36).

10.3389/fnut.2022.1058025

TABLE 2 Changes in chemical valence states changes of C, O, and P on CSHAC before and after carotenoid adsorption.

Samples	C1s (%)			O1s (%)		P2p (%)		
	C=C/C-C	C-O/C-P	C=O/O-C=O	C=O/P=O	C-O/C-P	C-P=O	C-P-O	C-O-P
CSHAC	49.03	40.00	10.97	26.5	73.5	30	50	20
CSHAC/carotenoids	85.6	8.0	6.4	53.17	46.83	4.5	56.6	38.9

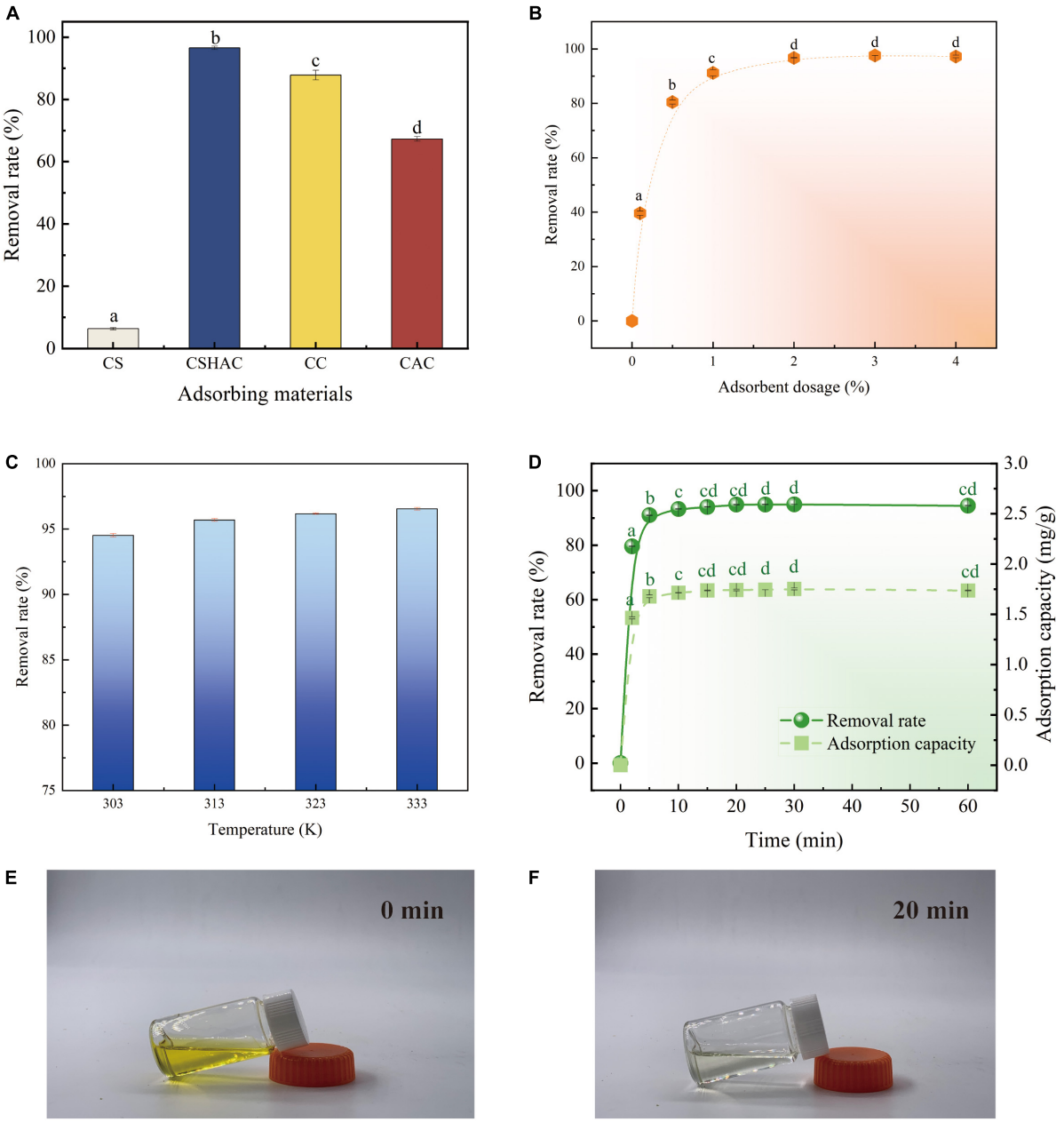

FIGURE 5
(A) Variations in carotenoid removal efficiency using various adsorbents and commercial decolorizers (adsorbent dosage is 2%; temperature is 333 K; time is 20 min). **(B)** Effect of CSHAC on carotenoid removal. **(C)** The carotenoid removal efficiency of CSHAC at adsorption equilibrium and different temperatures. **(D)** Contact time versus adsorption capacity and removal rate of CSHAC for carotenoids. **(E,F)** Photographs of refined camellia oil before and after adsorption for 20 min by CSHAC. Each value manifests the mean ± standard deviation of triplicate determinations and the mean values with diverse letters (a–d) differ significantly ($P < 0.05$).

The C1s spectrum recorded for CSHAC/carotenoids was depicted in Figure 4J. Compared with CSHAC, the C-C/C=C content of CSHAC/carotenoids increased after carotenoid adsorption owing to the carotenoids attached to the CSHAC surface. Consistent with the above FTIR analysis, π–π interactions promoted the adsorption of carotenoids. The result of the O1s spectrum recorded for CSHAC/carotenoids (Figure 4K) indicated that the ratio and binding energies of each component of CSHAC/carotenoids differed from those of CSHAC (Figure 4H). Evidently, the C-O content was reduced after carotenoid adsorption, which indicated that it participated in carotenoid complexation. Compared the P2p spectra of CSHAC (Figure 4I) with CSHAC/carotenoids (Figure 4L). A slight shift was observed in all three peaks, which was attributed to the reaction between the adsorbent and adsorbate during adsorption. The results of the relative contents of functional groups were listed in Table 2. After carotenoid adsorption, the molar percentage of C-P=O (relative to the total P) evidently decreased from 30 to 4.5%. In contrast, the molar percentage of C-P-O increased from 50 to 56.6%. This indicated that the C-P=O group served as an active component for carotenoid adsorption and transformed into the C-P-O group (35). Therefore, the enhanced functional groups and aromatic structure could facilitate the adsorption of carotenoids and improve the decolorization efficiency of camellia oil by CS-based modified activated carbon.

Adsorption performance

Effect of sorbent material

By comparing CSH, CSHAC, CC, and CAC (Figure 5A), the carotenoid removal rate of CSHAC (96.5%) was the highest among the materials tested in the same conditions. The high specific surface area and three-dimensional pore structure of CSHAC exhibited high adsorption efficiency. The carotenoid removal efficiencies of commercial decolorization agents CC and CAC were 87 and 67%, respectively, highlighting the excellent adsorption effect of CSHAC. Hence, we concentrated on CSHAC and chose it as the best decolorization adsorbent for refined camellia oil.

Effect of CSHAC dosage

Figure 5B exhibited the effect of the CSHAC dosage on carotenoid adsorption performance. As the dosage of CSHAC increased from 0.01 to 2% (w/w), the carotenoid adsorption efficiency increased, reaching a plateau when the concentration of CSHAC exceeded 2%. The initial sharp increase was due to the augment in the specific surface area and abundant activation sites for carotenoid adsorption. The optimal CSHAC dose at which optimum carotenoid removal efficiency was achieved was 2%. Further experiments proceeded under these conditions. Moreover, it was evident from the data in Table 3 that peroxide and free fatty acids were removed using CSHAC. Therefore, the porous structure of the CS adsorbent might be effective for refining oil.

Effect of temperature

High carotenoid adsorption efficiency on CSHAC was achieved at high temperatures (Figure 5C). Adsorption was an endothermic process. The increase in temperature facilitated the oxidation and movement of carotenoid molecules in solution. The carotenoid removal efficiency increased when the temperature at 303–333 K.

The thermodynamic parameters were used for describing the thermodynamic behavior of carotenoid removal on CSHAC. Enthalpy (ΔH, kJ/mol), entropy [ΔS, kJ/(mol K)], and Gibbs free energy (ΔG, kJ/mol) were calculated as follows (37):

$$K = \frac{q_e}{C_e} \tag{4}$$

$$\ln K = \frac{-\Delta H}{RT} + \frac{\Delta S}{R} \tag{5}$$

$$\Delta G = -RT \ln K \tag{6}$$

where K is a constant, T (K) is the absolute temperature, and R [8.314 J/(mol·K)] is the universal gas constant.

Table 4 showed the parameters of thermodynamics. A positive value of ΔH manifested the endothermic nature of the carotenoid adsorption (38). The value of ΔS was positive, which confirmed an increase in disorder at the solid-solution interface (39). The value of ΔG was negative at the four temperatures, which indicated that carotenoid adsorption onto CSHAC was spontaneous (40).

Effect of contact time

An ultrafast adsorption rate was fulfilled on CSHAC, and the kinetic equilibrium could be accomplished rapidly

TABLE 3 Amounts of free fatty acid and peroxide value in camellia oil samples bleached with 2% CSHAC.

Treatment	Free fatty acid (mg/g)	Peroxide value (g/100 g)
Refined camellia oil	0.92 ± 0.0018	0.32 ± 0.0034
Bleaching camellia oil	0.76 ± 0.0064	0.24 ± 0.0005

Values were expressed as means ± standard deviation.

TABLE 4 Thermodynamic parameters for adsorption of carotenoids on CSHAC (CSHAC dosage, 2%).

Temperature (K)	ΔH (kJ/mol)	ΔS [J/(mol·K)]	ΔG (kJ/mol)
303	11.879875	39.40836	−3.506539
313			−535.9501
323			−879.929
333			−1193.325

(20 min) in refined camellia oil (Figure 5D). The ultrafast adsorption efficiency of CSHAC could be ascribed to three causes. (i) CSHAC (Figures 5E,F) manifested a morphology consisting of mesoporous, which facilitated the diffusion rate of adsorbate molecules. (ii) Abundant active groups (aromatic rings and oxygen functional groups) exposed on the surface of CSHAC could π−π conjugate with carotenoids, causing rapid adsorption. (iii) Hydrophobicity as one of the properties of CSHAC mainly contributed to an increase in the diffusion rate of carotenoids in the liquid membrane and pores of CSHAC, i.e., it greatly reduced the time for adsorption equilibrium.

Adsorption kinetics

The kinetic behavior of carotenoid adsorption onto CSHAC was further simulated by using kinetic models: pseudo-first-order (PFO) kinetic and pseudo-second-order (PSO) kinetic models were given as Eqs 7 and 8, respectively. And the linear equation of intra-particle diffusion (IPD) was given by Eq. 9 (41). q_e and q_t are the adsorption capacities (mg/g) of CSHAC at equilibrium and time t, respectively; k_1 (L/min), k_2 (g/mg min), and k_d (mg/g $min^{0.5}$) refer to rate constants; and C is a constant.

$$\ln\left(q_e - q_t\right) = lnq_e - k_1 \cdot t \tag{7}$$

$$\frac{t}{q_t} = \frac{1}{k_2 \cdot q_e^2} + \frac{t}{q_e} \tag{8}$$

$$q_t = k_d \cdot t^{0.5} + C \tag{9}$$

Figure 6 exhibited the experimental data fitted using the PFO, PSO, and IPD models. As is evident from the corresponding adsorption kinetics fitting parameters in

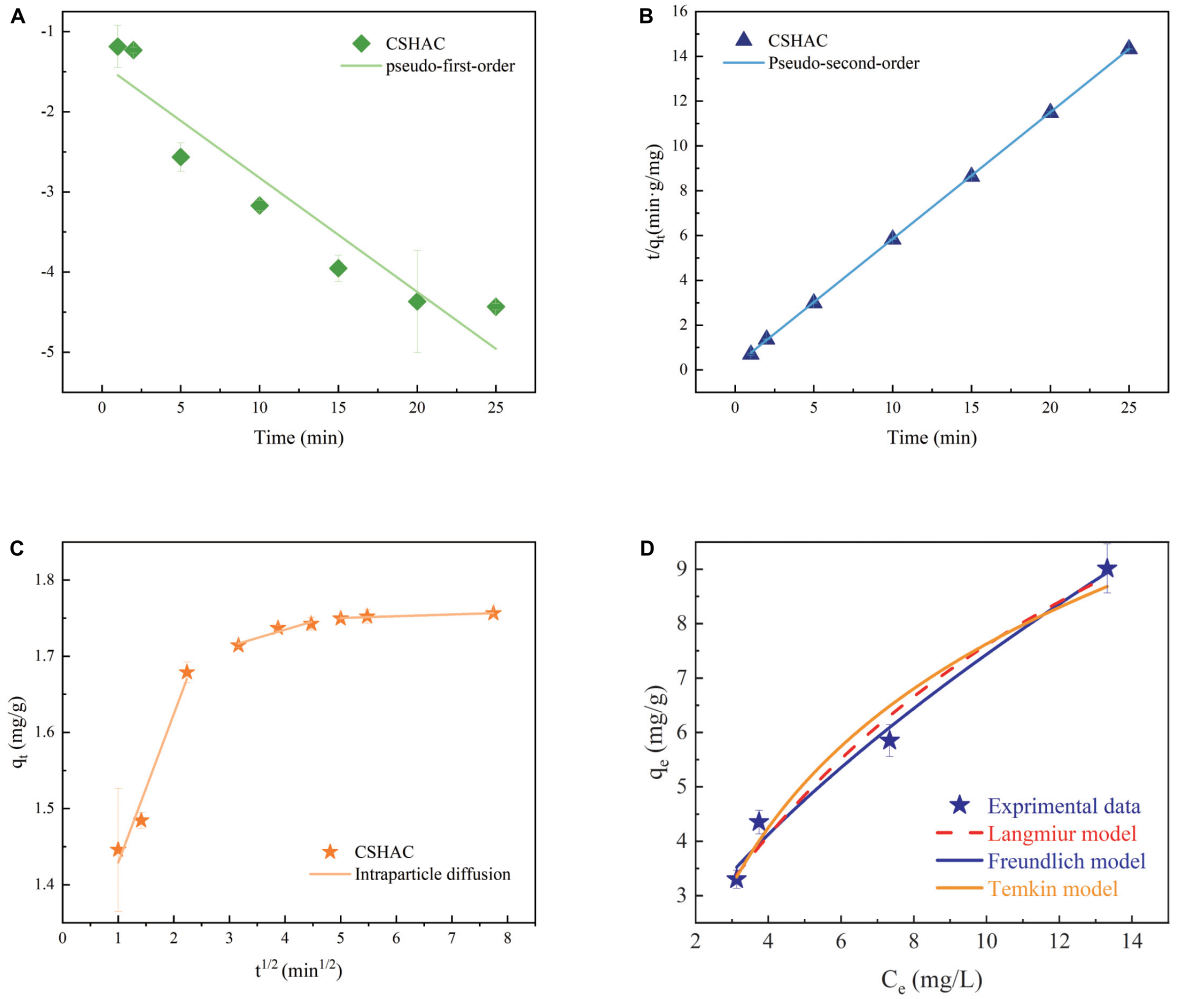

FIGURE 6
Kinetics model for adsorption of carotenoids. **(A)** PFO kinetics, **(B)** PSO kinetics, and **(C)** IPD. **(D)** Langmuir, Freundlich, and Temkin model descriptions of carotenoid adsorption onto CSHAC (CSHAC dosage, 2%; temperature, 333 K).

TABLE 5 Kinetic models parameters for carotenoid adsorption on CSHAC.

PFO kinetic model			PSO kinetic model			IPD model					
$q_{e,cal}$ (mg/g)	k_1 (L/min)	R^2	$q_{e,cal}$ (mg/g)	k_2 [g/(mg·min)]	R^2	k_{d1} [mg/(g·min$^{0.5}$)]	$R_1{}^2$	k_{d2} [mg/(g·min$^{0.5}$)]	$R_2{}^2$	k_{d3} [mg/(g·min$^{0.5}$)]	$R_3{}^2$
0.24	0.1381	0.9336	1.77	1.5803	0.9999	0.1952	0.9675	0.0218	0.9156	0.0023	0.9416

Table 5, the PSO kinetics adsorption model exhibited a higher correlation coefficient value (R^2) during the fitting of the carotenoid adsorption experimental data of CSHAC. Figure 6 also suggested that the theoretical adsorption capacity value fitted by the PSO model was closer to the experimental data of q_e. Hence, carotenoid adsorption on CSHAC might be a chemical adsorption rate-controlling step (42). And the IPD model showed that the adsorption process had three stages, as shown in Figure 6. The first fitting stage indicated the spread of adsorbate molecules through the liquid film around the CSHAC and the outer adsorption on the sorbent surface. The second portion referred to the penetration of the adsorbate into the interlayer of the adsorbent. Finally, the plateau portion was ascribed to the equilibrium stage. In this work, the result of no plot passed the origin, manifesting that although the adsorption process contained IPD, it was not the only rate-limiting step (43). Therefore, carotenoid adsorption on CSHAC was affected in two manners: chemical adsorption and IPD.

Adsorption isotherms

The assessment of the adsorption isotherms is fundamental to depict the connection between the equilibrium adsorption capacity for carotenoids onto CSHAC and the remaining concentration of carotenoids at a fixed temperature. In order to understand the behavior of an adsorptive system, adsorption isotherm studies are necessary (32).

To simulate the monolayer adsorption behavior by using the Langmuir isotherm model (Eq. 10) (44):

$$q_e = \frac{q_m k_L C_e}{1 + k_L C_e} \tag{10}$$

TABLE 6 The adsorption isotherm model parameters of the Langmuir, Freundlich, and Temkin models for carotenoid adsorption on CSHAC (CSHAC dosage, 2%).

Model	Parameters	Evaluation			
		R^2	$AdjR^2$	χ^2	SSE
Langmuir model	q_m = 17.63 mg/g; k_L = 0.08 L/mg	0.9762	0.9642	0.22	0.44
Freundlich model	k_F = 1.69 mg/g; n = 1.56	0.9853	0.9779	0.14	0.27
Temkin model	a_T = 0.79 L/mg; b_T = 751.38	0.9657	0.9485	0.32	0.64

where q_e (mg/g) and q_m (mg/g) are the equilibrium and maximum adsorption capacity of CSHAC for carotenoids, respectively. k_L (L/mg) is the adsorption constant of the Langmuir isotherm model.

To illustrate multilayer (≥ 2 layers) adsorption behavior by using the Freundlich isotherm model (Eq. 11) (45):

$$q_e = k_F C_e^{\frac{1}{n}} \tag{11}$$

where k_F (mg/g) is the Freundlich model constant. n is a constant used for evaluating the intensity of the interaction between CSHAC and carotenoids.

The Temkin isotherm model suggests that the adsorption heat decreases linearly rather than logarithmically with the adsorption capacity. This model is appropriate for adsorption with a heterogeneous surface and strong interaction between the adsorbate and adsorbent. This model can be described by Eq. 12 (38):

$$q_e = \frac{RT}{b_T} ln\,(a_T C_e) \tag{12}$$

where a_T (L/g) and b_T are the Temkin constants.

In order to evaluate the fitness of the models more comprehensively, the adjusted correlation coefficient ($adjR^2$), chi-square (χ^2), and residual sum of squares (SSE) were used to

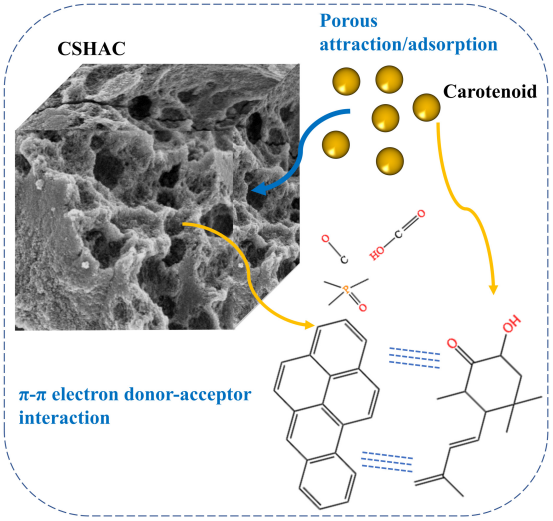

FIGURE 7
Proposed mechanisms for carotenoid adsorption on CSHAC.

consider the influence of the number of parameters of various models by Eqs 13–15:

$$adjR^2 = 1 - \frac{\sum_{i=1}^{n}\left(q_{exp,i} - q_{cal,i}\right)^2}{\sum_{i=1}^{n}\left(q_{exp,i} - q_{mean}\right)^2} \cdot \frac{(N-1)}{(N-P)} \quad (13)$$

$$\chi 2 = \sum_{i=1}^{n} \frac{\left(q_{exp,i} - q_{cal,i}\right)^2}{q_{cal,i}} \quad (14)$$

$$SSE = \sum_{i=1}^{n}\left(q_{exp,i} - q_{cal,i}\right)^2 \quad (15)$$

The adsorption isotherm experiment of CSHAC on adsorbing carotenoids with various concentrations of CSHAC (0.25, 0.5, 0.75, and 1%) at 333 K. As depicted in **Figure 6D**, Langmuir, Freundlich, and Temkin isotherm models were used to fit the experimental data. The corresponding parameters were listed in **Table 6**. The correlation coefficients, such as $adjR^2$, χ^2, and *SSE* values (**Table 6**) indicated that the adsorption of carotenoids onto CSHAC could be more accurately using the Freundlich model than the other models. Thus, the results manifested that the adsorption of carotenoids by CSHAC was a surface multilayer process (46). The result of $0 < 1/n < 1$, after fitting using the Freundlich model, further indicated that carotenoids were easily adsorbed by CSHAC. For the Temkin model, the fitting results were reasonable, manifesting high correlation coefficients. It could be concluded that there were strong π–π electron-donor-acceptor interactions between CSHAC and carotenoid molecules (47).

Proposed adsorption mechanism

Adsorption mechanisms (**Figure 7**) were proposed according to the structural characteristics of CSHAC and carotenoids depicted in available studies (48, 49) and the results reported herein. XPS results indicated that the presence of C=C, C-O, C-P=O, and O-C=O groups on the CSHAC surface was likely to facilitate the uptake of carotenoids. Owing to the structural characteristics of carotenoid molecules, they were prone to π–π interactions with CSHAC during adsorption. In addition, carotenoids were adsorbed onto the inner structure of IPD. The role of the inner structure was to pre-adsorb and increase the surface area and pore volume to provide more active sites. In summary, the superior adsorption performance of CSHAC was mainly ascribed to the number of C-, O-, and P-containing functional groups and its exceedingly high pore volume.

Conclusion

In this study, p-doped activated carbon (CSHAC) was successfully produced using a simple method and used for efficient adsorption of carotenoids from refined camellia oil. The results showed that CSHAC had a better adsorption capacity for carotenoids than those of existing commercial decolorizers. This remarkable performance of CSHAC was ascribed to its stereoscopic structure with massive micropores and mesopores and the richness of active sites. The adsorption process of CSHAC was primarily dominated by chemical adsorption, with C=C, C-P=O, C=O, and O-C=O groups as active components, and the mechanism might be the π–π interactions between carotenoids and CSHAC. Pore filling facilitated the physical adsorption of carotenoids by CSHAC. Therefore, CSHAC has the potential to substitute commercial adsorbents for decolorization of camellia oil.

Data availability statement

The original contributions presented in this study are included in the article/supplementary material, further inquiries can be directed to the corresponding author.

Author contributions

RT, YL, DC, LG, and ND performed the experiments. RT analyzed the data and wrote the original manuscript. JY and DH revised the manuscript. HL, WL, and KL conceived and designed the experiments. All authors reviewed the manuscript and approved the submitted version.

Funding

This research was funded by the China Agriculture Research System of MOF and MARA.

Conflict of interest

The authors declare that the research was conducted in the absence of any commercial or financial relationships that could be construed as a potential conflict of interest.

Publisher's note

All claims expressed in this article are solely those of the authors and do not necessarily represent those of their affiliated organizations, or those of the publisher, the editors and the reviewers. Any product that may be evaluated in this article, or claim that may be made by its manufacturer, is not guaranteed or endorsed by the publisher.

References

1. Yang R, Zhang L, Li P, Yu L, Mao J, Wang X, et al. A review of chemical composition and nutritional properties of minor vegetable oils in China. *Trends Food Sci Technol.* (2018) 74:26–32. doi: 10.1016/j.tifs.2018.01.013

2. Zeb A, Murkovic M. Determination of thermal oxidation and oxidation products of β-carotene in corn oil triacylglycerols. *Food Res Int.* (2013) 50:534–44. doi: 10.1016/j.foodres.2011.02.039

3. Seçilmiş ŞS, Yanık DK, Fadiloğlu S, Göğüş F. A comparative study on performance of industrial and microwave techniques for sunflower oil bleaching process. *Food Chem.* (2021) 365:130488. doi: 10.1016/j.foodchem.2021.130488

4. Abdi E, Gharachorloo M, Ghavami M. Investigation of using egg shell powder for bleaching of soybean oil. *LWT.* (2021) 140:110859. doi: 10.1016/j.lwt.2021.110859

5. Sun Y, Shi X-L, Yang Y-L, Suo G, Zhang L, Lu S, et al. Biomass-derived carbon for high-performance batteries: from structure to properties. *Adv Funct Mater.* (2022) 32:2201584. doi: 10.1002/adfm.202201584

6. Shen M, Song W, Shi X, Wang S, Wang H, Liu J, et al. New insights into physicochemical properties of different particulate size-fractions and dissolved organic matter derived from biochars and their sorption capacity for phenanthrene. *J Hazard Mater.* (2022) 434:128867. doi: 10.1016/j.jhazmat.2022.128867

7. Xu S, Wen L, Yu C, Li S, Tang J. Activation of peroxymonosulfate by MnFe2O4@BC composite for bisphenol A degradation: the coexisting of free-radical and non-radical pathways. *Chem Eng J.* (2022) 442:136250. doi: 10.1016/j.cej.2022.136250

8. Fu Q, Xu X, Miao R, Wang M, Zhou H, He L, et al. Mn-embedded porous rubber seed shell biochar for enhanced removal of copper ions and catalytic efficacy of the used adsorbent for hydrogenation of furfural. *Chem Eng J.* (2022) 441:136065. doi: 10.1016/j.cej.2022.136065

9. Qu S, Yuan Y, Yang X, Xu H, Mohamed AK, Zhang J, et al. Carbon defects in biochar facilitated nitrogen doping: the significant role of pyridinic nitrogen in peroxymonosulfate activation and ciprofloxacin degradation. *Chem Eng J.* (2022) 441:135864. doi: 10.1016/j.cej.2022.135864

10. Lachos-Perez D, Torres-Mayanga PC, Abaide ER, Zabot GL, De Castilhos F. Hydrothermal carbonization and liquefaction: differences, progress, challenges, and opportunities. *Bioresour Technol.* (2022) 343:126084. doi: 10.1016/j.biortech.2021.126084

11. Fang J, Zhan L, Ok YS, Gao B. Minireview of potential applications of hydrochar derived from hydrothermal carbonization of biomass. *J Ind Eng Chem.* (2018) 57:15–21. doi: 10.1016/j.jiec.2017.08.026

12. Hambly AJ, van Duijneveldt JS, Gates PJ. Identification of β-carotene oxidation products produced by bleaching clay using UPLC-ESI-MS/MS. *Food Chem.* (2021) 353:129455. doi: 10.1016/j.foodchem.2021.129455

13. Fan Y, Wang H, Deng L, Wang Y, Kang D, Li C, et al. Enhanced adsorption of Pb(II) by nitrogen and phosphorus co-doped biochar derived from *Camellia oleifera* shells. *Environ Res.* (2020) 191:110030. doi: 10.1016/j.envres.2020.110030

14. Foletto EL, Paz DS, Gündel A. Acid-activation assisted by microwave of a Brazilian bentonite and its activity in the bleaching of soybean oil. *Appl Clay Sci.* (2013) 83–84:63–7. doi: 10.1016/j.clay.2013.08.017

15. Babayemi AK, Onukwuli OD, Eluno EE, Otolorin JA. Optimizing process parameters of palm oil bleaching on locally prepared animal bone–based activated carbon using response surface methodology. *Environ Qual Manag.* (2021) 30:43–51. doi: 10.1002/tqem.21729

16. Igansi A, Engelmann J, Lutke SF, Porto FB, Pinto LAA, Cadaval TRS Jr. Isotherms, kinetics, and thermodynamic studies for adsorption of pigments and oxidation products in oil bleaching from catfish waste. *Chem Eng Commun.* (2019) 206:1410–24. doi: 10.1080/00986445.2018.1539965

17. Abdullah RF, Rashid U, Hazmi B, Ibrahim ML, Tsubota T, Alharthi FA. Potential heterogeneous nano-catalyst via integrating hydrothermal carbonization for biodiesel production using waste cooking oil. *Chemosphere.* (2022) 286:131913. doi: 10.1016/j.chemosphere.2021.131913

18. Fan X, Wu Y, Tu R, Sun Y, Jiang E, Xu X. Hydrodeoxygenation of guaiacol via rice husk char supported Ni based catalysts: the influence of char supports. *Renew Energy.* (2020) 157:1035–45. doi: 10.1016/j.renene.2020.05.045

19. Thommes M, Kaneko K, Neimark AV, Olivier JP, Rodriguez-Reinoso F, Rouquerol J, et al. Physisorption of gases, with special reference to the evaluation of surface area and pore size distribution (IUPAC technical report). *Pure Appl Chem.* (2015) 87:1051–69. doi: 10.1515/pac-2014-1117

20. Ozpinar P, Dogan C, Demiral H, Morali U, Erol S, Samdan C, et al. Activated carbons prepared from hazelnut shell waste by phosphoric acid activation for supercapacitor electrode applications and comprehensive electrochemical analysis. *Renew Energy.* (2022) 189:535–48. doi: 10.1016/j.renene.2022.02.126

21. Zhao H, Lu X, Wang Y, Sun B, Wu X, Lu H. Effects of additives on sucrose-derived activated carbon microspheres synthesized by hydrothermal carbonization. *J Mater Sci.* (2017) 52:10787–99. doi: 10.1007/s10853-017-1258-4

22. Wang J, Guo X. Adsorption kinetic models: physical meanings, applications, and solving methods. *J Hazard Mater.* (2020) 390:122156. doi: 10.1016/j.jhazmat.2020.122156

23. Sun Y, Liu R, Wen S, Wang J, Chen L, Yan B, et al. Antibiofouling Ultrathin Poly(amidoxime) Membrane for Enhanced U(VI) recovery from wastewater and seawater. *ACS Appl Mater Interfaces.* (2021) 13:21272–85. doi: 10.1021/acsami.1c02882

24. Chen S, Guo Y, Zhang J, Guo Y, Liang X. CuFe2O4/activated carbon adsorbents enhance H2S adsorption and catalytic oxidation from humidified air at room temperature. *Chem Eng J.* (2022) 431:134097. doi: 10.1016/j.cej.2021.134097

25. Suhas, Gupta VK, Singh LP, Chaudhary M, Kushwaha S. A novel approach to develop activated carbon by an ingenious hydrothermal treatment methodology using *Phyllanthus emblica* fruit stone. *J Clean Prod.* (2021) 288:125643. doi: 10.1016/j.jclepro.2020.125643

26. Serafin J, Baca M, Biegun M, Mijowska E, Kaleńczuk RJ, Sreńscek-Nazzal J, et al. Direct conversion of biomass to nanoporous activated biocarbons for high CO2 adsorption and supercapacitor applications. *Appl Surf Sci.* (2019) 497:143722. doi: 10.1016/j.apsusc.2019.143722

27. Lazzarini A, Piovano A, Pellegrini R, Leofanti G, Agostini G, Rudić S, et al. A comprehensive approach to investigate the structural and surface properties of activated carbons and related Pd-based catalysts. *Catal Sci Technol.* (2016) 6:4910–22. doi: 10.1039/C6CY00159A

28. Sylla NF, Ndiaye NM, Ngom BD, Momodu D, Madito MJ, Mutuma BK, et al. Effect of porosity enhancing agents on the electrochemical performance of high-energy ultracapacitor electrodes derived from peanut shell waste. *Sci Rep.* (2019) 9:13673. doi: 10.1038/s41598-019-50189-x

29. Bharath G, Rambabu K, Banat F, Hai A, Arangadi AF, Ponpandian N. Enhanced electrochemical performances of peanut shell derived activated carbon and its Fe3O4 nanocomposites for capacitive deionization of Cr(VI) ions. *Sci Total Environ.* (2019) 691:713–26. doi: 10.1016/j.scitotenv.2019.07.069

30. Zhang X, Lv L, Qin Y, Xu M, Jia X, Chen Z. Removal of aqueous Cr(VI) by a magnetic biochar derived from Melia azedarach wood. *Bioresour Technol.* (2018) 256:1–10. doi: 10.1016/j.biortech.2018.01.145

31. Wei M, Marrakchi F, Yuan C, Cheng X, Jiang D, Zafar FF, et al. Adsorption modeling, thermodynamics, and DFT simulation of tetracycline onto mesoporous and high-surface-area NaOH-activated macroalgae carbon. *J Hazard Mater.* (2022) 425:127887. doi: 10.1016/j.jhazmat.2021.127887

32. Zeng H, Zeng H, Zhang H, Shahab A, Zhang K, Lu Y, et al. Efficient adsorption of Cr (VI) from aqueous environments by phosphoric acid activated eucalyptus biochar. *J Clean Prod.* (2021) 286:124964. doi: 10.1016/j.jclepro.2020.124964

33. Yakout SM, El-Deen GS. Characterization of activated carbon prepared by phosphoric acid activation of olive stones. *Arab J Chem.* (2016) 9:S1155–62. doi: 10.1016/j.arabjc.2011.12.002

34. Zhang B, Xu P, Qiu Y, Yu Q, Ma J, Wu H, et al. Increasing oxygen functional groups of activated carbon with non-thermal plasma to enhance mercury removal efficiency for flue gases. *Chem Eng J.* (2015) 263:1–8. doi: 10.1016/j.cej.2014.10.090

35. Zhou M, Xu Y, Luo G, Zhang Q, Du L, Cui X, et al. Facile synthesis of phosphorus-doped porous biochars for efficient removal of elemental mercury from coal combustion flue gas. *Chem Eng J.* (2022) 432:134440. doi: 10.1016/j.cej.2021.134440

36. Chen S, Wang J, Wu Z, Deng Q, Tu W, Dai G, et al. Enhanced Cr(VI) removal by polyethylenimine- and phosphorus-codoped hierarchical porous carbons. *J Colloid Interface Sci.* (2018) 523:110–20. doi: 10.1016/j.jcis.2018.03.057

37. Qu J, Wang Y, Tian X, Jiang Z, Deng F, Tao Y, et al. KOH-activated porous biochar with high specific surface area for adsorptive removal of chromium (VI) and naphthalene from water: affecting factors, mechanisms and reusability exploration. *J Hazard Mater.* (2021) 401:123292. doi: 10.1016/j.jhazmat.2020.123292

38. Jung K-W, Lee SY, Choi J-W, Lee YJ. A facile one-pot hydrothermal synthesis of hydroxyapatite/biochar nanocomposites: adsorption behavior and mechanisms for the removal of copper(II) from aqueous media. *Chem Eng J.* (2019) 369:529–41. doi: 10.1016/j.cej.2019.03.102

39. Wang C, Lin G, Zhao J, Wang S, Zhang L, Xi Y, et al. Highly selective recovery of Au(III) from wastewater by thioctic acid modified Zr-MOF: experiment and DFT calculation. *Chem Eng J.* (2020) 380:122511. doi: 10.1016/j.cej.2019.122511

40. Alqadami AA, Naushad M, ALOthman ZA, Alsuhybani M, Algamdi M. Excellent adsorptive performance of a new nanocomposite for removal of toxic Pb(II) from aqueous environment: adsorption mechanism and modeling analysis. *J Hazard Mater.* (2020) 389:121896. doi: 10.1016/j.jhazmat.2019.121896

41. Wu F-C, Tseng R-L, Juang R-S. Initial behavior of intraparticle diffusion model used in the description of adsorption kinetics. *Chem Eng J.* (2009) 153:1–8. doi: 10.1016/j.cej.2009.04.042

42. Reçber ZB, Burhan H, Bayat R, Nas MS, Calimli MH, Demirbas O, et al. Fabrication of activated carbon supported modified with bimetallic-platin ruthenium nano sorbent for removal of azo dye from aqueous media using enhanced ultrasonic wave. *Environ Pollut.* (2022) 302:119033. doi: 10.1016/j.envpol.2022.119033

43. Xie R, Zhou L, Smith AE, Almquist CB, Berberich JA, Danielson ND. A dual grafted fluorinated hydrocarbon amine weak anion exchange resin polymer for adsorption of perfluorooctanoic acid from water. *J Hazard Mater.* (2022) 431:128521. doi: 10.1016/j.jhazmat.2022.128521

44. Jung K-W, Lee SY, Lee YJ. Facile one-pot hydrothermal synthesis of cubic spinel-type manganese ferrite/biochar composites for environmental remediation of heavy metals from aqueous solutions. *Bioresour Technol.* (2018) 261:1–9. doi: 10.1016/j.biortech.2018.04.003

45. Xue H, Wang X, Xu Q, Dhaouadi F, Sellaoui L, Seliem MK, et al. Adsorption of methylene blue from aqueous solution on activated carbons and composite prepared from an agricultural waste biomass: a comparative study by experimental and advanced modeling analysis. *Chem Eng J.* (2022) 430:132801. doi: 10.1016/j.cej.2021.132801

46. Ye Z-L, Deng Y, Lou Y, Ye X, Zhang J, Chen S. Adsorption behavior of tetracyclines by struvite particles in the process of phosphorus recovery from synthetic swine wastewater. *Chem Eng J.* (2017) 313:1633–8. doi: 10.1016/j.cej.2016.11.062

47. Song Q, Liang J, Fang Y, Cao C, Liu Z, Li L, et al. Selective adsorption behavior/mechanism of antibiotic contaminants on novel boron nitride bundles. *J Hazard Mater.* (2019) 364:654–62. doi: 10.1016/j.jhazmat.2018.10.054

48. Chetima A, Wahabou A, Zomegni G, Rahman AN, Bup DN. Bleaching of neutral cotton seed oil using organic activated carbon in a batch system: kinetics and adsorption isotherms. *Processes.* (2018) 6:22. doi: 10.3390/pr6030022

49. Pohndorf RS, Cadaval TRS, Pinto LAA. Kinetics and thermodynamics adsorption of carotenoids and chlorophylls in rice bran oil bleaching. *J Food Eng.* (2016) 185:9–16. doi: 10.1016/j.jfoodeng.2016.03.028

frontiers | Frontiers in Nutrition

TYPE Original Research
PUBLISHED 07 December 2022
DOI 10.3389/fnut.2022.1064812

OPEN ACCESS

EDITED BY
Mehanathan Muthamilarasan,
University of Hyderabad, India

REVIEWED BY
Pavan Kumar,
Guru Angad Dev Veterinary and Animal Sciences University, India
Amene Nematollahi,
Fasa University of Medical Sciences, Iran

*CORRESPONDENCE
Yanyan Huang
huang_yanyan@fosu.edu.cn
Xin-An Zeng
xazeng@scut.edu.cn

SPECIALTY SECTION
This article was submitted to Nutrition and Food Science Technology, a section of the journal Frontiers in Nutrition

RECEIVED 08 October 2022
ACCEPTED 23 November 2022
PUBLISHED 07 December 2022

CITATION
Wang L-H, Li Z, Qin J, Huang Y, Zeng X-A and Aadil RM (2022) Investigation on the impact of quality characteristics and storage stability of foxtail millet induced by air cold plasma.
Front. Nutr. 9:1064812.
doi: 10.3389/fnut.2022.1064812

Investigation on the impact of quality characteristics and storage stability of foxtail millet induced by air cold plasma

Lang-Hong Wang[1,2,3], Zhongyan Li[2], Jiale Qin[2], Yanyan Huang[1]*, Xin-An Zeng[1,3]* and Rana Muhammad Aadil[4]

[1]Guangdong Provincial Key Laboratory of Intelligent Food Manufacturing, School of Food Science and Engineering, Foshan University, Foshan, China, [2]College of Food Science and Technology, Northwest University, Xi'an, China, [3]School of Food Science and Engineering, South China University of Technology, Guangzhou, China, [4]National Institute of Food Science and Technology, University of Agriculture, Faisalabad, Pakistan

The aim of this work was to investigate the effects of dielectric barrier discharge-air cold plasma (DBD-ACP, 15–35 kV, 2–12 min) on the quality of foxtail millets. The *L* and *b** values were evaluated by a digital colorimeter representing that the color of millets was significantly changed at 25 kV for 4–12 min or at 35 kV for 2–12 min. The results were consistent with the change of total yellow pigment in millets, indicating that DBD-ACP damaged the carotenoids if the treatment condition was too high. The activity of lipoxygenase and lipase, involving the oxidation and hydrolysis of lipids of millet, decreased significantly induced by DBD-ACP. For example, the lipoxygenase and lipase activity of Mizhi millet was decreased from 44.0 to 18.7 U $g^{-1}min^{-1}$, 56.0–15.1 U/(mg pro) ($p<0.05$) after being exposed to 25 kV for 2–12 min, respectively. Changes of color, lipoxygenase and lipase activity, and malondialdehyde content of millets were determined during accelerated storage (40 ± 2°C and 75% Relative Humidity) for 15 days after being treated by DBD-ACP under 15 and 25 kV for 4 min. Results showed that millets treated by DBD-ACP at 15 kV kept a better color with lower malondialdehyde content, and lower lipoxygenase and lipase activity compared to control. This work implied that DBD-ACP is an underlying approach for the storage of foxtail millets.

KEYWORDS

foxtail millet, dielectric barrier discharge-air cold plasma, lipoxygenase, lipase, accelerated storage

Introduction

Foxtail millet (*Setaria italica*) has a long planting history in China as one of the essential coarse grain crops, especially in the northern area (1). Currently, the cultivation area of foxtail millet reaches 10.57×10^6 ha worldwide, with a high production of about 2.29×10^6 t (2). This kind of grain crop is rich in nutritional components, comprising 12.5% protein, 8.0% crude fiber, 4.3% fat content, 3.3% ash content, and around 61% carbohydrates (3). It is deemed a medicinal and edible cereal crop having various health effects such as strengthening the stomach, promoting digestion and absorption, anti-oxidation, and anti-inflammation (4). In addition, foxtail millet can also be used to treat type II diabetes and cardiovascular diseases (5). Foxtail millet must be dehulled before eating or being used for food processing. However, the storage stability of foxtail millet without a shell is seriously reduced, and it is easy to fade and produces an aging odor, which seriously affects its appearance and nutritional value. Studies have shown that millet aging results from the interaction between the external environment and its components (6). Specifically, the hydrolysis and oxidation of lipids induced by the endogenous lipase and lipoxygenase (LOX) are one of the problems that are prone to occur in the rancidity process of foxtail millet (6, 7). Foxtail millet contains high lipids (> 4%), and the content of polyunsaturated fatty acids accounts for about 85%, which is much higher than that of crops such as corn and rice (8). Lipase could decompose the triglycerides into free fatty acids and reduce the pH value, which causes the rancidity of foxtail millet. LOX oxidizes polyunsaturated fatty acids with a 1-*cis*, 4-*cis*-pentadiene structure, including linoleic and linolenic acid, to form hydroperoxides with the release of highly active oxygen free radicals, thus leading to the outcomes of fading and the generation of aging odor (7). Therefore, exploring effective treatment methods to inactivate lipase and lipoxygenase is of great significance for stabilizing the quality of foxtail millet during storage.

The exploitation of "green," no additives, and safe, sustainable means, namely, "clean label," for food processing, has been increasingly researched in recent years. Plasma is mainly composed of positive and negative ions, free radicals, electrons, and the excited state or ground state of atoms (9). Non-thermal plasma technology could be considered a "clean label" owing to no production of residues, which may be an alternative means in the food industry. In recent years, the application of non-thermal plasma in food processing has been widely investigated for the inactivation of endogenous enzymes of food products to extend shelf life and maintain quality (10–14). For example, plasma can inactivate polyphenol oxidase in fruits and vegetables and inhibit the degree of enzymatic browning (15, 16). However, there is a lack of published studies on how this technology affects the foxtail millet and its storage stability.

Shaanxi province is an important foxtail millet production area in China, abounding with famous varieties of Mizhi millet and Ansai millet, cultivated in Yulin and Yan'an city, respectively. In this study, the effects of dielectric barrier discharge-air cold plasma (DBD-ACP) on the lipase, lipoxygenase (LOX) activity, and the appearance, including color, total carotenoids content, morphology, and DPPH free radical scavenging capacity of foxtail millets, i.e., Mizhi and Ansai, were investigated. Additionally, the effects of DBD-ACP on the storage stability of foxtail millets were assessed based on the change of color, total carotenoids, the relative activity of lipoxygenase and lipase, and malondialdehyde (MDA) content during an accelerated storage study for 15 days.

Materials and methods

Raw materials

The current year's harvested foxtail millets Mizhi (Jingu 21 variety) and Ansai (Yangu 12 variety) (**Figure 1**) were purchased from a local market in Xi'an, P. R. China. Linoleic acid and *p*-nitrophenyl laurate were from Sigma–Aldrich Co. (St. Louis, MO, USA). 2,2′-diphenyl-2-picrylhydrazyl hydrate (DPPH) and other chemicals used in this study were obtained from Aladdin Chemical Co. (Shanghai, China). All chemicals were of analytical reagent grade. Ultrapure water was used to prepare the samples throughout the whole experiment.

Dielectric barrier discharge-air cold plasma treatment of foxtail millet

A dielectric barrier discharge plasma system was applied in this study as described by Pan et al. (17), which mainly consisted of two electrodes with an outer diameter of 50 mm (DBD-50), a high-voltage alternating current power source (CTP-2000K), a voltage regulator (Nanjing Suman Electronics Co., Ltd., Nanjing, Jiangsu, China), and two glass dielectric barriers of 1.2 mm in thickness. Foxtail millets with uniform size and color were treated at different voltages (0, 15, 25, and 35 kV) for 0, 2, 4, 8, and 12 min, the frequency was set at 10 kHz, and the discharge spacing was 7 mm. The experimental results were repeated three times, and the average was calculated.

Instrumental color of foxtail millet

The color parameters lightness (L) and yellowness (b^*), were determined at six different points of each sample using a digital colorimeter (VS450 Non-contact colorimeter, Xrite Company, USA) after being blank calibration, to reflect the color change of foxtail millet before and after being treated by DBD-ACP.

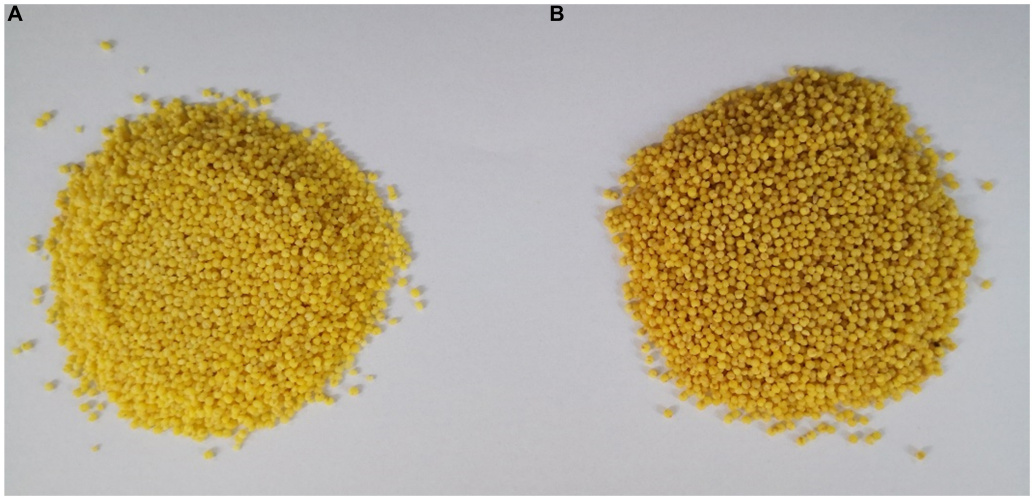

FIGURE 1
The appearance of foxtail millet. **(A)** Mizhi. **(B)** Ansai.

Determination of total carotenoid

Total carotenoids of foxtail millet were extracted and analyzed based on a method reported by Abdel-Aal and Rabalski (18) with slight modifications. For the experiment, 0.50 g of foxtail millet flour with different treatments was homogenized in 10.0 mL of water-saturated 1-butanol and kept shaking for 3.0 h at room temperature. The resultants were centrifuged at 6,000 × g for 10 min at 4°C, and the supernatants were collected and filtered through 0.45 μm filters to analyze the total yellow pigment. A UV–Vis spectrophotometer (UV-1800, Shimadzu Scientific Instruments Co., Ltd., Tokyo, Japan) was used to measure the absorbance at 450 nm to measure total carotenoids. All the extraction and analysis of total carotenoids were conducted in dim light to minimize photo-oxidative reactions.

Determination of lipase and lipoxygenase activity

The extraction and activity determination of lipase were performed according to Lampi et al. (19) with some modifications. For 1.0 h, 1.0 g of ground foxtail millet samples with various treatments were thoroughly mixed with 0.1 M potassium phosphate buffer pH 7.0. After centrifuging the mixture at 8,000 × *g* for 15 min at 4°C, the crude enzyme solution in the supernatants was collected. The activity of lipase and LOX in the supernatant was evaluated using the kits obtained from Nanjing Jiancheng Bioengineering Institute and Suzhou Grace Biotechnology Co., Ltd., China, respectively.

Diphenyl-2- picrylhydrazyl hydrate free radical scavenging activity

The DPPH radical scavenging activity of foxtail millets was measured by mixing 6 mg of grounded foxtail millets with 2.0 mL of 70% ethanol and 2.0 mL of 0.1 mM DPPH in an ethanolic solution. Afterward, the mixture was shaken and incubated in the dark at ambient temperature for 2.0 h. The absorbance of samples was recorded at 517 nm, and the radical scavenging ability of DBD-ACP treated and untreated millets was expressed as percent free radical scavenging activity.

$$\text{Scavenging activity}(\%) = \frac{A_{517nm}blank - A_{517nm}sample}{A_{517nm}blank}$$

Scanning electron microscopy observation

The surface microstructure of foxtail millets was visualized by scanning electron microscopy (SEM, S-3400N, Hitachi, Japan). The samples of foxtail millets before and after being treated by DBD-ACP at 35 kV for 12 min were fixed on SEM discs with double-sided carbon tape and sputter-coated with platinum for 60 s. The SEM images were magnified 600 times and captured at an accelerating voltage of 10.0 kV.

Storage analysis for accelerated aging

To evaluate the effects of DBD-ACP under 15 and 25 kV for 4 min on the quality of millets during storage, untreated millets (control) and DBD-ACP treated millets that were kept in Petri

dishes in an incubator (40 ± 2°C and 75% RH) for accelerated aging by 15 days. The change of color indexes and the content of total carotenoids, activity of lipoxygenase and lipase, and MDA content were measured every 3 days.

Malondialdehyde concentration

The MDA concentration of foxtail millet being treated and untreated by DBD-ACP or accelerated storage was evaluated using an MDA determination kit (Beijing Solarbio Science and Technology Co., Ltd.). 0.1 g millet powder was thoroughly mixed with 1.0 mL extracting solution. After incubation in an ice-water bath for 30 min, the mixture was centrifuged at 8,000 × g for 10 min, and the supernatant was kept to determine the MDA concentration following the protocol.

Statistical analyses

Statistical analysis was performed using OriginPro 8.0 (Origin Lab, Northampton, MA, USA) in triplicate with three independent experiments and results expressed as means ± SD. Analysis of variance (ANOVA) followed by Tukey's test was carried out using SPSS 22.0 software (IBM, NY, USA), and values were considered significantly different if $p < 0.05$.

Results and discussion

Effect of dielectric barrier discharge-air cold plasma on color indexes of foxtail millet

In the CIELAB color representation system, L and b^* represent the lightness and yellowness of samples, respectively. As shown in Table 1, the L and b^* values of both Mizhi and Ansai had no significant change ($p > 0.05$) after exposure to DBD-ACP under 15 kV with increasing treatment time. In addition, no significant difference in L and b^* values were observed for Mizhi and Ansai millet under 25 kV treatment less than 4 min ($p > 0.05$), suggesting that DBD-ACP treatment at 15 kV for 2–12 min or 25 kV for 2–4 min had little effect on the color of millet. However, the levels of L value increased after DBD-ACP treatment at high voltage, especially at 35 kV with increasing time ($p < 0.05$), in which the L value of Mizhi and Ansai millet increased from 64.23 and 60.51 to 72.5 and 68.68, respectively. The b^* value decreased from 49.04 to 46.46 to 42.13 and 40.74, indicating that color changes (bleaching) occurred in millets after being treated with DBD-ACP at 35 kV. Several studies have revealed that DBD-ACP at high voltage induced a significant or slight color change in food, including cherry tomato, Spirulina algae, carrot Juice, Pistachio nuts, banana slices, and grains (14, 20–27). For example, a study conducted by Chaple et al. reported a similar change in color values (L and b^*) of wheat flour for plasma treated at voltages of 80 kV for 5–30 min (26). Pearl millets were also noticed for the variations in color values produced by atmospheric pressure cold plasma treatment at 40 and 45 kV for 5–15 min (28). These published articles show that DBD-ACP can cause the destruction of pigment materials to some degree. Similarly, the increase in L and decrease in b^* values in this work are possibly due to the degradation of carotenoids by ozone or free radicals, as carotenoids are responsible for the yellow color of foxtail millet (29).

Effect of dielectric barrier discharge-air cold plasma on total carotenoids in foxtail millet

Carotenoids are the main yellow pigment components of foxtail millet, reflecting the quality of millet and having good nutrition function (1, 30). To confirm the effect of DBD-ACP on the pigment of foxtail millet Mizhi and Ansai, total carotenoids were extracted before and after exposure

TABLE 1 Effect of DBD-ACP on color indexes of foxtail millets.

Millet	Voltage (kV)	Time (min)	Instrumental color	
			Lightness (L)	Yellowness (b^*)
Mizhi	0	—	64.23 ± 0.24a	49.04 ± 0.17a
	15	2	64.22 ± 0.27a	49.24 ± 0.19a
		4	64.31 ± 0.31a	49.21 ± 0.31a
		8	64.30 ± 0.26a	49.28 ± 0.25a
		12	64.43 ± 0.19b	49.18 ± 0.28a
	25	2	64.36 ± 0.21a	48.88 ± 0.34a
		4	64.91 ± 0.43ab	48.82 ± 0.32a
		8	65.10 ± 0.31b	48.50 ± 0.31a
		12	67.07 ± 0.25c	46.63 ± 0.24b
	35	2	65.22 ± 0.29b	47.83 ± 0.26b
		4	67.35 ± 0.25c	46.88 ± 0.32c
		8	68.36 ± 0.20d	44.43 ± 0.17d
		12	70.51 ± 0.19e	42.13 ± 0.19e
Ansai	0	—	60.51 ± 0.26a	46.46 ± 0.33a
	15	2	60.61 ± 0.17a	46.48 ± 0.21a
		4	60.69 ± 0.13a	46.35 ± 0.25a
		8	60.70 ± 0.41a	46.39 ± 0.31a
		12	60.68 ± 0.35a	46.39 ± 0.40a
	25	2	60.61 ± 0.31a	46.43 ± 0.14a
		4	60.97 ± 0.33a	46.20 ± 0.16a
		8	62.06 ± 0.26b	45.19 ± 0.26b
		12	63.85 ± 0.23c	43.70 ± 0.24c
	35	2	61.66 ± 0.27b	45.11 ± 0.27b
		4	62.09 ± 0.28b	44.02 ± 0.31c
		8	64.69 ± 0.21c	42.09 ± 0.32d
		12	67.68 ± 0.20d	40.74 ± 0.19e

Different letters within a column are significantly different ($p < 0.05$).

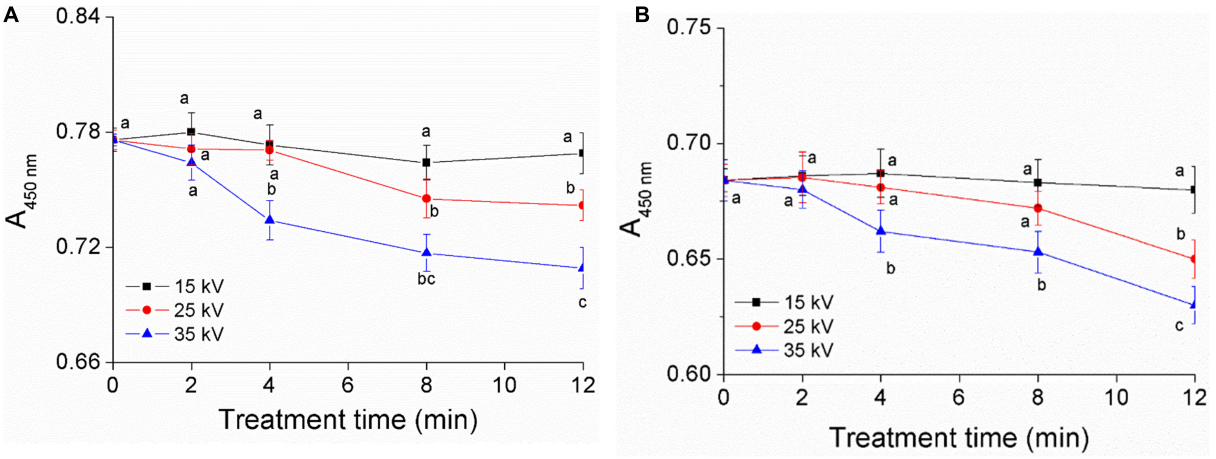

FIGURE 2
Effect of DBD-ACP treatment on yellow pigment of foxtail millet. **(A)** Mizhi. **(B)** Ansai.

of millets to DBD-ACP under various voltage and treatment times. The absorbance of carotenoids in millet is the highest at 445–450 nm, which could be used as an indicator to reflect its content, qualitatively (30). **Figures 2A,B** show the changes of A_{450nm} of Mizhi and Ansai under different voltages and treatment times, respectively. It can be seen that the A_{450nm} of Mizi millet and Ansai millet are 0.78 and 0.68, respectively. Under the voltage of 15 kV, the absorbance of extracted carotenoids in the Mizhi and Ansai millet had no significant change ($p > 0.05$). When the treatment voltage reached 35 kV, the absorbance of yellow pigment was significantly decreased ($p < 0.05$), indicating that carotenoids in millet were damaged to a certain extent. The decrease of carotenoids was also observed by Paixão et al., in which the degradation of carotenoids in siriguela juice was due to exposure to a higher amount of ionized reactive species by plasma (31). Thus, it can be hypothesized that the degradation of superficial carotenoids could be associated with the oxidation of pigments and fading of the color, which is mediated by the presence of oxygen and nitrogen radicals produced by DBD-ACP treatment.

Effect of dielectric barrier discharge-air cold plasma on enzyme activity in foxtail millet

Inactivation of LOX treated by DBD-ACP under voltages of 15, 25, and 35 kV with various treatment times was initially evaluated. As shown in **Figure 3A**, the activity of LOX in foxtail millet Mizhi gradually decreased after exposure to DBD-ACP treatment ($p < 0.05$). For example, when DBD-ACP treated millets at 15 kV for 2–12 min, the relative activity of LOX was decreased from 44.0 U g^{-1} min^{-1} to 38.4, 34.3, 27.6, and 22.9 U g^{-1} min^{-1}. For DBD-ACP treatment at 25 kV, the relative activity of LOX was 32.8 U g^{-1} min^{-1} at 2 min, and the figure decreased sharply to 30.1, 24.6, and 18.7 U g^{-1} min^{-1} after 4, 8, and 12 min, respectively. Correspondingly, lower activity of LOX, i.e., 28.1, 23.5, 18.7, and 14.3 U g^{-1} min^{-1} were obtained for foxtail millet Mizhi treated by DBD-ACP treatment at 35 kV for 2, 4, 8, and 12 min, respectively. The relative activity of LOX in the Ansai millet is shown in **Figure 3B**, exhibiting a similar behavior with the increase of voltage and time, indicating that DBD-ACP has a significant inactivation effect on LOX in millets. Since LOX is one of the key enzymes that promote the aging of millet (8), the inactivation of LOX by DBD-ACP may play a positive role in delaying the aging process of millet.

Figures 3C,D show the inactivation of lipase in the foxtail millet of Mizhi and Ansai, respectively. The lipase activity of millets after being treated by DBD-ACP decreased rapidly with the increase in voltage and treatment time ($p < 0.05$). For example, the lipase activity in the Mizhi millet was inactivated from 56.0 to 18.0 U/(mg pro), 15.1 and 8.8 U/(mg pro), decreased by DBD-ACP treatment at 35 kV for 2–12 min to 67.8, 73.0, and 84.3% in comparison with the untreated millet. These results were in accordance with several previous studies that DBD-ACP treatment is effective in enzymes, including proteinase, pectinase, and alkaline protease (11, 32, 33). The enzymatic inactivation mechanism of DBD-ACP is considered to cause conformational changes, including lower the proportion of α-helix structure due to reacting with a variety of hydrogen peroxide (H_2O_2), ozone (O_3) and nitrate ions (NO_3^-) as well as hydroxyl radical (OH^-), superoxide (O_2^-), and singlet oxygen generated by DBD-ACP with the side chain of the enzyme molecules (34–36).

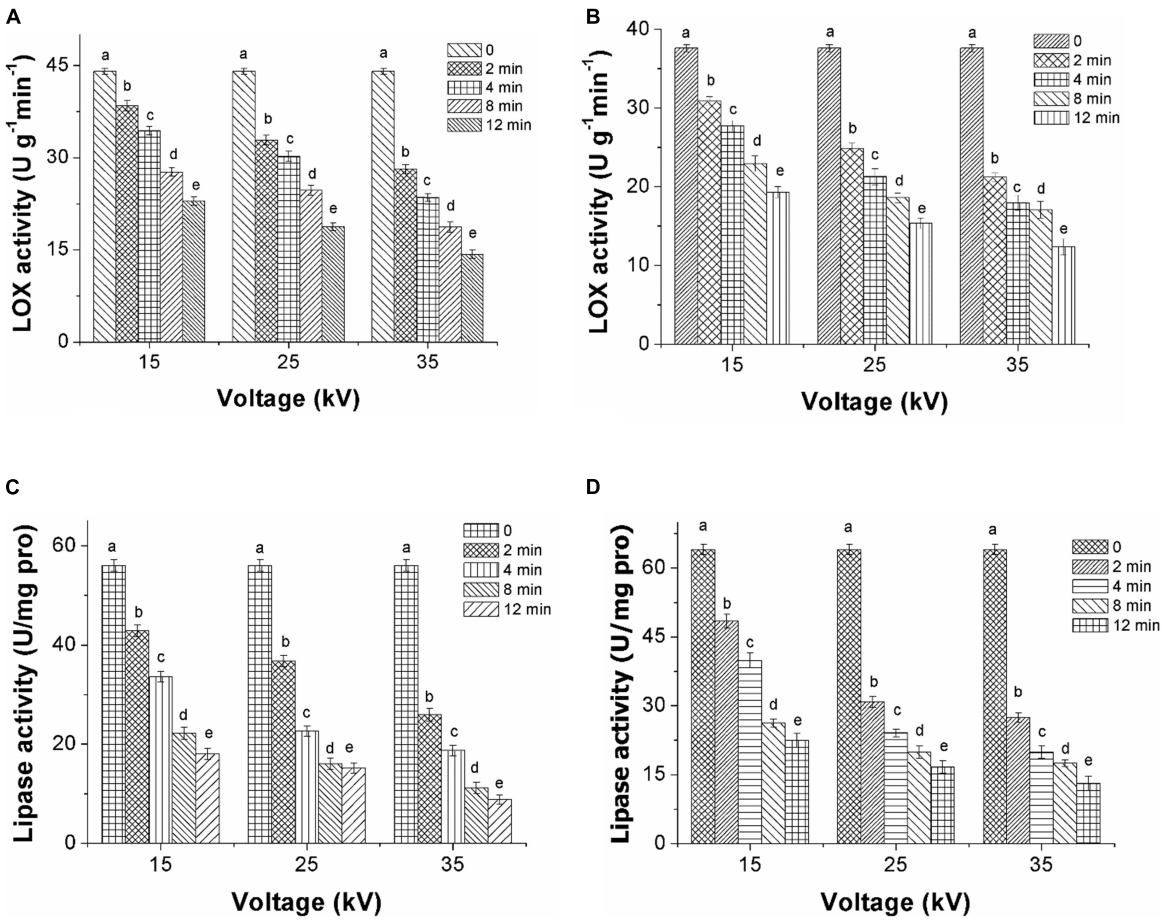

FIGURE 3
Decrease of LOX and lipase activity of foxtail millet induced by DBD-ACP. **(A,C)** Mizhi. **(B,D)** Ansai.

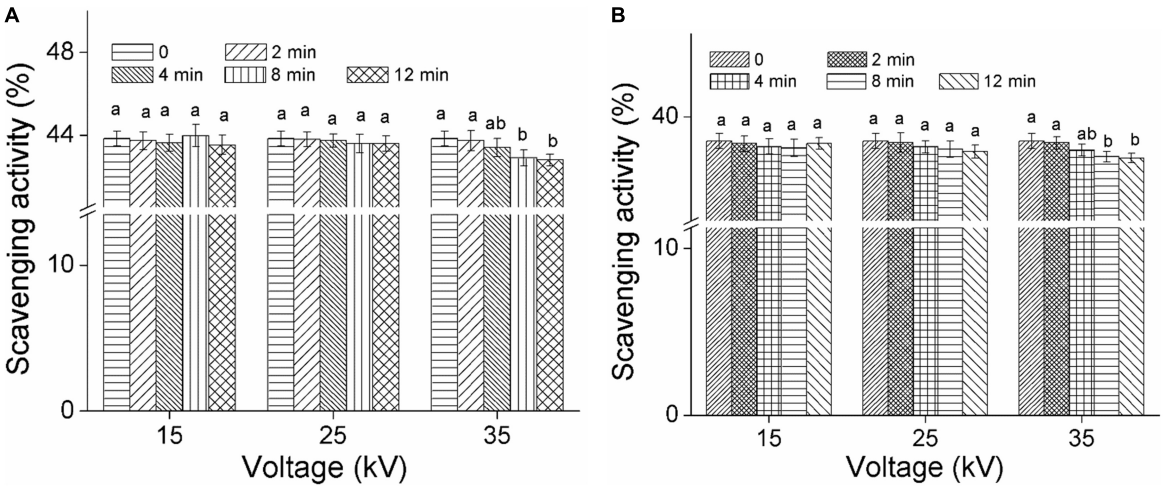

FIGURE 4
Effect of DBD-ACP on DPPH free radical scavenging activity (%) of foxtail millet. **(A)** Mizhi. **(B)** Ansai.

Effect of dielectric barrier discharge-air cold plasma on antioxidant activity of foxtail millet

Figures 4A,B show the DPPH radical scavenging ability of foxtail millet Mizhi and Ansai by DBD-ACP treatment, respectively. As can be seen from the figures, the DPPH radical scavenging ability of Mizhi and Ansai did change insignificantly under plasma treatment (15 and 25 kV) ($p > 0.05$), and maintained about 43.8 and 38.5%, respectively. This result implied that DBD-ACP treatment at relatively low voltage did not change the antioxidant activity. The results of this study were consistent with a work conducted by Tolouie et al. (16), who reported the DPPH free radical scavenging activity of wheat germ did not alter significantly during DBD-ACP treatment. Similar results were reported by Amini and Ghoranneviss (37) and Ramazzina et al. (14), who found that DBD-ACP treatment did not affect the antioxidant capacity of fresh walnuts and kiwifruit. However, the scavenging ability of DPPH free radical of millets after exposure to DBD-ACP at 35 kV showed a slight decrease, significantly ($p < 0.05$) when DBD-ACP treatment for 8 and 12 min was compared to the control. These findings agree with grape juice and chokeberries that, when treated with cold plasma show a lower DPPH radical scavenging ability at higher treatment voltage or time (38, 39). Therefore, it can be inferred that the effect of DBD-ACP on DPPH radical scavenging ability or antioxidant activity is probably dependent on the plasma processing parameters.

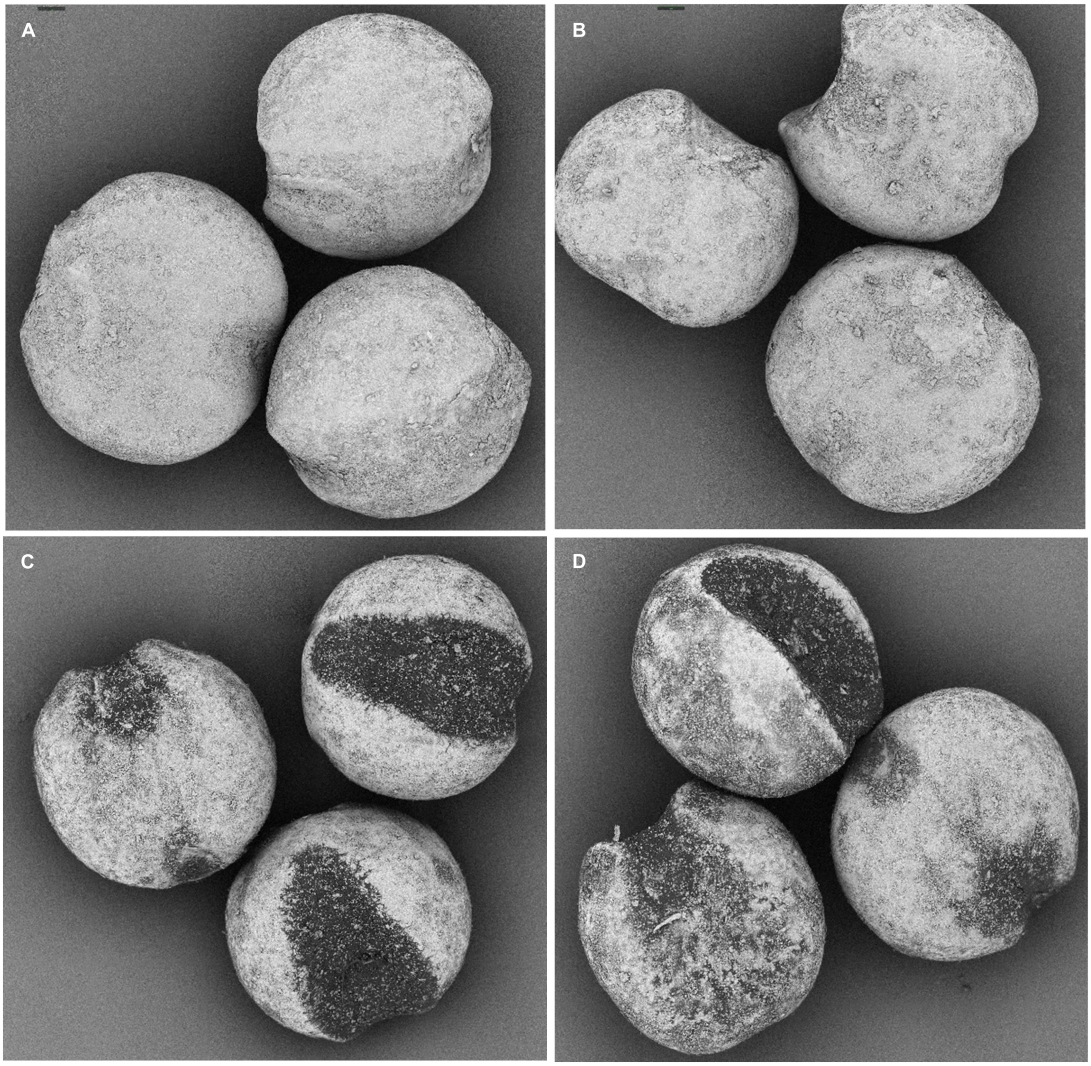

FIGURE 5
Morphological images of untreated foxtail millet, **(A)** Mizhi and **(C)** Ansai, and after being treated by DBD-ACP at 35 kV for 12 min, **(B)** Mizhi, **(D)** Ansai.

TABLE 2 Changes in color indexes of foxtail millets with different treatment.

	Lightness (L)			Yellowness (b^*)		
			Mizhi millet			
Storage days	0	15	25	0	15	25
0	64.33 ± 0.21a	64.41 ± 0.30a	64.94 ± 0.18a	49.19 ± 0.21a	49.30 ± 0.22a	48.45 ± 0.24a
3	64.54 ± 0.25ab	64.42 ± 0.41a	65.41 ± 0.26a	48.94 ± 0.26a	49.42 ± 0.23a	47.03 ± 0.40b
6	64.91 ± 0.42b	64.50 ± 0.22a	65.93 ± 0.27a	48.04 ± 0.30b	49.32 ± 0.19a	46.72 ± 0.32b
9	65.22 ± 0.22bc	64.53 ± 0.26a	66.48 ± 0.27b	47.47 ± 0.25b	49.06 ± 0.35a	46.0 ± 0.27a
12	65.58 ± 0.28c	65.18 ± 0.24b	67.63 ± 0.42c	46.89 ± 0.21c	48.71 ± 0.23b	44.58 ± 0.34d
15	66.35 ± 0.19d	65.77 ± 0.31c	69.80 ± 0.30d	46.07 ± 0.22d	47.01 ± 0.31c	42.03 ± 0.25e
			Ansai millet			
0	60.56 ± 0.15a	60.62 ± 0.22a	62.92 ± 0.26a	46.52 ± 0.23a	46.43 ± 0.21a	45.22 ± 0.24a
3	60.47 ± 0.11a	60.72 ± 0.29a	63.83 ± 0.32b	46.60 ± 0.31a	46.39 ± 0.40a	45.01 ± 0.26a
6	61.05 ± 0.13b	60.62 ± 0.42a	64.75 ± 0.31c	46.01 ± 0.11b	45.75 ± 0.31b	44.41 ± 0.32b
9	62.17 ± 0.25c	61.13 ± 0.35a	65.39 ± 0.32d	45.44 ± 0.20c	45.01 ± 0.26c	42.63 ± 0.11c
12	63.18 ± 0.36d	62.16 ± 0.19b	66.88 ± 0.34e	44.58 ± 0.22d	44.85 ± 0.34c	41.46 ± 0.24d
15	63.37 ± 0.26d	62.73 ± 0.22c	68.15 ± 0.40f	43.78 ± 0.18e	44.23 ± 0.27d	39.44 ± 0.26e

Different letters within a column are significantly different ($p < 0.05$).

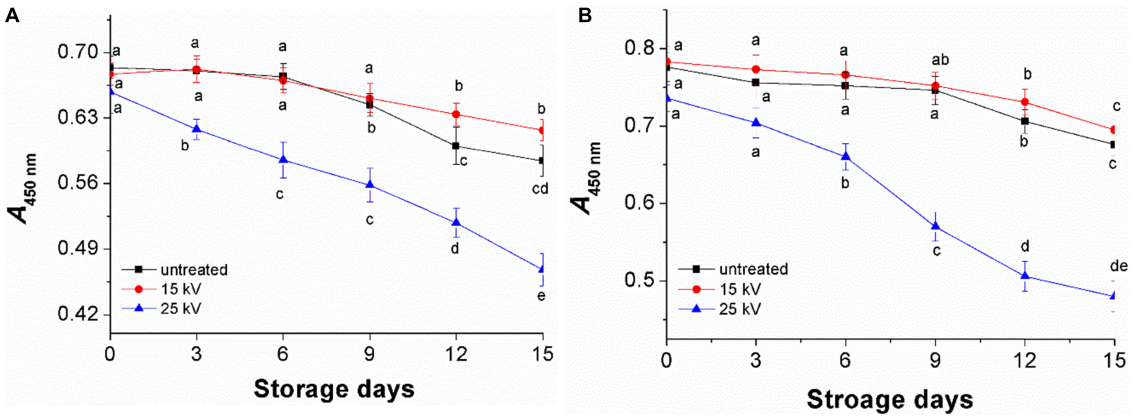

FIGURE 6
The changes of yellow pigment of foxtail millets during accelerated agingstorage. **(A)** Mizhi. **(B)** Ansai.

Morphological observation of foxtail millet

The surface morphology of foxtail millets before and after being treated by DBD-ACP at 35 kV for 12 min was observed by SEM. Figures 5A,C show the surface of the untreated Mizhi and Ansai millet, describing the intact morphology of dehulled millet with evident furrows caused by the shelling treatment. The DBD-ACP treated millets show a morphology with a well-defined texture and large grooves with no significant cracks were observed (Figures 5B,D). These results were consistent with a work done by Thirumdas et al. (40), reporting that brown rice showed fissures and hollow depressions under cold plasma treatment. This may be due to differences in the texture between the rice and foxtail millet. Therefore, it could be concluded that DBD-ACP treatment does not produce mechanical damage to the surface of foxtail millets under these conditions.

Color changes of foxtail millet during storage

Untreated foxtail millets (control) and treated at 15 and 25 kV for 4 min were kept for accelerated aging storage by 15 days. The results showed a moderate increase in L and a decrease in b^* values of untreated millets (Table 2). Compared to the control, millets treated at 15 kV had better color indexes, indicating that DBD-ACP treatment at 15 kV has a positive effect on millets on keeping a better appearance. However, much more significant variations were observed in the millets treated by DBD-ACP at 25 kV. Similar results were found in the changes of $A_{450\ nm}$ representing the total carotenoids, where millets exposed to 25 kV showed a significant reduction during storage compared to the control and millets treated at 15 kV (Figures 6A,B). These results may be related to ozone (O_3), nitrate ion (NO_3^-), superoxide (O_2^-), and singlet oxygen produced by

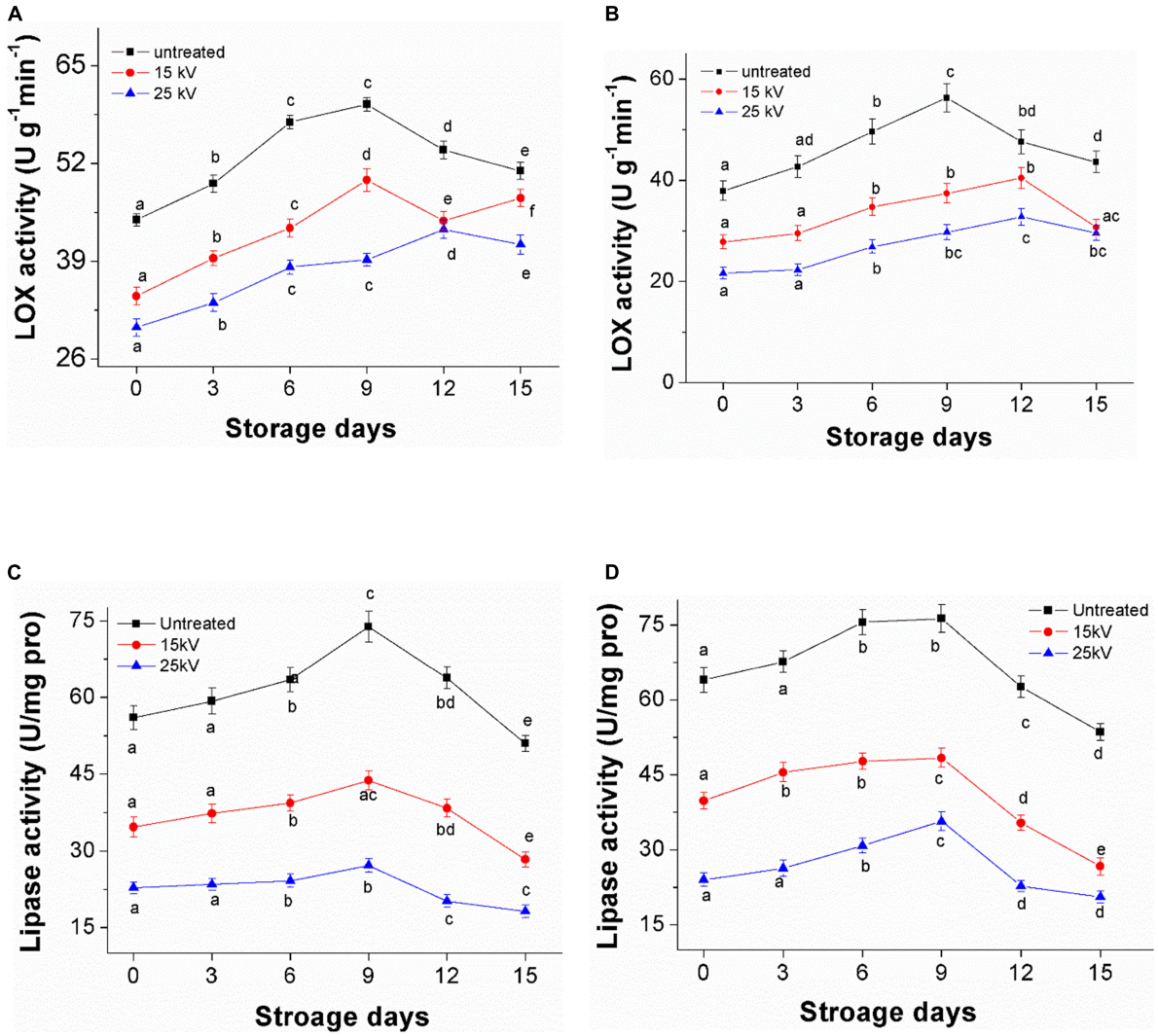

FIGURE 7
Changes of LOX and lipase activity of foxtail millet during accelerated aging storage. **(A,C)** Mizhi. **(B,D)** Ansai.

DBD-ACP at high voltage remaining on the surface of millet, which accelerates the destruction of the millet pigment in the aging storage (14).

Activity of lipoxygenase and lipase during storage

Figure 7 presents the LOX and lipase activities of millets during 15 days of accelerated aging storage. LOX and lipase activity were observed to increase gradually in the first 9 days of storage and then to decrease regardless of treatments. For example, the activity of LOX for untreated Mizhi and Ansai millet during storage was 44.5 and 37.9 U g^{-1} min^{-1} on day zero, increasing to a minimum of 59.8 and 56.3 U g^{-1} min^{-1} after 9 days of storage, respectively (Figures 7A,B). The lipase activity for untreated Mizhi and Ansai millet during storage was only 56.0 and 64.0 U/(mg pro), increasing to a minimum of 73.8 and 76.3 U/(mg pro) after 9 days of storage, respectively (Figures 7C,D). However, the treated millets by DBD-ACP at 15 and 25 kV were found to have maintained a significantly lower value of LOX and lipase activity than that of the control. These results concur with a previous study by Tolouie et al. (16), in which DBD-ACP-treated wheat germ was found to maintain a low LOX and lipase activity during storage.

Production of malondialdehyde

As shown in Figure 8A, the MDA content of Mizhi millet that was untreated by DBD-ACP was found to be slowly increased, from 12.5 to 18.9 mg/g, 32.5 and 60.1 mg/g on

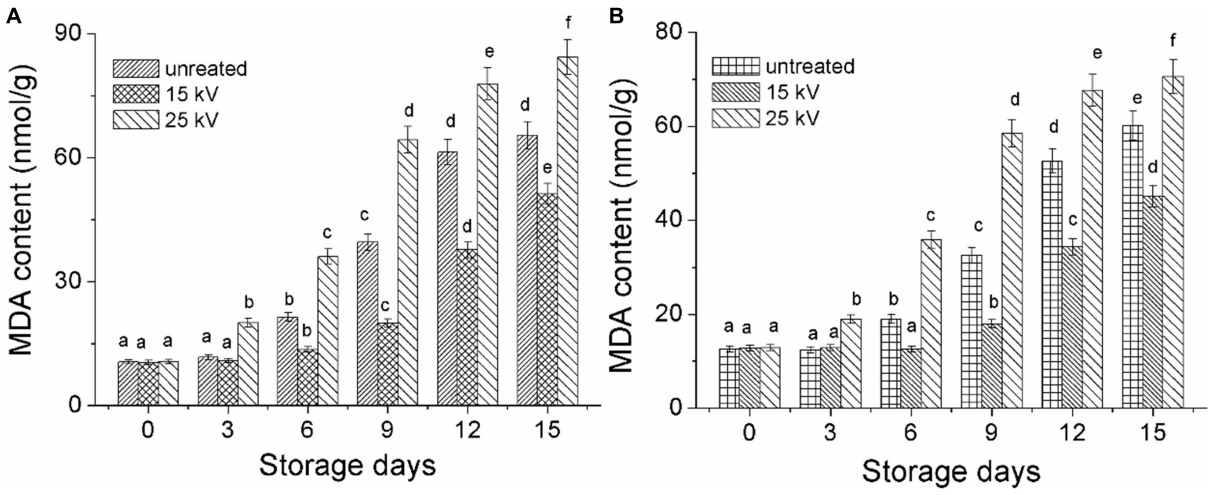

FIGURE 8
Changes in MDA content of foxtail millet during accelerated aging storage. **(A)** Mizhi. **(B)** Ansai. Different letters with the same column are significantly different ($p < 0.05$).

the days of 0, 6, 9, and 15 ($p < 0.05$). Whereas millet treated with DBD-ACP at 15 kV had significantly lower MDA content than the control. The accumulation of MDA is related to the oxidation of lipids, especially unsaturated fatty acids induced by LOX and lipase. Consequently, the MDA contents of the 15 kV treated millet were low during the accelerated storage (41). However, it was found that MDA content drastically increased for millets treated by DBD-ACP at 25 kV. This increase in MDA content be associated with the reactive species and hydroxyl free radicals generated by DBD-ACP at high voltage that initiate lipid oxidation by attacking various compounds, including unsaturated fatty acids. These results concur with previous reports in which cold plasma increased the MDA content of pistachio walnuts and peanuts at different powers (24, 40). Ansai millets with different treatments also exhibited similar results during the same storage conditions (**Figure 8B**). These results, along with the changes in color indexes, total carotenoids, and antioxidant activity indicated that nutritional losses of foxtail millets were associated with ROS-triggered lipid peroxidation and destruction of millet pigment, which was greatly alleviated by DBD-ACP treatment under severe conditions, suggesting that when using DBD-ACP to delay millet aging, appropriate treatment conditions are required.

Conclusion

This work investigated the effects of DBD-ACP on the quality and storage stability of foxtail millets. DBD-ACP treatment was found to cause a noticeable decrease in the activity of lipoxygenase and lipase of foxtail millets. For example, LOX and lipase activity decreased from 44.0 to U g^{-1} min^{-1}, 56.0–8.8 U/(mg pro) by DBD-ACP treatment at 35 kV for 12 min, respectively. Moreover, DBD-ACP has no significant impact on foxtail's antioxidant activity and surface morphology. However, it has a certain destructive effect on the total carotenoids that affect the color of foxtail millet if the voltage is at 35 kV for 4–12 min or 25 kV for 8–12 min. After being treated by DBD-ACP under 15 and 25 kV for 4 min, the stability of foxtail millets was determined during accelerated storage analysis for 15 days. Compared to the controls, millets treated by DBD-ACP at 15 and 25 kV were found to have maintained a significantly lower value of LOX and lipase activity during the accelerating aging storage. Additionally, millets treated by DBD-ACP at 15 kV exhibited a better color index, higher total carotenoids, and lower MDA content during storage. Comparatively, DBD-ACP at 25 kV induced damages in color, total carotenoids, and higher MDA content of millets suggesting side effects occurred due to reactive oxygen species. The elucidation of DBD-ACP under suitable treatment conditions could be applied to stabilize the quality of the foxtail millet. These results implied that DBD-ACP is an underlying approach for the storage of foxtail millets. Further work should be done to enhance the understanding of DBD-ACP on foxtail millets and to evaluate the feasibility of using DBD-ACP to delay the shelf life of dehulled foxtail millets.

Data availability statement

The original contributions presented in this study are included in the article/supplementary material, further inquiries can be directed to the corresponding authors.

Author contributions

L-HW: conceptualization, methodology, formal analysis, data curation, and writing—original draft. ZL: methodology, formal analysis, and data curation. JQ: methodology, formal analysis, and visualization. YH: resources, methodology, and supervision. X-AZ: resources, visualization, supervision, project administration, and funding acquisition. RMA: writing—review and editing. All authors contributed to the article and approved the submitted version.

Funding

This research was supported by the Project of Science and Technology Department of Shaanxi Province (Grant No. 2021JQ-448), the Key Laboratory Project of Guangdong Province (Grant No. 2022B1212010015), the Guangdong Provincial Department of Agriculture and Rural Affairs Agricultural Research and Technology Promotion Demonstration (Grant No. 2022KJ144), and the National Natural Science Foundation of China (Grant No. 3210160758).

Conflict of interest

The authors declare that the research was conducted in the absence of any commercial or financial relationships that could be construed as a potential conflict of interest.

Publisher's note

References

1. Yang Y, Jia G, Deng L, Ling Q, Chen E, Cong X, et al. Genetic variation of yellow pigment and its components in foxtail millet (*Setaria italica* (L.) P. Beauv.) from different eco-regions in China. *J Integr Agric.* (2017) 16:2459–69. (16)61598-8 doi: 10.1016/S2095-3119

2. Sachdev N, Sangeeta G, Laishram R. Foxtail millet: a potential crop to meet future demand scenario for alternative sustainable protein. *J Sci Food Agric.* (2021) 101:831–42. doi: 10.1002/jsfa.10716

3. Sharma R, Savita S. Anti-nutrient & bioactive profile, in vitro nutrient digestibility, techno-functionality, molecular and structural interactions of foxtail millet (*Setaria italica* L.) as influenced by biological processing techniques. *Food Chem.* (2022) 368:130815. doi: 10.1016/j.foodchem.2021.130815

4. Sarita E, Singh E. Potential of millets: nutrients composition and health benefits. *J Sci Innov Res.* (2016) 5:46–50. doi: 10.31254/jsir.2016.5204

5. Ren X, Chen J, Molla M, Wang C, Diao X, Shen Q. In vitro starch digestibility and in vivo glycemic response of foxtail millet and its products. *Food Funct.* (2016) 7:372–9. doi: 10.1039/c5fo01074h

6. Sruthi N, Rao P. Effect of processing on storage stability of millet flour: a review. *Trends Food Sci Tech.* (2021) 112:58–74. doi: 10.1016/j.tifs.2021.03.043

7. Sunil C, Chacko N. Microwave assisted de-husking of foxtail millet. *J Agric Eng.* (2019) 55:21–33.

8. Liang K, Liu Y, Liang S. Analysis of the characteristics of foxtail millet during storage under different light environments. *J Cereal Sci.* (2021) 101:103302. doi: 10.1016/j.jcs.2021.103302

9. Ali M, Cheng J, Sun D. Effects of dielectric barrier discharge cold plasma treatments on degradation of anilazine fungicide and quality of tomato (*Lycopersicon esculentum* Mill) juice. *Int J Food Sci Tech.* (2021) 56:69–75. doi: 10.1111/ijfs.14600

10. Thirumdas, R, Annapure U. Enzyme inactivation in model systems and food matrixes by cold plasma. In: Bermudez-Aguirre D editor. *Advances in Cold Plasma Applications for Food Safety and Preservation*. San Diego, CA: Elsevier (2020). p. 229–52. doi: 10.1016/B978-0-12-814921-8.00007-4

11. Chutia H, Kalita D, Mahanta C, Ojah N, Choudhury A. Kinetics of inactivation of peroxidase and polyphenol oxidase in tender coconut water by dielectric barrier discharge plasma. *LWT Food Sci Technol.* (2019) 101:625–9. doi: 10.1016/j.lwt.2018.11.071

12. Surowsky B, Bußler S, Schlüter O. Cold plasma interactions with food constituents in liquid and solid food matrices. In: Misra NN, Schlüter O, Cullen PJ editors. *Cold Plasma in Food and Agriculture*. London: Elsevier (2016). p. 179–204. doi: 10.1016/B978-0-12-801365-6.00007-X

13. Dantas A, Batista J, Lima M, Fernandes F, Rodrigues S, Magnani M, et al. Effect of cold plasma on açai pulp: enzymatic activity, color and bioaccessibility of phenolic compounds. *LWT Food Sci Technol.* (2021) 149:111883. doi: 10.1016/j.lwt.2021.111883

14. Ramazzina I, Berardinelli A, Rizzi F, Tappi S, Ragni L, Sacchetti G, et al. Effect of cold plasma treatment on physico-chemical parameters and antioxidant activity of minimally processed kiwifruit. *Postharvest Biol Technol.* (2015) 107:55–65. doi: 10.1016/j.postharvbio.2015.04.008

15. Chen Y, Cheng J, Sun D. Chemical, physical and physiological quality attributes of fruit and vegetables induced by cold plasma treatment: mechanisms and application advances. *Crit Rev Food Sci Nutr.* (2020) 60:2676–90. doi: 10.1080/10408398.2019.1654429

16. Tolouie H, Mohammadifar M, Ghomi H, Yaghoubi A, Hashemi M. The impact of atmospheric cold plasma treatment on inactivation of lipase and lipoxygenase of wheat germs. *Innov Food Sci Emerg Technol.* (2018) 47:346–52. doi: 10.1016/j.ifset.2018.03.002

17. Pan Y, Zhang Y, Cheng J, Sun D. Inactivation of *Listeria monocytogenes* at various growth temperatures by ultrasound pretreatment and cold plasma. *LWT Food Sci Technol.* (2020) 118:108635. doi: 10.1016/j.lwt.2019.108635

18. Abdel-Aal E, Rabalski I. Effect of baking on free and bound phenolic acids in wholegrain bakery products. *J Cereal Sci.* (2013) 57:312–8. doi: 10.1016/j.jcs.2012.12.001

19. Lampi A, Yang Z, Mustonen O, Piironen V. Potential of faba bean lipase and lipoxygenase to promote formation of volatile lipid oxidation products in food models. *Food Chem.* (2020) 311:125982. doi: 10.1016/j.foodchem.2019.125982

20. Zhang X, Zhong C, Mujumdar A, Yang X, Deng L, Wang J, et al. Cold plasma pretreatment enhances drying kinetics and quality attributes of chili pepper (*Capsicum annuum* L.). *J Food Eng.* (2019) 241:51–7. doi: 10.1016/j.jfoodeng.2018.08.002

21. Misra N, Keener K, Bourke P, Mosnier J, Cullen P. In-package atmospheric pressure cold plasma treatment of cherry tomatoes. *J Biosci Bioeng.* (2014) 118:177–82. doi: 10.1016/j.jbiosc.2014.02.005

22. Beyrer M, Pina-Perez M, Martinet D, Andlauer W. Cold plasma processing of powdered Spirulina algae for spore inactivation and preservation of bioactive compounds. *Food Control.* (2020) 118:107378. doi: 10.1016/j.foodcont.2020.107378

23. Umair M, Jabbar S, Senan A, Sultana T, Nasiru M, Shah A, et al. Influence of combined effect of ultra-sonication and high-voltage cold plasma treatment on quality parameters of carrot juice. *Foods.* (2019) 8:593. doi: 10.3390/foods8110593

24. Makari M, Hojjati M, Shahbazi S, Askari H. Elimination of *Aspergillus flavus* from pistachio nuts with dielectric barrier discharge (DBD) cold plasma and its impacts on biochemical indices. *J Food Qual.* (2021) 2021:9968711. doi: 10.1155/2021/9968711

25. Gu Y, Shi W, Liu R, Xing Y, Yu X, Jiang H. Cold plasma enzyme inactivation on dielectric properties and freshness quality in bananas. *Innov Food Sci Emerg Technol.* (2021) 69:102649. doi: 10.1016/j.ifset.2021.102649

26. Chaple S, Sarangapani C, Jones J, Carey E, Causeret L, Genson A, et al. Effect of atmospheric cold plasma on the functional properties of whole wheat (*Triticum aestivum* L.) grain and wheat flour. *Innov Food Sci Emerg Technol.* (2020) 66:102529. doi: 10.1016/j.ifset.2020.102529

27. Sarangapani C, Devi R, Thirumdas R, Trimukhe A, Deshmukh R, Annapure U. Physico-chemical properties of low-pressure plasma treated black gram. *LWT Food Sci Technol.* (2017) 79:102–10. doi: 10.1016/j.lwt.2017.01.017

28. Lokeswari R, Sharanyakanth P, Jaspin S, Mahendran R. Cold plasma effects on changes in physical, nutritional, hydration, and pasting properties of pearl millet (*Pennisetum glaucum*). *IEEE Trans Plasma Sci.* (2021) 49:1745–51. doi: 10.1109/TPS.2021.3074441

29. Li S, Zhao W, Liu S, Li P, Zhang A, Zhang J, et al. Characterization of nutritional properties and aroma compounds in different colored kernel varieties of foxtail millet (*Setaria italica*). *J Cereal Sci.* (2021) 100:103248. doi: 10.1016/j.jcs.2021.103248

30. Shen R, Yang S, Zhao G, Shen Q, Diao X. Identification of carotenoids in foxtail millet (*Setaria italica*) and the effects of cooking methods on carotenoid content. *J Cereal Sci.* (2015) 61:86–93. doi: 10.1016/j.jcs.2014.10.009

31. Paixão L, Fonteles T, Oliveira V, Fernandes F, Rodrigues S. Cold plasma effects on functional compounds of siriguela juice. *Food Bioprocess Technol.* (2019) 12:110–21. doi: 10.1007/s11947-018-2197-z

32. Tang L, Hatab S, Yan J, Miao W, Nyaisaba B, Piao X, et al. Changes in biochemical properties and activity of trypsin-like protease (*Litopenaeus vannamei*) treated by atmospheric cold plasma (ACP). *Foods.* (2022) 11:1277. doi: 10.3390/foods11091277

33. Karaca B, Csiszár E, Bozdogan F. Effects of atmospheric plasma pretreatments on pectinase efficiency in bioscouring of linen fabrics. *Plasma Chem Plasma Process.* (2011) 31:623–33. doi: 10.1007/s11090-011-9302-7

34. Tappi S, Berardinelli A, Ragni L, Rosa M, Guarnieri A, Rocculi P. Atmospheric gas plasma treatment of fresh-cut apples. *Innov Food Sci Emerg Technol.* (2014) 21:114–22. doi: 10.1016/j.ifset.2013.09.012

35. Xu L, Hou H, Farkas B, Keener K, Garner A, Tao B. High voltage atmospheric cold plasma modification of bovine serum albumin. *LWT Food Sci Technol.* (2021) 149:111995. doi: 10.1016/j.lwt.2021.111995

36. Zhang H, Xu Z, Shen J, Li X, Ding L, Ma J, et al. Effects and mechanism of atmospheric-pressure dielectric barrier discharge cold plasmaon lactate dehydrogenase (LDH) enzyme. *Sci Rep.* (2015) 5:10031. doi: 10.1038/srep10031

37. Amini M, Ghoranneviss M. Effects of cold plasma treatment on antioxidants activity, phenolic contents and shelf life of fresh and dried walnut (*Juglans regia* L.) cultivars during storage. *LWT Food Sci Technol.* (2016) 73:178–84. doi: 10.1016/j.lwt.2016.06.014

38. Pankaj S, Wan Z, Colonna W, Keener K. Effect of high voltage atmospheric cold plasma on white grape juice quality. *J Sci Food Agric.* (2017) 97:4016–21. doi: 10.1002/jsfa.8268

39. Park Y, Puligundla P, Mok C. Decontamination of chokeberries (*Aronia melanocarpa* L.) by cold plasma treatment and its effects on biochemical composition and storage quality of their corresponding juices. *Food Sci Biotechnol.* (2021) 30:405–11. doi: 10.1007/s10068-020-00867-8

40. Thirumdas R, Saragapani C, Ajinkya M, Deshmukh R, Annapure U. Influence of low pressure cold plasma on cooking and textural properties of brown rice. *Innov Food Sci Emerg Technol.* (2016) 37:53–60. doi: 10.1016/j.ifset.2016.08.009

41. Yadav B, Spinelli A, Govindan B, Tsui Y, McMullen L, Roopesh M. Cold plasma treatment of ready-to-eat ham: influence of process conditions and storage on inactivation of *Listeria innocua*. *Food Res Int.* (2019) 123:276–85. doi: 10.1016/j.foodres.2019.04.065

frontiers | Frontiers in Nutrition

TYPE Original Research
PUBLISHED 04 January 2023
DOI 10.3389/fnut.2022.1094906

OPEN ACCESS

EDITED BY
Zhi-Hong Zhang,
Jiangsu University, China

REVIEWED BY
Jing-Kun Yan,
Dongguan University of Technology, China
Gulden Goksen,
Tarsus University, Turkey
Umair Shabbir,
Ulster University, United Kingdom

*CORRESPONDENCE
Zhong Han
✉ fezhonghan@scut.edu.cn
Xinan Zeng
✉ xazeng@scut.edu.cn

†These authors have contributed equally to this work

SPECIALTY SECTION
This article was submitted to Nutrition and Food Science Technology, a section of the journal Frontiers in Nutrition

RECEIVED 10 November 2022
ACCEPTED 12 December 2022
PUBLISHED 04 January 2023

CITATION
Cai J, Liang Z, Li J, Manzoor MF, Liu H, Han Z and Zeng X (2023) Variation in physicochemical properties and bioactivities of *Morinda citrifolia* L. (Noni) polysaccharides at different stages of maturity. *Front. Nutr.* 9:1094906. doi: 10.3389/fnut.2022.1094906

Variation in physicochemical properties and bioactivities of *Morinda citrifolia* L. (Noni) polysaccharides at different stages of maturity

Jinlin Cai[1,2†], Zijian Liang[3†], Jian Li[1,2], Muhammad Faisal Manzoor[1,2], Hongsheng Liu[1], Zhong Han[1,2*] and Xinan Zeng[1,2*]

[1]School of Food Sciences and Engineering, South China University of Technology, Guangzhou, China, [2]Guangdong Key Laboratory of Food Intelligent Manufacturing, Foshan University, Foshan, China, [3]Faculty of Veterinary and Agricultural Sciences, School of Agriculture and Food, University of Melbourne, Parkville, VIC, Australia

Introduction: *Morinda citrifolia* L. (Noni) as an evergreen plant is a rich source of natural polysaccharides.

Objective: The present work aims to investigate the maturation-related changes in polysaccharides of *Morinda citrifolia* L. (Noni) at five stages of maturity (stages from the lowest to highest degree – 1, 2, 3, 4, and 5).

Methods: The chemical composition (carbohydrate, protein, uronic acid, and sulfate radical) of Noni polysaccharides was determined by different chemical assays. Ion chromatography system was used to analyze the monosaccharide composition, and the molecular weight was measured by HPGPC. The polysaccharides were also analyzed by FT-IR and their radical scavenging effect against DPPH, hydroxyl radicals and ABTS was evaluated. The UV-vis assay and gel electrophoresis assay were performed to investigate the DNA damage protective effect.

Results: Results indicated the significant effect of fruit maturities on the extraction yields, molecular weights, uronic acid contents, sugar levels, monosaccharide compositions and proportions, antioxidant capacities, and DNA protective effects of Noni polysaccharides. However, no fruit maturity stage had prominent impact on the sulfuric radical contents and preliminary structure characteristics. Noni polysaccharides extracted at stage 5 (N5) had the largest extraction yield (8.26 ± 0.14%), the highest sugar content (61.94 ± 1.86%) and the most potent scavenging effect on DPPH (IC_{50}: 1.06 mg/mL) and ABTS (IC_{50}: 1.22 mg/mL) radicals. The stronger DPPH and ABTS radical scavenging activities of N5 might be contributed by its higher content of fucose and rhamnose and smaller molecular weight. Noni polysaccharides extracted at stage 4 (N4) showed the highest uronic acid content (4.10 ± 0.12%), and the superior performance in scavenging hydroxyl radicals and

protecting DNA. The greater hydroxyl radical scavenging effect of N4 might be attributed to its higher percentage of the low molecular weight counterpart. Moreover, the DNA protective effects of N4 displayed a positive correlation with its hydroxyl radical scavenging ability.

Conclusion: Overall, stage 4 and stage 5 could be ideal stages of fruit maturity aiming at high-quality Noni polysaccharides extraction. This study provided valuable information for the selection of suitable Noni polysaccharides to cater for various industrial applications.

KEYWORDS

Noni polysaccharides, fruit maturity stages, extraction yield, antioxidant activity, DNA protective effect

Introduction

Morinda citrifolia L. (Noni) is an evergreen plant native to tropical and subtropical regions (1). Noni fruit and its products have been attracting great attention from nutraceutical and pharmaceutical industries worldwide due to the increasing public awareness of their excellent pharmacological properties (2). Nutritional analysis of Noni has shown the presence of proteins, amino acids, organic acids, polyphenols, and vitamins in the fruit (3). In addition, Noni fruit is also a good source of natural polysaccharides (4). In Polynesia, India, Malaysia, Indonesia, and China, Noni fruit has been perceived as a traditional herb for over 2,000 years (5). Several *in vitro* and *in vivo* studies have reported that Noni fruit and its derived products exhibit anti-inflammatory, antidiabetic and antiproliferative activities as well as free radical scavenging activity (6, 7). As natural metabolites of Noni fruit, the Noni polysaccharides are claimed to be closely related to its therapeutic properties (8).

The changes of compositions in Noni fruit are induced by various biochemical and physiological reactions arising in fruit growth, development, and maturity (9), thereinto, the maturity of Noni fruit is vital to the quality of Noni polysaccharides. As the maturity progresses, plant polysaccharides are susceptible to diverse structure changes (debranching, acetylation/deacetylation, methylation/demethylation, depolymerization) catalyzed by enzymes. These modifications are correlated to softening and senescence of the plant, which can be observed along with the modifications in physiochemical properties (color, flesh breakdown, softening) and biological activities (antioxidant activity, anti-diabetic activity, immunomodulatory activity) since the early stage of ripening (10). The quality parameters of polysaccharides are highly important for selecting raw materials when producing high value-added Noni polysaccharides and their products. To find the ideal fruit maturity stage for extracting high-quality Noni polysaccharides, it is worthwhile to explore the differences of polysaccharides in Noni fruit during the ripening process. However, limited studies have been reported on this topic. Therefore, the present work intends to comprehensively investigate the variations in the extraction yields, physicochemical properties and bioactivities of Noni polysaccharides during fruit maturation. This information will provide practical insights into the selection of raw materials for extracting high-quality Noni polysaccharides.

Materials and methods

Material and chemicals

Noni fruits were purchased from Xisha Noni Co., Ltd. (Hainan, China). The pre-treatment process of Noni fruit is the same as in our previous study (11). The polysaccharides extracted from Noni fruit at different maturity stages (stage 1–stage 5) were coded N1, N2, N3, N4, and N5, respectively.

Bovine serum albumin (BSA), coomassie blue staining solution, 2,2-diphenyl-1-picrylhydrazyl (DPPH), and 2,2′-azino-bis (3-ethylbenzothiazoline-6-sulfonic acid) (ABTS) were obtained from Shanghai Aladdin Biochemical Technology Co., Ltd. (Shanghai, China). Pullulan standards of different molecular weights (4.4, 9.9, 21.4, 43.5, 124, 277, and 404 kDa) were acquired from Polymer Standards Service Co., Ltd. (Mainz, Germany). Standards of monosaccharides including fucose (Fuc), D-glucose (Glu), rhamnose (Rha), xylose (Xyl), mannose (Man), galactose (Gal), arabinose (Ara), glucuronic acid (GlcA), and galacturonic acid (GalA) and ctDNA were purchased from Sigma Chemical Co., Ltd. (St. Louis, MO, USA). pUC18 DNA was purchased from Solarbio Co., Ltd. (Beijing, China). All chemicals were of analytical reagent grade.

Extraction and isolation of polysaccharides

In our previous study, hot-water extraction has been optimized by the response surface method (11). Briefly, Noni powder and ultrapure water were mixed at a ratio of 1–41.9 and heated at 77.7°C for 117.6 min, followed by the centrifugation at 3663 *g*, for 15 min. The supernatant was collected as the polysaccharide solution and then concentrated. The concentrate was then mixed with 4 times the volume of ethanol (100%) and placed in a refrigerator at 4°C for 12 h for precipitation. Afterward, the crude polysaccharides were harvested *via* centrifugation (3663 *g*, 15 min) and freeze-drying successively. The polysaccharide yield was calculated as follows:

$$\text{Yield } (\%) = \frac{\text{Weight of crude Noni polysaccharides } (\text{g})}{\text{Weight of Noni fruit powders } (\text{g})}$$

The purification of crude Noni polysaccharides followed the Sevag method, where the deproteinated solution was dialyzed and reprecipitated with ethanol, then collected and freeze-dried to give the purified polysaccharide for further analysis. The polysaccharides extracted from Noni fruit at different maturity stages (stage 1–stage 5) were coded N1, N2, N3, N4, and N5, respectively.

Determination of chemical composition

The total carbohydrate content of Noni polysaccharides was measured by the phenol-sulfuric acid method (12). The protein content of Noni polysaccharide was determined following the Bradford method using BSA as the standard (13). The contents of uronic acids and sulfate radicals were determined by the corresponding reporter method (11).

Determination of monosaccharide composition

The monosaccharide composition was evaluated as illustrated by Chen et al. (14). The polysaccharide samples were mixed with trifluoroacetic acid (2:1, w/v) and hydrolyzed at 105°C for 6 h. Subsequently, trifluoroacetic acid (4 M) was removed by rotary evaporation, then added with 5 ml methanol and further evaporated to remove residual trifluoroacetic acid (repeat 4 times). The final sample residue was dissolved in ultrapure water and the pH was adjusted to neutral for analysis. Ion chromatography system (ICS 5000, Dionex, CA) and Carbopac PA1 column (250 mm × 4 mm) were used to analyze the monosaccharide composition of the samples.

Determination of molecular weights

High performance gel permeation chromatograph (HPGPC) with a triple column system was used to assess the molecular weight. ACQUITY APC AQ 900 2.5 μm column (4.6 mm × 150 mm), ACQUITY APC AQ 450 2.5 μm column (4.6 mm × 150 mm), and ACQUITY APC AQ 125 2.5 μm column (4.6 mm × 150 mm) were employed for the analysis of the molecular weight distribution. Both HPGPC and columns were purchased from Waters Corporation (USA). The analysis was performed with following settings: refractive index model, flow rate 0.4 ml/min, injection volume 40μL, mobile phase 100 mM $NaNO_3$.

Analysis of fourier transform-infrared (FT-IR) spectroscopy

In FT-IR analysis, potassium bromide (KBr) pellet was prepared by mixing 2 mg polysaccharide sample with KBr powder and further pressing. A vector 33 IR spectrophotometer (Bruker, Ettlingen, Germany) was used to measure the spectrum of the samples from KBr pellet in the range of 400–4000 cm^{-1}.

Analysis of antioxidant activity

DPPH and hydroxyl radicals scavenging activities were measured based on the previously reported methods (15, 16). The radical scavenging effect on ABTS was evaluated using the method of Xu et al. (17). Noni polysaccharides solution at different concentrations (0.2, 0.4, 0.6, 0.8, and 1.0 mg/ml) were selected for the analysis.

Analysis of DNA damage protective effect

UV-*vis* assay

The protective effect against the DNA damage induced by hydroxyl radical was measured according to a previously reported method with some modifications (18). In brief, Noni polysaccharide phosphate buffer solution (0.2 M, pH 7.4) at different concentrations (2.0, 4.0, 6.0, 8.0, and 10.0 mg/ml), 0.5 mM Na_2EDTA, 3.2 mM $FeCl_3$, 5 mM H_2O_2, and 2.94 mM ctDNA were mixed in a ratio of 16: 4: 2: 3: 4 (v/v/v/v/v). To initiate the reaction, 0.075 ml 12 mM ascorbic acid was added in the mixture, then incubated in water bath at 55°C for 20 min. The reaction was terminated by adding 0.25 ml 0.6 M trichloroacetic acid, followed by the addition of 0.15 ml 0.35 M 2-thiobarbituric acid and heating at 105°C for 15 min. The mixture was determined at 530 nm and the buffer was used

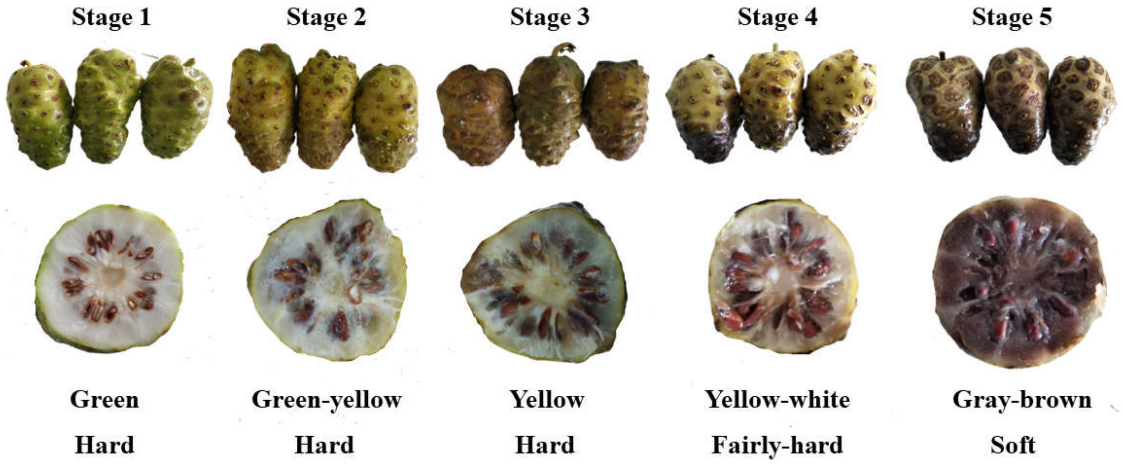

FIGURE 1
Noni fruit at different maturity stages (stages 1–5).

TABLE 1 Chemical composition and extraction yield of Noni polysaccharide at different maturity stages.

Maturity	Extraction yield (%)	Sugar (%)	Sulfuric radical (%)	Protein (%)	Uronic acid (%)
N1	3.86 ± 0.21^{e}	57.85 ± 1.25^{c}	1.87 ± 0.15^{c}	nd	1.19 ± 0.03^{e}
N2	5.20 ± 0.18^{d}	59.01 ± 0.98^{b}	2.01 ± 0.16^{b}	nd	2.62 ± 0.15^{d}
N3	6.11 ± 0.09^{c}	61.28 ± 1.80^{a}	2.08 ± 0.20^{a}	nd	3.56 ± 0.06^{c}
N4	7.13 ± 0.12^{b}	61.32 ± 2.01^{a}	2.07 ± 0.18^{a}	nd	4.10 ± 0.12^{a}
N5	8.26 ± 0.14^{a}	61.94 ± 1.86^{a}	2.08 ± 0.17^{a}	nd	3.88 ± 0.08^{b}

The data are presented as mean values ± standard deviation. nd, not detected. Data marked with different letters are significantly different at $p < 0.05$.

as the blank. The protection effect against DNA damage was calculated as follows:

$$\text{Protective effect}\,(\%) = \frac{A_0 - (A_1 - A_2)}{A_0} \times 100$$

Where A_0 is the absorbance of the control without Noni polysaccharides, A_1 is the absorbance of the reaction system with Noni polysaccharides, A_2 is the absorbance of the reaction system without ctDNA.

Gel electrophoresis assay

The evaluation of protective action for supercoiled pUC18 plasmid DNA against hydroxyl radical was according to the method of Wang et al. (18) with slight modifications. The reaction mixture contained 0.05 M PBS (9 μL), plasmid DNA (3 μL), Noni polysaccharide (8 mg/ml, 10 μL), 1 mM $FeSO_4$ (4 μL), and 1 mM H_2O_2 (4 μL). The mixture was incubated at 37°C for 30 min, before mixing with loading buffer (0.05% bromophenol blue, 40 mM EDTA and 50% glycerol) at a ratio of 3:1 (v/v). Then, 6 μL of mixture was electrophoresed on 1% agarose gel for 30 min under 150 V condition. A Gel Documentation system (Hercules, CA, USA) was used to visualize and photograph the DNA gel.

Statistical analysis

Each experiment was performed in triplicates, and the means ± standard deviations were reported as the results. The significant difference of mean values was measured by one-way ANOVA with Duncan's multiple range tests at 95% confidence level using SPSS (SPSS, Chicago, USA). Pearson's correlation analysis was used to identify the relationships between physicochemical properties and bioactivities of the samples. The Probit model from SPSS was applied to calculate the IC_{50} value.

Results and discussion

Appearance changes during ripening process

The appearance of Noni fruit at five maturity stages are shown in Figure 1. During fruit maturation, the color of fruit skin changed from green to brown. Carotenoids and chlorophyll (Chl) pigments have been found to be associated with color changes from green to yellow and brown in fruits.

TABLE 2 Retention time, molecular weight (M_w), and amount of soluble polysaccharide fractions from five Noni polysaccharide samples.

Samples	Peak	Retention time (min)	M_w (kDa)	Area account (%)
N1	Peak A	10.707	97.96	22.74
	Peak B	12.947	10.57	46.07
	Peak C	14.542	3.61	31.18
N2	Peak A	10.621	107.38	22.52
	Peak B	12.933	10.69	47.22
	Peak C	14.488	3.98	30.25
N3	Peak A	10.797	118.55	21.89
	Peak B	12.051	21.75	39.16
	Peak C	14.480	3.68	38.95
N4	Peak A	10.758	102.44	21.57
	Peak B	12.086	21.14	34.78
	Peak C	14.488	3.74	43.65
N5	Peak A	11.120	129.50	21.35
	Peak B	11.974	23.14	29.78
	Peak C	14.507	3.78	48.87

The degradation/catabolism of Chl is an enzymatic process with two pathways. The phytol and Mg are removed from Chl by the effects of chlorophyllase and Mg-dechelatase results in the opening of the backbone of the Chl ring structure subsequently leading to the deepening of peel color (19). On the other hand, Chl-degrading peroxidase can directly catabolize Chl pigment (20). The firmness of fruit remained hard in the early three stages but changed from hard to soft after stage 4. A decline in fruit firmness was associated with pectolytic enzymes, which are responsible for the polysaccharide degradation in the cell wall (21). The changes in the cell wall structure indicated the possible variation in the physicochemical properties of Noni polysaccharides during fruit softening.

Chemical composition

Table 1 summarized the extraction yields and chemical compositions of Noni polysaccharide samples. The polysaccharide yield was increased in the following order: N5 > N4 > N3 > N2 > N1. N5 had the highest yield (8.26 ± 0.14%), while the lowest yield (3.86 ± 0.21%) was recorded for N1. Our result also revealed the similar sugar contents (61–62%) of N3, N4, and N5, which were significantly ($p < 0.05$) higher as compared to N1 and N2. During fruit ripening, cell wall polysaccharides such as pectin, cellulose and hemicellulose undergo solubilization, catabolism, and de-esterification by pectin methyl esterase, polygalacturonase, cellulase, and β-glucosidase, resulting in fruit softening as well as reduction in the molecular weight of cell wall polysaccharides. These results made the extraction of polysaccharides in stages 4 and 5 easier, with higher extraction rates and sugar contents in N4 and N5 than in the other three samples (22). The similar trend was also observed in the content of sulfuric radical. No protein was detected in all five Noni polysaccharide samples due to the complete removal of all free protein *via* pre-treatment. There were significant differences in the uronic acid level among all five sample, where N4 ranked the highest value. It is stated that the uronic acid concentration is positively correlated with the biological activities of polysaccharides (23), hence the N4 sample may have better bioactivities. Overall, stage 4 and stage 5 could be ideal maturity stages for the extraction of high-quality Noni polysaccharides.

Molecular weight

Significant variations were observed among the molecular weight (M_w) distribution for the Noni polysaccharide samples from five maturity stages. Table 2 showed the similar molecular weight values of N1, N2, N3, N4, and N5. Three polysaccharide fractions were detected in HPGPC, where the molecular weights were 97.96–129.50 kDa for peak A, 10.57–23.14 kDa for peak B, and 3.61–3.98 kDa for peak C. The main differences in molecular weight distribution occurred in the proportions of medium-M_w (Peak B) and low-M_w (Peak C) fractions. In N1, N2, and N3, the medium-M_w fractions accounted for the main components, while the major constituents of N4 and N5 were low-M_w fractions. The highest percentage of low-M_w fraction (48.87%) was recorded for N5, while N2 contained the highest medium-M_w fraction proportion (47.22%). Indeed, during fruit ripening, the polysaccharides in cell wall can be gradually degraded by pectinase, resulting in an increase of low-M_w polysaccharide fractions and fruit softening (10). The results illustrated that the molecular weight distribution of Noni polysaccharides can be affected by the ripeness of Noni fruit.

FTIR analysis

As depicted in Figure 2, the FT-IR spectra of five Noni polysaccharide samples were recorded in the range of 4000–400 cm^{-1}. All samples showed characteristic polysaccharide signals at around 3360, 2920, 1730, 1622, 1420, and 1100 cm^{-1}. The strong absorption signals at around 3360 and 1622 cm^{-1} were ascribed to the deformation vibration and stretching vibration of hydroxyl clusters (12). The absorption bands at around 2920 cm^{-1} were characteristic of the axial stretching of the C-H bond of methyl groups. Absorption signals at around 1730 and 1622 cm^{-1} corresponded to C=O stretching vibration of carboxylic acid, confirming the presence of certain amount

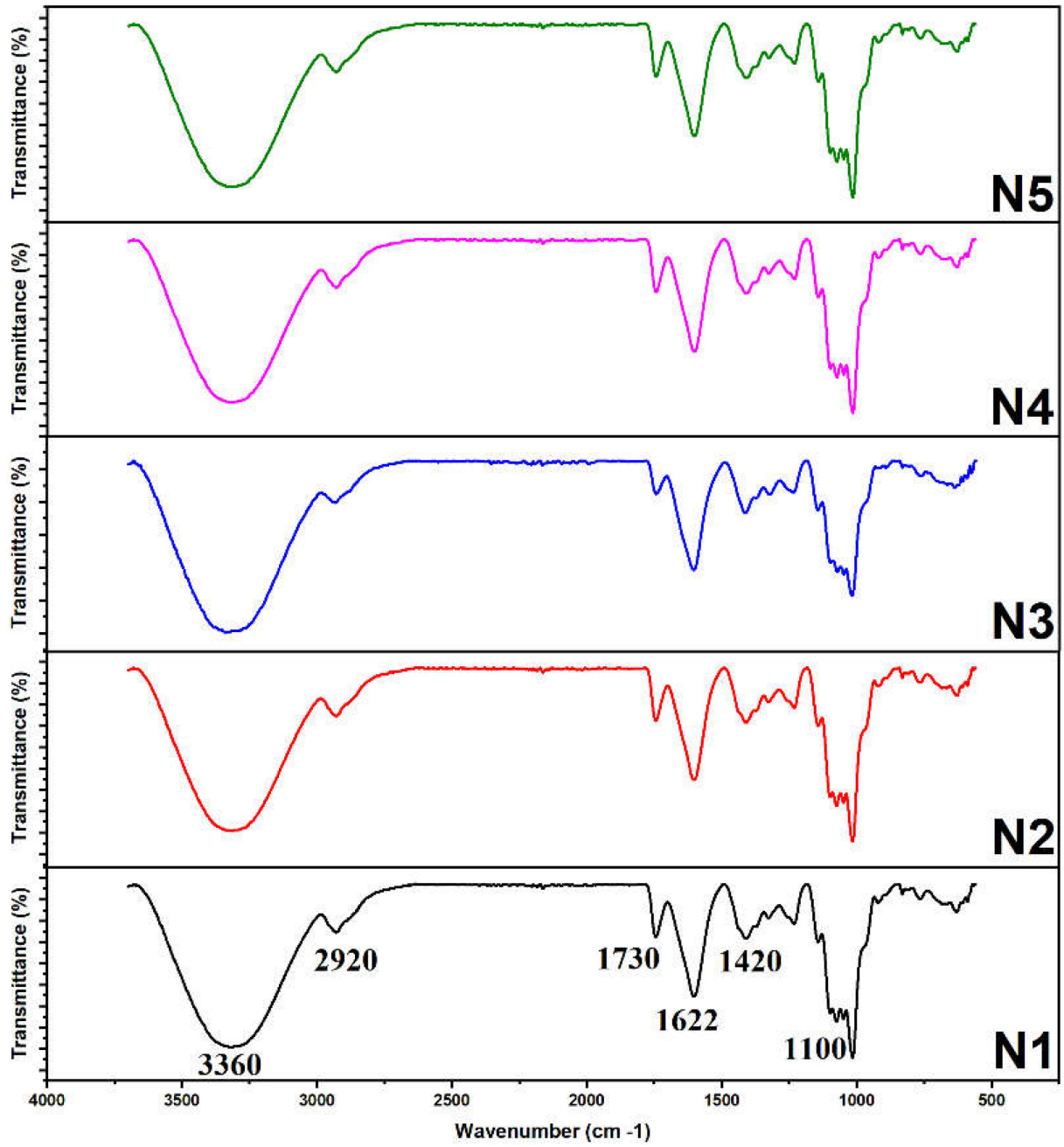

FIGURE 2
FT-IR spectra of five Noni polysaccharide samples extracted at different maturity stages.

of uronic acid in polysaccharide samples (24). The existence of carbonyl clusters was also revealed by the band at 1420 cm^{-1}. In addition, prominent signals in the range of 1000–1200 cm^{-1} implied that all samples contained pyranose ring structure and glycosidic bond. The FT-IR spectra of the five samples were similar, which indicated that the maturity of Noni fruit had no significant impact on the type of glycosidic bonds and the primary structure of Noni polysaccharides.

Monosaccharide composition

The monosaccharide concentrations of Noni polysaccharide samples are listed in Table 3. Results demonstrated that the monosaccharide constituents of N2, N3, N4, and N5 were measured as Fuc, Ara, Gal, Glu, Xyl, Man, Rha, GalA, GluA, which are in good agreement with the previous report (11). However, Xyl and Man were not detected in N1. The

TABLE 3 Monosaccharide concentrations (mg/L) of Noni polysaccharide samples extracted at five stages of maturity.

Maturity	Fuc	Ara	Gal	Glu	Xyl	Man	Rha	GalA	GluA
N1	0.400 ± 0.020	0.088 ± 0.009	0.070 ± 0.012	0.010 ± 0.002	nd	nd	0.180 ± 0.005	0.967 ± 0.021	0.222 ± 0.011
N2	0.410 ± 0.017	1.396 ± 0.012	2.905 ± 0.030	0.010 ± 0.003	0.037 ± 0.009	0.315 ± 0.012	0.190 ± 0.003	2.424 ± 0.144	0.195 ± 0.006
N3	0.422 ± 0.011	2.807 ± 0.012	3.909 ± 0.104	2.992 ± 0.042	0.078 ± 0.005	0.420 ± 0.011	0.192 ± 0.002	3.319 ± 0.044	0.240 ± 0.016
N4	0.536 ± 0.021	3.025 ± 0.015	3.282 ± 0.066	2.895 ± 0.036	0.078 ± 0.006	0.339 ± 0.006	0.201 ± 0.002	3.875 ± 0.115	0.222 ± 0.005
N5	0.585 ± 0.023	2.816 ± 0.021	3.799 ± 0.031	3.674 ± 0.029	0.015 ± 0.002	0.302 ± 0.002	0.198 ± 0.005	3.668 ± 0.075	0.207 ± 0.005

nd, not detected.

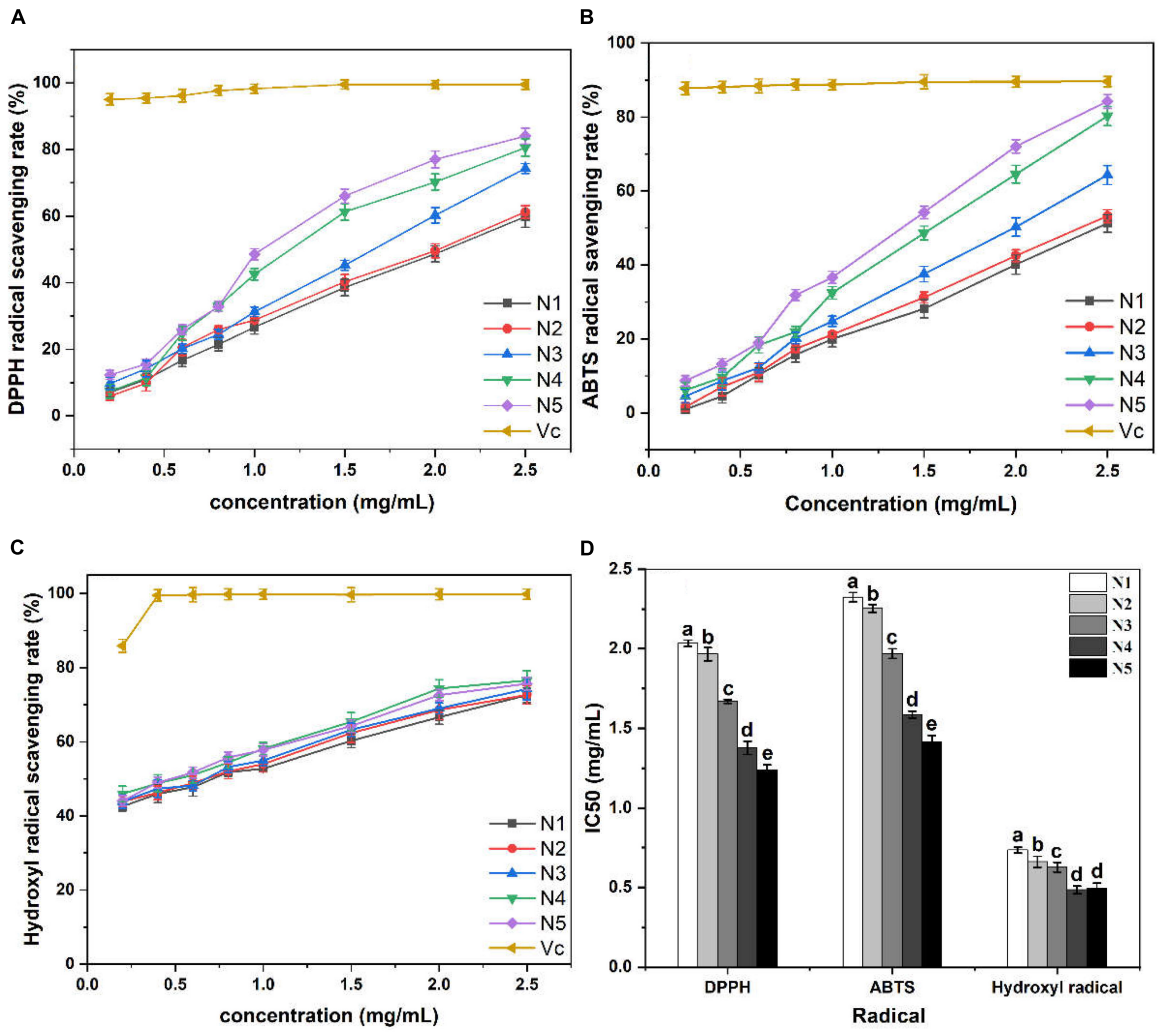

FIGURE 3
Scavenging activity of Noni polysaccharide samples on DPPH **(A,D)**, ABTS **(B,D)**, and hydroxyl radical **(C,D)**. Data marked with different letters are significantly different at $p < 0.05$.

maximum concentrations of Gal (3.909 ± 0.104 mg/L) and Man (0.420 ± 0.011 mg/L) were found in N3, while the highest values of Ara (3.025 ± 0.015 mg/L) and GalA (3.875 ± 0.115 mg/L) were observed in N4. Moreover, the N5 sample had significantly higher levels of Fuc (0.585 ± 0.023 mg/L) and Glu (3.674 ± 0.029 mg/L) than the other samples. Similar trends in glucose content were reported in sweet cherries and Natal plum (25, 26), where the glucose concentrations also peaked in the final maturity stage. As ripening progresses, glucose increase due to the action of the enzyme invertase through glycolysis in fruits and vegetables (27). The dominant monosaccharides in N3, N4, and N5 were

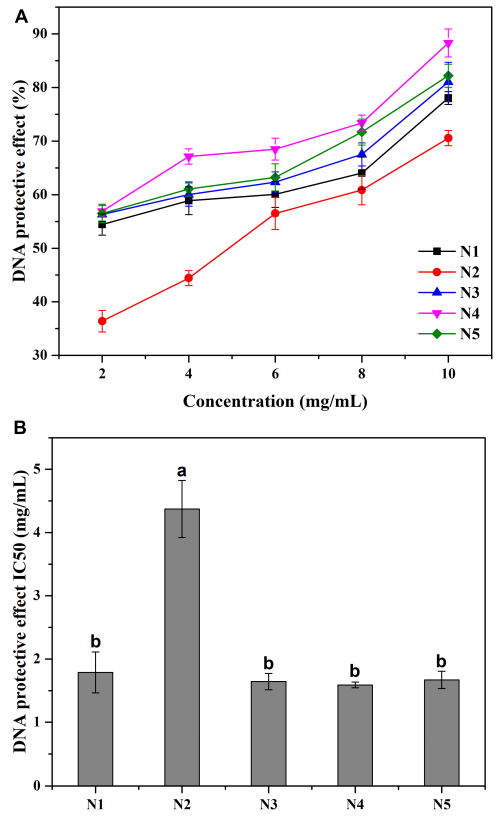

FIGURE 4
(A) The protective effect against •OH radical induced DNA damage at different concentrations of Noni polysaccharide samples. **(B)** The IC_{50} value of different Noni polysaccharide samples. Data marked with different letters are significantly different at $p < 0.05$.

Ara, Gal, Glu and GalA, while N1 was mainly made up of Fuc, Rha, GalA, and GluA. The composition of N2 sample was closer to N3, N4, and N5, which was composed of Ara, Gal, and GalA. These results demonstrated that the content and constituent of monosaccharides in Noni polysaccharide samples were influenced by the fruit maturity stages.

Antioxidant capacity

Scavenging activity on DPPH radical

As shown in Figures 3A, D, all polysaccharide samples demonstrated DPPH radical scavenging activities that were positively correlated with the tested concentrations. However, the ascorbic acid group showed the significantly ($p < 0.05$) higher DPPH radical scavenging capacity than the five polysaccharide samples. In fact, the IC_{50} values for scavenging of DPPH radicals were measured to be 2.03 mg/ml (N1), 1.96 mg/ml (N2), 1.66 mg/ml (N3), 1.37 mg/ml (N4), and 1.23 mg/ml (N5). Therefore, it can be concluded that the N5 sample exhibited the superior DPPH radical scavenging ability among the five samples tested. Antioxidants can scavenge DPPH radicals by donating hydrogen to form stable DPPH-H molecules with DPPH radicals (28). It was evident that N5 showed the strongest proton donating ability and could serve as DPPH radical scavengers, acting possibly as antioxidants in the five polysaccharide samples.

Scavenging activity on ABTS radical

The results of the ABTS radical scavenging ability of the five samples are depicted in Figures 3B, D. All samples performed the ABTS scavenging activity in a dose-response manner. N5 exhibited higher ABTS radical scavenging ability as compared to the other polysaccharide samples at each concentration, albeit being significantly ($p < 0.05$) lower than that of the ascorbic acid group. The blue–green $ABTS^+$ free radicals will be reduced to colorless ABTS under the action of antioxidants (29). The lowest IC_{50} value was observed in the N5 sample (1.41 mg/ml), which validated that stage 5 could be the optimum maturity stage for

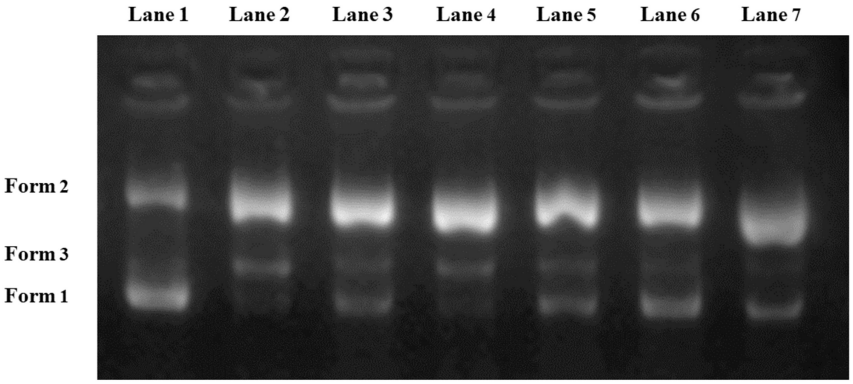

FIGURE 5
Oxidative damage protective ability of Noni polysaccharide to pUC18 supercoiled plasmid DNA. Lane 1: native DNA; Lane 2: DNA + H_2O_2 + $FeSO_4$; Lane 3–Lane 7: DNA + Noni polysaccharide (N1, N2, N3, N4, N5) + H_2O_2 + $FeSO_4$.

TABLE 4 Matrix for correlation analysis.

Value	IC_{50} of DPPH assay	IC_{50} of ABTS assay	IC_{50} of hydroxyl assay	IC_{50} of DNA protective effect
Sugar content (%)	−0.926*	−0.901*	−0.883*	−0.450
Sulfuric radical (%)	−0.778	−0.748	−0.803	−0.128
Uronic acid (%)	−0.878	−0.856	−0.991*	−0.266
Fuc (mg/L)	−0.950*	−0.968**	−0.936*	−0.432
Ara (mg/L)	−0.861	−0.832	−0.870	−0.333
Gal (mg/L)	−0.696	−0.664	−0.721	−0.011
Glu (mg/L)	−0.857	−0.806	−0.840	−0.642
Xyl (mg/L)	−0.313	0.264	−0.402	−0.123
Man (mg/L)	−0.527	−0.487	−0.587	0.085
Rha (mg/L)	−0.892*	−0.884*	−0.966**	−0.205
GalA (mg/L)	−0.878	−0.856	−0.913*	−0.255
GluA (mg/L)	−0.077	0.027	−0.060	−0.732
High-M_w parts (%)	0.989**	0.977**	0.950*	0.515
Medium-M_w parts (%)	0.987**	0.984**	0.909*	0.622
Low-M_w parts (%)	−0.989**	−0.985**	−0.914*	−0.615

*$p < 0.05$.
**$p < 0.01$.

extracting Noni polysaccharides with high reducing power to scavenge ABTS radicals.

Scavenging activity on hydroxyl radical

Hydroxyl radicals are the most reactive radicals, which can cause oxidative damage to human tissue and induce severe cell death (30). It is important to find natural antioxidants to scavenge hydroxyl radicals since there are no enzymatic systems known to neutralize them in the human body. The results of the hydroxyl radical scavenging test are presented in **Figures 3C, D**, which revealed that all measured polysaccharide samples exerted dose-dependent scavenging effects on hydroxyl radicals. N4 exhibited stronger hydroxyl radical scavenging ability than the other four samples at the concentrations ranging from 0.2 to 2.5 mg/ml. Moreover, the IC_{50} values of all tested samples were different, which followed the order of N4 < N5 < N3 < N1 < N2. Generally, polysaccharides with high uronic acid content and low molecular weight possess strong antioxidant activity (27). In this part, the IC_{50} values of N5 (0.49 mg/ml) was not significantly different from N4 (0.48 mg/ml) with higher uronic acid content ($p > 0.05$), which may be related to its smaller molecular weight.

DNA protective effect

UV-*vis* assay

Free radicals especially hydroxyl radicals, may cause a variety of DNA damages to the human body, such as altering signaling cascades, making gene misexpression and increasing replication errors. As shown in **Figure 4**, all five samples showed prominent DNA protective abilities in a concentration-dependent manner. At the tested concentrations of 2–10 mg/L, the strongest DNA protective action was detected in N4 at 10 mg/ml with the protective rate as 88.31%. Meanwhile, the IC_{50} values of the five samples showed a similar trend to the hydroxyl radical scavenging test. N4 had the lowest IC_{50} value of the DNA protective effect (1.59 mg/ml), while the IC_{50} value of N2 was significantly ($p < 0.05$) higher when comparing with the other samples. In this experiment, DNA damaged by hydroxyl radicals can easily form pink acidic thiobarbituric acid-reactive substance (TBARS) under acidic and high-temperature conditions (31). The results suggested that all Noni polysaccharide samples could suppress the generation of TBARS and thus protect DNA against hydroxyl radical-induced damage. It is worth noting that the DNA protective effects of five samples were positively related to their hydroxyl radical scavenging abilities.

Gel electrophoresis assay

Supercoiled pUC18 plasmid DNA has been extensively employed as a test model for detecting the potential active substances that protect DNA against oxidative damage (32). For the pUC18 plasmid DNA model, three forms can be displayed on gel electrophoresis, including Form 1 (supercoiled form), Form 2 (open circular form) and Form 3 (linear form). The migration speed of three forms followed the order of Form 1 > Form 3 > Form 2. Generally, undamaged plasmid

DNA mainly consists of the supercoiled form, while the open circular form and linear form will be generated once the DNA is damaged.

As illustrated in **Figure 5**, the control group (Lane 1) mainly displayed in the supercoiled band (Form 1). In the meantime, Lane 2 showed that most of the normal DNA with supercoiled structure was converted into linear form and open circular form after adding H_2O_2 and $FeSO_4$. Lane 3–Lane 7 exhibited the protective effects of the five samples on DNA. According to the electrophoresis results, N4 showed the strongest DNA protective ability since its Form 1 band was brighter than that of the other samples. The electrophoresis feature of N2 (Lane 4) was similar to that of Lane 2, indicating that N2 had the lowest DNA protective activity. Although the reaction system was different from the UV-*vis* method, these results further validated N4 as the most promising protectant against DNA strand scission caused by hydroxyl radicals.

Correlation analysis

Pearson analysis was performed to elucidate the correlation between the physicochemical characteristics and biological activities of the five Noni polysaccharide samples. As shown in **Table 4**, it can be seen that the antioxidant ability of each polysaccharide sample showed a prominent linear correlation with its sugar content, monosaccharide concentration and the ratio of different molecular weight fractions. The contents of sugar, Fuc and Rha revealed a strong negative correlation with the antioxidant abilities of Noni polysaccharides ($p < 0.05$), indicating that the Noni polysaccharide with high sugar, Fuc and Rha contents had superior antioxidant abilities. It was reported that the Fuc and Rha exerted antioxidative properties by scavenging reactive oxygen species (33), which is consistent with our correlation analysis. Furthermore, the ratio of three molecular weight fractions (high-M_w, medium-M_w, and low-M_w) were significantly correlated with the IC_{50} value of radicals scavenging activity ($p < 0.05$). For the IC_{50} value of radical assay, the ratio of high-M_w and medium-M_w component showed a positive correlation ($p < 0.05$), while the ratio of the low-M_w component demonstrated a negative correlation ($p < 0.05$), indicating that the Noni polysaccharide with a smaller molecular weight showed better radical scavenging ability. Previous studies also reported the superior antioxidative ability of low-molecular-weight polysaccharides, which was attributed to their larger surface area and greater water solubility facilitating the reaction with radicals (34, 35). From **Table 4**, the contents of uronic acid and GalA also displayed a significant linear correlation with the IC_{50} value of hydroxyl assay with the coefficient of −0.991 and −0.913 ($p < 0.05$). The results showed that polysaccharides with high uronic acid content had stronger hydroxyl radical scavenging ability, which was similar to other polysaccharides reported before (36). Although the physicochemical properties of Noni polysaccharide did not show an obvious correlation with the DNA protective effect, a close positive correlation was seen between the DNA protective effect and radical scavenging activity (not shown in **Table 4**). Based on our analysis, the bioactivities of Noni polysaccharide samples were not impacted by a single factor but a function of multiple factors.

Conclusion

Remarkable changes in physicochemical properties and bioactivities of Noni polysaccharides occurred during the fruit ripening process. The highest polysaccharide yield and sugar content were seen at stage 5, whereas the highest uronic acid level was recorded at stage 4. Our results confirmed that the monosaccharide concentrations and proportions, molecular weights, antioxidant activities and DNA protective abilities of Noni polysaccharides varied significantly among five maturity stages, which indicates the necessity for selecting suitable polysaccharides to meet different industrial and nutritional requirements. However, the maturity stages have no remarkable influence on the sulfuric radical content and preliminary structure. Noni polysaccharide extracted at stage 5 showed the strongest scavenging activities against DPPH and ABTS radicals, while the hydroxyl radical scavenging capacity reached the peak at stage 4. Overall, stage 4 and stage 5 are the ideal stages of maturity for extracting high-quality Noni polysaccharides.

Data availability statement

The original contributions presented in this study are included in the article/supplementary material, further inquiries can be directed to the corresponding authors.

Author contributions

JC: conceptualization, experiment, data analyses, and writing. ZL: writing. JL: experiment and data analyses. HL and ZH: review and editing. MM: experiment and editing. XZ: supervision, funding, and review. All authors contributed to the article and approved the submitted version.

Funding

This research was supported by the National Natural Science Foundation of China (32172348 and 31972205), the S&T Projects of Guangdong Province (202102080346), the 111 Project (B17018), the R&D Projects in Key Areas of Guangdong Province (2019B020212004), the China Postdoctoral Science

Foundation (2022M721196), and the Guangdong Basic and Applied Basic Research Foundation (2022A1515110186).

Conflict of interest

The authors declare that the research was conducted in the absence of any commercial or financial relationships that could be construed as a potential conflict of interest.

Publisher's note

All claims expressed in this article are solely those of the authors and do not necessarily represent those of their affiliated organizations, or those of the publisher, the editors and the reviewers. Any product that may be evaluated in this article, or claim that may be made by its manufacturer, is not guaranteed or endorsed by the publisher.

References

1. Jahurul MHA, Patricia M, Shihabul A, Norazlina MR, Ramlah George MR, Noorakmar AW, et al. A review on functional and nutritional properties of noni fruit seed (*Morinda citrifolia* L.) and its oil. *Food Biosci.* (2021) 41:101000. doi: 10.1016/j.fbio.2021.101000

2. Li X, Liu Y, Shan Y, Wang Y, Li Z, Bi Y, et al. MicroRNAs involved in the therapeutic functions of noni (*Morinda citrifolia* L.) fruit juice in the treatment of acute gouty arthritis in mice induced with monosodium urate. *Foods.* (2021) 10:1638. doi: 10.3390/foods10071638

3. Motshakeri M, Ghazali HM. Nutritional, phytochemical and commercial quality of noni fruit: a multi-beneficial gift from nature. *Trends Food Sci Techol.* (2015) 45:118–29. doi: 10.1016/j.tifs.2015.06.004

4. Zhang ZH, Wang LH, Zeng XA, Han Z, Charles BS. Non-thermal technologies and its current and future application in the food industry: a review. *Int J Food Sci Technol.* (2019) 54:1–13. doi: 10.1111/ijfs.13903

5. West BJ, Deng S, Isami F, Uwaya A, Jensen CJ. The potential health benefits of noni juice: a review of human intervention studies. *Foods.* (2018) 7:58. doi: 10.3390/foods7040058

6. Shen ZY, Zhao YY, Qiao ZH, Xie Z, Guan RQ, Liu ZY, et al. Anthraquinones with potential antiproliferative activities from the fruits of *Morinda citrifolia*. *Nat Prod Res.* (2021). [Epub ahead of print]. doi: 10.1080/14786419.2021.2012670

7. Chanda S, Dave R, Kaneria M. In vitro antioxidant property of some Indian medicinal plants. *Res J Med Plants.* (2011) 5:169–79. doi: 10.3923/rjmp.2011.169.179

8. Sousa SG, Oliverira LA, Magalhaes DD, de Brito TV, Batista JA, Pereira CMC, et al. Chemical structure and anti-inflammatory effect of polysaccharide extracted from *Morinda citrifolia* Linn (noni). *Carbohyd Polym.* (2018) 197:515–23. doi: 10.1016/j.carbpol.2018.06.042

9. Pino JA, Marquez E, Quijano CE, Castro D. Volatile compounds in noni *(Morinda citrifolia* L.) at two ripening stages. *Food Sci Tech Brazil.* (2010) 30:183–7. doi: 10.1590/S0101-20612010000100028

10. John A, Yang J, Liu J, Jiang Y, Yang B. The structure changes of water-soluble polysaccharides in papaya during ripening. *Int J Biol Macromol.* (2018) 115:152–6. doi: 10.1016/j.ijbiomac.2018.04.059

11. Li J, Niu DB, Zhang Y, Zeng XA. Physicochemical properties, antioxidant and antiproliferative activities of polysaccharides from *Morinda citrifolia* L. (noni) based on different extraction methods. *Int J Biol Macromol.* (2020) 150:114–21. doi: 10.1016/j.ijbiomac.2019.12.157

12. Zhang DY, Li SJ, Xiong QP, Jiang CX, Lai XP. Extraction, characterization and biological activities of polysaccharides from *Amomum villosum*. *Carbohydr Polym.* (2013) 95:114–22. doi: 10.1016/j.carbpol.2013.03.015

13. Bradford MMA. A rapid and sensitive method for quantitation of microgram quantities of protein utilizing the principle of protein-dye binding. *Anal Biochem.* (1976) 25:248–56.

14. Chen C, You LJ, Abbasi AM, Fu X, Liu RH. Optimization for ultrasound extraction of polysaccharides from mulberry fruits with antioxidant and hyperglycemic activity in vitro. *Carbohydr Polym.* (2015) 130:122–32. doi: 10.1016/j.carbpol.2015.05.003

15. Ren BB, Chen C, Li C, Fu X, You L, Liu RH. Optimization of microwave-assisted extraction of *Sargassum thunbergii* polysaccharides and its antioxidant and hypoglycemic activities. *Carbohydr Polym.* (2017) 173:192–201. doi: 10.1016/j.carbpol.2017.05.094

16. Liang Z, Zhang P, Xiong Y, Johnson SK, Fang Z. Phenolic and carotenoid characterization of the ethanol extract of an Australian native plant *Haemodorum spicatum*. *Food Chem.* (2023) 399:133969. doi: 10.1016/j.foodchem.2022.133969

17. Xu J, Xu LL, Zhou QW, Hao SX, Zhou T, Xie HJ. Isolation, purification, and antioxidant activities of degraded polysaccharides from *Enteromorpha prolifera*. *Int J Biol Macromol.* (2015) 81:1026–30. doi: 10.1016/j.ijbiomac.2015.09.055

18. Wang R, Hu X, Pan JH, Zhang GW, Gong DM. Interaction of isoeugenol with calf thymus DNA and its protective effect on DNA oxidative damage. *J Mol Liq.* (2019) 282:356–65. doi: 10.1016/j.molliq.2019.03.018

19. Charoenchongsuk N, Ikeda K, Itai A, Oikawa A, Murayama H. Comparison of the expression of chlorophyll-degradation-related genes during ripening between stay-green and yellow-pear cultivars. *Sci Hortic.* (2015) 181:89–94. doi: 10.1016/j.scienta.2014.10.005

20. Suzuki Y, Amano T, Shioi Y. Characterization and cloning of the chlorophyll-degrading enzyme pheophorbidase from cotyledons of radish. *Plant Physiol.* (2006) 140:716–25. doi: 10.1104/pp.105.071290

21. Jarvis MC. Structure and properties of pectin gels in plant cell walls. *Plant Cell Environ.* (1984) 7:153–64. doi: 10.1111/1365-3040.ep11614586

22. Ali S, Ullah MA, Nawaz A, Naz S, Shah AA, Gohari G, et al. Carboxymethyl cellulose coating regulates cell wall polysaccharides disassembly and delays ripening of harvested banana fruit. *Postharvest Biol Technol.* (2022) 191:111978. doi: 10.1016/j.postharvbio.2022.111978

23. Yuan Q, Lin S, Fu Y, Nie XR, Liu W, Su Y, et al. Effects of extraction methods on the physicochemical characteristics and biological activities of polysaccharides from okra (*Abelmoschus esculentus*). *Int J Biol Macromol.* (2019) 127:178–86. doi: 10.1016/j.ijbiomac.2019.01.042

24. Lin LH, Xie JH, Liu SC, Shen MY, Tang W, Xie MY. Polysaccharide from *Mesona chinensis*: extraction optimization, physicochemical characterizations and antioxidant activities. *Int J Biol Macromol.* (2017) 99:665–73. doi: 10.1016/j.ijbiomac.2017.03.040

25. Mahmood T, Anwar F, Abbas M, Boyce MC, Saari N. Compositional variation in sugars and organic acids at different maturity stages in selected small fruits from Pakistan. *Int J Biol Macromol.* (2012) 13:1380–92. doi: 10.3390/ijms13021380

26. Ndou A, Tinyani PP, Slabbert RM, Sultanbawa Y, Sivakumar D. An integrated approach for harvesting natal plum (*Carissa macrocarpa*) for quality and functional compounds related to maturity stages. *Food Chem.* (2019) 293:499–510. doi: 10.1016/j.foodchem.2019.04.102

27. Yang M, Zhou D, Xiao H, Fu X, Kong Q, Zhu C, et al. Marine-derived uronic acid-containing polysaccharides: structures, sources, production, and nutritional functions. *Trends Food Sci Technol.* (2022) 122:1–12. doi: 10.1016/j.tifs.2022.02.013

28. Sheng J, Sun Y. Antioxidant properties of different molecular weight polysaccharides from *Athyrium multidentatum* (doll.) Ching. *Carbohydr Polym.* (2014) 108:41–5. doi: 10.1016/j.carbpol.2014.03.011

29. Xu Z, Li X, Feng S, Liu J, Zhou L, Yuan M, et al. Characteristics and bioactivities of different molecular weight polysaccharides from camellia seed cake. *Int J Biol Macromol.* (2016) 91:1025–32. doi: 10.1016/j.ijbiomac.2016.06.067

30. Chen G, Fang C, Ran C, Tan Y, Yu Q, Kan J. Comparison of different extraction methods for polysaccharides from bamboo shoots (*Chimonobambusa quadrangularis*) processing by-products. *Int J Biol Macromol.* (2019) 130:903–14. doi: 10.1016/j.ijbiomac.2019.03.038

31. Li XC, Mai WQ, Wang L, Han WJ. A hydroxyl-scavenging assay based on DNA damage in vitro. *Anal Biochem.* (2013) 438:29–31. doi: 10.1016/j.ab.2013.03.014

32. Singh BN, Singh BR, Singh RL, Prakash D, Dhakarey R, Upadhyay G, et al. Oxidative DNA damage protective activity, antioxidant and anti-quorum sensing potentials of *Moringa oleifera*. *Food Chem Toxicol.* (2009) 47:1109–16. doi: 10.1016/j.fct.2009.01.034

33. Deniaud-Bouët E, Hardouin K, Potin P, Kloareg B, Hervé C. A review about brown algal cell walls and fucose-containing sulfated polysaccharides: cell wall context, biomedical properties and key research challenges. *Carbohydr Polym.* (2017) 175:395–408. doi: 10.1016/j.carbpol.2017.07.082

34. Feng Y, Yang T, Zhang Y, Zhang A, Gai L, Niu D. Potential applicaitions of pulsed electric field in the fermented wine industry. *Front Nutr.* (2022) 10:1048632. doi: 10.3389/fnut.2022.1048632

35. Qi J, Kim SM. Effects of the molecular weight and protein and sulfate content of *Chlorella ellipsoidea* polysaccharides on their immunomodulatory activity. *Int J Biol Macromol.* (2018) 107:70–7. doi: 10.1016/j.ijbiomac.2017.08.144

36. Li XB, Jiang FC, Liu MY, Qu Y, Lan ZQ, Dai XL, et al. Synthesis, characterization, and bioactivities of polysaccharide metal complexes: a review. *J Agric Food Chem.* (2022) 70:6922–42. doi: 10.1021/acs.jafc.2c01349

frontiers | Frontiers in Nutrition

TYPE Original Research
PUBLISHED 10 January 2023
DOI 10.3389/fnut.2022.1111880

OPEN ACCESS

EDITED BY
Zhi-Hong Zhang,
Jiangsu University, China

REVIEWED BY
Lingxiao Yi,
University of Massachusetts Amherst, United States
Qun Huang,
Guizhou Medical University, China
Zhen Feng,
Northeast Agricultural University, China

*CORRESPONDENCE
Fangming Deng
✉ fmdenghnau@sina.com
Lingyan Zhao
✉ LYzhaohnau@hunau.edu.cn

SPECIALTY SECTION
This article was submitted to Nutrition and Food Science Technology, a section of the journal Frontiers in Nutrition

RECEIVED 30 November 2022
ACCEPTED 20 December 2022
PUBLISHED 10 January 2023

CITATION
Wang Z, Zhang Y, Chen C, Fan S, Deng F and Zhao L (2023) A novel bacteriocin isolated from *Lactobacillus plantarum* W3-2 and its biological characteristics. *Front. Nutr.* 9:1111880. doi: 10.3389/fnut.2022.1111880

A novel bacteriocin isolated from *Lactobacillus plantarum* W3-2 and its biological characteristics

Zengguang Wang[1], Yixuan Zhang[1], Chengcheng Chen[2], Shichao Fan[3], Fangming Deng[1]* and Lingyan Zhao[1]*

[1]College of Food Science and Technology, Hunan Agricultural University, Changsha, China, [2]Hunan Guotai Foods Co., Ltd., Yueyang, Hunan, China, [3]Junjie Food Technology Co., Ltd., Shaoyang, China

In this study, screening bacteriocin-producing strains from 2,000 plant-derived strains by agar well diffusion method was conducted. The corresponding produced bacteriocin was purified and identified by Sephadex gel chromatography, reversed-phase high-performance liquid chromatography (RP-HPLC), and liquid chromatography coupled with tandem mass spectrometry (LC-MS/MS). Meanwhile, the biological characteristics of bacteriocin were investigated. The targeted strain W3-2 was obtained and identified as *Lactobacillus plantarum* by morphological observation and 16S rRNA gene sequence analysis. Correspondingly, a novel bacteriocin (named plantaricin W3-2) produced by *L. plantarum* W3-2 with a molecular weight of 618.26 Da, and an amino acid sequence of AVEEE was separated, purified by Sephadex gel chromatography and RP-HPLC, and identified by LC-MS/MS. Further characteristics analysis displayed that plantaricin W3-2 had good thermal, pH stability, and broad-spectrum antimicrobial ability. In conclusion, plantaricin W3-2 can be used as a new food preservative.

KEYWORDS

bacteriocin, lactic acid bacteria, biological characteristics, separation and purification, antimicrobial activity

1. Introduction

Antimicrobial peptides (AMPs) are a kind of small molecular peptides with antimicrobial activity, which widely exist in animals, plants, and microorganisms (1). Natural antimicrobial peptides have an antimicrobial effect on bacteria, fungi, and viruses (2). Recently, bacteriocin, as a kind of natural antimicrobial peptide, has been extensively studied and become a potential alternative to chemical preservatives. Bacteriocins, which are ribosomally synthesized in prokaryotes, can inhibit or kill phylogenetically related and/or unrelated microorganisms, but they have no antimicrobial effect on bacteriocin-producing strains themselves (3).

A large number of bacteriocin-producing lactic acid bacterias (LABs) have been successfully isolated from Chinese traditional fermented food. Yi Lanhua et al. isolated *Lactobacillus pentosum* DZ35 from salting meat products and obtained bacteriocin pentocin DZ1 and pentocin DZ2, with molecular weights of 4004.03 and 12719.37 Da, respectively (4). Benmouna et al. isolated *Enterococcus* CM9 from camel milk–producing bacteriocin with a molecular weight of 7.6 KDa (5). Ramakrishnan et al. isolated *Lactobacillus rhamnosus* L34 from curds producing bacteriocin with a molecular weight of 5.6 KDa (6). Although a great deal of work has been carried out to study the purification, structure, and characteristics of bacteriocin secreted by LABs, most bacteriocins could not be widely and effectively used in food because of narrow antimicrobial spectrum, poor thermal stability, and high production cost (7). Nisin is the only natural preservative approved by FAO/WHO to be used in food (8). Therefore, novel bacteriocins with a broad antimicrobial spectrum and good thermal stability remain to be explored.

In this study, LAB isolated from the plant-derived strain library with antimicrobial activity were screened and identified. Purification, characterization, and antimicrobial properties of a novel bacteriocin were studied to get a novel bacteriocin and evaluate its potential as a biological preservative.

2. Materials and methods

2.1. Strains and medium

Indicator strains are as follows: *Escherichia coli* (CGMCC9181), *Staphylococcus aureus* (ATCC6538), *Listeria monoeytogenes* (ATCC19115), *Bacillus subtilis*, *Salmonella*, *Bacillus cereus* [CMCC(B)63301], *Shigella* [CMCC(B)51105], *Micrococcus luteus* [CMCC(B)28001], *Pseudomonas aeruginosa* (ATCC15442), and *Proteusbacillus vulgaris* [CMCC(B)49027].

Test strains: 2,000 test strains used in this study were obtained from the plant-derived strain library in the Food Science and Technology of Hunan Agricultural University.

de Man, Rogosa and Sharpe (MRS) broth: caseinase digest 10.0 g/L, beef paste powder 10.0 g/L, yeast paste powder 4.0 g/L, diammonium hydrogen citrate 2.0 g/L, sodium acetate 5.0 g/L, magnesium sulfate heptahydrate 0.2 g/L, manganese sulfate tetrahydrate 0.05 g/L, dipotassium hydrogen phosphate 2.0 g/L, glucose 20.0 g/L, and tween-80 1.08 g/L.

Nutrient broth: Peptone 10.0 g/L, beef paste powder 3.0 g/L, and sodium chloride 5.0 g/L.

2.2. Preparation of cell-free fermentation supernatant (CFS)

Strains were inoculated in MRS broth and cultivated at 37°C for 24 h. CFS was obtained by centrifugation at 4°C and 10,000 r/min for 15 min to remove the bacteria precipitate. The supernatant was collected and filtered through 0.22 μm filter membrane to remove residual bacteria. Samples were stored at 4°C for further analysis (9, 10).

2.3. Screening of the antimicrobial potential strains

The bacteriocin-producing potential strains against *E. coli* and *S. aureus* were investigated using the agar well diffusion method according to Bian et al. with a sight modification (11). The pH of CFS was adjusted to 6 using 1 M NaOH (12, 13). Fifteen milliliters of 2% (v/v) plain agar were poured onto a plate to solidify. Three oxford cups were put on it; 100 μl of indicator strain (10^8 CFU ml^{-1}) was inoculated into 200 ml of nutrient broth medium at 50°C. A 20 ml of the mixture was poured onto the agar medium and allowed to solidify. Then, the Oxford cups were removed; 200 μl of CFS (pH = 6) was poured into holes. The plate was placed at 4°C for 4 h and incubated for 12 h at 37°C. The antimicrobial activity was reflected by the growth-free inhibition zones, and the lactic acid solution (pH = 6) was used as the control. The diameters of the inhibition zone were measured with a digital caliper (MNT-150, Shanghai, China) by cross method to determine the antimicrobial activity (14).

2.4. Determination of the antimicrobial substances

To clarify whether the antimicrobial activity was derived from the hydrogen peroxide in CFS, 2 mg/ml catalase was added to CFS (pH = 6) at a ratio of 1:1 (v/v) and incubated at 37°C for 2 h. The antimicrobial activity was detected following the description as outlined in Section "Screening of the antimicrobial potential strains" using CFS (pH = 6) as the control, and the CFS with antimicrobial activity was selected for protease test (15, 16). After eliminating the impact of hydrogen peroxide and organic acids, 1 ml of CFS was treated for 2 h at 37°C with 1 mg/ml final concentration of trypsin, protease K, and pepsin (17). The antimicrobial activity was detected following the description as outlined in Section "Screening of the antimicrobial potential strains." CFS with no protease process was used as the control.

2.5. Identification of bacteriocin-producing strains

2.5.1. Morphological characteristics observation

Bacteriocin-producing strains were inoculated into MRS broth and cultured at 37°C for 24 h. After incubation, the colony

color and morphology of the strain were observed. A light microscope (CX31, 10 × 100/Oil, Olympus, Tokyo, Japan) was used to observe the colony morphology characteristics of the strain.

2.5.2. 16S rRNA gene sequence analysis

Genomic DNA was extracted using bacterial genomic DNA extraction kit (Solarbio, Beijing Solarbio Technology Co., Ltd., Beijing, China). 16S rDNA gene sequence was amplified using the forward primer 5′-AGAGTTTGATCCTGGCTCAG-3′ and the reverse primer 5′-CTACGGCTACCTTGTTACGA-3′. The PCR amplification products were recovered by AxyPrep DNA Gel Recovery Kit (Solarbio, Beijing Solarbio Technology Co., Ltd., Beijing, China) and sequenced by Shanghai Paisano Co., Ltd. (Shanghai, China). 16S rRNA gene sequences were submitted to the NCBI database for homology analysis using the BLAST tool. A phylogenetic tree was constructed by MEGA6 software.

2.6. Isolation and purification of bacteriocins

2.6.1. Extraction of bacteriocin

The CFS was concentrated twice using a rotary evaporator at 55°C, mixed with ethyl acetate in a ratio of 1:2, stirred at 100 rpm at 25°C for 2 h, and placed overnight for stratification. The upper organic phase was pooled and evaporated under a vacuum at 55°C using a rotary evaporator (Yarong, SY-5000, Shanghai, China) to obtain the crude bacteriocin extract (18). Samples were stored at 4°C for further analysis.

2.6.2. Sephadex gel chromatography

In all, 2 ml of crude bacteriocin extract was initially filtered with 0.22 μm filter membrane, then samples were loaded in Sephadex G-25 gel chromatography column (Henghuibio, 1.5 cm × 80 cm, Beijing, China) to eliminate impurities, The samples were eluted with sterile water (pH5.5) with a linear gradient at a flow rate of 0.5 ml/min and measured by UV detector at 280 nm. The fractions were collected according to an automatic collection device (19). Using *S. aureus* as an indicator strain, the antimicrobial activity of each fraction was detected by agar well diffusion method.

The fractions with antimicrobial effect were pooled, concentrated, dried, and dissolved in PBS (pH 5.5) as well as loaded onto the Sephadex LH-20 gel chromatography column (Henghuibio, 1.5 cm × 80 cm, Beijing, China) and eluted by 80% methanol at a flow rate of 0.25 ml/min with a UV detector at 280 nm. Each of fractions was collected, and antimicrobial activity was detected (17). The active fractions with antimicrobial activity were pooled for full-wavelength scanning, with the maximum absorption peak as the detection wavelength for the next purification.

2.6.3. RP-HPLC purification

Fractions with antimicrobial effect collected from the Sephadex LH-20 gel chromatography column (Henghuibio, 1.5 cm × 80 cm, Beijing, China) were filtered with 0.22-μm filter membrane and further purified by RP-HPLC (SCG100-V2, Suzhou Sepure Instruments Co., Ltd., Suzhou, China) (20). The purification conditions were as follows: C18 column (Phenomenex Jupiter C18, 4.6 mm × 250 mm, Phenomenex, USA), mobile phase A comprised 85% water and 15% acetonitrile (containing 0.07% trifluoroacetic acid), gradient: 100% A within 35 min, flow rate at 1 ml/min, the volume of samples loaded into the system was 500 μl. UV detector was set at 220 nm (21). A component of each peak was collected, concentrated by freezing, and then, dissolved in PBS (pH 5.5). Antimicrobial activity was detected by agar well diffusion method using *S. aureus* as an indicator strain.

2.6.4. Identification of bacteriocin

Nano liquid chromatography coupled with tandem mass spectrometry analysis was performed to determine the molecular mass and amino acid sequence of the purified bacteriocin. The bacteriocin purified by RP-HPLC (SCG100-V2, Suzhou Sepure Instruments Co., Ltd., Suzhou, China) was reduced by 10 mM DL-dithiothreitol (Sigma-Aldrich, St. Louis, MO, USA) at 56°C for 1 h and alkylated by 50 mM iodoacetamide (Sigma-Aldrich, St. Louis, MO, USA) at room temperature in dark for 40 min. Lyophilize the extracted bacteriocin to near dryness. Resuspend peptides in 20 μl of 0.1% formic acid (Sigma-Aldrich, St. Louis, MO, USA) before LC-MS/MS analysis. The analysis of bacteriocin was conducted by nano LC-MS/MS in an Easy-nLC 1200 system (Thermo Fisher Scientific, Waltham, MA, USA) coupled with a Q Exactive™ Hybrid Quadrupole-Orbitrap™ Mass Spectrometer (Thermo Fisher Scientific, Waltham, MA, USA) with an electrospray nanospray source. An in-house built reverse-phase nanocolumn (150 μm × 15 cm, 1.9 μm, 100 Å, Dr. Maisch GmbH, Germany) packed with Acclaim PepMap was used. Mobile phase A consisted of 0.1% formic acid in water, mobile phase B comprised 20% of 0.1% formic acid in water- 80% acetonitrile. Liquid chromatography linear gradient: from 4 to 8% B for 2 min, from 8 to 28% B for 43 min, from 28 to 40% B for 10 min, from 40 to 95% B for 1 min, and from 95 to 95% B for 10 min. Total flow rate is at 600 nL/min. A first-order mass spectrometry spectrum was obtained in a full-scan positive ion mode of m/z 300–1800. The second-order mass spectrometry data were collected using collision-induced dissociation to capture the *b* and *y* ions (22). The data acquisition and analysis were conducted by PEAKS Studio 8.5 software.

2.7. Thermal stability of plantaricin W3-2

Plantaricin W3-2 was heated at 60, 70, 80, 90, 100, and 121°C for 10 min, then cooled to room temperature. The antimicrobial activity was detected by agar well diffusion method, using unheated plantaricin W3-2 as the control (23).

2.8. pH stability of plantaricin W3-2

pH value of plantaricin W3-2 was adjusted to 2, 3, 4, 5, 6, 7, 8, 9, 10, 11, and 12 with 1 mol/L HCL and 1 mol/L NaOH, respectively, and heated at 37°C for 2 h by water bath, then pH value was adjusted back to 6. The antimicrobial activity was detected by agar well diffusion method, using untreated plantaricin W3-2 as the control (24, 25).

2.9. Antimicrobial spectrum of plantaricin W3-2

The antimicrobial spectrum of plantaricin W3-2 was studied using the agar well diffusion method. *E. coli* (CGMCC9181), *S. aureus* (ATCC6538), *L. monoeytogenes* (ATCC19115), *B. subtilis*, *Salmonella*, *B. cereus* [CMCC(B)63301], *Shigella* [CMCC(B)51105], *M. luteus* [CMCC(B)28001], *P. aeruginosa* (ATCC15442), and *P. vulgaris* [CMCC(B)49027] were used as indicator strains.

TABLE 1 Strains retained antimicrobial activity against *Escherichia coli* and *Staphylococcus aureus* after eliminating the influence of organic acid.

Strain number	Strain source	Mycelial morphology	Diameter of inhibition zone (mm)	
			E. coli	*S. aureus*
Lactic acid (pH6)	–	–	–	–
17	Fermented pepper	Bacilli	15.39 ± 0.14^{cd}	12.52 ± 0.04^{L}
38	Fermented pepper	Bacilli	16.08 ± 0.24^{b}	16.34 ± 0.06^{C}
3-3	Fermented mustard	Bacilli	13.75 ± 0.08^{g}	12.43 ± 0.04^{L}
3-20	Fermented mustard	Bacilli	14.10 ± 0.16^{f}	15.94 ± 0.13^{D}
Z3-10	Fermented pepper	Bacilli	11.19 ± 0.04^{m}	12.82 ± 0.08^{K}
Z3-19	Fermented pepper	Bacilli	12.13 ± 0.11^{k}	11.69 ± 0.04^{N}
Z3-27	Fermented pepper	Bacilli	13.20 ± 0.02^{i}	13.06 ± 0.08^{J}
Z3-35	Fermented pepper	Bacilli	16.06 ± 0.17^{b}	15.97 ± 0.08^{D}
Z3-37	Fermented pepper	Bacilli	11.98 ± 0.06^{k}	11.26 ± 0.07^{O}
Z3-38	Fermented pepper	Bacilli	13.77 ± 0.09^{g}	12.76 ± 0.07^{K}
C1-4	Fermented radish	Coccus	14.01 ± 0.12^{f}	16.77 ± 0.08^{AB}
C1-5	Fermented radish	Coccus	15.21 ± 0.11^{d}	15.17 ± 0.08^{F}
C1-10	Fermented radish	Coccus	12.76 ± 0.09^{j}	11.17 ± 0.04^{OP}
C1-13	Fermented radish	Coccus	12.02 ± 0.17^{k}	11.09 ± 0.06^{P}
C1-20	Fermented radish	Coccus	15.54 ± 0.05^{c}	11.65 ± 0.06^{N}
C1-24	Fermented radish	Coccus	15.37 ± 0.08^{cd}	13.03 ± 0.08^{J}
C2-2	Fermented radish	Coccus	11.66 ± 0.07^{l}	11.84 ± 0.07^{M}
C2-4	Fermented radish	Coccus	13.36 ± 0.07^{hi}	11.95 ± 0.07^{M}
W3-2	Fermented pepper	Bacilli	17.54 ± 0.06^{a}	16.68 ± 0.04^{B}
X13-5	Fermented pepper	Coccus	13.55 ± 0.10^{gh}	16.89 ± 0.06^{A}
X13-6	Fermented pepper	Coccus	13.36 ± 0.07^{hi}	13.72 ± 0.04^{I}
X13-7	Fermented pepper	Bacilli	15.52 ± 0.12^{c}	14.83 ± 0.06^{G}
X13-11	Fermented pepper	Bacilli	14.43 ± 0.04^{e}	14.19 ± 0.04^{H}
Z1-2	Fermented mustard	Bacilli	15.21 ± 0.04^{d}	15.34 ± 0.05^{E}
Z3-27	Fermented mustard	Bacilli	13.16 ± 0.07^{i}	13.01 ± 0.10^{J}

"–" Means no inhibition. Values represent means of three independent replicates ± SD. Different letters within a column indicate statistically significant differences between the means ($p < 0.05$).

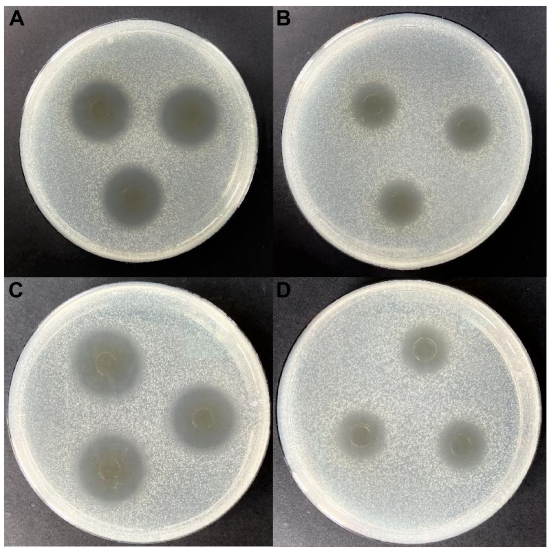

FIGURE 1
Antimicrobial activity of the cell-free fermentation supernatant (CFS) of strain W3-2 against *Staphylococcus aureus* and *Escherichia coli*. **(A)** Before eliminating the contribution of hydrogen peroxide to the antimicrobial activity on *S. aureus*. **(B)** After eliminating the contribution of hydrogen peroxide to the antimicrobial activity on *S. aureus*. **(C)** Before eliminating the contribution of hydrogen peroxide to the antimicrobial activity on *E. coli*. **(D)** After eliminating the contribution of hydrogen peroxide to the antimicrobial activity on *E. coli*.

2.10. Statistical analysis

The study was carried out using three experimental replicates. Results are presented as mean ± SD. Analysis of variance (ANOVA) was used, and the means were separated at a significance level of $p < 0.05$. The data were analyzed and processed using Excel, IBM SPSS Statistics 26, and Origin 2019 software.

3. Results and discussion

3.1. Screening and identification of bacteriocin-producing lactic acid bacteria

3.1.1. Screening bacteriocin-producing lactic acid bacteria

Lactic acid bacteria can produce organic acids and hydrogen peroxide, which can inhibit the growth of other strains (26, 27). Both of them have been reported to act on the cytoplasmic membrane by neutralizing its electrochemical potential and increasing its permeability, resulting in bacteriostasis and ultimately death of susceptible bacteria (28). In this study, isolating and screening bacteriocin-producing strains from 2,000 plant-derived strains by agar well diffusion method with *E. coli* and *S. aureus* as indicator strains were conducted. Results indicated that 25 strains were initially isolated after eliminating the contribution of organic acid (Table 1). Further elimination of the contribution of hydrogen peroxide, only strain W3-2 exhibited the strongest antimicrobial activity with the diameters of the inhibition zone against *E. coli* and *S. aureus* exceeded 16 mm (Figure 1). Therefore, strain W3-2 was selected for subsequent tests.

In order to confirm the antimicrobial active substance is bacteriocin, the CFS of strain W3-2 was treated with trypsin, pepsin, and proteinase K, respectively. As shown in Table 2, results displayed that the diameters of the inhibition zone against *S. aureus* decreased from 16.68 ± 0.04 to 10.25 ± 0.18 mm, 10.55 ± 0.24 mm, and 13.22 ± 0.15 mm after being treated with trypsin, pepsin, and proteinase K, respectively. These results indicated that bacteriocin was the main antimicrobial substance in CFS of W3-2. Bacteriocin can damage the structure of cell membrane, making the cell membrane form pores, leading to cell rupture and the outflow of small molecules, such as potassium ions, magnesium ions, phosphorus ions, amino acids, and ATP (29). The low level of ATP and ion deficiency in cells result in the inhibition of the synthesis of DNA, RNA, proteins, and polysaccharides, ultimately leading to cell death (30). Bacteriocin BM1122 led to the separation of the plasma wall of *S. aureus* and the formation of pores in *E. coli* and could inhibit the formation of biofilm, disrupt the normal cell cycle, thus damage the integrity of cell membrane (31). In addition, bacteriocin can also induce cell death by changing the permeability of cell membrane or the activity of intracellular enzymes, inhibiting the germination of spores and the respiration of sensitive bacteria interfering with the normal metabolism of nucleic acids, proteins, and other substances in cells (32).

3.1.2. Identification of strain W3-2

Strain W3-2 was further identified by colony morphology and 16S rRNA gene sequence analysis. As shown in Figure 2A, the colonies of strain W3-2 were medium-sized, raised, creamy white, rounded, and with neat edges. It is a gram-positive strain with single or arranged in chains, rod-shaped, and spore-free (Figure 2B). The strain W3-2 was amplified by PCR, and the gel electrophoresis results of the PCR are shown in Figure 2C.

TABLE 2 The diameters of the inhibition zone of strain W3-2 against *Staphylococcus aureus* after protease treatment.

Treatment	Diameter of inhibition zone (mm)
CK	16.68 ± 0.04
Trypsin	10.25 ± 0.18
Pepsin	10.55 ± 0.24
Proteinase K	13.22 ± 0.15

TABLE 3 The diameters of the inhibition zone of plantaricin W3-2 against various indicator strains.

Strain properties	Indicator strains	Source	Diameter of inhibition zone (mm)
Gram-positive bacteria	*Staphylococcus aureus*	ATCC6538	29.14 ± 0.12
	Listeria monocytogenes	ATCC19115	28.88 ± 0.15
	Bacillus subtilis	Lab preservation	21.02 ± 0.22
	Bacillus cereus	CMCC(B)63301	28.79 ± 0.15
	Micrococcus luteus	CMCC(B)28001	21.80 ± 0.05
Gram-negative bacteria	*Pseudomonas aeruginosa*	ATCC15442	26.91 ± 0.18
	Escherichia coli	CMCC9181	27.32 ± 0.14
	Salmonella	Lab preservation	21.70 ± 0.42
	Shigella	CMCC(B)51105	22.29 ± 0.06
	Proteus mirabilis	CMCC(B)49027	23.47 ± 0.15

Results showed that the 16S rRNA gene sequence length of strain W3-2 was 1,466 bp, and the homology with *Lactobacillus plantarum* was more than 99.86% (Figure 2D). Combined morphological characteristics with 16S rRNA gene sequence analysis, strain W3-2 was identified as *L. plantarum*. Swapnil et al. isolated a bacteriocin-producing *L. plantarum* from the colon part of honey bee and the rectum region of stomach (33).

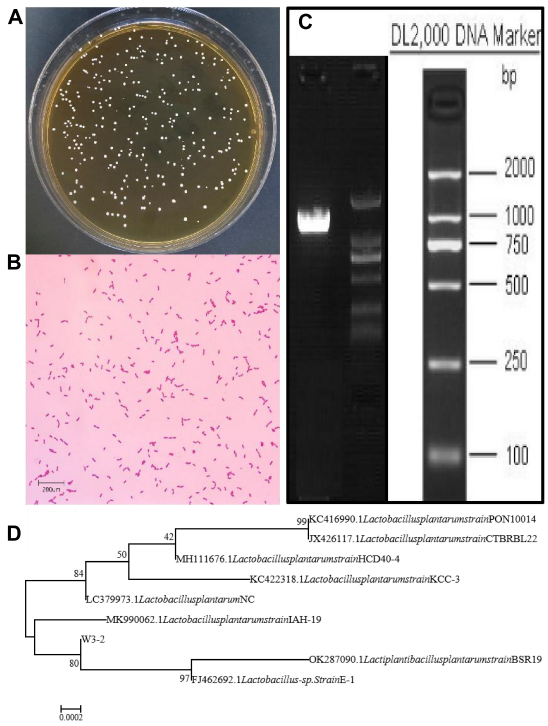

FIGURE 2
Identification of strain W3-2. **(A)** Colony morphology of strain W3-2. **(B)** Microscopy feature of strain W3-2 after Gram staining (10 × 100/Oil). **(C)** Agarose gel electrophoresis of PCR amplification products of strain W3-2. **(D)** Phylogenetic tree of strain W3-2 based on 16S rRNA sequence.

Mills et al. isolated *L. plantarum* from handmade cheese that can inhibit the growth of *Listeria* (34).

3.2. Purification and identification of the bacterin

3.2.1. Sephadex gel chromatography and RP-HPLC purification

The ethyl acetate extracted bacteriocin produced by *L. plantarum* W3-2 was purified by gel filtration chromatography. As shown in Figure 3A, there were four elution peaks in the purification process of Sephadex G-25. It was proved that only the second elution peak had antimicrobial activity against *S. aureus*, while the other three elution peaks had no inhibitory effect. The eluent of tubes 59–70 was collected and concentrated (Figure 3B). After further purification by Sephadex LH-20 (Figure 3C), a single elution peak with similar antimicrobial activity was appeared. The eluent corresponding to the 44th–51th tubes was collected for subsequent purification (Figure 3D). There were five absorption peaks after being purified by RP-HPLC (Figure 3E). Except for the one at 5.578 min, the other absorption peaks had no antimicrobial effect. Therefore, eluent at peak time of 5.578 min was collected for further analysis.

3.2.2. Identification of bacteriocin structure by LC-MS/MS

Eluent at a retention time of 5.578 min was collected and identified by LC-MS/MS. As shown in Figure 4A, the primary mass spectrometry displayed that the molecular weight of the bacteriocin was 618.26 Da and named as plantaricin W3-2. The primary mass spectrum peak was further analyzed by *De novo*, and the secondary mass spectrum was finally obtained. As shown in Figure 4B, the entire amino acid sequence was detected as AVEEE. Plantaricin W3-2 is a polypeptide composed of five amino acids with

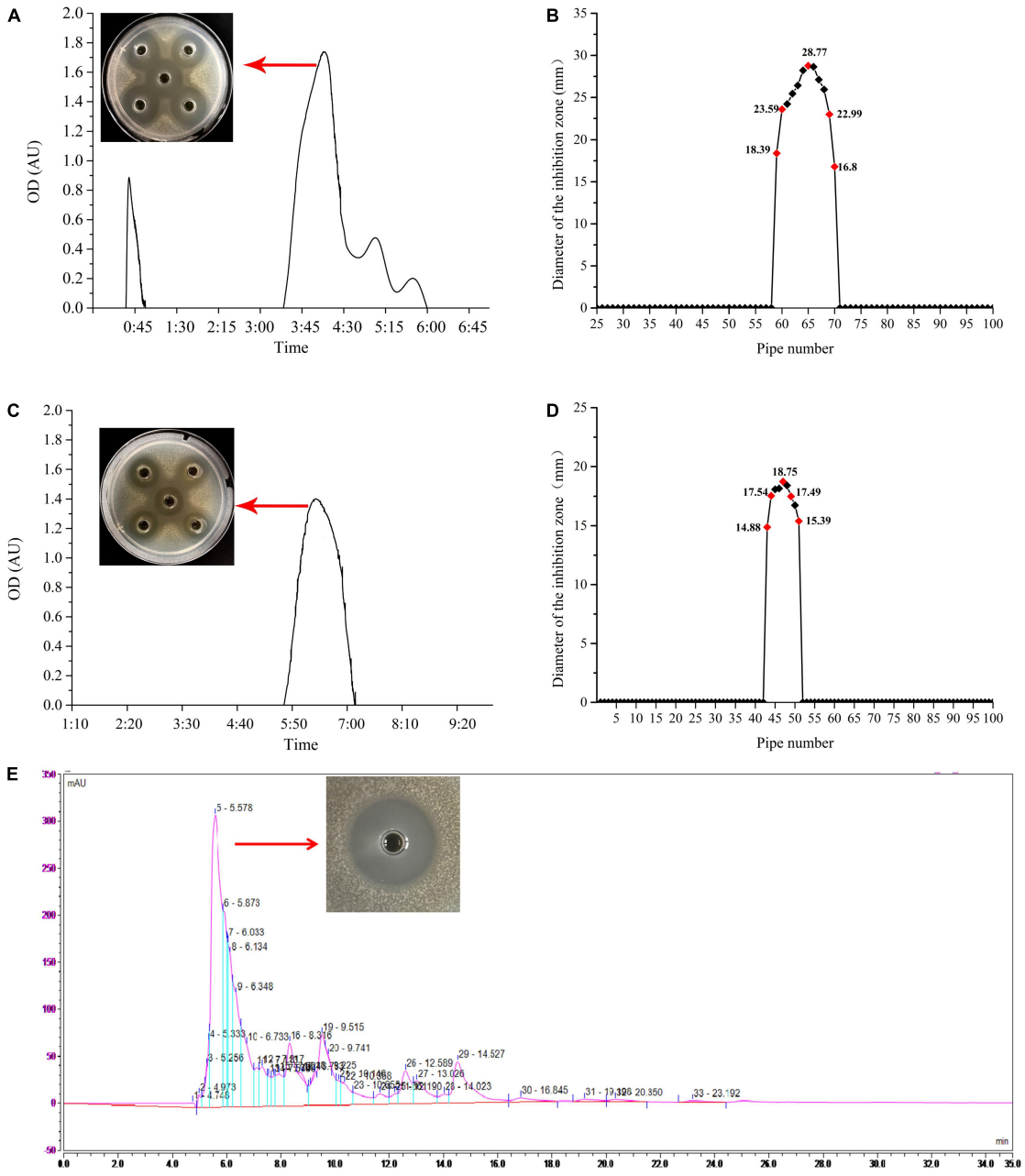

FIGURE 3
The process of purification of the bacteriocin produced by strain W3-2. **(A)** Sephadex G-25 gel profile. **(B)** Sephadex G-25 elution curve. **(C)** Sephadex LH-20 gel profile. **(D)** Sephadex LH-20 elution curve. **(E)** Reversed-phase high-performance liquid chromatography (RP-HPLC) purification profile.

antimicrobial activity. Bacteriocins, with the same molecular weight and amino acid sequence, have not been reported in the present study.

Most of the molecular weights of bacteriocins reported at present are between 1 and 10 KDa. For example, plantaricin SLG1 produced by *L. plantarum* SLG1 isolated from yak cheese has a molecular weight of 1083.25 Da (35); plantaricin JY22 produced by *L. plantarum* JY22 isolated from the intestine of golden carp has a molecular weight of 4.1 KDa (36); and plantaricin H5 produced by *L. plantarum* H5 isolated from the intestinal flora of sturgeon has a molecular weight of 3.0 KDa (37). Plantaricin W3-2 has a molecular weight of 618.26 Da, which belongs to the small molecular weight bacteriocin. Similarly, the molecular weight of the plantarum C010 is 260.1161 Da produced by *L. plantarum* C010 isolated from cow manure (17).

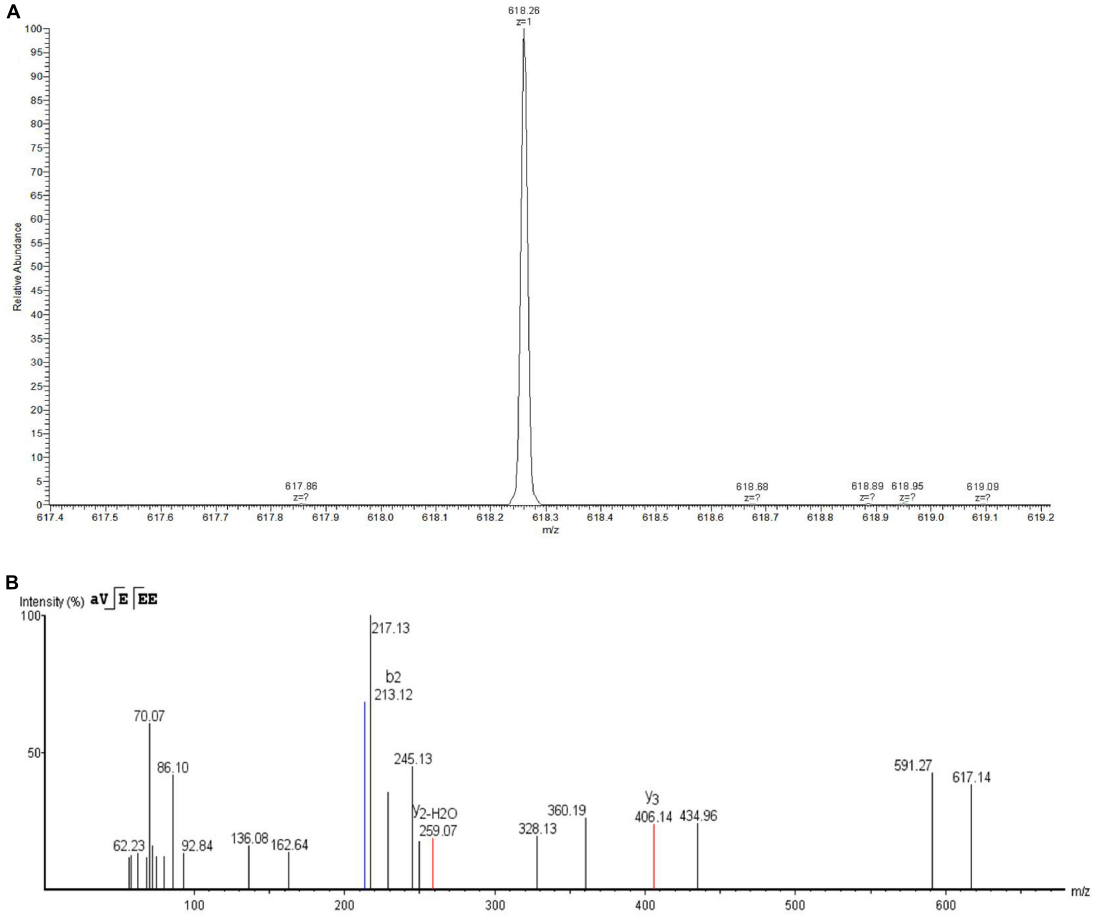

FIGURE 4
Identification of plantaricin W3-2 by liquid chromatography coupled with tandem mass spectrometry (LC-MS/MS). **(A)** Primary mass spectrometry of plantaricin W3-2. **(B)** Secondary mass spectrometry of plantaricin W3-2.

3.3. Biological characteristic of plantaricin W3-2

3.3.1. Thermal stability of plantaricin W3-2

Thermal stability of plantaricin W3-2 was envaulted. As depicted in **Figure 5A**, compared to control group, no significant difference in antimicrobial effect on *S. aureus* by plantaricin W3-2 was observed after exposure to 60, 70, and 80°C for 10 min. After being treated at 100°C, 82.2% antimicrobial activity was retained. Further, the increase in temperature to 121°C, and 73.4% antimicrobial activity was kept. Those results elucidated that plantaricin W3-2 had good thermal stability. The reason may be ascribed to small hydrophobic proteins, almost without tertiary structure, with strong hydrophobic region and stable cross-linking structure. The good thermal stability of the plantaricin W3-2 is similar to the bacteriocin produced by *L. plantarum* SLG1 isolated from yak cheese, which exhibits good antimicrobial activity even after being heated at 100°C for 20 min (35).

3.3.2. pH stability of plantaricin W3-2

Results of pH stability of plantaricin W3-2 are shown in **Figure 5B**, and the antimicrobial activity of plantaricin W3-2 was significantly affected by the change in pH. It was enhanced by acidic environment, while inhabited by basic environment. The antimicrobial activity on *S. aureus* was the largest at pH 2, with diameter of 24.6 mm. The inhibition zone was gradually decreased with the increase in pH and retained 64.3% antimicrobial activity at pH 11. These results proved that plantaricin W3-2 not only had a good antimicrobial effect in acidic environment but also retained its function in a basic environment.

3.3.3. Antimicrobial spectrum of plantaricin W3-2

Ten kinds of common pathogenic bacteria in food were used as indicator strains to test the antimicrobial effect of plantaricin W3-2. Results showed that the diameters of the inhibition zone of plantaricin W3-2 against *S. aureus*, *Listeria*

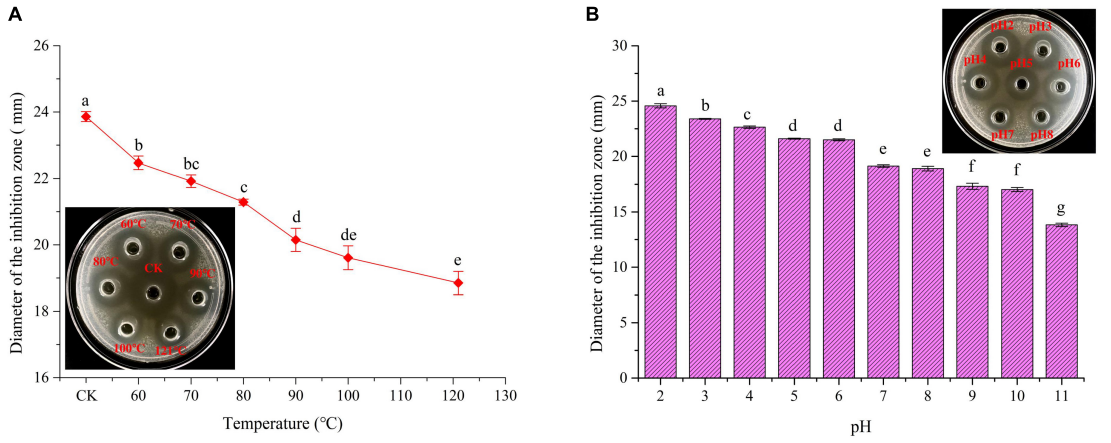

FIGURE 5
Thermal and pH stability of plantaricin W3-2. **(A)** Thermal stability of plantaricin W3-2, inserted: picture was corresponding inhibition zone, CK was the control group. **(B)** pH stability of plantaricin W3-2. Different letters indicate statistically significant differences between the means ($p < 0.05$).

monocytogenes, and *B. cereus* reached 28 mm. For *B. subtilis*, *M. luteus, E. coli*, *P. aeruginosa*, *Salmonella*, *Shigella*, *Proteus*, and other indicator strains, the diameter of the inhibition zone of plantaricin W3-2 was around 21 mm (Table 3). These results demonstrated that plantaricin W3-2 had broad-spectrum antimicrobial activity.

4. Conclusion

In conclusion, *L. plantarum* W3-2 was screened from 2,000 strains in the plant-derived strain library in our laboratory, and corresponding plantaricin W3-2 with 618.26 Da and AVEEE amino acid sequence were obtained. Further, characteristics analysis displayed that plantaricin W3-2 had good thermal, pH stability, and broad-spectrum antimicrobial ability. Safety, application, and antimicrobial mechanism against foodborne pathogens of the plantaricin W3-2 will be investigated in our further studies.

Data availability statement

The original contributions presented in this study are included in the article/supplementary material, further inquiries can be directed to the corresponding authors.

Author contributions

FD and LZ designed the work. ZW performed the experimental work and prepared the initial draft of the manuscript. CC and SF critically revised the manuscript. All authors contributed to the article and approved the submitted version.

Funding

This research was funded by the National Natural Science Foundation of China (Project No. 31401675), the Hunan Provincial Department of Science and Technology Support Program (Project Nos. 2015NK3011 and 2016NK2110), the Double First-class Construction Project of Hunan Agricultural University (Project No. SYL201802006), and the National Modern Agricultural Industrial Technology System (Project No. CARS-24-E-02).

Conflict of interest

CC was employed by Hunan Guotai Foods Co., Ltd. SF was employed by Junjie Food Technology Co., Ltd.

The remaining authors declare that the research was conducted in the absence of any commercial or financial relationships that could be construed as a potential conflict of interest.

Publisher's note

All claims expressed in this article are solely those of the authors and do not necessarily represent those of their affiliated organizations, or those of the publisher, the editors and the reviewers. Any product that may be evaluated in this article, or claim that may be made by its manufacturer, is not guaranteed or endorsed by the publisher.

References

1. Simonson A, Aronson M, Medina S, Guler M. Supramolecular peptide assemblies as antimicrobial scaffolds. *Molecules.* (2020) 25:25122751. doi: 10.3390/molecules25122751

2. Luong H, Thanh T, Tran T. Antimicrobial peptides – advances in development of therapeutic applications. *Life Sci.* (2020) 260:118407. doi: 10.1016/j.lfs.2020.118407

3. Piard J, Muriana P, Desmazeaud M, Klaenhammer T. Purification and partial characterization of lacticin 481, a lanthionine-containing bacteriocin produced by *Lactococcus lactis* Subsp. Lactis Cnrz 481. *Appl Environ Microbiol.* (1992) 58:279–84. doi: 10.1128/AEM.58.1.279-284.1992

4. Yi L, Qi T, Hong Y, Deng L, Zeng K. Screening of bacteriocin-producing lactic acid bacteria in Chinese homemade pickle and Dry-cured meat, and bacteriocin identification by genome sequencing. *LWT-Food Sci Technol.* (2020) 125:109177. doi: 10.1016/j.lwt.2020.109177

5. Benmouna Z, Dalache F, Karam N, Zadi-Karam H. Optimization and some characteristics of bacteriocin produced by *Enterococcus* Sp Cm9 collected from Mauritanian camel milk. *Emir J Food Agric.* (2018) 30:275–82. doi: 10.9755/ejfa.2018.v30.i4.1662

6. Ramakrishnan S, Kumawat D, Sunil K, Kumar S. Purification and characterization of a bacteriocin from *Lactobacillus rhamnosus* L34. *Ann Microbiol.* (2013) 63:387–92. doi: 10.1007/s13213-012-0486-8

7. Yi L, Luo L, Lu X. Efficient exploitation of multiple novel bacteriocins by combination of complete genome and peptidome. *Front Microbiol.* (2018) 9:01567. doi: 10.3389/fmicb.2018.01567

8. Kaktcham P, Kouam E, Tientcheu M, Temgoua J, Wacher C, Ngoufack F, et al. Nisin-producing *Lactococcus lactis* Subsp. Lactis 2mt isolated from freshwater Nile tilapia in cameroon: bacteriocin screening, characterization, and optimization in a low-cost medium. *LWT-Food Sci Technol.* (2019) 107:272–9. doi: 10.1016/j.lwt.2019.03.007

9. Merlich A, Galkin M, Choiset Y, Limanska N, Vasylieva N, Ivanytsia V, et al. Characterization of the Bacteriocin Produced by *Enterococcus* Italicus Onu547 isolated from Thai fermented cabbage. *Folia Microbiol.* (2019) 64:535–45. doi: 10.1007/s12223-019-00677-4

10. Arakawa K. Basic antibacterial assay to screen for bacteriocinogenic lactic acid bacteria and to elementarily characterize their bacteriocins. *Methods Mol Biol.* (2019) 1887:15–22. doi: 10.1007/978-1-4939-8907-2_2

11. Bian X, Evivie S, Muhammad Z, Luo G, Liang H, Wang N, et al. In vitro assessment of the antimicrobial potentials of *Lactobacillus helveticus* strains isolated from traditional cheese in Sinkiang china against food-borne pathogens. *Food Funct.* (2016) 7:789–97. doi: 10.1039/c5fo01041a

12. Pinto A, Barbosa J, Albano H, Isidro J, Teixeira P. Screening of bacteriocinogenic lactic acid bacteria and their characterization as potential probiotics. *Microorganisms.* (2020) 8:393. doi: 10.3390/microorganisms8030393

13. Ndlovu B, Schoeman H, Franz C, Toit M. Screening, identification and characterization of bacteriocins produced by wine-isolated lab strains. *J Appl Microbiol.* (2015) 118:1007–22. doi: 10.1111/jam.12752

14. Wu S, Lei W, Zhou H, You S, Wu N, Song Y, et al. Screening and identification of lactic acid bacteria with antibacterial activity in the milk of Nanshan pasture. *China Brewing.* (2019) 38:108–12. doi: 10.11882/j.issn.0254-5071.2019.05.021

15. Qiao X, Du R, Wang Y, Han Y, Zhou Z. Isolation, characterisation and fermentation optimisation of bacteriocin-producing *Enterococcus faecium*. *Waste Biomass Valorization.* (2020) 11:3173–81. doi: 10.1007/s12649-019-00634-9

16. Jia L, Gao J, Xing X, Tian Y, Guo J, Hao L. The research on biological characteristics of *Bacillus subtilis* Hjd.A32 Which produced bacteriocine. *J Chin Inst Food Sci.* (2020) 20:66–73. doi: 10.16429/j.1009-7848.2020.05.009

17. Zhang, M, Zeng X, Fang L, Xu J, Cheng X, Yao M, et al. Purification and physicochemical stability analysis of bacteriocin produced by *Lactobacillus plantarum* C010. *Food Ferment Ind.* (2022):1–9. doi: 10.13995/j.cnki.11-1802/ts.031575

18. Ren S, Yuan X, Liu F, Fang F, Iqbal H, Zahran S, et al. Bacteriocin from *Lacticaseibacillus rhamnosus* Sp. A5: isolation, purification, characterization, and antibacterial evaluation for sustainable food processing. *Sustainability.* (2022) 14:9571. doi: 10.3390/su14159571

19. Ge J, Sun Y, Xin X, Wang Y, Ping W. Purification and partial characterization of a novel bacteriocin synthesized by *Lactobacillus paracasei* Hd1-7 isolated from Chinese sauerkraut juice. *Sci Rep.* (2016) 6:19366. doi: 10.1038/srep19366

20. Wei Y, Wang J, Liu Z, Pei J, Brennan C, Abd El-Aty A. Isolation and characterization of bacteriocin-producing *Lacticaseibacillus rhamnosus* Xn2 from Yak yoghurt and its bacteriocin. *Molecules.* (2022) 27:2066. doi: 10.3390/MOLECULES27072066

21. Yi L, Dang Y, Wu J, Zhang L, Liu X, Liu B, et al. Purification and characterization of a novel bacteriocin produced by *Lactobacillus crustorum* Mn047 isolated from Koumiss from Xinjiang, China. *J Dairy Sci.* (2016) 99:7002–15. doi: 10.3168/jds.2016-11166

22. Hu Y, Liu X, Shan C, Xia X, Wang Y, Dong M, et al. Novel bacteriocin produced by *Lactobacillus alimentarius* Fm-Mm4 from a traditional Chinese fermented meat Nanx Wudl: purification, identification and antimicrobial characteristics. *Food Control.* (2017) 77:290–7. doi: 10.1016/j.foodcont.2017.02.007

23. Afrin S, Hoque M, Sarker A, Satter M, Bhuiyan M. Characterization and profiling of bacteriocin-like substances produced by lactic acid bacteria from cheese samples. *Access Microbiol.* (2021) 3:000234. doi: 10.1099/acmi.0.000234

24. Kęska P, Stadnik J, Zielińska D, Kołożyn-Krajewska D. Potential of bacteriocins from lab to improve microbial quality of Dry-cured and fermented meat products. *Acta Sci Pol Technol Aliment.* (2017) 16:119–26. doi: 10.17306/j.Afs.0466

25. Zhang J, Yang Y, Yang H, Bu Y, Yi H, Zhang L, et al. Purification and partial characterization of bacteriocin Lac-B23, a novel bacteriocin production by *Lactobacillus plantarum* J23, isolated from Chinese traditional fermented milk. *Front Microbiol.* (2018) 9:2165. doi: 10.3389/fmicb.2018.02165

26. Chen J, Pang H, Wang L, Ma C, Wu G, Liu Y, et al. Bacteriocin-producing lactic acid bacteria strains with antimicrobial activity screened from Bamei Pig Feces. *Foods.* (2022) 11:709. doi: 10.3390/foods11050709

27. Gaspar C, Donders G, Palmeira-de-Oliveira R, Queiroz J, Tomaz C, Martinez-de-Oliveira J, et al. Bacteriocin production of the probiotic *Lactobacillus acidophilus* Ks400. *Amb Express.* (2018) 8:153. doi: 10.1186/s13568-018-0679-z

28. Dalie D, Deschamps A, Richard-Forget F. Lactic acid bacteria–potential for control of mould growth and mycotoxins: a review. *Food Control.* (2010) 21:370–80. doi: 10.1016/j.foodcont.2009.07.011

29. Parapouli M, Delbes-Paus C, Kakouri A, Koukkou A, Montel M, Samelis J. Characterization of a wild, novel Nisin a-producing *Lactococcus* strain with an *L. lactis* Subsp. Cremoris genotype and an *L. lactis* Subsp. Lactis phenotype, isolated from Greek raw milk. *Appl Environ Microbiol.* (2013) 79:3476–84. doi: 10.1128/AEM.00436-13

30. Christensen D, Hutkins R. Collapse of the proton motive force in *Listeria monocytogenes* caused by a bacteriocin produced by *Pediococcus acidilactici*. *Appl Environ Microbiol.* (1992) 58:3312–5. doi: 10.1128/aem.58.10.3312-3315.1992

31. Lu Y, Yan H, Li X, Gu Y, Wang X, Yi Y, et al. Physicochemical properties and mode of action of a novel bacteriocin Bm1122 with broad antibacterial spectrum produced by *Lactobacillus crustorum* Mn047. *J Food Sci.* (2020) 85:1523–35. doi: 10.1111/1750-3841.15131

32. Daba G, Ishibashi N, Gong X, Taki H, Yamashiro K, Lim Y, et al. Characterisation of the action mechanism of a *Lactococcus*-specific bacteriocin, lactococcin Z. *J Biosci Bioeng.* (2018) 126:603–10. doi: 10.1016/j.jbiosc.2018.05.018

33. Khetre S, Deshpande K, Bakshi P. Isolation and purification of bacteriocin produced by *Lactobacillus plantarum* isolated from honey bees gut and its inhibitory action against major human colon pathogens. *Int J Curr Microbiol Appl Sci.* (2020) 9:281–91. doi: 10.1080/00218839.2020.1746019

34. Mills S, Serrano L, Griffin C, O'Connor P, Schaad G, Bruining C, et al. Inhibitory activity of *Lactobacillus plantarum* Lmg P-26358 against *Listeria innocua* when used as an adjunct starter in the manufacture of cheese. *Microb Cell Fact.* (2011) 10:1–11. doi: 10.1186/1475-2859-10-S1-S7

35. Pei J, Li X, Han H, Tao Y. Purification and characterization of plantaricin Slg1, a novel bacteriocin produced by *Lb. plantarum* isolated from yak cheese. *Food Control.* (2018) 84:111–7. doi: 10.1016/j.foodcont.2017.07.034

36. Lv X, Miao L, Ma H, Bai F, Lin Y, Sun M, et al. Purification, characterization and action mechanism of plantaricin Jy22, a novel bacteriocin against *Bacillus cereus* produced by *Lactobacillus plantarum* Jy22 from golden carp intestine. *Food Sci Biotechnol.* (2018) 27:695–703. doi: 10.1007/s10068-017-0280-2

37. Ghanbari M, Jami M, Kneifel W, Domig K. Antimicrobial activity and partial characterization of bacteriocins produced by lactobacilli isolated from sturgeon fish. *Food Control.* (2013) 32:379–85. doi: 10.1016/j.foodcont.2012.12.024

frontiers | Frontiers in Nutrition

TYPE Original Research
PUBLISHED 11 January 2023
DOI 10.3389/fnut.2022.1110706

OPEN ACCESS

EDITED BY
Zhi-Hong Zhang,
Jiangsu University, China

REVIEWED BY
Juan Wei,
Gansu Agricultural University, China
Weiwei Cheng,
Nanjing University of Finance and Economics, China

*CORRESPONDENCE
Fangxue Hang
✉ hangfx@163.com

SPECIALTY SECTION
This article was submitted to Nutrition and Food Science Technology, a section of the journal Frontiers in Nutrition

RECEIVED 29 November 2022
ACCEPTED 20 December 2022
PUBLISHED 11 January 2023

CITATION
Luo M, Wang C, Wang C, Xie C, Hang F, Li K and Shi C (2023) Effect of alkaline hydrogen peroxide assisted with two modification methods on the physicochemical, structural and functional properties of bagasse insoluble dietary fiber. *Front. Nutr.* 9:1110706. doi: 10.3389/fnut.2022.1110706

Effect of alkaline hydrogen peroxide assisted with two modification methods on the physicochemical, structural and functional properties of bagasse insoluble dietary fiber

Mengying Luo[1], Cheng Wang[1], Chenshu Wang[1], Caifeng Xie[1,2], Fangxue Hang[1,2]*, Kai Li[1,2] and Changrong Shi[3]

[1]College of Light Industry and Food Engineering, Guangxi University, Nanning, China, [2]Provincial and Ministerial Collaborative Innovation Center for Sugar Industry, Nanning, China, [3]Faculty of Science, Centre for Agriculture and the Bioeconomy, Queensland University of Technology, Brisbane, QLD, Australia

Bagasse is one of major by-product of sugar mills, but its utilization is limited by the high concentration of lignin. In this study, the optimal alkaline hydrogen peroxide (AHP) treatment conditions were determined by the response surface optimization method. The results showed that the lignin removal rate was 62.23% and the solid recovery rate was 53.76% when bagasse was prepared under optimal conditions (1.2% H_2O_2, 0.9% NaOH, and 46°C for 12.3 h), while higher purity of bagasse insoluble dietary fiber (BIDF) was obtained. To further investigate the modification effect, AHP assisted with high-temperature-pressure cooking (A–H) and enzymatic hydrolysis (A–E) were used to modify bagasse, respectively. The results showed that the water holding capacity (WHC), oil holding capacity (OHC), bile salt adsorption capacity (BSAC), and nitrite ion adsorption capacity (NIAC) were significantly improved after A-H treatment. With the A–E treatment, cation exchange capacity (CEC) and BSAC were significantly increased, while WHC, OHC, and glucose adsorption capacity (GAC) were decreased. Especially, the highest WHC, OHC, BSAC and NIAC were gained by A–H treatment compared to the A–E treatment. These changes in the physicochemical and functional properties of bagasse fiber were in agreement with the microscopic surface wrinkles and pore structure, crystallinity and functional groups. In summary, the A–H modification can effectively improve the functional properties of bagasse fiber, which potentially can be applied further in the food industry.

KEYWORDS

sugarcane bagasse, insoluble dietary fiber, modification, physicochemical properties, structural properties, functional properties

1. Introduction

Sugarcane is an annual or perennial tropical and subtropical herbaceous plant. It is widely loved by consumers because of its sweetness and the presence of various nutrients that are very beneficial to human metabolism. Sugarcane is not only consumed in the fruit market but is also an important cash crop for the production of sugar worldwide (1). Sugarcane is mainly grown in Brazil, India, China, and so on, most of which is used for producing sugar, and the by-product is bagasse. It was found that about 700 million tons of bagasse were produced by sugar production factories worldwide every year (2). At present, bagasse is used for feed production or is discarded indiscriminately, which causes environmental pollution. To the best of our knowledge, bagasse can be used as a potential high-value ingredient in food products, such as dietary fiber.

Dietary fiber (DF) can neither be digested nor absorbed to produce energy. Therefore, it was once considered a "nutrient-free substance" and did not get enough attention for a long time. However, with the in-depth development of nutrition and related science, scientists found that DF has a very important physiological role, such as lower the risk of diabetes, obesity, and intestinal diseases (3). Thus, researchers started to add DF as a food ingredient to meet the growing demand for healthy products. According to water solubility, DFs can be divided into soluble dietary fibers (SDF) and insoluble dietary fibers (IDF). IDF is much more abundant than SDF in plant foods (4) and a good source of food bases with functional groups that can effectively bind to glucose, oil, water, and toxic metal ions (5). However, classic extraction and hydrolysis cannot fully expose these functional groups. Many physical, chemical, and biological methods have been applied to modify IDF from different biomass sources to obtain better functional and processing properties (6). According to Zhang et al., hydroxypropylation, carboxymethylation, and complex enzymes (cellulase and hemicellulase) have been reported to improve the water-holding capacity, α-amylase inhibition activity, glucose delay index, and bile acid salt binding capacity of coconut cake dietary fiber (7). Zhang et al. investigated the effect of modifications (Acetylated, cross-linking and cellulose-hydrolyzed) on the millet bran dietary fiber (8). Acetylated modified millet bran dietary fiber had the highest adsorption capacity of bile acid salt and cholesterol. The highest adsorption capacity of copper ions and nitrite ions was observed after cross-linking modification. The highest glucose delay index activity and α-amylase inhibition activity were observed for cellulose-hydrolyzed millet bran dietary fiber. Zhuang et al. reported that mixing alkaline hydrogen peroxide-treated sugarcane dietary fiber with pre-emulsified sesame oil resulted in a batter with improved texture and gave good organoleptic scores (9). It can be deduced that different modifications have different effects on the structural, physicochemical, and functional properties of the same dietary fiber. However, every modification method has its limitations. Therefore, it is of great interest to evaluate the effects of modification methods and select the appropriate method for a specific food need. Currently, there is no reported study on the effect of modification methods on bagasse insoluble dietary fiber.

As the bagasse of the sugar factory is dark gray, its fibrous hydration property is poor, and the high lignin content will affect the fermentation. Alkaline hydrogen peroxide (AHP) is reported to be a green and mild pretreatment that adds value to agricultural by-products and effectively removes lignin (10). However, no one has used this method to optimize the effect of bagasse delignification. Therefore, we first designed four variables (hydrogen peroxide concentration, sodium hydroxide concentration, temperature, and time) to conduct response surface optimization experiments to obtain the process conditions of low lignin content and high solid recovery.

High-temperature-pressure cooking (HTPC) treatment could remove the lignin of plant cell and partially degrades the hemicellulose and cellulose molecules (11). Enzymatic hydrolysis (EH) treatment could destroy one or more specific chemical chains of the cell wall depending on the type and source of the enzyme (12). All of these methods can alter the microstructure and composition of DFs, resulting in both desirable and undesirable effects on structural and functional properties (13). However, to our knowledge, there is no comparative information on the effect of AHP assisted with HTPC or EH on bagasse dietary fiber properties, respectively. Therefore, this study also deeply discussed AHP assisted with HTPC (A–H) and AHP assisted with EH (A–E) were used to modify bagasse, respectively, and then the changes in physicochemical, structural, and functional properties of bagasse dietary fiber before and after modification were evaluated.

2. Materials and methods

2.1. Materials

Bagasse was provided by a sugar production factory, East Sugar Company, located in Nanning province, China. The bagasse was washed in flowing tap water and dried in an oven for 48 h (DHG-90338S-III, Shanghai, China) at 60°C. Then samples were smashed and sieved through a 40 mesh sieve to obtain a bagasse powder and stored at room temperature until use. Hemicellulase (2×10^5 U/g) was purchased from Macklin (Shanghai, China). Other chemicals used were of analytical grade.

2.2. Bagasse insoluble dietary fiber preparation by alkaline hydrogen peroxide treatment

BIDF was prepared with alkaline hydrogen peroxide following the previous study (14) with modifications. Concentrations of 0.6, 0.9, and 1.2% (w/v, NaOH) and 0.5,

1.0, and 1.5% (w/v, H_2O_2) were prepared for the pretreatment of 1 g of bagasse with a solid loading of 1:60. This means that 1 g of bagasse was added to 60 mL of the solution containing the alkaline peroxide. The mixture was agitated continuously using a magnetic stirring water bath at 120 rpm, and the temperature and the reaction time were set to the desired degree of 35°C, 45°C, or 55°C for 8, 12, or 16 h. The material was collected by filter and washed with distilled water until neutralized, freeze-dried for 36 h, and finally weighed to obtain the solids recovery. Finally, it was milled and passed the sieved (60 mesh) to obtain powders, and BIDF was obtained. Lignin content was obtained by a two-step acid hydrolysis method. The combination of acid-soluble and acid-insoluble lignin constitutes the total lignin concentration. The percent lignin removal and percent solid yield was calculated as follows:

$$\textbf{percent lignin removal}\ (\%) = \frac{W_0 - W_1}{W_0} \times 100 \quad (1)$$

$$\textbf{percent solid yield}\ (\%) = \frac{M_1}{M_0} \times 100 \quad (2)$$

where W_0 and W_1 are the percentages of total lignin content before and after AHP treatment, respectively; M_0 and M_1 are the weights of dry samples before and after AHP treatment, respectively.

2.3. AHP assisted with two modification methods

2.3.1. AHP assisted with high-temperature-pressure cooking (A–H)

2 g BIDF and 60 mL distilled water (1:30, w/v) were added to the pressure-resistant tube, well mixed, and placed in a capacitive pressure steam sterilizer (XYR20, Zhejiang, China). The temperature was set to 120°C for 1 h. After the high-temperature-pressure cooking treatment, the material in the pressure-resistant tube was poured into Petri dishes and subsequently freeze-dried for 36 h. Finally, the freeze-dried samples were milled and passed through a 60-mesh sieve. H-BIDF was obtained.

2.3.2. AHP assisted with enzymatic hydrolysis (A–E)

10 g BIDF was mixed with 400 mL distilled water (1:40, w/v) in a conical flask and adjusted to pH = 5.5 with 0.1 M acetic acid solution. Then, 0.5 g hemicellulase was added and the mixture was placed in a shaker and reacted at 50°C for 1 h. The hydrolysis reaction was stopped by heating at 95°C for 10 min and washed with distilled water until neutralized. After that, it was freeze-dried, milled, and sieved, and E-BIDF was obtained.

2.4. Approximate chemical composition and physical properties

The chemical composition of the bagasse and its derivatives (BIDF, H-BIDF and E-BIDF) were determined by AOAC official methods (15), including moisture (method 925.09), total dietary fiber (TDF), SDF, IDF (method 991.43) and ash (method 942.05). The contents of cellulose, hemicellulose, and lignin were determined as described by Liu et al. (16). Briefly, the samples were first subjected to two-step acid hydrolysis, and sand core filtration and the residue obtained was dried to constant weight, cauterized to obtain the acid-insoluble lignin content, and the filtrate was measured at UV absorption 240 nm to obtain the acid-soluble lignin concentration. Subsequently, the concentration of sugars in the hydrolysate was determined by high-performance liquid chromatography (LC 1260 ll, Agilent, USA, equipped with a Shodex SP0810 column and guard column) and converted to obtain the concentrations of cellulose and hemicellulose. The column temperature was 80°C, the mobile phase was ultra-pure water, the flow rate was 0.5 mL/min, and the run time was 50 min.

The color was measured using a spectrophotometer (CS-420, CHNSpec technology, China) to obtain the values of L, a, and b. "L" represents the brightness of the object: 0-100 means from black to white, "a" represents the red-green color of the object: a positive value indicates red, a negative value indicates green, "b" represents the yellow-blue color of the object: positive values indicate yellow, negative values indicate blue. The whiteness index (WI) was calculated as the following equation:

$$\mathbf{WI} = 100 - \sqrt{(100 - L)^2 + a^2 + b^2} \quad (3)$$

2.5. Structural properties

2.5.1. Scanning electron microscopy

The samples dried to constant weight were directly glued to the conductive adhesive and sprayed with gold for 45 s using an Oxford Quorum SC7620 sputter coater at 10 mA; the sample morphology was subsequently photographed using a ZEISS Sigma 300 scanning electron microscope at a voltage of 3 kV.

2.5.2. Fourier-transform infrared spectroscopy

The changes in molecular structure were analyzed using an infrared spectrometer (Nicolet 670, USA). Four samples dried to constant weight were mixed completely with potassium bromide (1:100, w/w), then placed in a mold and pressed into transparent sheets on a hydraulic press, and finally, the samples were tested in an infrared spectrometer. The FT-IR spectral wave number was in the range of 400–4,000 cm^{-1} with a scan number of 32 and a resolution of 4 cm^{-1}.

2.5.3. X-ray diffraction

The XRD patterns of four samples were obtained by a Bruker D8 Advanced diffractometer operating at 40 kV and 30 mA. The diffraction angle (2θ) was in the 10°-60° range using a step size of 0.02° and the scanning rate was 1.2°/min. The crystallinity index (CI) was calculated by the classic formula:

$$\mathbf{CI}\,(\%) = \frac{\mathbf{I_{002}-I_{AM}}}{\mathbf{I_{002}}} \times \mathbf{100} \quad (4)$$

where I_{AM} is the lowest intensity of the peak at the angle of around 18° and I_{002} was the maximum intensity of the peak located at the angle of 22°.

2.6. Physicochemical and functional properties

2.6.1. Water holding capacity

WHC was determined by the method (17) with some modifications. An appropriate amount of dietary fiber was first weighed, saturated with excess water, shaken, and allowed to stand at room temperature for 2 h. The excess water was then filtered off using a 700 mesh filter cloth, a portion of which was carefully removed from the wet sample, weighed, and dried to a constant weight in a hot air drying oven (105°C). The WHC was calculated as the following equation:

$$\mathbf{WHC}\ (\mathbf{g/g}) = \frac{\mathbf{M_1-M_2}}{\mathbf{M_2}} \quad (5)$$

where M_1 and M_2 are the weights of the wet and dry samples, respectively.

2.6.2. Oil holding capacity

OHC was determined by the method (18) with some modifications. Firstly, 0.25 g DF samples and 10 mL corn oil were added into 50 mL centrifuge tubes. Then, they were mixed well and left at room temperature for 4 h, centrifuged at 1,144 g for 20 min. Finally, the excess oil was discarded and the residues were weighed. The OHC was calculated as the following equation:

$$\mathbf{OHC}\ (\mathbf{g/g}) = \frac{\mathbf{M_1-M_2}}{\mathbf{M_2}} \quad (6)$$

where M_1 and M_2 are the weights of the wet and dry samples, respectively.

2.6.3. Cation exchange capacity

The CEC was based on the methods (19) with some modifications. 1 g IDF sample was weighed in a conical flask, mixed with 0.1 M hydrochloric acid at a stock-liquid ratio of 1:70 (w/v), and acidified with magnetic stirring at room temperature for 24 h. The fibers were then washed with distilled water until the wash was free of Cl^- (detected by 10% $AgNO_3$ solution), and the solid residue was freeze-dried for 36 h. Disperse 0.1 g of acidified dried sample in 10 mL of 5% NaCl solution and stir magnetically at room temperature for 2 h. Add 1 drop of phenolphthalein indicator and titrate with 0.01 M NaOH until the color of the solution turns slightly red and read the volume of NaOH solution consumed. The cation exchange capacity was expressed as the amount of NaOH consumed per g of sample. The CEC was calculated as the following equation:

$$\mathbf{CEC}\ (\mathbf{mmol/g}) = \frac{\mathbf{0.01(V_1-V_2)}}{\mathbf{M}} \quad (7)$$

where V_1 is the volume of sodium hydroxide consumed by titrating the dietary fiber sample (mL); V_2 is the volume of sodium hydroxide consumed by titrating the blank (mL); M is the mass of the dietary fiber sample.

2.6.4. Glucose adsorption capacity

The GAC was based on the method (20) with some modifications. Briefly, 0.5 g of IDF sample and 50 mL of glucose solution (50 mmol/L) were mixed well in a conical flask, which was placed under adsorption in a shaker at 37°C for 6 h and centrifuged at 3,000 g for 10 min. 1 mL of supernatant was transferred into a test tube and then mixed with 2.0 mL of dinitro-salicylate (DNS) reagent. The mixture was incubated in boiling water for 5 min and cooled flowing water to room temperature. Finally, add 9 mL of distilled water into the tube and mix well. The residual content of glucose was measured by the absorbance value of the solution at 540 nm by InfiniteM200PRO (Tecan, Austria) and quantified based on the standard curve. The GAC was calculated as the following equation:

$$\mathbf{GAC}\ (\mathbf{mg/g}) = \frac{\mathbf{M_1-M_2}}{\mathbf{M}} \quad (8)$$

where M_1 is the mass of glucose in the solution before adsorption, M_2 is the mass of glucose in the solution after adsorption, and M is the mass of the dietary fiber sample.

2.6.5. Bile salt adsorption capacity

The BSAC was based on the method (21) with some modifications. 0.1 g of IDF sample was added to the conical flask, and then 5 mL of sodium cholate phosphate buffer (pH = 7) was added to mimic the small intestinal environment. Adsorbed in a shaker at 37°C for 2 h, centrifuged at 4,000 g for 10 min. 1 mL of supernatant was taken in a corked test tube, and 6 mL of 45% sulfuric acid and 1 mL of 0.3% furfural were added sequentially. Mix well and place the reaction in a constant temperature water bath at 65°C for 30 min. Immediately after the reaction, the reaction was cooled in an ice water bath, and the absorbance value was measured at 620 nm using InfiniteM200PRO (Tecan,

Austria) and compared with the standard curve. The formula was calculated as follows:

$$\mathbf{BSAC}\ (\mathbf{mg/g}) = \frac{\mathbf{M_1 - M_2}}{\mathbf{M}} \quad (9)$$

Where M_1 is the mass of sodium cholate in the solution before adsorption, M_2 is the mass of sodium cholate in the solution after adsorption, and M is the mass of the dietary fiber sample.

2.6.6. Nitrite ion adsorption capacity

The NIAC was based on the method (22) with some modifications. 0.1 g of IDF sample was mixed with 10 mL of $NaNO_2$ solution (10 μg/mL) with the pH adjusted to 2.0 and 7.0, simulating the stomach and small intestinal environment. The mixture was incubated at 37°C for 2 h, then centrifuged at 1,144 g for 10 min. The supernatant (1 mL) was transferred into a colorimetric tube, mixing with 2 mL p-aminobenzene sulfonic acid (0.4%, w/v) and 1 mL hydrochloride naphthodiamide (0.2%), and then ultra-pure water was added to the tube until the volume reached to 50 mL. After the mixture was reacted in the dark for 15 min, the residual content of glucose was measured by the absorbance value of the solution at 538 nm by InfiniteM200PRO (Tecan, Austria) and quantified based on the standard curve. The NIAC was calculated as the following equation:

$$\mathbf{NIAC}\ (\mu\mathbf{g/g}) = \frac{\mathbf{M_1 - M_2}}{\mathbf{M}} \quad (10)$$

where M_1 is the mass of $NaNO_2$ in the solution before adsorption, M_2 is the mass of $NaNO_2$ in the solution after adsorption, and M is the mass of the dietary fiber sample.

2.7. Statistical analyses

All experiments were performed in triplicate and the results were expressed as mean ± standard deviation (SD). Statistical analysis was carried out by IBM SPSS statistical software (version 27.0, SPSS Inc., Chicago, IL, USA). $P < 0.05$ was considered to be statistically significant.

3. Results and discussion

3.1. Response surface optimization experimental results

It was reported that strong oxidants produced by hydrogen peroxide under suitable alkaline conditions cause lignin oxidation and biomass depolymerization (23). Cabrera et al. concluded that there was no significant change in biomass structure under low alkaline conditions (24). In contrast, high alkaline conditions lead to a significant dissolution of hemicellulose, reducing the recovery of cellulose from insoluble material. Thus, the use of response surface design for AHP process optimization of bagasse is essential.

In this experiment, we used 4 factors and 3 levels to evaluate the effect of AHP delignification, and the results of each experiment are shown in Table 1. The percent lignin removal ranged from 48.12 to 68.71 and the percent solid yield ranged from 40.6 to 64.7. The response equations for lignin removal and solids recovery were obtained based on the analysis of the data, where X_1, X_2, X_3, and X_4 are time, temperature, sodium hydroxide concentration and peroxide concentration, respectively.

Percent lignin removal (%) $= -52.94698 + 2.75083X_1 + 2.43963X_2 + 51.56389X_3 + 1.43667X_4 + 0.004125X_1X_2 - 1.20417X_1X_3 + 0.5025X_1X_4 - 0.3333X_2X_3 + 0.27X_2X_4 + 12.35X_3X_4 - 0.05382812X_1^2 - 0.022363X_2^2 - 11.36111X_3^2 - 17.47X_4^2$

Percent solid yield (%) $= 22.13619 + 0.892875X_1 + 0.622225X_2 + 53.94111X_3 + 13.62033X_4 - 0.003125X_1X_2 + 1.62708X_1X_3 + 0.1525X_1X_4 - 0.333333X_2X_3 - 0.415X_2X_4 - 20.66667X_3X_4 - 0.143583X_1^2 - 0.002886X_2{}^2 - 29.85926X_3^2 + 13.50567X_4^2$

After the analysis by Design-Expert 13.0 software, it is known that this equation is a suitable mathematical model for each parameter of the AHP treatment process, so this regression equation can be used to determine the best treatment process for alkaline hydrogen peroxide. The response surface plots of lignin removal rate and solids yield are shown in Figures 1, 2. If the curve is steeper, it indicates that the factor has more influence on the response value. The degree of influence of the four experimental factors on the lignin removal rate was temperature > time > sodium hydroxide concentration > hydrogen peroxide concentration. And the degree of influence on solid recovery was sodium hydroxide concentration > time > temperature > hydrogen peroxide concentration.

The optimal process conditions for bagasse pretreatment were obtained as a treatment time of 12.26 h, a temperature of 46.003°C, a sodium hydroxide concentration of 0.85%, and a hydrogen peroxide concentration of 1.19%. Considering the operability, the optimal conditions were adjusted to 12.3 h treatment time, 46°C temperature, 0.9% sodium hydroxide concentration, and 1.2% hydrogen peroxide concentration, and three validation tests were conducted under these optimal conditions, and the lignin removal rate of bagasse was 62.23% and the solid yield was 53.76%, which were similar to the predicted values of the model. This indicates that the model predicts accurate parameters and has a certain guiding significance for practical operation.

10.3389/fnut.2022.1110706

TABLE 1 The design and results of the Box-Behnken experiment.

Run	X_1: Time(h)	X_2: Temperatuere (°C)	X_3: NaOH(w/v)	X_4: H_2O_2(w/v)	Response 1: Percent lignin removal (%)	Response 2: Percent solid yield (%)
1	16	55	0.9	1	67.93	41.5
2	16	45	0.6	1	62.7	46.3
3	12	45	1.2	1.5	61.2	47.6
4	12	45	1.2	0.5	61.89	48.7
5	8	45	0.9	1.5	50.76	60.8
6	12	55	1.2	1	68.71	40.6
7	16	45	0.9	1.5	60.86	52.32
8	8	45	0.9	0.5	56.42	56.4
9	12	45	0.9	1	63.5	54.5
10	16	35	0.9	1	61.48	49.7
11	12	45	0.9	1	62.03	54.15
12	12	55	0.9	1.5	60.59	52.4
13	12	55	0.9	0.5	62.47	51.1
14	8	55	0.9	1	57.77	50.5
15	12	45	0.9	1	65	47.3
16	12	55	0.6	1	61.4	52.1
17	12	35	0.6	1	48.5	57.4
18	8	35	0.9	1	51.98	58.2
19	12	45	0.6	1.5	49.4	64
20	8	45	0.6	1	52.21	58.21
21	12	35	0.9	1.5	48.12	64.7
22	12	35	1.2	1	59.81	49.9
23	16	45	0.9	0.5	62.5	46.7
24	12	45	0.9	1	62.4	53.7
25	12	45	0.9	1	62.07	54.14
26	12	45	0.6	0.5	57.5	52.7
27	16	45	1.2	1	67.63	41.2
28	8	45	1.2	1	62.92	45.3
29	12	35	0.9	0.5	55.4	55.1

3.2. Effect on approximate chemical composition and color

The proximate composition and color of the four samples were listed in Table 2. Bagasse treated with optimized AHP reduced acid-insoluble lignin and acid-soluble lignin content by 71.85 and 20.04%, respectively, and significantly increased IDF, SDF, TDF, and cellulose content ($P < 0.05$). In the food industry, color is one of the important parameters of food ingredients and affects the acceptability of food products by consumers (25). In addition, changes in food color help us to distinguish changes in the physical and chemical properties of raw food materials (26). The WI of bagasse increased from 67.69 to 84.05, which can significantly increase consumer acceptance. Compared to BIDF, although H-BIDF and E-BIDF showed a decrease in whiteness, the ash removal rate was significantly higher, 96.15 and 93.75%, respectively. Besides, the cellulose, hemicellulose, and content of H-BIDF were significantly decreased ($P < 0.05$). However, the cellulose content of E-BIDF increased and the hemicellulose content decreased by 80.17% and 2.06%,

respectively. This indicates that HTPC treatment degrades some cellulose and hemicellulose of BIDF, while hemicellulase significantly degrades hemicellulose of BIDF, which may help dietary fiber to expose more functional groups and better perform its functional properties *in vivo*.

3.3. Structural properties

3.3.1. Scanning electron microscopy

The SEM images of the bagasse and its modified derivatives (BIDF, H-BIDF and E-BIDF) are shown in Figure 3. Each sample had different morphological characteristics. It was found that bagasse were long strips of fibers and the structure was relatively flat and complete, which is consistent with the previous study (27). After AHP treatment, striated cracks were formed on the BIDF surface, which could be due to lignin degradation. Compared with BIDF, the surface of H-BIDF became rougher and formed water ripple-like folds and pore layers, which might have a positive impact on the functional properties of the sample. The structural integrity of E-BIDF was destroyed and its surface was uneven, forming a large number of honeycomb microstructures, which may be due to the massive degradation of wall polysaccharides caused by hemicellulase. Numerous studies have shown that the irregular surface and porous structure contribute to the adsorption capacity of the material (28), which is crucial for the subsequent adsorption of ions and molecules. Nevertheless, this special structure could increase the relative surface area, and lead to the increase of WHC, OHC, BSAC, NIAC.

3.3.2. Fourier-transform infrared spectroscopy

The FT-IR images of the bagasse with its modified derivatives (BIDF, H-BIDF, and E-BIDF) were recorded from 400 to 4,000 cm^{-1} in Figure 4. It can be seen from the figure that the four fiber samples have similar characteristic peaks and show common fingerprints of lignocellulose fibers (29). The wide band positioned around 3,422 cm^{-1} was mainly due to the extension of O-H bound to hydrogen and hydroxyl groups produced by cellulose and hemicellulose (30). Compared with bagasse, the three modified bagasse dietary fibers had obvious blue shifts at the frequency band of 3,422 cm^{-1}, which indicated that their organic molecules of hydrogen bonding may be partly destroyed (31). The wide band was positioned around 2,922 cm^{-1} to represent the aliphatic saturated C-H stretching vibration in cellulose and hemicelluloses or the stretching vibration peak of -OH in the hemicellulose molecule or intermolecular. The characteristic peak of C=O near 1,731 cm^{-1} indicates that the AHP pretreatment of bagasse effectively degraded the C=O of the fiber. The peak around 1,622 cm^{-1} is the characteristic peak of the lignin benzene ring, which indicates a redshift after the three treatments. In addition, it can be seen that the peak intensity of E-BIDF increases significantly, which is attributed to the large reduction of hemicellulose and the relative increase of lignin content after enzymatic hydrolysis. The peak at 1,055 cm^{-1} was assigned to the C-OH stretching and β-glycosidic linkages of the cellulose glucose ring. The absorption peak with an intensity near 890 cm^{-1} represents the breakage of β-glycosidic bonds, which can be seen to be the most pronounced after HTPC treatment. According to FT-IR spectra, bagasse fibers were modified in three ways and their chemical structures were disrupted to different degrees.

3.3.3. X-ray diffraction

The XRD patterns of the bagasse and its derivatives (BIDF, H-BIDF and E-BIDF) were illustrated in Figure 5. Cellulose has a crystalline structure, in contrast to lignin and hemicellulose (amorphous) (32). As can be seen in the figure, all the samples had the characteristic crystalline peaks at 15.8° and 21.9° 2θ, indicating that they are all double helix type I cellulose (33). The CI of bagasse was 47.5%, and after AHP treatment, the CI of BIDF was significantly increased to 63.8%, similar to the results of the ginseng dietary fiber study (34). After HTPC treatment of BIDF, the CI of H-BIDF (59.8%) was significantly decreased, which indicated that a portion of the cellulose crystalline region was destroyed. It may be the effect of HTPC to promote fiber dissolution (35), as in Table 2 a significant increase in soluble dietary fiber content. However, after being treated by the enzymatic digestion of hemicellulose, the CI of E-BIDF (68.7%) was increased, which was due to the degradation of hemicellulose. The result suggested that enzymatic treatment of bagasse dietary fiber was helpful to improve the structural stability of cellulose.

3.4. Physicochemical and functional properties

3.4.1. Water holding capacity and oil holding capacity

The WHC and OHC of the bagasse and modified derivatives were shown in Figure 6. It was reported that insoluble fiber with high WHC can accelerate the speed of defecation, reduce the pressure in the rectum and urinary system, relieve the symptoms of urinary system diseases and prevent constipation (36), and enable the rapid discharge of toxic substances from the body. IDF can adsorb oil and other components through hydrophobic interaction and capillary adsorption, helping the body remove excess fat, and thereby reducing the risk of chronic diseases (37). This study found that the amount of lignin was negatively correlated with WHC and OHC, while the amount of hemicellulose would be positively correlated. The results for WHC were similar to those of Qi et al. (18), but the opposite conclusion for OHC may be due to the

10.3389/fnut.2022.1110706

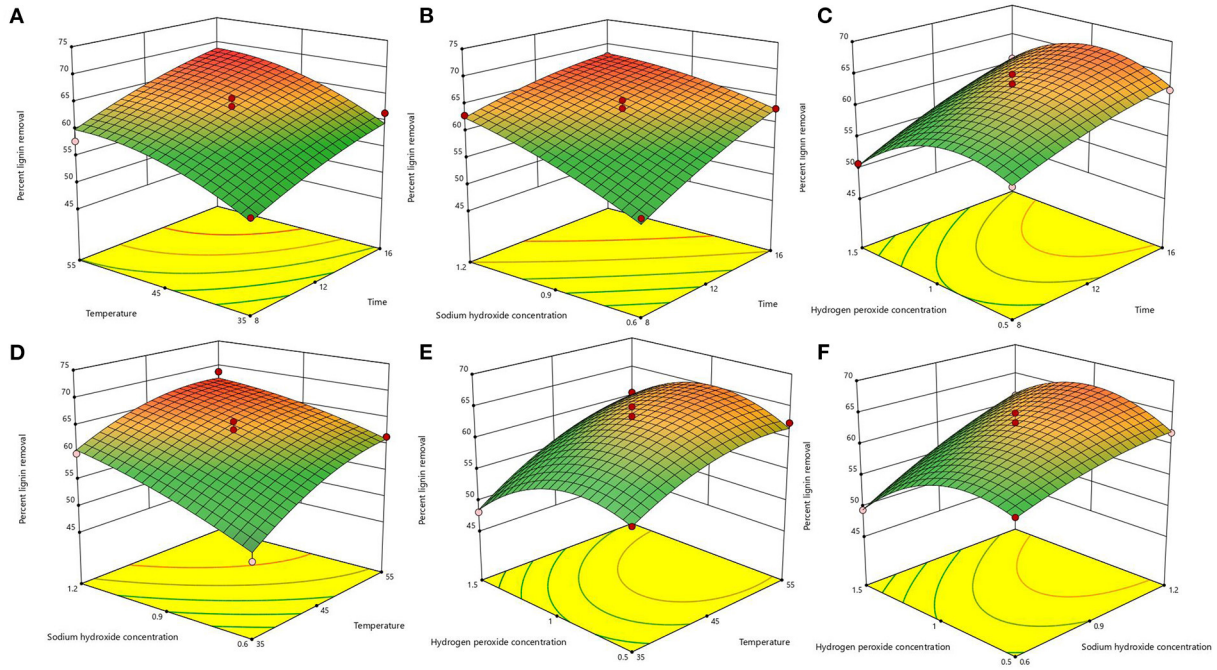

FIGURE 1
Response surface plots of the interaction for lignin removal. **(A)** temperature and time; **(B)** sodium hydroxide concentration and time; **(C)** hydrogen peroxide concentration and time; **(D)** sodium hydroxide concentration and temperature; **(E)** hydrogen peroxide concentration and temperature; **(F)** hydrogen peroxide concentration and sodium hydroxide concentration.

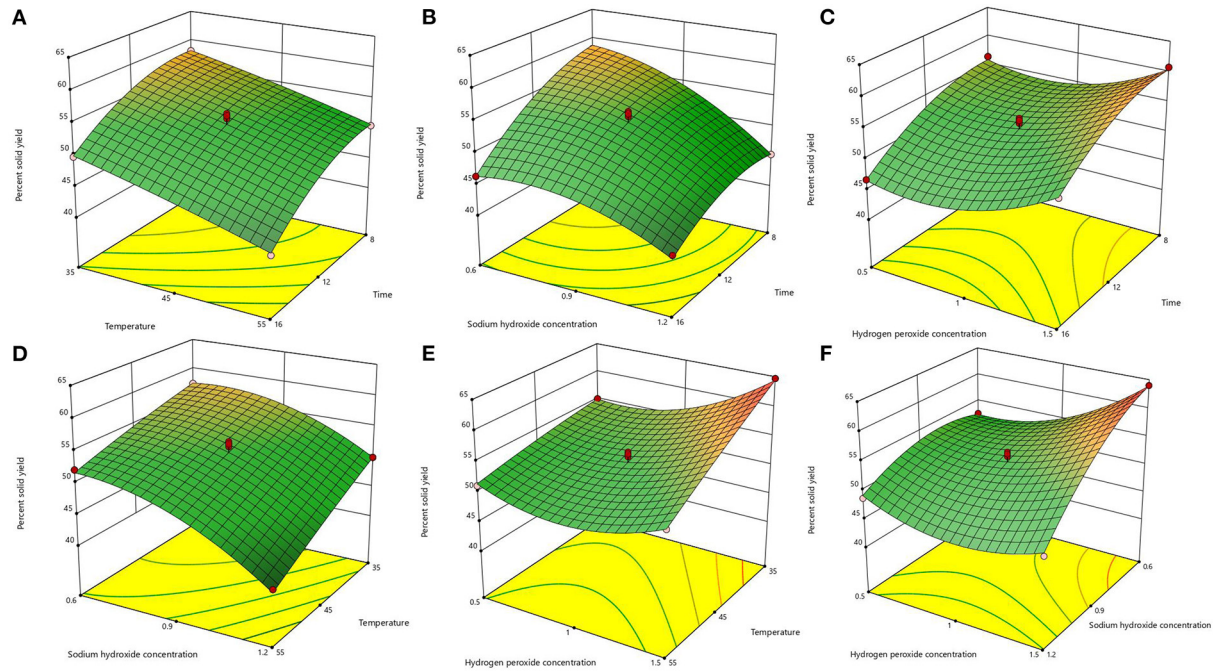

FIGURE 2
Response surface plots of the interaction for solid yield. **(A)** temperature and time; **(B)** sodium hydroxide concentration and time; **(C)** hydrogen peroxide concentration and time; **(D)** sodium hydroxide concentration and temperature; **(E)** hydrogen peroxide concentration and temperature; **(F)** hydrogen peroxide concentration and sodium hydroxide concentration.

TABLE 2 The approximate chemical composition and color of bagasse insoluble dietary fiber modified by different methods.

Sample	Bagasse	BIDF	H-BIDF	E-BIDF
Moisture (g/100 g)	7.26 ± 0.04^{a}	7.14 ± 0.33^{a}	7.21 ± 0.02^{a}	6.64 ± 0.08^{b}
IDF (g/100 g)	86.77 ± 0.71^{c}	95.52 ± 0.23^{a}	95.46 ± 0.13^{a}	91.76 ± 0.13^{b}
SDF (g/100 g)	0.27 ± 0.06^{d}	0.53 ± 0.02^{c}	0.86 ± 0.07^{a}	0.70 ± 0.01^{b}
TDF (g/100 g)	87.04 ± 0.65^{c}	96.04 ± 0.20^{a}	96.32 ± 0.07^{a}	92.46 ± 0.14^{b}
Cellulose (g/100 g)	38.20 ± 0.71^{d}	68.90 ± 0.99^{b}	63.65 ± 0.35^{c}	72.65 ± 0.49^{a}
Hemicellulose (g/100g)	18.55 ± 0.49^{a}	17.65 ± 0.64^{a}	15.25 ± 0.64^{b}	3.50 ± 0.00^{c}
Acid-insoluble lignin (g/100 g)	22.98 ± 1.05^{a}	6.47 ± 0.33^{c}	7.09 ± 0.37^{c}	10.28 ± 0.45^{b}
Acid-soluble lignin (g/100 g)	5.24 ± 0.04^{a}	4.19 ± 0.15^{b}	4.00 ± 0.01^{b}	3.20 ± 0.04^{c}
Ash (g/100 g)	2.07 ± 0.13^{a}	2.08 ± 0.10^{a}	0.08 ± 0.00^{b}	0.13 ± 0.01^{b}
L	70.43 ± 0.13^{d}	88.24 ± 0.07^{a}	83.57 ± 0.04^{c}	85.35 ± 0.19^{b}
a	2.73 ± 0.01^{a}	-0.06 ± 0.15^{d}	0.59 ± 0.17^{b}	0.22 ± 0.03^{c}
b	12.74 ± 0.04^{a}	10.77 ± 0.13^{c}	12.14 ± 0.07^{b}	9.89 ± 0.10^{d}
WI	67.69 ± 0.11^{d}	84.05 ± 0.14^{a}	79.56 ± 0.08^{c}	82.32 ± 0.11^{b}

Different letters (a, b, c, d) denote significantly different in the column ($p < 0.05$).

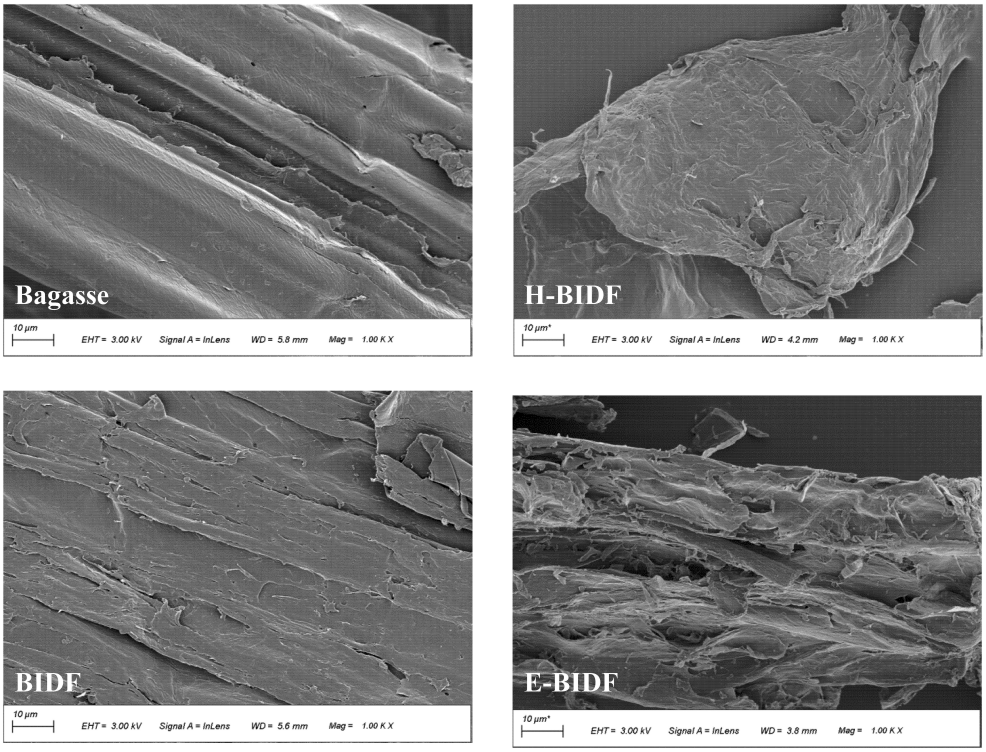

FIGURE 3
The SEM images of bagasse, BIDF, H-BIDF and E-BIDF at ×1,000 magnification.

presence of non-dietary fiber impurities in rice bran dietary fiber. H-BIDF showed the highest WHC (14.95 g/g) and OHC (11.12 g/g), mainly due to the significant degradation of lignin by the AHP process, in addition to the possibility that the combined HTPC treatment disrupted the intermolecular forces of DF.

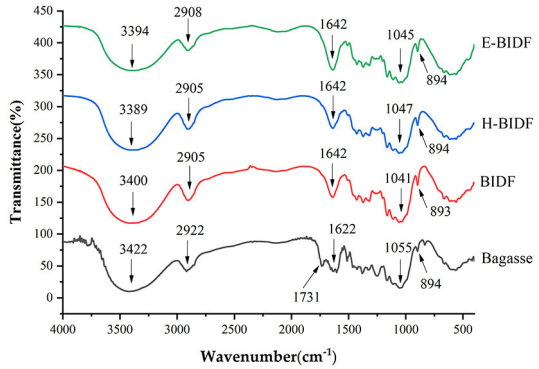

FIGURE 4
The FT-IR images of bagasse, BIDF, H-BIDF and E-BIDF.

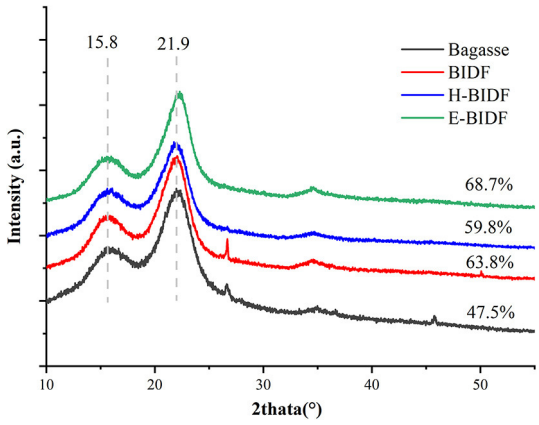

FIGURE 5
The XRD patterns of bagasse, BIDF, H-BIDF and E-BIDF.

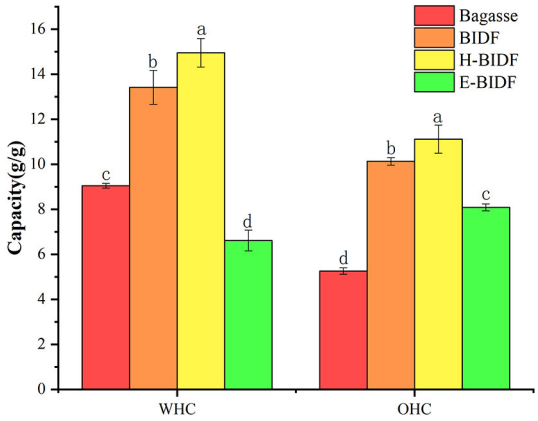

FIGURE 6
The WHC and OHC of bagasse, BIDF, H-BIDF and E-BIDF. Different letters (a, b, c, d) denote significantly different in the column ($p < 0.05$).

3.4.2. Cation exchange capacity

The chemical structure of dietary fiber contains some carboxyl and hydroxyl side chain groups that can be reversibly exchanged with organic cations, thus affecting the pH value of the digestive tract and creating a more retentive environment for digestion and absorption (38). Results in Figure 7A suggested that bagasse treated with optimized alkaline hydrogen peroxide significantly increased the CEC by 28.6%. In addition, the BIDF treated with hemicellulase hydrolysis significantly improved the CEC of BIDF ($P < 0.05$). It was reported that the CEC was mainly related to the anion-bearing functional groups such as carboxyl and hydroxyl phenolic groups on the fiber (39), which may be the main reason for the increased CEC of E-BIDF (0.14 mmol/g). On the contrary, the hydrothermal reaction of HTPC may destroy its carboxyl and hydroxyphenyl groups, which harmed its CEC.

3.4.3. Glucose adsorption capacity

GAC is one of the main evaluation indicators of the functional properties of dietary fiber, which could adsorb glucose molecules and delay the rise of blood glucose after meals, thus reducing the risk of diabetes (40). Results in Figure 7B suggested that the adsorption capacity of BIDF (10.73 mg/g) to glucose increased significantly ($P < 0.05$) after bagasse (6.47 mg/g) was treated with alkaline hydrogen peroxide. However, the glucose adsorption capacity of H-BIDF (5.58 mg/g) and E-BIDF (3.89 mg/g) decreased compared to BIDF ($P < 0.05$). This may be due to the destruction of the active site for glucose adsorption by multiple hydrothermal treatments.

3.4.4. Bile salt adsorption capacity

The BSAC is commonly used as an index to assess the adsorption of lipophilic substances. On the one hand, dietary fiber with high BSAC can inhibit the absorption of cholesterol and promote its excretion (41). On the other hand, when the content of cholate decreases, the human body will automatically convert cholesterol into sodium cholate for supplementation, thereby promoting cholesterol consumption. A previous study (42) had shown that sugarcane fibers may bind sodium bile salts and our study subsequently confirmed it. Results in Figure 7C suggested that bagasse (2.43 mg/g) treated with AHP significantly increased the bile salt adsorption capacity of BIDF (8.24 mg/g) ($P < 0.05$), which indicated delignification of lignin was important to improve BSAC. H-BIDF (16.36 mg/g) and E-BIDF (15.86 mg/g) had a positive effect on improving BSAC, which may be due to their relatively high oil holding capacity or porous structure.

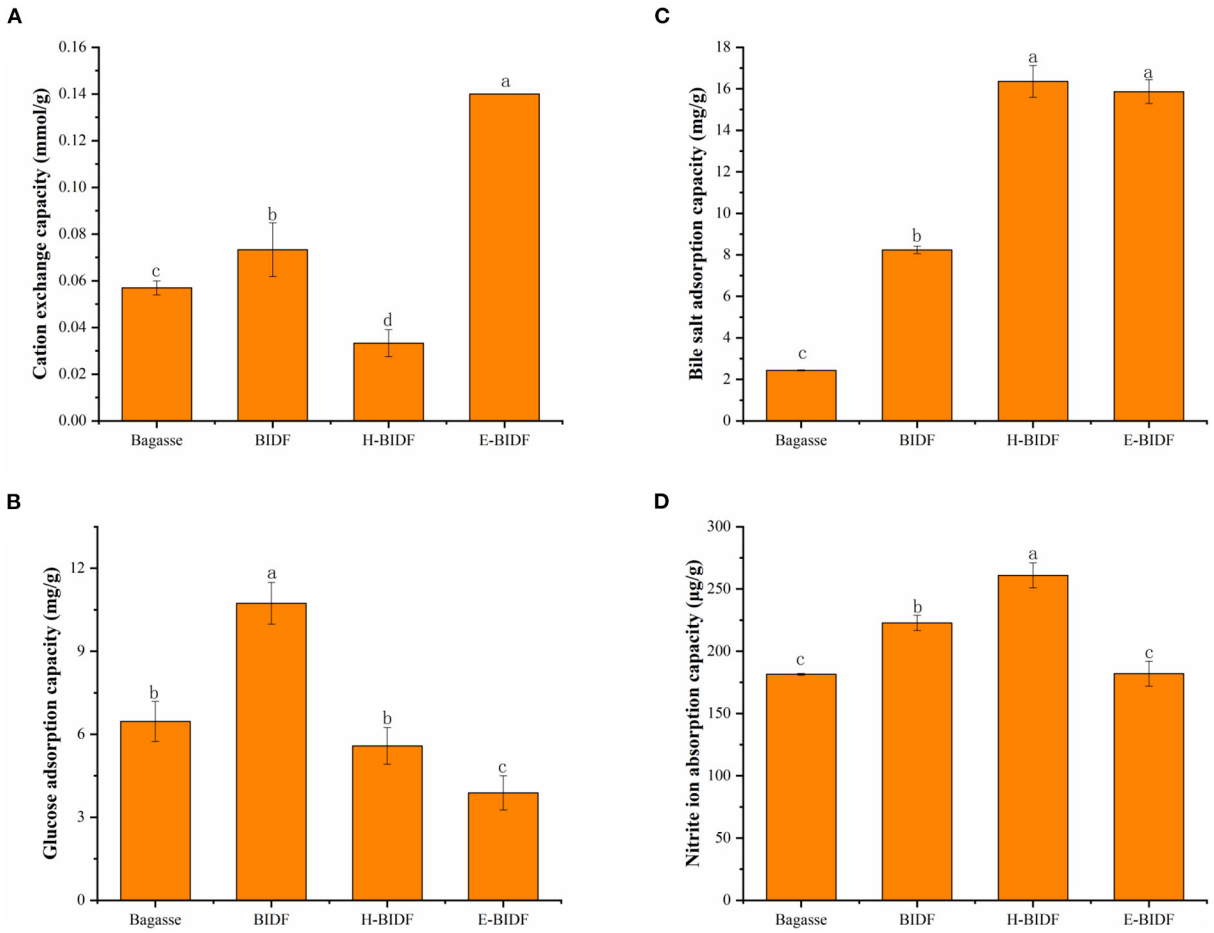

FIGURE 7
The CEC **(A)**, GAC **(B)**, BSAC **(C)**, and NIAC **(D)** of bagasse, BIDF, H-BIDF and E-BIDF. Different letters (a, b, c, d) denote significantly different in the column ($p < 0.05$).

3.4.5. Nitrite ion adsorption capacity

The NIAC is also a meaningful functional property of dietary fiber, which can usually prevent toxicity in humans following excessive nitrite intake (43). In this study, the NIAC of four fibers were measured at pH 2.0 and pH 7.0, respectively. The results showed that none of the four fibers had NIAC at pH 7.0, similar to that of wheat bran insoluble dietary fibers (44). As the picture depicted in Figure 7D, BIDF (222.74 μg/g) showed a stronger NIAC than bagasse (181.44 μg/g) at pH 2.0 ($P < 0.05$). Particularly, the H-BIDF demonstrated the highest NIAC (260.88 μg/g), which might be because of its wrinkled surface and the exposure of more functional groups. However, the NIAC of E-BIDF (182.02 μg/g) was decreased significantly ($P < 0.05$) after BIDF was hydrolyzed by hemicellulase, which may be due to the positive correlation between the size of NIAC and hemicellulose content.

4. Conclusions

In this study, response surface experiments were performed to obtain optimal AHP experimental conditions. The functional properties of BIDF were significantly enhanced compared to bagasse, indicating the importance of lignin removal for the modification of dietary fibers. Meanwhile, bagasse was modified using A-H and A-E treatments, respectively, and its modification effects were evaluated in terms of physicochemical, structural and functional properties to find a suitable modification method. The results showed that the structural integrity of the modified bagasse insoluble dietary fiber was disrupted and more folds or pores were formed, which could be responsible for the significant increase in its functional properties. Compared with BIDF, H-BIDF became less crystalline and part of the cellulose was degraded, which was also supported by FT-IR spectroscopy, resulting in a further increase of WHC, OHC, BSAC, and

NIAC. Adsorption of water, oil, bile salts and nitrite ions can help fecal transport more comfortably and promote cholesterol degradation while taking away toxicogenic ions. It can be shown that A-H modification could be a guide to prevent constipation and obesity. On the contrary, the crystallinity and microscopic porosity increased after hemicellulase modification. Although WHC, OHC and NIAC of E-BIDF decreased, it obtained the highest CEC. High CEC creates a more durable environment for digestion and absorption by reversibly exchanging with organic cations, thus affecting the pH of the digestive tract. A-E modification was useful for the prevention of digestive tract diseases. In general, the modification methods were highly selective for improving physical, chemical and functional properties and can provide some guidance for the development of foods with specific functions. In the case of bagasse insoluble dietary fiber, A-H treatment was a better modification method.

Data availability statement

The original contributions presented in the study are included in the article/supplementary material, further inquiries can be directed to the corresponding author.

Author contributions

ML: data curation, writing—original draft, writing—review, editing, investigation, and formal analysis. ChengW: methodology, investigation, and formal analysis. ChensW: data curation, validation, formal analysis, and investigation. CX: supervision, project administration, and funding acquisition. FH: conceptualization, methodology, and resources. KL: conceptualization and resources. CS: visualization, investigation, and formal analysis. All authors have read and agreed to the published version of the manuscript.

Funding

This financial support from the National Key R&D Program of China (2021YFE0114400), the Research Program of Agriculture Research System of China (CARS-17), and the Natural Science Foundation of China (no. 32160570) were acknowledged.

Acknowledgments

The authors would like to thank all those who contributed directly or indirectly to the project. The authors also thank Jianliang Liao from Shiyanjia Lab (www.shiyanjia.com) for the SEM and FT-IR analysis.

Conflict of interest

The authors declare that the research was conducted in the absence of any commercial or financial relationships that could be construed as a potential conflict of interest.

Publisher's note

All claims expressed in this article are solely those of the authors and do not necessarily represent those of their affiliated organizations, or those of the publisher, the editors and the reviewers. Any product that may be evaluated in this article, or claim that may be made by its manufacturer, is not guaranteed or endorsed by the publisher.

References

1. Sangnark A, Noomhorm A. Effect of dietary fiber from sugarcane bagasse and sucrose ester on dough and bread properties. *Food Sci Technol.* (2004) 37:697–704. doi: 10.1016/j.lwt.2004.02.015

2. Yu P, Liang Y, Dong H, Hu H, Liu S, Peng L, et al. Rational synthesis of highly porous carbon from waste bagasse for advanced supercapacitor application. *ACS Sustain Chem Eng.* (2018) 6:15325–32. doi: 10.1021/acssuschemeng.8b03763

3. He Y, Wang B, Wen L, Wang F, Yu H, Chen D, et al. Effects of dietary fiber on human health. *Food Sci Hum Well.* (2022) 11:1–10. doi: 10.1016/j.fshw.2021.07.001

4. Wang C, Yang Z, Guo X, Zhu K. Effects of insoluble dietary fiber and ferulic acid on the quality of steamed bread and gluten aggregation properties. *Food Chem.* (2021) 364:130444. doi: 10.1016/j.foodchem.2021.130444

5. Yang X, Dai J, Zhong Y, Wei X, Wu M, Zhang Y, et al. Characterization of insoluble dietary fiber from three food sources and their potential hypoglycemic and hypolipidemic effects. *Food Funct.* (2021) 12:6576–87. doi: 10.1039/D1FO00521A

6. Gan J, Xie L, Peng G, Xie J, Chen Yi, Yu Q. Systematic review on modification methods of dietary fiber. *Food Hydrocoll.* (2021) 119:106872. doi: 10.1016/j.foodhyd.2021.106872

7. Zheng Y, Tian H, Li Y, Wang X, Shi P. Effects of carboxymethylation, hydroxypropylation and dual enzyme hydrolysis combination with heating on physicochemical and functional properties and antioxidant activity of coconut cake dietary fibre. *Food Chem.* (2021) 336:127688. doi: 10.1016/j.foodchem.2020.127688

8. Zheng Y, Xu B, Shi P, Tian H, Li Y, Wang X, et al. The influences of acetylation, hydroxypropylation, enzymatic hydrolysis and crosslinking on improved adsorption capacities and in vitro hypoglycemic properties of millet bran dietary fibre. *Food Chem.* (2022) 368:130883. doi: 10.1016/j.foodchem.2021.130883

9. Zhuang X, Han M, Kang Z, Wang K, Bai Y, Xu X, et al. Effects of the sugarcane dietary fiber and pre-emulsified sesame oil on low-fat meat batter physicochemical property, texture, and microstructure. *Meat Sci.* (2016) 113:107–15. doi: 10.1016/j.meatsci.2015.11.007

10. Ho MC, Ong VZ, Wu TY. Potential use of alkaline hydrogen peroxide in lignocellulosic biomass pretreatment and valorization – a review. *Renew Sust Energ Rev.* (2019) 112:75–86. doi: 10.1016/j.rser.2019.04.082

11. Zia-ur-Rehman, Islam M, Shah WH. Effect of microwave and conventional cooking on insoluble dietary fibre components of vegetables. *Food Chem.* (2003) 80:237–40. doi: 10.1016/S0308-8146(02)00259-5

12. Santala O, Kiran A, Sozer N, Poutanen K, Nordlund E. Enzymatic modification and particle size reduction of wheat bran improves the mechanical properties and structure of bran-enriched expanded extrudates. *J Cereal Sci.* (2014) 60:448–56. doi: 10.1016/j.jcs.2014.04.003

13. Peerajit P, Chiewchan N, Devahastin S. Effects of pretreatment methods on health-related functional properties of high dietary fibre powder from lime residues. *Food Chem.* (2012) 132:1891–8. doi: 10.1016/j.foodchem.2011.12.022

14. Sangnark A, Noomhorm A. Effect of particle sizes on in-vitro calcium and magnesium binding capacity of prepared dietary fibers. *Food Res Int.* (2003) 36:91–6. doi: 10.1016/S0963-9969(02)00112-6

15. AOAC. *Official Methods of Analysis*. Washington, DC: Association of Official Analytical Chemists. (2019). Available online at: https://www.aoac.org/official-methods-of-analysis-21st-edition-2019/

16. Liu Y, Li W, Li K, Annamalai PK, Pratt S, Hassanpour M, et al. Tailored production of lignin-containing cellulose nanofibrils from sugarcane bagasse pretreated by acid-catalyzed alcohol solutions. *Carbohyd Polym.* (2022) 291:119602. doi: 10.1016/j.carbpol.2022.119602

17. Qin L, Liu Z, Liu T, Liu S, Zhang J, Wu J, et al. A bioinspired, strong, all-natural, superhydrophobic cellulose-based straw. *Int J Biol Macromol.* (2022) 220:910–9. doi: 10.1016/j.ijbiomac.2022.08.118

18. Qi J, Yokoyama W, Masamba KG, Majeed H, Zhong F, Li Y. Structural and physico-chemical properties of insoluble rice bran fiber: effect of acid-base induced modifications. *RSC Adv.* (2015) 5:79915–23. doi: 10.1039/C5RA15408A

19. Song Y, Su W, Mu YC. Modification of bamboo shoot dietary fiber by extrusion-cellulase technology and its properties. *Int J Food Prop.* (2018) 21:1219–32. doi: 10.1080/10942912.2018.1479715

20. Ou S, Kwok K, Li Y, Fu L. *In vitro* study of possible role of dietary fiber in lowering postprandial serum glucose. *J Agr Food Chem.* (2001) 49:1026–9. doi: 10.1021/jf000574n

21. Wang Y, Zhou YL, Cheng YK, Jiang ZY, Jin Y, Zhang HS, et al. Enzymo-chemical preparation, physico-chemical characterization and hypolipidemic activity of granular corn bran dietary fibre. *J Food Sci Tech Mys.* (2015) 52:1718–23. doi: 10.1007/s13197-013-1140-6

22. Luo X, Wang Q, Fang D, Zhuang W, Chen C, Jiang W, et al. Modification of insoluble dietary fibers from bamboo shoot shell: structural characterization and functional properties. *Int J Biol Macromol.* (2018) 120(Pt B):1461–7. doi: 10.1016/j.ijbiomac.2018.09.149

23. Lewis SM, Holzgraefe DP, Berger LL, Fahey GC, Gould JM, Fanta GF. Alkaline hydrogen peroxide treatments of crop residues to increase ruminal dry matter disappearance in sacco. *Anim Feed Sci Tech.* (1987) 17:179–99. doi: 10.1016/0377-8401(87)90002-2

24. Cabrera E, Muñoz MJ, Martín R, Caro I, Curbelo C, Díaz AB. Alkaline and alkaline peroxide pretreatments at mild temperature to enhance enzymatic hydrolysis of rice hulls and straw. *Bioresource Technol.* (2014) 167:1–7. doi: 10.1016/j.biortech.2014.05.103

25. Liu Y, Yi S, Ye T, Leng Y, Alomgir Hossen M, Sameen DE, et al. Effects of ultrasonic treatment and homogenization on physicochemical properties of okara dietary fibers for 3D printing cookies. *Ultrason Sonochem.* (2021) 77:105693. doi: 10.1016/j.ultsonch.2021.105693

26. Feng Y, Yang T, Zhang Y, Zhang A, Gai L, Niu D. Potential applications of pulsed electric field in the fermented wine industry. *Front Nutr.* (2022) 9:1048632. doi: 10.3389/fnut.2022.1048632

27. Gai L, Ren E, Tian W, Niu D, Sun W, Hang F, et al. Ultrasonic-assisted dual-alkali pretreatment and enzymatic hydrolysis of sugarcane bagasse followed by candida tropicalis fermentation to produce xylitol. *Front Nutr.* (2022) 9:913106. doi: 10.3389/fnut.2022.913106

28. Wang C, Luo M, Xie C, Li K, Hang F, Shi C, et al. Effective Adsorption of Colorants from Sugarcane Juice by Bagasse-Based Biochar-Hydroxyapatite Composite. *Foods.* (2022) 11:2171. doi: 10.3390/foods11142171

29. Wong Sak Hoi L, Martincigh BS. Sugar cane plant fibres: Separation and characterisation. *Ind Crop Prod.* (2013) 47:1–12. doi: 10.1016/j.indcrop.2013.02.017

30. Zheng Y, Li Y. Physicochemical and functional properties of coconut (Cocos nucifera L) cake dietary fibres: effects of cellulase hydrolysis, acid treatment and particle size distribution. *Food Chem.* (2018) 257:135–42. doi: 10.1016/j.foodchem.2018.03.012

31. Wang C, Ma Y, Zhu D, Jian-Guo Z, Thakur K, Zhao-Jun W. Physicochemical and functional properties of dietary fiber from Bamboo Shoots (Phyllostachys praecox). *Emir J Food Agr.* (2017) 29:509–17. doi: 10.9755/ejfa.2017-02-274

32. Zhang YH, Lynd LR. Toward an aggregated understanding of enzymatic hydrolysis of cellulose: noncomplexed cellulase systems. *Biotechnol Bioeng.* (2004) 88:797–824. doi: 10.1002/bit.20282

33. Hua M, Lu J, Qu D, Liu C, Zhang L, Li S, et al. Structure, physicochemical properties and adsorption function of insoluble dietary fiber from ginseng residue: a potential functional ingredient. *Food Chem.* (2019) 286:522–9. doi: 10.1016/j.foodchem.2019.01.114

34. Jiang G, Bai X, Wu Z, Li S, Zhao C, Ramachandraiah K. Modification of ginseng insoluble dietary fiber through alkaline hydrogen peroxide treatment and its impact on structure, physicochemical and functional properties. *Food Sci Technol.* (2021) 150:111956. doi: 10.1016/j.lwt.2021.111956

35. Rahmawati A, Murdiati A, Marsono Y, Anggrahini S. Changes of complex carbohydrates of white jack bean (Canavalia Ensiformis) during autoclaving-cooling cycles. *Curr Res Nutr Food S.* (2018) 6:470–80. doi: 10.12944/CRNFSJ.6.2.21

36. Chao HC, Lai MW, Kong MS, Chen SY, Chen CC, Chiu CH. Cutoff volume of dietary fiber to ameliorate constipation in children. *J Pediatr.* (2008) 153:45–9. doi: 10.1016/j.jpeds.2007.12.044

37. Matsuhiro B, Lillo LE, Sáenz C, Urzúa CC, Zárate O. Chemical characterization of the mucilage from fruits of Opuntia ficus indica. *Carbohyd Polym.* (2006) 63:263–7. doi: 10.1016/j.carbpol.2005.08.062

38. Lyu B, Wang H, Swallah MS, Fu H, Shen Y, Guo Z, et al. Structure, properties and potential bioactivities of high-purity insoluble fibre from soybean dregs (Okara). *Food Chem.* (2021) 364:130402. doi: 10.1016/j.foodchem.2021.130402

39. Chau C, Huang Y. Comparison of the chemical composition and physicochemical properties of different fibers prepared from the peel of citrus sinensis L. Cv Liucheng. *J Agr Food Chem.* (2003) 51:2615–8. doi: 10.1021/jf025919b

40. Zheng Y, Wang X, Tian H, Li Y, Shi P, Guo W, et al. Effect of four modification methods on adsorption capacities and in vitro hypoglycemic properties of millet bran dietary fibre. *Food Res Int.* (2021) 147:110565. doi: 10.1016/j.foodres.2021.110565

41. Chen H, Li J, Yao R, Yan S, Wang Q. Mechanism of lipid metabolism regulation by soluble dietary fibre from micronized and non-micronized powders of lotus root nodes as revealed by their adsorption and activity inhibition of pancreatic lipase. *Food Chem.* (2020) 305:125435. doi: 10.1016/j.foodchem.2019.125435

42. Chong RWW, Ball M, McRae C, Packer NH. Comparing the chemical composition of dietary fibres prepared from sugarcane, psyllium husk and wheat dextrin. *Food Chem.* (2019) 298:125032. doi: 10.1016/j.foodchem.2019.125032

43. Li W, Shan F, Sun S, Corke H, Beta T. Free radical scavenging properties and phenolic content of Chinese black-grained wheat. *J Agr Food Chem.* (2005) 53:8533–6. doi: 10.1021/jf051634y

44. Zhang M, Liao A, Thakur K, Huang J, Zhang J, Wei Z. Modification of wheat bran insoluble dietary fiber with carboxymethylation, complex enzymatic hydrolysis and ultrafine comminution. *Food Chem.* (2019) 297:124983. doi: 10.1016/j.foodchem.2019.124983

frontiers | Frontiers in Nutrition

TYPE Original Research
PUBLISHED 22 February 2023
DOI 10.3389/fnut.2023.1126562

OPEN ACCESS

EDITED BY
Debao Niu,
Guangxi University,
China

REVIEWED BY
Wen'Jun Liu,
Chongqing Technology and Business University,
China
Xiaodan Hui,
University of Louisville,
United States

*CORRESPONDENCE
Qianyun Ma
✉ maqianyun@126.com
Jianfeng Sun
✉ causunjf@hebau.edu.cn

SPECIALTY SECTION
This article was submitted to Nutrition and Food Science Technology, a section of the journal Frontiers in Nutrition

RECEIVED 18 December 2022
ACCEPTED 13 January 2023
PUBLISHED 22 February 2023

CITATION
Wang W, Zhang F, Dai X, Liu Y, Mu J, Wang J, Ma Q and Sun J (2023) Changes in vinegar quality and microbial dynamics during fermentation using a self-designed drum-type bioreactor.
Front. Nutr. 10:1126562.
doi: 10.3389/fnut.2023.1126562

Changes in vinegar quality and microbial dynamics during fermentation using a self-designed drum-type bioreactor

Wenxiu Wang[1], Fan Zhang[1], Xinpeng Dai[1], Yaqiong Liu[1], Jianlou Mu[1], Jie Wang[1], Qianyun Ma[1]*and Jianfeng Sun[1,2,3]*

[1]College of Food Science and Technology, Hebei Agricultural University, Baoding, China, [2]Hebei Technology Innovation Centre of Agricultural Products Processing, Baoding, China, [3]Sino-US and Sino-Japan Joint Centre of Food Science and Technology, Baoding, China

The bioreactor based on solid-state fermentation technology has been developed for vinegar production, standardization of fermentation process and stabilization of vinegar quality. The microbial community diversity, and volatile compounds of six cultivars of vinegar samples fermented in a self-designed solid-state fermentation bioreactors were investigated using Illumina MiSeq platform and gas chromatography mass spectrometry (GC-MS) technology. The correlations between the richness and diversity of microbiota and volatile profiles, organic acids, as well as physicochemical indicators were explored by R software with the coplot package. The findings indicated that *Acetobacter*, *norank-c-Cyanobacteria*, and *Weissella* played key roles during fermentation process. *Norank-f-Actinopolyporaceae*, *norank-c-Cyanobacteria*, *Pediococcus*, and *Microbacterium* had significant correlations with the physicochemical characteristics. The most common bacterial species were associated with a citric acid content, whereas the least number of bacterial species correlated with malic acid content. Findings could be helpful for the bioreactor optimization, and thus reaching the level of pilot scale and industrialization.

KEYWORDS

microbial community diversity, fermentation, volatile compounds, heatmap package, bioreactor

1. Introduction

Chinese grain vinegar is a traditional fermented condiment, which plays an indispensable role in an individual's daily diet (1). Traditional vinegar fermentation has evolved into the classic solid-state fermentation (SSF) style over thousand years (2). In general, vinegar fermentation goes through three steps, including starch saccharification, alcohol fermentation, and acetic acid fermentation (AAF) (3), among which AAF is the most important step as the acetic acid and flavor compounds are formed during the fermentation (4). During the fermentation process, the complex microbial community can provides a variety of enzymes to transform raw materials into a variety of flavor components and functional substances, mainly organic acids and volatile components (5).

In the last decade, the studies on Chinese vinegar research have mainly focused on the dynamics and diversity of microbial communities, and mainly adopted culture-dependent or culture-independent methods (6, 7). Meanwhile, the major microorganisms, volatile flavor compounds, organic acids and amino acids have been identified. Li et al. (8) investigated the bacterial dynamics and metabolite changes in solid-state AAF of Shanxi aged vinegar and discovered eight organic acids, 16 free amino acids, and 66 aroma compounds. Zhou et al. (9) explored the volatile aroma

patterns of Beijing rice vinegar in different stages and identified the potential biomarkers for traditional Chinese cereal vinegar. In addition, Ai et al. (10) investigated the microbial diversity of Sichuan bran vinegar, and *Lactobacillus*, *Acetobacter*, *Trichoderma*, and *Candida* were considered as the dominant genera. These studies help us to better understand the mechanism of traditional vinegar fermentation process, as well as the dynamic changes of volatilization, physicochemical properties, and microbial community structure during fermentation.

Currently, Chinese vinegar is generally produced under open and non-sterile environmental conditions (11). These fermentation methods have been used for many years. However, there are still plenty of shortcomings, such as a large occupation area, low degree of mechanization, heavy labor intensity, and low efficiency. These drawbacks make the fermentation process uncontrollable, leading to the inconsistency of quality between different batches (12). Therefore, the traditional fermentation is inadequate to satisfy the practical requirements of modern vinegar production. To address these deficiencies, it is necessary to improve the mechanization and intensive level of SSF of vinegar.

The rapid development of bioreactors based on SSF technology opens a new way for vinegar production, standardizing fermentation process and stabilizing vinegar quality (13). It has the advantages of short fermentation time, controllable working environment and a high degree of mechanization when compared with the traditional fermentation method. In recent years, with the in-depth study of SSF bioreactor, it has been applied in the cultivation of animal and plant cell lines, and production of enzymes (14), ethanol (15), organic acids, pigments (16), and beer.

Combining the principle of multilateral co-fermentation of traditional vinegar SSF with mechanized equipment, the rotary drum type vinegar SSF bioreactor was designed to suit the vinegar fermentation process in our preliminary study. The bioreactor is composed of a power system, baffle, ventilation, and vinegar drenching device, which can complete the steps of inoculation, fermentation, vinegar drenching, and vinegar fumigation in the bioreactor. The baffle device combines the functions of cooling and stirring into one, which reduces the minimum speed of the reactor and reduces energy consumption. The intermittent vinegar drenching process and vinegar fumigation methods were also proposed for the characteristics of the bioreactor. The intermittent rotation strengthens heat and mass transfer, which is beneficial for the growth of microorganisms. In addition, the convective transport is enhanced by increasing the surface contact of the base with wet air and cooling water due to the mixing process. Unfortunately, despite these advantages, the utilization of bioreactors to produce vinegar on an industrial scale has not yet been fully realized. Thus, in order to further improve the design of the bioreactor to meet the needs of industrial scale production, it is essential to deeply understand the fermentation performance of the bioreactor and explore the changes of metabolites during fermentation. In addition, since the coexistence of various microorganisms has a significant influence on the unique flavor and taste of vinegar, a deep understanding of the microbial composition is also required.

Therefore, the aim of this study is to deeper insight into the changes in vinegar quality indexes and microbial dynamics during AAF in this self-designed rotary drum bioreactor. The objectives of this study were to monitor the changes of physicochemical properties, organic acid content and volatile flavor components. The diversity and succession of microbial communities were explored using high-throughput sequencing technology. Furthermore, the potential correlation between dominant bacteria and vinegar quality indexes was determined through multivariate data analysis. The findings in this study could be helpful for the bioreactor optimization, and thus reaching the level of pilot scale and industrialization.

2. Materials and methods

2.1. Materials and reagents

The fermentation raw materials including flour, bran, rice chaff, and Daqu were collected from the local farmers market of Baoding city in Hebei Province, China. The high-activity yeast culture was purchased from Angel Yeast Co., Ltd. Amylase (1×10^5 U/ml) and glucoamylase (1×10^5 U/ml) were purchased from Shanghai Yuanye Biotechnology Co., Ltd. (Shanghai, China). Lactic acid, acetic acid, oxalic acid, citric acid, malic acid, succinic acid, and tartaric acid were chromatographic grade and purchased from Shanghai Yuanye Biotechnology Co., Ltd. The DNA extraction kit was obtained from United States Omega Bio-Tek (Winooski, VT, United States). Other standard compounds were of analytical purity and purchased from Tianjin Tianli Chemical Reagent Co., Ltd. (Tianjin, China).

2.2. Fermentation of vinegar and sample collection

In this study, the SSF of vinegar was carried out using a self-designed rotary drum bioreactor, as shown in Figure 1. The motor drives the bioreactor to rotate continuously.

Composition: the reactor is composed of a tank, inlet, baffle, support, fan, transmission device, tug, air inlet pipe, air outlet pipe, water inlet pipe, water outlet pipe, observation hole, sampling hole, vinegar spraying sieve plate, and vinegar spraying pipe.

Fermentation processing: the feed inlet of the biochemical reactor is upward. First, flour, bran, rice husk, and Daqu were added to the bioreactor at mass ratio of 1:2:1:0.1. The solid material entered the reactor through the material inlet *via* the conveyor belt. The reactor was rotated for 5 min through the gear transmission, and the materials were rotated under the action of the inner baffle of the reactor. Afterwards, the materials automatically fell and were mixed with the rotation. The liquid materials (water, activated yeast, amylase, and glucoamylase) were added into the reactor through the inlet pipe, and were stirred entirely by rotating the bioreactor for 20 min, which promoted vinegar fermentation. At the stage of saccharification and alcohol fermentation, the fermentation culture temperature was maintained at 28–32°C. The oxygen content at the outlet pipe and the internal material temperature were kept at 18–20% and 32–35°C, respectively. On the 19th day of the fermentation, the total acid contents in the vinegar declined, which suggested the end of the AAF stage. Consequently, the fermentation proceeded into the maturation stage, lasting for 5–7 days. After the fermentation, the acetic acid in the fermented grains of solid vinegar was soaked into the water through the water inlet pipe. After the immersion, the vinegar permeated into the juice tank through the solid–liquid isolation sieve plate, and then flowed into the storage tank *via* the bottom vinegar pouring pipe. Afterwards, one side of the tank was opened, the reactor was rotated, and the fermented grains were released

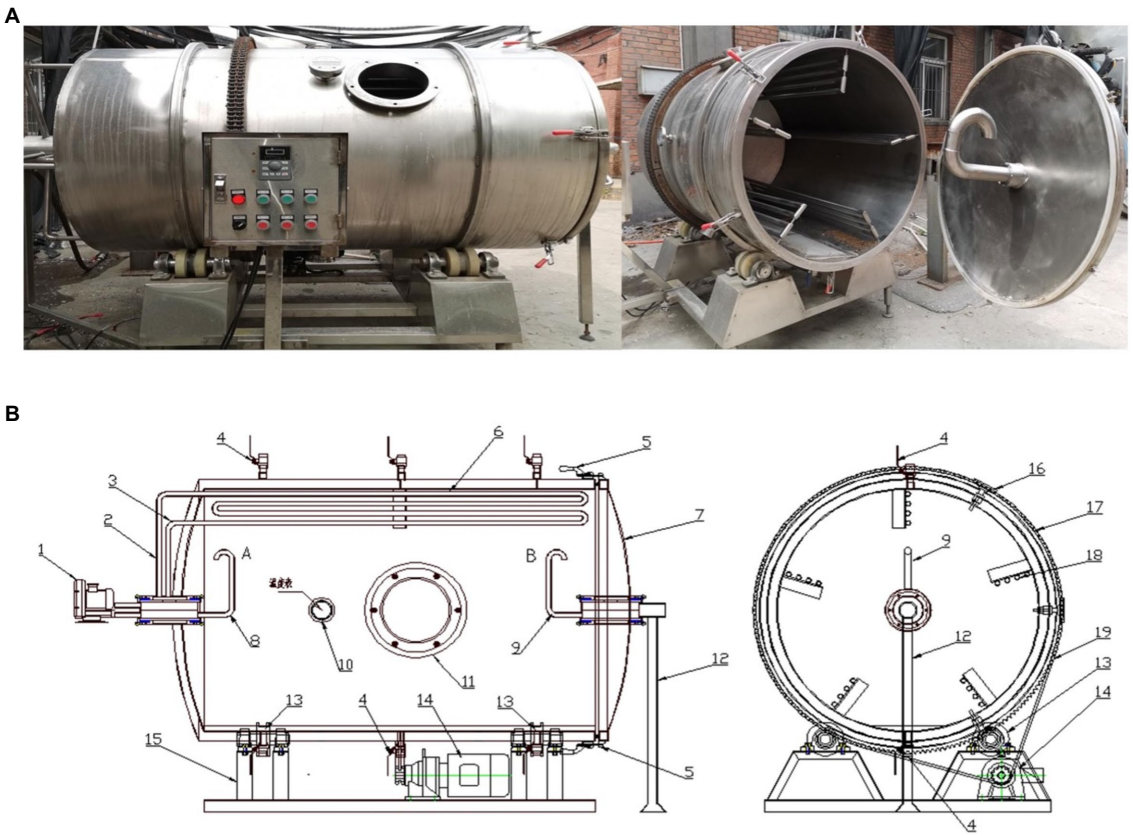

FIGURE 1
The self-designed drum-type bioreactor: **(A)** Physical map; **(B)** Structural sketch.

immediately. When fumigating vinegar, high-temperature steam was injected into the baffle to heat the vinegar grains.

During fermentation, 100–150 ml of vinegar samples from three vinegar drenching valves were collected on the 1st, 4th, 7th, 11th, 15th, and 19th day of the solid-state acetic acid fermentation process, and then mixed thoroughly to ensure the uniformity and representativeness of the samples. All samples were stored at −80°C until used for further analysis.

2.3. Physicochemical properties analysis

The changes of physicochemical properties, including ethanol, total acid, involatile acid compounds, and reducing sugar content of the collected vinegar samples were determined according to GB 5009.225-2016 (National food safety standards, determination of ethanol concentration in wine), GB/T 12456-2008 (Determination of total acid in foods), GB 5009.235-2016 (National food safety standards, determination of amino nitrogen in food), and GB 5009.7-2016 (National food safety standards, determination of reducing sugar in food), respectively.

2.4. Organic acids analysis

Organic acids were measured by high-performance liquid Chromatography (HPLC; 1200 Agilent, Santa Clara, CA, United States) referring to a previous method (17). The standard solutions of acetic acid (2.5 mg/ml), lactic acid (1.5 mg/ml), oxalic acid (0.05 mg/ml), tartaric acid (0.1 mg/ml), malic acid (0.05 mg/ml), citric acid (0.75 mg/ml), and succinic acid (0.1 mg/ml) were prepared and filtered into a liquid phase bottle through a 0.22-μm water-soluble filter. Afterwards, 5.0 ml of vinegar sample was treated with 2.0 ml of potassium ferrocyanide (106 g/L) and 2 ml of zinc sulfate (300 g/L), centrifuged at 2,500 *g* for 5 min, and then the supernatant was filtered through a 0.22-μm filter prior to HPLC analysis. The instrument used was equipped with an automatic injector and a photodiode array detector UV at 210 nm. Separation was realized using a Sep-Pak C18 column (5 μm, 4.6 × 250 mm) at 30°C. The mobile phase was 0.02 mol/L NaH_2PO_4, with a flow rate of 0.9 ml/min, and the injection volume of samples was 10 μl. Finally, each organic acid was quantified by calculating the peak area.

2.5. Volatile profiles analysis

Volatile compounds of the vinegar samples were analyzed by utilizing head space solid phase microextraction coupled with gas chromatography mass spectrometry (HS-SPME-GC/MS) analysis (7890A-5975C, Agilent, Santa Clara, CA, United States) (18). Briefly, 6 ml of vinegar and 1.5 g of NaCl were pipetted into a 15 ml of headspace vial, tightly capped and equilibrated at 40°C in a thermostatic bath. The sample was then extracted by SPME head at the same temperature for 40 min. After extraction, the fiber was immediately inserted into the

injection port of GC-MS to thermally desorb the analyte at 240°C for 6 min.

GC/MS analyses were performed on an Agilent 7890A GC and an Agilent 5953C MS equipped with a capillary column (30 m × 0.25 mm, 0.25-μm thickness, TG-WAXMS, Thermo Scientific) (19). The GC operation condition was as follow: inlet temperature of 250°C, a split ratio of 1:1, helium carrier gas flow of 1 ml/min. The oven temperature was maintained at 40°C for 5 min, followed by an increase of 10°C/min to 180°C, and then programmed to 230°C at 5°C/min, and held for 10 min. The MS was generated in the electron impact mode at 70 eV of ionization energy using the full scan mode (14–400 amu). The temperature of MS source and quadrupole was set at 230 and 150°C, respectively.

The volatile compounds were then identified by matching the MS with the NIST05 mass spectral database and quantitatively calculated using the peak-area normalization method. All samples were analyzed in triplicate.

2.6. Microbial community analysis

2.6.1. DNA extraction and qPCR analysis

To monitor the dynamic changes in a microbial community, samples were collected periodically on the surface of fermentation materials in the bioreactor on the day 1, 4, 7, 11, 15, and 19 during the AAF process. For each day, each 150 g of sample was collected at three different locations and mixed thoroughly to ensure the uniformity and representativeness of samples. All samples were put into sterile sealed bags and stored in a freezer at −80°C. Then DNA extraction was performed using the Soil DNA Kit (Omega Bio-Tek, Norcross, GA, United States). The concentration of extracted DNA was measured by a NanoDrop 2000 UV-vis spectrophotometer (Thermo Scientific, Wilmington, MA, United States) and checked by 1% agarose gel electrophoresis. Bacterial primers 338F (5′-ACTCCTACGGGAG GCAGCAG-3′) and 806R (5′-GGA CTACHVGGGTWTCTAAT-3′) with specific barcode were employed to amplify the V3-V4 region of bacterial 16S rRNA genes by thermocycler PCR system (ABI GeneAmp® 9,700, Waltham, MA, United States). The PCR reaction was run as the method from our lab, which has been published by Ma et al. (20).

2.6.2. Sequencing and data analysis

For the sequencing and data analysis, the method described by Ma et al. (20) was followed. Trimmomatic quality-filtered raw fastq files before FLASH combined them with the following standard. The reads were truncated at any site with an average quality score of 20 over a 50 bp sliding window; sequences with overlap longer than 10 bp were merged according to their overlap with a mismatch of no more than 2 bp; and sequences of each sample were separated according to barcodes (exactly matching) and Primers (two nucleotides mismatched were allowed). Reads with unclear bases were filtered out. UPARSE (version 7.1)[1] was used to cluster operational taxonomic units (OTUs) using a 97 percent similarity cut-off. RDP Classifier (version 2.11)[2] was used to compare the taxonomy of each 16S rRNA gene sequence to the SILVA (version 132)[3] 16S rRNA database. The confidence level was set at 70%.

1 http://drive5.com/uparse/

2 https://sourceforge.net/projects/rdp-classifier/

3 https://www.arb-silva.de/

2.7. Data analysis

All the determinations were conducted in triplicate unless otherwise stated. Statistical analysis was performed using SPSS 22.0 (SPSS Inc., Chicago, IL, United States) and Origin9.1. Principal component analysis (PCA) was performed using the i-sanger tools to cluster samples according to the relative abundance of microbes. The correlation between bacterial community and physicochemical indicators, organic acids and volatile compounds were investigated by Spearman's correlation coefficient at $|\rho| > 0.7$ with statistically significance ($p < 0.01$). The results were visualized with heatmap by using R software with the "corrplot" package.

3. Results and discussion

3.1. Physicochemical properties and organic acids contents during fermentation

The changes in physicochemical indices including the ethanol (**2A**), total acid (**2B**), amino nitrogen (**2C**), and reducing sugar contents (**2D**) are shown in Figure 2. These characteristics are the key indicators of process control, and the factors of forming unique flavor. The highest ethanol content of 5.6% was observed at the initial stage of AAF, whereas it dramatically decreased to 0% on the 15th day of AAF. During AAF, ethanol is oxidized to acetaldehyde under the catalysis of ethanol dehydrogenase, and then acetaldehyde is oxidized to acetic acid under the catalysis of aldehyde dehydrogenase (21). Thus, it can be seen a significant increase in the total acid content (Figure 2B) from the 1st (1.95 g/100 ml) day to the 19th day (7.18 g/100 ml) of AAF. This observation was in agreement with previous studies (21). Amino nitrogen is related to the degradation of nitrogen-containing compounds (22). As shown in Figure 2C, amino nitrogen concentration showed an increased tendency from 2.46 to 3.45 g/100 ml. According to the Figure 2D, the reducing sugar concentration reached a maximum of 2.10 g/100 ml on the 11th fermentation day, and then decreased to 1.23 g/100 ml at the end of the AAF process. The microbial communities and metabolites are involved in the complicated interactions during AAF, leading to the degradation of oligosaccharides and polysaccharides into the reducing sugar (2). At the later fermentation stage, the decrease in reducing sugar content was due to the growth of microorganisms could be at the expense of reducing sugar (23).

Dynamics of organic acid contents during AAF are shown in Figure 3. Seven kinds of organic acids including acetic acid, lactic acid, oxalic acid, succinic acid, tartaric acid, citric acid, and malic acid were detected by HPLC analysis. Acetic acid and lactic acid are the two dominant organic acids observed in this study, taking accounts 83.95% of the total organic acids at the end of AAF. These acids have been reported as the dominant organic acids in typical Chinese vinegar, such as Shanxi aged vinegar, Zhenjiang aromatic vinegar, and Tianjin duliu vinegar (10). The acetic acid content was sharply increased from 7.74 (1st fermentation day) to 44.44 g/100 ml (19th fermentation day), while the lactic acid content showed a decrease from 40.70 (1st fermentation day) to 16.27 g/100 ml (19th fermentation day). From the 4th day of AAF, the lactic acid content began to decrease. The increased oxygen content made the metabolisms of lactic acid bacteria slow. Simultaneously, the lactic acid was utilized by part of acetic acid bacteria such as acetic anhydride utilized one carbon source, converting the lactic acid into the acetic acid.

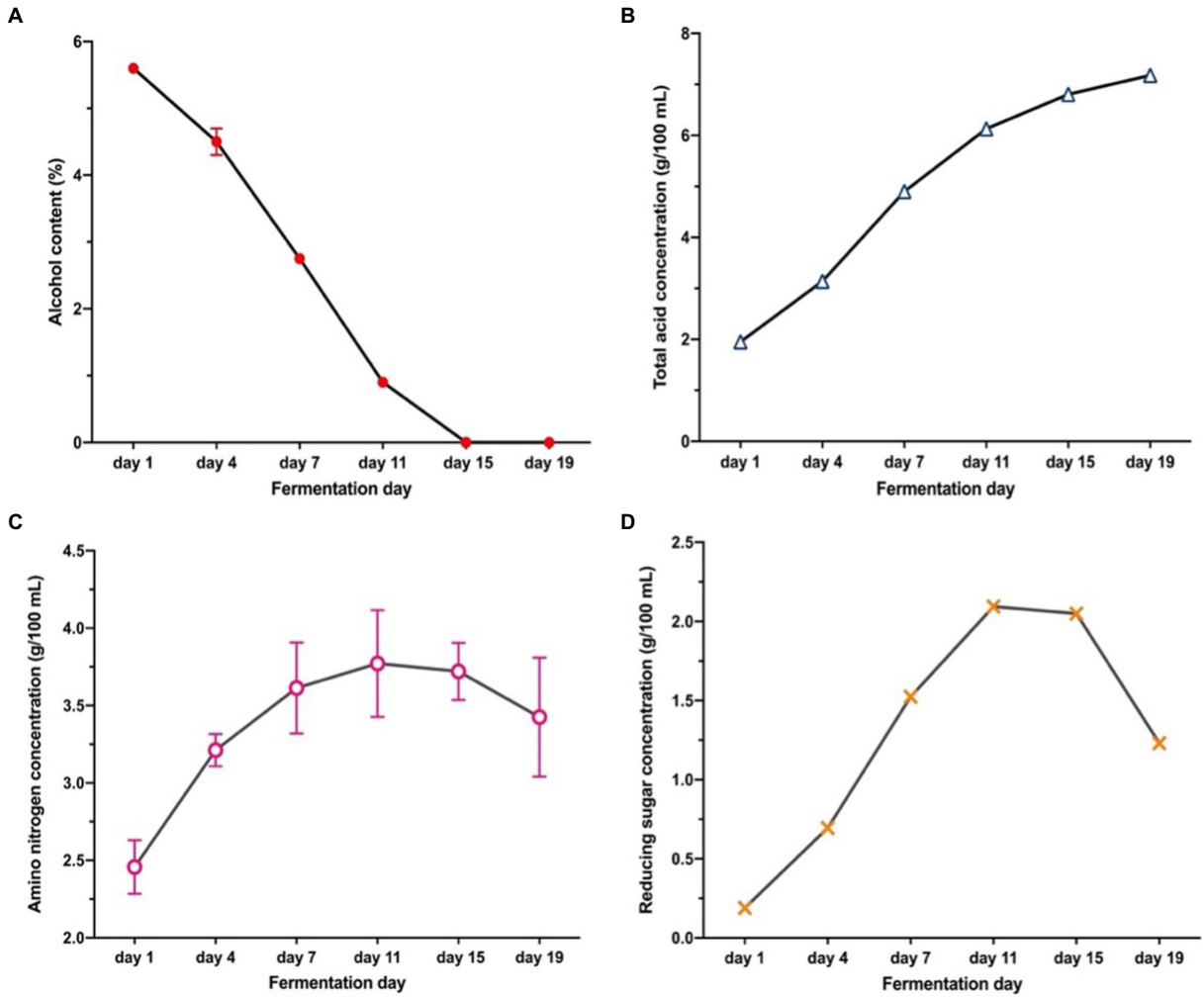

FIGURE 2
Changes in physical and chemical indicators during vinegar fermentation: **(A)** Ethanol content; **(B)** Total acid; **(C)** Amino nitrogen; **(D)** Reducing sugar content.

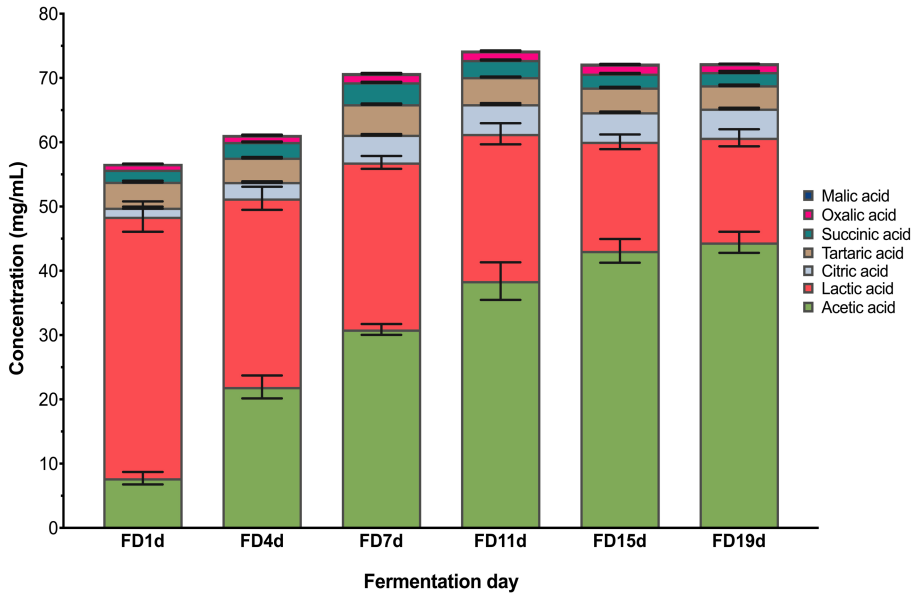

FIGURE 3
Changes in organic acids during vinegar fermentation.

The ratio of lactic acid to acetic acid gradually decreasing, and this ratio was less than 1 on the 11th day of fermentation, indicating that the acetic acid content exceeded lactic acid content. During the alcoholic fermentation of the early stage of AAF, the anaerobic condition is favorable for the metabolisms of lactic acid bacteria to produce lactic acid. On the 3rd day of fermentation, the acetic acid bacteria were introduced from the outside and began to proliferate in the reactor, leading to the rapid production of the acetic acid. Consequently, the content of acetic acid exceeded the lactic acid content, accounting for the largest proportion of total organic acids. However, the high lactic acid content can soothe the pungent taste of acetic acid (24). Additionally, the contents of citric acid and tartaric acid were also abundant during AAF, increasing from 1.40 to 4.56 g/100 ml and decreased from 4.04 to 3.62 g/100 ml during AAF, respectively ($p < 0.05$). The succinic acid content showed a gradual upward trend, while the malic acid content decreased during AAF.

3.2. Analysis of volatile compounds during fermentation

Volatile compounds give vinegar a special flavor. Most volatile compounds are derived from microbial metabolic reactions, while others can be derived from degradation or Maillard reactions (25). In this study, 64 volatile components were identified and quantified during AAF, as shown in Table 1. Based on their retention time, they were classified into esters, alcohols, acids, phenols, aldehydes, ketones, and heterocycles. At the early stage of fermentation, the concentration of all volatile compounds was low (39.94 mg/100 ml). After the yeast culture, fermentation gradually entered the alcoholic fermentation stage, aroma concentration bursting. The total concentration of these compounds reached 1203.91 mg/100 ml at the end of AAF.

Esters are the most common aroma category in vinegar and contributed to the fruity and baking flavors of the product (26). Herein, 25 esters was recognized in the vinegar, which were produced by microorganisms during AAF or synthesized by acid esterification in the presence of ethanol. The number of ester compounds was increased to 23 on the 7th day of AAF, and then reduced to 6 until the end of AAF. The ethyl acetate content on the 15th day was significantly higher than that of other esters, accounting for 42.03% of the total ester contents.

Alcohols mainly originated from the alcohol fermentation stage that provided the precursors for the synthesis of organic acids (4). In this study, 12 alcohols were identified. Most alcohols showed a decreased tendency during AAF. Ethanol accounts for the highest proportion of all the types of alcohol, decreasing from 22.44 to 3.51% throughout the fermentation process. Octanol and Heptanol were not detected in the later stage.

Acidic compounds have a crucial influence on the sensory characteristics of vinegar (27). A total of six acids were detected with a concentration of 63.79% at the end of fermentation, among which the most abundant was acetic acid, accounting for 80.05% of all the acids contents by the end of fermentation. The sufficient acid content might restrict the growth of other bacteria, and increase the mellow and aftertaste of the fermented products, and improve their flavor. Meanwhile, they can aid in the creation of esters. Aldehydes, phenols, ketones, and pyrazines were also present in minute levels during the experiment.

3.3. Dynamics of microbial community during fermentation

After filtering low-quality reads, removing adapters, barcodes, and primers, and detecting chimera, roughly 39,705 to 59,287 effective tags, with various phylogenetic OTUs ranging from 16 to 48 *via* 97 percent sequence identity cutoff, were obtained for bacterial dynamics and diversity. At the genus level, taxonomic affiliations of 97 percent sequence similarity clusters revealed a substantial taxonomic shift during the AAF process.

The bacterial community consisted of 48 genera, including six genera with relative content greater than 1%, which comprised *Lactobacillus*, *Acetobacter*, *Cyanobacteria*, *Pediococcus*, *Weissella*, and *Mitochondria* (Figure 4A). *Lactobacillus* and *Acetobacter* were the most common genera, accounting for more than 90% of all sequences. On days 1 to 19 of AAF, *Lactobacillus* accounted for the greatest percentage, ranging from 43.98 to 78.97 percent. *Lactobacillus* is an anaerobe that thrives during aerobic fermentation but is inhibited by low pH and high acidity. Increased acetic acid levels in fermentation cultures resulted in acidic stress, which favored acid-tolerant bacteria (28). The relative content of *Acetobacter* was only 13.1% on the first day of AAF and increased rapidly to 56.3% on day 4 during fermentation, then decreased slightly, and stabilized between 45 and 50%. *Acetobacter* has effectively dominated the entire fermentation process, and its relative abundance has dramatically increased. After the high acidity and low pH incubation stage, the structure of the bacterial community may be modified to the features of acidophilic and aerobic communities, according to these findings. During the AAF process, changes in modest proportions in the *Cyanobacteria* (4.34–0.04%), *Pediococcus* (1.22–0%), and *Weissella* (0.09–0.01%) groups were also noted. These findings revealed that Lactobacillus and Acetobacter were competing spontaneously. Acetobacter was a fierce competitor in the bacterial community's succession. Alpha diversity indexes representing the number of OTUs, Sobs, Chao, Shannon, Simpson, Ace, and Coverage index were determined to further confirm whether our sequencing results were sufficient to analyze the food fermentation ecosystem, and these indexes demonstrated that the richness of diversity varied during AAF (Table 2). The Sobs and Ace indicate the actually observed richness value, whereas the Chao is used to estimate OTU counts in samples. The microbiological diversity in samples is depicted by both Simpson and Shannon. Herein, the OTUs, Sobs, Chao, Shannon, and Ace index decreased during the AAF process, while the Simpson index increased significantly. This result illustrates that the solid acid fermentation improves the intestinal flora richness and diversity in vinegar samples. The diversity and richness of gut flora may play a role in human obesity and other chronic disorders. Each sample library's coverage is represented by coverage. In this investigation, all of the coverage values found are greater than 0.99. This conclusion shows that the sequence in the sample was extremely likely to be discovered, and that the distribution of the bacterial community of samples might be represented by this finding. In addition, the number of microbial genera detected in this study was less than that in traditional fermented vinegar, while the relative abundance of *Lactobacillus* and *Acetobacter* was higher. The reason could be that the drum-type bioreactor is a relatively closed environment and the whole fermentation process is carried out in it, reducing the contact with the external condition, thus reducing the contamination by miscellaneous bacteria, and consequently providing a favorable fermentation environment for microorganisms.

10.3389/fnut.2023.1126562

TABLE 1 Identification of different compounds during the fermentation processing by using rotary drum reactor.

Variables	Compounds	Relative content (%)					
		F1d	F4d	F7d	F11d	F15d	F19d
Esters	Ethyl acetate (S1)	7.97 ± 1.21	10.10 ± 1.20	13.68 ± 2.45	16.27 ± 2.67	8.04 ± 1.13	3.25 ± 0.24
	Ethyl caproate (S2)	1.19 ± 0.02	3.53 ± 0.56	3.39 ± 0.47	2.28 ± 0.43	1.75 ± 0.15	1.30 ± 0.01
	Ethyl caprylate (S3)	4.72 ± 0.23	4.59 ± 0.83	3.25 ± 0.63	2.51 ± 0.27	1.09 ± 0.06	ND
	Ethyl nonyl (S4)	0.82 ± 0.04	0.55 ± 0.02	0.39 ± 0.03	0.01 ± 0.00	ND	ND
	Ethyl decate (S5)	0.62 ± 0.01	1.27 ± 0.02	0.45 ± 0.01	0.52 ± 0.01	0.51 ± 0.01	ND
	Diethyl succinate (S6)	1.39 ± 0.01	0.88 ± 0.03	2.43 ± 0.02	1.67 ± 002	0.98 ± 0.03	ND
	Phenethyl acetate (S7)	1.20 ± 0.02	2.38 ± 0.43	3.87 ± 0.03	3.74 ± 0.13	4.56 ± 1.32	4.68 ± 0.86
	Benzyl acetate (S8)	ND	ND	0.25 ± 0.01	ND	ND	ND
	Ethyl myristate (S9)	0.98 ± 0.03	0.73 ± 0.04	0.28 ± 0.00	0.32 ± 0.07	ND	ND
	Propionolactone (S10)	3.88 ± 0.21	3.44 ± 0.02	4.68 ± 0.12	4.30 ± 0.18	4.25 ± 1.29	2.62 ± 0.48
	Propionolactone (S11)	ND	0.03 ± 0.00	0.26 ± 0.00	0.30 ± 0.00	0.57 ± 0.05	ND
	Ethyl palmitate (S12)	6.94 ± 0.78	4.37 ± 0.58	3.82 ± 0.26	3.04 ± 0.69	4.07 ± 0.08	ND
	Ethyl laurate (S13)	0.93 ± 0.05	0.45 ± 0.00	0.53 ± 0.01	0.58 ± 0.10	0.64 ± 0.01	ND
	Ethyl oleate (S14)	1.12 ± 0.02	0.54 ± 0.01	0.83 ± 0.02	0.87 ± 0.08	ND	ND
	Ethyl linoleate (S15)	0.93 ± 0.01	0.97 ± 0.02	2.21 ± 0.23	0.98 ± 0.01	ND	ND
	Isoamyl acetate (S16)	0.71 ± 0.01	0.41 ± 0.01	4.89 ± 1.29	1.62 ± 0.00	1.62 ± 0.02	2.79 ±
	Ethyl heptanate (S17)	0.82 ± 0.00	0.53 ± 0.02	0.41 ± 0.01	0.22 ± 0.00	0.47 ± 0.00	ND
	Hexyl acetate (S18)	1.88 ± 0.19	1.81 ± 0.03	5.12 ± 1.29	0.93 ± 0.02	0.54 ± 0.02	0.34 ± 0.02
	Heptane acetate (S19)	ND	ND	0.17 ± 0.02	0.20 ± 0.00	0.44 ± 0.00	ND
	Ethyl benzoate (S20)	0.84 ± 0.06	0.66 ± 0.02	0.66 ± 0.04	0.58 ± 0.01	ND	1.12 ± 0.05
	Ethyl phenylacetate (S21)	0.55 ± 0.00	0.25 ± 0.00	0.73 ± 0.02	0.56 ± 0.04	0.85 ± 0.04	ND
	Ethyl 3-phenylpropionate (S22)	0.65 ± 0.01	0.78 ± 0.18	ND	ND	0.78 ± 0.02	ND
	Diethyl azelaite (S23)	2.53 ± 0.04	0.67 ± 0.02	0.31 ± 0.00	0.76 ± 0.03	ND	ND
	Diethyl succinate (S24)	0.66 ± 0.01	0.42 ± 0.01	ND	0.57 ± 0.01	0.96 ± 0.02	ND
	Diethyl succinate (S25)	0.51 ± 0.00	0.71 ± 0.03	0.11 ± 0.00	0.06 ± 0.00	0.98 ± 0.01	ND
Alcohols	Ethanol (S26)	22.44 ± 2.78	11.48 ± 2.46	6.45 ± 1.28	5.07 ± 1.29	3.51 ± 0.78	2.01 ± 0.78
	Isoamyl alcohol (S27)	1.82 ± 0.03	1.50 ± 0.01	1.46 ± 0.39	0.80 ± 0.02	2.12 ± 0.18	2.31 ± 0.49
	Phenyl ethanol (S28)	1.16 ± 0.01	2.06 ± 0.02	3.42 ± 0.89	3.11 ± 0.78	3.73 ± 0.27	3.70 ± 1.29
	Hexanol (S29)	3.91 ± 1.10	3.64 ± 0.76	3.39 ± 1.29	2.05 ± 0.37	1.07 ± 0.21	ND
	Octanol (S30)	1.11 ± 0.00	1.21 ± 0.03	0.16 ± 0.03	ND	ND	ND
	1-Nonanol (S31)	1.05 ± 0.01	0.96 ± 0.24	0.54 ± 0.02	0.32 ± 0.02	0.52 ± 0.04	ND
	Heptanol (S32)	0.87 ± 0.03	0.74 ± 0.28	0.05 ± 0.00	ND	ND	ND
	Isobutanol (S33)	ND	ND	ND	0.05 ± 0.00	ND	ND
	(R) - (-) - 2-butanol (S34)	0.71 ± 0.02	ND	ND	ND	ND	ND
	2,3-butanediol (S35)	3.34 ± 0.02	6.62 ± 1.28	4.26 ± 1.38	1.18 ± 0.02	1.02 ± 0.04	0.33 ± 0.00
	(2R, 3R) - (-) - 2,3-butanediol (S36)	ND	0.55 ± 0.05	0.09 ± 0.01	1.61 ± 0.02	1.12 ± 0.05	0.47 ± 0.01
	Cis-4-decene-1-ol (S37)	1.00 ± 0.04	1.66 ± 0.42	0.02 ± 0.00	0.36 ± 0.01	0.56 ± 0.02	ND
Acids	Acetic acid (S38)	8.21 ± 1.13	8.64 ± 1.39	12.02 ± 2.37	18.14 ± 2.74	18.79 ± 3.78	48.50 ± 9.76
	Caproic acid (S39)	5.49 ± 0.98	6.53 ± 1.18	5.80 ± 1.19	6.80 ± 2.38	11.99 ±	6.68 ± 2.04
	Butyrate (S40)	ND	ND	ND	ND	2.53 ± 0.89	3.73 ± 1.20
	Heptanic acid (S41)	ND	ND	0.36 ± 0.04	ND	2.68 ± 0.48	1.27 ± 0.67
	Bitter (S42)	2.37 ± 0.45	6.76 ± 0.02	1.68 ± 0.02	4.50 ± 0.46	4.68 ± 1.38	2.34 ± 0.45
	Palmitic acid (S43)	ND	ND	0.76 ± 0.04	7.55 ± 1.29	1.29 ± 0.02	1.27 ± 0.38

(Continued)

10.3389/fnut.2023.1126562

TABLE 1 (Continued)

Variables	Compounds	Relative content (%)					
		F1d	F4d	F7d	F11d	F15d	F19d
Phenols	4-vinyl-2-methoxyphenol(S44)	0.42 ± 0.02	0.80 ± 0.00	0.37 ± 0.01	0.27 ± 0.01	0.61 ± 0.06	0.60 ± 0.01
	2-methoxy-4-methylphenol (S45)	ND	ND	0.42 ± 0.02	0.71 ± 0.07	3.24 ± 1.23	2.15 ± 0.55
	4-ethyl-2-methoxyphenol (S46)	0.71 ± 0.04	0.32 ± 0.00	0.37 ± 0.01	0.44 ± 0.01	1.27 ± 0.06	0.79 ± 0.18
	Phenol (S47)	1.09 ± 0.02	0.96 ± 0.01	0.55 ± 0.00	0.40 ± 0.05	0.57 ± 0.02	0.80 ± 0.02
	Guaiacol (S48)	1.09 ± 0.01	1.81 ± 0.01	3.89 ± 0.57	4.12 ± 0.28	4.67 ± 1.29	4.53 ± 1.28
Aldehydes	Benzaldehyde (S49)	0.37 ± 0.02	3.24 ± 0.01	0.92 ± 0.01	1.52 ± 0.43	1.74 ± 0.23	1.31 ± 0.09
	Phenylacetaldehyde (S50)	0.18 ± 0.00	ND	ND	ND	0.85 ± 0.04	1.64 ± 0.58
	2-hydroxy-3-methylbenzaldehyde (S51)	ND	ND	ND	ND	ND	0.15 ± 0.04
	2-hydroxy-6-methylbenzaldehyde (S52)	0.54 ± 0.01	0.41 ± 0.00	2.12 ± 0.03	1.88 ± 0.28	1.36 ± 0.28	1.43 ± 0.05
	Furfural (S53)	ND	ND	ND	ND	ND	ND
Ketone	2-pyrrolidone (S54)	ND	ND	ND	ND	ND	1.74 ± 0.27
	3-hydroxy-2-butanone (S55)	ND	ND	0.13 ± 0.01	1.41 ± 0.24	4.89 ± 1.29	1.77 ± 0.43
	6-methyl-3,5-pentadiene-2-one (S56)	0.37 ± 0.02	1.46 ± 0.34	0.23 ± 0.00	0.43 ± 0.19	0.34 ± 0.02	0.46 ± 0.01
	3-acetyl-2-butanone (S57)	ND	ND	0.08	2.77 ± 0.56	ND	1.87 ± 0.76
	2- piperazine(S58)	ND	ND	ND	ND	1.41 ± 0.13	ND
	2,3-butanedione (S59)	ND	ND	0.17 ± 0.00	ND	ND	ND
Heterocycles	Trichloromethane (S60)	ND	0.31 ± 0.02	0.27 ± 0.04	0.31 ± 0.06	ND	ND
	Sixteen alkane (S61)	ND	ND	ND	ND	0.25 ± 0.00	0.41 ± 0.01
	2,3,5,6-tetramethylpyrazine (S62)	ND	ND	ND	0.92 ± 0.03	1.08 ± 0.03	1.45 ± 0.13
	2,3,5-trimethylpyrazine (S63)	ND	ND	0.25 ± 0.01	ND	0.41 ± 0.01	ND
	3-methyl-bicyclo [4.1.0] heptane (S64)	ND	ND	ND	ND	1.02 ± 0.07	0.41 ± 0.05

Values are mean ± standard deviation (SD), $n = 3$. FD, Fermentation day.

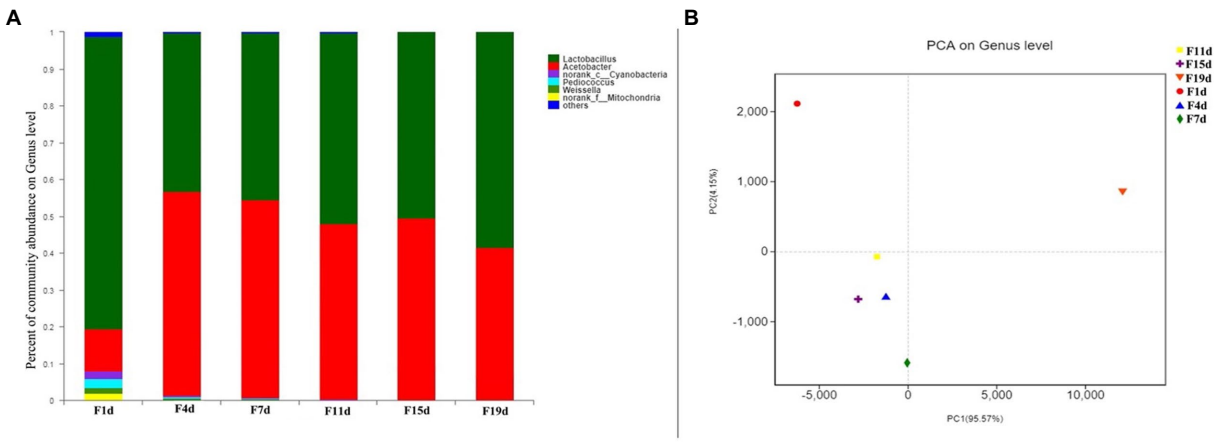

FIGURE 4
(A) Distribution of bacterial community at genus level during vinegar acid fermentation; **(B)** Principal component analysis of microorganism during fermentation.

To examine the differences and similarities in bacterial Illumina MiSeq sequencing at different fermentation stages, PCA analysis (Figure 4B) was used. Similarity analysis between groups was done on samples at the Genus level, as seen in the figure. In the same group, the obtained values are fairly consistent. The first principal component (PC1) accounted for 91.29% of the total variance, while the PC2 explained a further 8.25%. Based on the bacterial structure, the AAF process was divided into three stages: pre-fermentation stage (1 day), medium fermentation stage (4 days), and late fermentation stage (7–19 days). This division provided a succession of bacterial profiles at different stages of AAF. The OTUs from day 1 lie on the first quadrant, which was characterized mainly by *Lactobacillus*, followed *Acetobacter*, *Cyanobacteria, Pediococcus, Weissella*, and *Mitochondria*. In addition, sample on the 4th day exhibited distinctive characters, showing a significant difference with the bacterial structure of day 1. The patterns of OTUs from days 7, 11, 15, and 19

TABLE 2 Richness and diversity indexes from samples at different fermentation stages.

Fermentation day	OTUs	Sobs	Chao	Shannon	Simpson	Ace	Coverage
F-1d	48.00 ± 2.65^{a}	48.33 ± 2.52^{a}	50.06 ± 3.02^{a}	1.08 ± 0.18^{a}	0.59 ± 0.07^{c}	47.35 ± 4.84^{a}	0.9973 ± 0.0002^{b}
F-4d	34.33 ± 13.58^{a}	35.33 ± 5.51^{bc}	41.28 ± 5.71^{b}	0.77 ± 0.12^{b}	0.65 ± 0.08^{bc}	44.28 ± 7.01^{a}	0.9964 ± 0.0003^{d}
F-7d	33.00 ± 1.00^{ab}	37.33 ± 4.16^{b}	43.28 ± 2.75^{b}	0.63 ± 0.01^{c}	0.73 ± 0.01^{b}	44.85 ± 4.06^{a}	0.9974 ± 0.0002^{b}
F-11d	27.33 ± 1.53^{c}	30.00 ± 0.00^{c}	40.21 ± 10.24^{bc}	0.50 ± 0.06^{d}	0.78 ± 0.04^{ab}	40.89 ± 6.34^{a}	0.9964 ± 0.0002^{d}
F-15d	19.00 ± 1.00^{d}	21.33 ± 3.22^{d}	32.42 ± 14.22^{bc}	0.46 ± 0.12^{ed}	0.78 ± 0.08^{ab}	34.76 ± 18.00^{a}	0.9982 ± 0.0003^{a}
F-19d	16.67 ± 0.58^{e}	23.33 ± 2.31^{d}	29.83 ± 5.58^{c}	0.42 ± 0.02^{e}	0.81 ± 0.02^{a}	42.03 ± 15.24^{a}	0.9973 ± 0.0002^{bc}

Values are mean ± standard deviation (mean ± SD, $n = 3$). Values with different letters within the same column differ from each other statistically. F, Fermentation.

were well clustered, which were mainly characterized *by Lactobacillus* and *Acetobacter*. These results were in agreement with the microbial community diversity and richness analysis, which could be attributed to the changes in temperature, pH, and acidity during the AAF process.

3.4. Correlation analysis between bacterial community and various indicators

During the AAF process, microbial diversity and community play critical roles in flavor creation. Acetate esters are formed by yeast and bacteria through lipid and acetyl-CoA metabolisms or chemical esterification of alcohols and acids. Bacterial dynamics in relation to organic acid alterations in solid-state AAF were also investigated (Figures 5A). Lactic acid concentrations increased considerably from day one to day 19 in this study. Furthermore, *Lactobacillus*, the most common lactic acid bacteria, was the most common division in AAF. *Lactobacillus* members added a significant amount of lactic acid to vinegar, enhancing a mellow taste by reducing the annoying sour smell. Several yeast strains and molds from the genera *Aspergillus, Penicillium*, and *Candida* were among the citric acid-accumulating microorganisms. Until the end of AAF, the citric acid content gradually increased. Molds and yeast strains were also found to be involved in the AAF process, according to these findings. Furthermore, the concentrations of other organic acids were low, which could be owing to the poor diversity of acetic acid bacteria used in the AAF process (Figure 5A).

The majority of bacteria that produced amino acids were *Corynebacterium glutamicum*, and the increased amino acid concentration could be attributable to yeast autolysis during the vinegar starter and alcohol mash. The *Lactobacillus*, on the other hand, can produce some free amino acids by degrading proteins. The highest levels of free amino acids were found on day 11, followed by a minor decrease on day 17, and an increase on day 19. In the meantime, *Lactobacillus* relative abundance hit new highs. These findings suggested that yeast autolysis may occur in the early and middle stages of AAF, and that the *Lactobacillus* may be involved in the production of free amino acids during the AAF process.

Ester compounds were the main volatiles observed in the vinegar samples. Esters endow fruit-like aroma to vinegar. In this study, *Acetobacter, Norank-c-Cyanobacteria*, and *Weissella* were the three principal contributors to ester production. These microbes are also considered to play key roles in the process of fermentation. Moreover, the microorganisms associated with lipids were the most relevant, and those associated with ketones were the least relevant in this study, and these results are consistent with earlier published studies. On day 4 of AAF, the relative concentration of total esters increased substantially, followed by a drop. On day 4, the relative abundance of the microbial community at the genus level changed dramatically. During AAF, the Acetobacter genus was the most common ethyl acetate-producing bacteria. Many different microorganisms, such as yeast, can improves the production of ethyl acetate. In the first 11 days, the relative level of ethyl acetate increased, followed by a drop, as seen in Table 1. These findings corroborated previous observations that yeasts die out progressively during the AAF process. *Bacillus* sp. can also aid in the formation of esterase and organophosphorus chemicals. *Bacillales* and *Rhodospirillales* can work together to create acetate esters. The synthesis of acetate esters was strongly linked to the succession pattern of relative abundance of the *Bacillus* and *Acetobacter* genera, according to these findings. Furthermore, throughout the AAF process, the relative concentration of carboxylic acids, particularly acetic acid, rose considerably. This enhanced propensity was roughly in line with *Acetobacter* relative abundance dynamics (Figure 5C). These findings suggested that acetic acid was primarily produced from the *Rhodospirillales* family, which was consistent with prior reports indicating fermentation acid generation was primarily due to *Acetobacter* genus metabolism (29). However, starting on day 4, the relative proportion of total alcohol declined considerably, which was reflected in the shift in acetic acid content. The acetic acid bacteria are responsible for the decline of alcohol because ethanol can be converted to acetic acid, whereas yeasts are responsible for the accumulation of alcohol due to the conversion of fermentable carbohydrates into ethanol (Figure 5B). 3-hydroxy-2-butanone (acetoin) is a physiological metabolite secreted by a variety of bacteria that serve as a quality indicator for fermented items and a flavor component in vinegar (30). Acetoin biosynthetic microorganisms in diverse fermentation processes include *Acetobacter, Lactococcus, Klebsiella, Enterobacter,* and *Bacillus*. After day 7 of AAF, the relative concentration of acetoin increased dramatically, which was linked to the high relative abundance of *Lactobacillus* and *Acetobacter* was identified during the AAF process. Furthermore, vinegar is fermented from cereals by numerous bacteria and a variety of taste compounds are created to give vinegar their scent. The principal bioactive components in vinegar have been identified as pyrazine chemicals. Tetramethylpyrazine has piqued interest due to its several bioactivities. It has been widely utilized to treat a variety of ailments, including cardiovascular and hypertension problems.

However, the relative content of tetramethylpyrazine detected in this study was low. Bacillus is a high-yield bacterial strain for tetramethylpyrazine biosynthesis and is closely related to the formation of ligustrazine and its precursors, 2,3-butanedione and 3-hydroxybutanone.

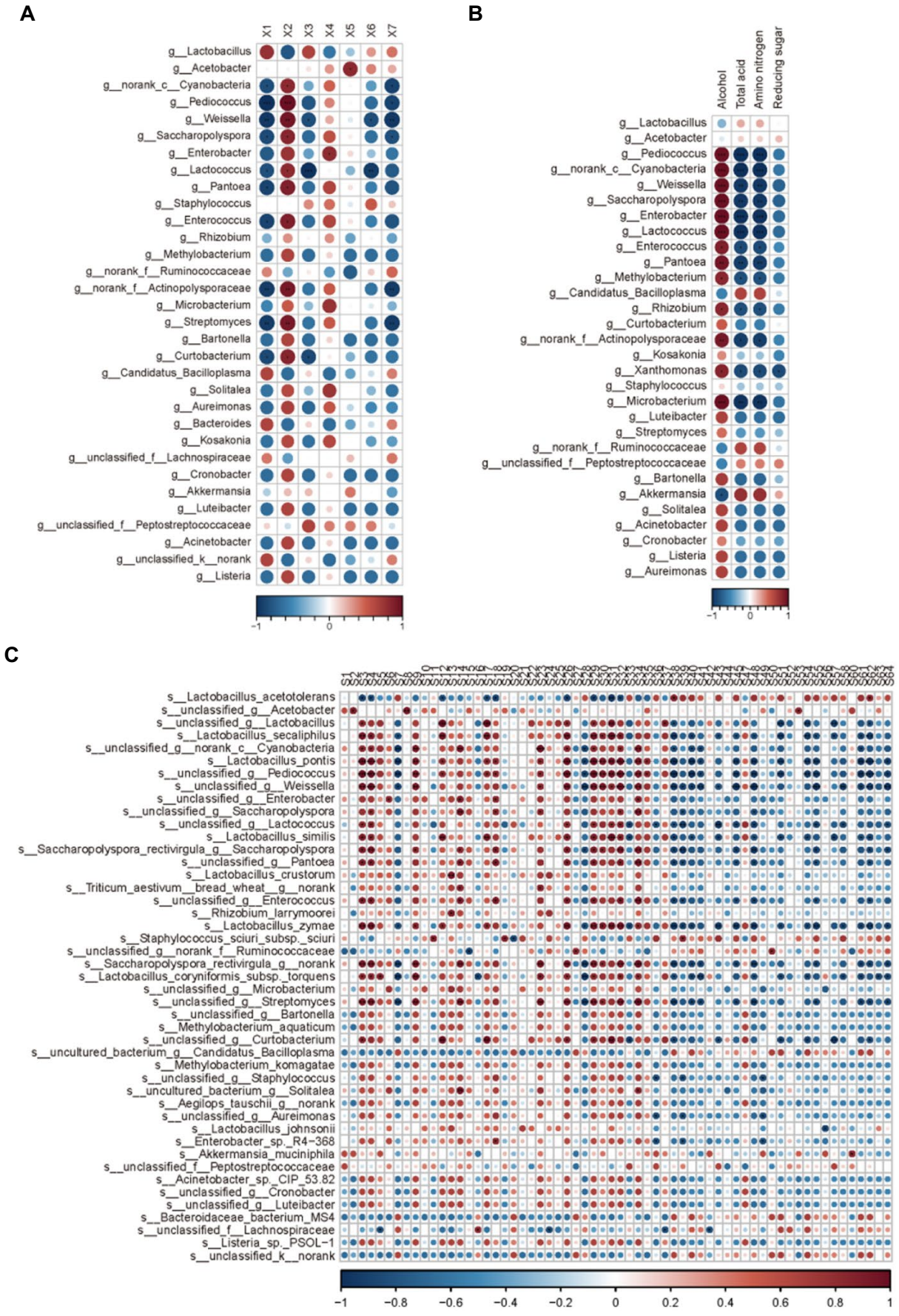

FIGURE 5
Correlation analysis between microbial community and various indicators: **(A)** organic acids; **(B)** Physical and chemical indicators; **(C)** Volatile compounds.

The relative content of *Bacillus* in this study was only relatively low (0.34–0.53%), which could be due to the insufficient oxygen flow in the bioreactor.

4. Conclusion

The bacterial composition and dynamic succession in the entire solid-state AAF vinegar was studied. *Lactobacillus* and *Acetobacter* are the most common bacteria associated in AAF. Bacterial diversity increased early in the AAF process and subsequently declined afterwards. The bacterial growth during the AAF process was related to pH, titratable acidity, and alcoholic degree. During the entire AAF process, the abundance of lactic acid and acetic acid bacteria was greater than 60%, implying that lactic acid and acetic acid bacteria had a significant impact on vinegar flavor. Furthermore, after AAF, the structure of the bacterial population may be altered to reflects the properties of acidophilic and aerobic communities. The interaction between metabolic processes, bacterial patterns, and fermentation settings are being explored in greater depth, providing new insights into the role of bacterial communities in fermentation. Changes in metabolites during the AAF process were also caused by the dynamics and diversity of microbial population succession. These preliminary findings represent a paradigm shift in our understanding of AAF systems, in which acidophilic and aerobic bacterial communities play critical roles in enhancing alcohol availability and vinegar acetic acid yield. This work established the relationship between bacterial dynamics and metabolite changes in AAF of vinegar production, which might be used as a guide for future AAF fermentation experiments to improve the quality of vinegar.

Data availability statement

The original contributions presented in the study are publicly available. This data can be found here: NCBI, accession number PRJNA934156.

Author contributions

WW: conceptualization, data curation, formal analysis, investigation, and writing original draft. FZ: methodology, formal analysis, writing—review and editing, and visualization. XD: writing—review and editing and visualization. YL and JM: investigation, resources, and writing—review and editing. JW: supervision and writing—review and editing. QM and JS: funding acquisition, project administration, supervision, validation, and writing—review and editing. All authors contributed to the article and approved the submitted version.

Funding

The authors are grateful to the Young Scholar Scientific Research Foundation of Hebei Agricultural University (YJ201850), the Program of the Hebei Youth Top-notch Talent Supporting Plan (0316027), Hebei Province "Three Three Three" Talent Project (A202005002).

Conflict of interest

The authors declare that the research was conducted in the absence of any commercial or financial relationships that could be construed as a potential conflict of interest.

Publisher's note

All claims expressed in this article are solely those of the authors and do not necessarily represent those of their affiliated organizations, or those of the publisher, the editors and the reviewers. Any product that may be evaluated in this article, or claim that may be made by its manufacturer, is not guaranteed or endorsed by the publisher.

References

1. Xia, M, Zheng, Y, Zhang, X, Xie, S, Wu, Y, Xia, T, et al. "Solid-state fermentation systems for vinegar production," in *Advances in Vinegar Production*. ed. A. Bekatorou. (Boca Raton, FL: CRC Press), (2019). 141–154.

2. Zhang, X, Wang, P, Xu, D, Wang, W, and Zhao, Y. Aroma patterns of Beijing rice vinegar and their potential biomarker for traditional Chinese cereal vinegars. *Food Res Int*. (2019) 119:398–410. doi: 10.1016/j.foodres.2019.02.008

3. Galanakis, C. "Food waste valorization opportunities for different food industries," in *The Interaction of Food Industry and Environment*. ed. C. Galanakis. (Amsterdam: Elsevier), (2020). 341–422.

4. Zhu, Y, Zhang, F, Zhang, C, Yang, L, Fan, G, Xu, Y, et al. Dynamic microbial succession of Shanxi aged vinegar and its correlation with flavor metabolites during different stages of acetic acid fermentation. *Sci Rep*. (2018) 8:8612. doi: 10.1038/s41598-018-26787-6

5. Hu, X, Tian, R, Wang, K, Cao, Z, Yan, P, Li, F, et al. The prokaryotic community, physicochemical properties and flavors dynamics and their correlations in fermented grains for Chinese strong-flavor baijiu production. *Food Res Int*. (2021a) 148:110626. doi: 10.1016/j.foodres.2021.110626

6. Wang, C. *New Approaches to Estimate Microbial Diversity of Alcoholic Fermentation*. [dissertation/master's thesis]. Spain: Universitat Rovira i Virgili (2016).

7. Zhang, X-L, Zheng, Y, Xia, M-L, Wu, Y-N, Liu, X-J, Xie, S-K, et al. Knowledge domain and emerging trends in vinegar research: a bibliometric review of the literature from WoSCC. *Foods*. (2020) 9:166. doi: 10.3390/foods9020166

8. Li, S, Li, P, Liu, X, Luo, L, and Lin, W. Bacterial dynamics and metabolite changes in solid-state acetic acid fermentation of Shanxi aged vinegar. *Appl Microbiol Biotechnol*. (2016) 100:4395–411. doi: 10.1007/s00253-016-7284-3

9. Zhou, Z, Jian, D, Gong, M, Zhu, S, Li, G, Zhang, S, et al. Characterization of the key aroma compounds in aged Zhenjiang aromatic vinegar by gas chromatography-olfactometry-mass spectrometry, quantitative measurements, aroma recombination and omission experiments. *Food Res Int*. (2020) 136:109434. doi: 10.1016/j.foodres.2020.109434

10. Ai, M, Qiu, X, Huang, J, Wu, C, Jin, Y, and Zhou, R. Characterizing the microbial diversity and major metabolites of Sichuan bran vinegar augmented by Monascus purpureus. *Int J Food Microbiol*. (2019) 292:83–90. doi: 10.1016/j.ijfoodmicro.2018.12.008

11. Vandenberghe, LP, Pandey, A, Carvalho, JC, Letti, LA, Woiciechowski, AL, Karp, SG, et al. Solid-state fermentation technology and innovation for the production of agricultural and animal feed bioproducts. *Syst Microbiol Biomanufact*. (2021) 1:142–65. doi: 10.1007/s43393-020-00015-7

12. Yan, B, and Zhang, H. "Lactic acid bacteria and fermented cereals," in *Lactic Acid Bacteria*. ed. W. Chen. (Singapore: Springer), (2019). 145–179.

13. Mishra, SS, Ray, RC, Panda, SK, and Montet, D. Technological innovations in processing of fermented foods an overview. *Fermented Foods*. eds. R. C. Ray and D. Montet. (Taylor & Francis), (2017). 21–45.

14. Demir, H, and Tari, C. Bioconversion of wheat bran for polygalacturonase production by aspergillus sojae in tray type solid-state fermentation. *Int Biodeterior Biodegradation*. (2016) 106:60–6. doi: 10.1016/j.ibiod.2015.10.011

15. Antunes, FA, Chandel, AK, dos Santos, JC, Milessi, TS, Peres, GF, and da Silva, SSR. Hemicellulosic ethanol production in fluidized bed reactor from sugar cane bagasse hydrolysate: interplay among carrier concentration and aeration rate. *ACS Sustain Chem Eng*. (2017) 5:8250–9. doi: 10.1021/acssuschemeng.7b01916

16. Razali, MAA, and Said, FM. Red pigment production by monascus purpureus in stirred-drum bioreactor. *Galeri Warisan Sains*. (2017) 1:13–5. doi: 10.26480/gws.01.2017.13.15

17. Bouatenin, KMJP, Kouamé, KA, Gueu-Kehi, ME, Djéni, NDT, and Djè, KM. Organic production of vinegar from mango and papaya. *Food Sci Nutr*. (2021) 9:190–6. doi: 10.1002/fsn3.1981

18. Xiao, Z, Dai, S, Niu, Y, Yu, H, Zhu, J, Tian, H, et al. Discrimination of Chinese vinegars based on headspace solid-phase microextraction-gas chromatography mass spectrometry of volatile compounds and multivariate analysis. *J Food Sci*. (2011) 76:C1125–35. doi: 10.1111/j.1750-3841.2011.02356.x

19. Plessi, M, Bertelli, D, and Miglietta, F. Extraction and identification by GC-MS of phenolic acids in traditional balsamic vinegar from Modena. *J Food Compos Anal*. (2006) 19:49–54. doi: 10.1016/j.jfca.2004.10.008

20. Ma, Q, Wang, W, Ma, Z, Liu, Y, Mu, J, Wang, J, et al. Enzymatic-modified dietary fibre fraction extracted from potato residue regulates the gut microbiotas and production of short-chain fatty acids of C57BL/6 mice. *J Funct Foods*. (2021) 84:104606. doi: 10.1016/j.jff.2021.104606

21. Wu, Y, Xia, M, Zhao, N, Tu, L, Xue, D, Zhang, X, et al. Metabolic profile of main organic acids and its regulatory mechanism in solid-state fermentation of Chinese cereal vinegar. *Food Res Int*. (2021) 145:110400. doi: 10.1016/j.foodres.2021.110400

22. Sankuan, X, Cuimei, Z, Bingqian, F, Yu, Z, Menglei, X, Linna, T, et al. Metabolic network of ammonium in cereal vinegar solid-state fermentation and its response to acid stress. *Food Microbiol*. (2021) 95:103684. doi: 10.1016/j.fm.2020.103684

23. Sukumaran, RK, Singhania, RR, Mathew, GM, and Pandey, A. Cellulase production using biomass feed stock and its application in lignocellulose saccharification for bio-ethanol production. *Renew Energy*. (2009) 34:421–4. doi: 10.1016/j.renene.2008.05.008

24. Peyer, LC, Zannini, E, and Arendt, EK. Lactic acid bacteria as sensory biomodulators for fermented cereal-based beverages. *Trends Food Sci Technol*. (2016) 54:17–25. doi: 10.1016/j.tifs.2016.05.009

25. Gong, M, Zhou, Z, Liu, S, Zhu, S, Li, G, Zhong, F, et al. Dynamic changes in physico-chemical attributes and volatile compounds during fermentation of Zhenjiang vinegars made with glutinous and non-glutinous japonica rice. *J Cereal Sci*. (2021) 100:103246. doi: 10.1016/j.jcs.2021.103246

26. Zhou, Z, Liu, S, Kong, X, Ji, Z, Han, X, Wu, J, et al. Elucidation of the aroma compositions of Zhenjiang aromatic vinegar using comprehensive two dimensional gas chromatography coupled to time-of-flight mass spectrometry and gas chromatography-olfactometry. *J Chromatogr A*. (2017) 1487:218–26. doi: 10.1016/j.chroma.2017.01.014

27. Mas, A, Torija, MJ, García-Parrilla, MDC, and Troncoso, AM. Acetic acid bacteria and the production and quality of wine vinegar. *Sci World J*. (2014) 2014:394671. doi: 10.1155/2014/394671

28. Bartkiene, E, Lele, V, Ruzauskas, M, Domig, KJ, Starkute, V, Zavistanaviciute, P, et al. Lactic acid bacteria isolation from spontaneous sourdough and their characterization including antimicrobial and antifungal properties evaluation. *Microorganisms*. (2020) 8:64. doi: 10.3390/microorganisms8010064

29. Andrés-Barrao, C, Saad, MM, Chappuis, M-L, Boffa, M, Perret, X, Pérez, RO, et al. Proteome analysis of Acetobacter pasteurianus during acetic acid fermentation. *J Proteome*. (2012) 75:1701–17. doi: 10.1016/j.jprot.2011.11.027

30. Hu, Y, Wang, H, Kong, B, Wang, Y, and Chen, Q. The succession and correlation of the bacterial community and flavour characteristics of Harbin dry sausages during fermentation. *LWT*. (2021b) 138:110689. doi: 10.1016/j.lwt.2020.110689

frontiers | Frontiers in Nutrition

TYPE Original Research
PUBLISHED 28 April 2023
DOI 10.3389/fnut.2023.1117460

OPEN ACCESS

EDITED BY
Debao Niu,
Guangxi University, China

REVIEWED BY
Dai Cheng,
Tianjin University of Science and Technology, China
Xiangui Mei,
Shandong Agricultural University, China
Mallikarjuna Rao Pichika,
International Medical University, Malaysia
Fang Wang,
Ludong University, China

*CORRESPONDENCE
Xiulian Li
✉ ouclixiulian@163.com
Jiayu Zhang
✉ zhangjiayu0615@163.com

†These authors have contributed equally to this work and share first authorship

RECEIVED 06 December 2022
ACCEPTED 30 March 2023
PUBLISHED 28 April 2023

CITATION
Ge X, Su Z, Wang Y, Zhao X, Hou K, Zheng S, Zeng P, Shi Z, Hu S, Wang Y, Zhou M, Zhang J and Li X (2023) Identifying the intervention mechanisms of polydatin in hyperuricemia model rats by using UHPLC-Q-Exactive Orbitrap mass spectroscopy metabonomic approach.
Front. Nutr. 10:1117460.
doi: 10.3389/fnut.2023.1117460

Identifying the intervention mechanisms of polydatin in hyperuricemia model rats by using UHPLC-Q-Exactive Orbitrap mass spectroscopy metabonomic approach

Xueli Ge[1†], Zhenguo Su[2†], Yuhao Wang[1], Xue Zhao[1], Kaifei Hou[1], Shuna Zheng[1], Pengjiao Zeng[3], Zhongqi Shi[1], Senhao Hu[1], Yuqing Wang[1], Mengchen Zhou[1], Jiayu Zhang[1]* and Xiulian Li[1]*

[1]School of Pharmacy, Binzhou Medical University, Yantai, China, [2]Affiliated Hospital of Binzhou Medical College, Yantai, China, [3]Medical Research Center, Affiliated Hospital of Qingdao University, Qingdao, Shandong, China

Introduction: Polydatin is a biologically active compound found in mulberries, grapes, and *Polygonum cuspidatum*, and it has uric acid-lowering effects. However, its urate-lowering effects and the molecular mechanisms underlying its function require further study.

Methods: In this study, a hyperuricemic rat model was established to assess the effects of polydatin on uric acid levels. The body weight, serum biochemical indicators, and histopathological parameters of the rats were evaluated. A UHPLC-Q-Exactive Orbitrap mass spectrometry-based metabolomics approach was applied to explore the potential mechanisms of action after polydatin treatment.

Results: The results showed a trend of recovery in biochemical indicators after polydatin administration. In addition, polydatin could alleviate damage to the liver and kidneys. Untargeted metabolomics analysis revealed clear differences between hyperuricemic rats and the control group. Fourteen potential biomarkers were identified in the model group using principal component analysis and orthogonal partial least squares discriminant analysis. These differential metabolites are involved in amino acid, lipid, and energy metabolism. Of all the metabolites, the levels of L-phenylalanine, L-leucine, *O*-butanoylcarnitine, and dihydroxyacetone phosphate decreased, and the levels of L-tyrosine, sphinganine, and phytosphingosine significantly increased in hyperuricemic rats. After the administration of polydatin, the 14 differential metabolites could be inverted to varying degrees by regulating the perturbed metabolic pathway.

Conclusion: This study has the potential to enhance our understanding of the mechanisms of hyperuricemia and demonstrate that polydatin is a promising potential adjuvant for lowering uric acid levels and alleviating hyperuricemia-related diseases.

KEYWORDS

polydatin, urate-lowing effects, metabolomics, mechanism, UHPLC-Q-Exactive Orbitrap

1. Introduction

Hyperuricemia (HUA) is a metabolic disease caused by the accumulation of excess uric acid (UA) in the serum due to abnormalities in purine metabolism or UA excretion (1). Along with the changes in diet and lifestyle, the prevalence of HUA has been increasing and mostly affects young people (2, 3). Overproduction of UA in the body can cause a series of complications, such as gout (4), diabetes, cardiovascular disease, and chronic kidney disease (5). Currently, the main therapy for HUA is urate reduction *via* the inhibition of UA production or acceleration of UA excretion. Effective drugs commonly exert rapid effects. However, the alleviation of symptoms is usually short-lived and recurs without continued drug treatment, which causes unwanted side effects (6–8). Therefore, it is necessary to develop alternative compounds that are more effective and less toxic for managing HUA.

In recent years, plant-derived natural compounds have been recognized as efficacious and largely benign and have found wide acceptance as medicines or lead compounds globally (9). Polydatin is a polyphenolic monomer compound abundant in mulberries, grapes, and *Polygonum cuspidatum* and has been shown to have a wide variety of bioactivities, such as liver and kidney protection, anti-inflammatory, antioxidant, and antitumor effects (10, 11). Many studies have demonstrated that polydatin has urate-lowering effects by inhibiting xanthine oxidase activity, reducing the UA synthesis rate, and downregulating mURAT1, mGLUT9, and mABCG2 expression to promote UA excretion in renal tissues (12, 13). In addition, polydatin mitigates kidney injury by inhibiting inflammasome activation (14). However, the underlying intervention mechanism of polydatin in lowering urate is complex and requires further investigation.

Small-molecule metabolites directly reflect pathological processes following external stimuli or disturbances. Alterations in endogenous metabolites have recently been used to study disease pathophysiology and evaluate the toxic and therapeutic effects of drugs (15, 16). Metabolomics provides a method for detecting and analyzing the types, quantities, and varying patterns of endogenous small-molecule metabolites (amino acids, lipids, sugars, etc.) from biological samples in a timely and comprehensive manner (17). Metabolomics has been successfully employed to screen potential biomarkers, characterize physiological or pathological conditions in various diseases, and evaluate metabolic pathway disorders (18–20). However, few studies have described the urate-lowering mechanisms of polydatin, focusing on endogenous small-molecule substances in animal experiments.

In the present study, we employed a metabolomics approach using UHPLC-Q-Exactive Orbitrap mass spectrometry (MS) to explore the mechanism underlying the urate-lowering effects of polydatin in rats. A rat model of potassium oxonate-induced HUA was established to analyze multiple targets, including a low concentration of UA, protection of kidney and renal function, and regulation of blood lipid levels to evaluate the amelioration of HUA by polydatin. Moreover, we screened potential biomarkers in serum samples to assess the therapeutic efficacy of polydatin. The regulation of the metabolic network by polydatin was illustrated using metabolic pathway analysis. This study elucidated the potential mechanisms of polydatin in moderating HUA and provided alternative prevention and treatment options for HUA.

2. Materials and methods

2.1. Chemical and reagents

Potassium oxonate was purchased from Sigma–Aldrich (St. Louis, MO, USA). Benzbromarone and polydatin (≥95% purity) were purchased from Yuan-Ye Biotechnology Technology (Shanghai, China). Carboxymethyl cellulose sodium was purchased from Aladdin (Shanghai, China). D-Fructose was obtained from Solarbio Technology (Beijing, China). HPLC-grade formic acid and acetonitrile were supplied by Fisher (Waltham, MA, USA). Deionized water was obtained using a Milli-Q system (Merck, USA).

2.2. Animals

A total of 32 male Sprague Dawley (SD) rats (200 ± 20 g) were purchased from Jinan Pengyue Laboratory Animal Breeding (License No: scxk (Ru) 20190003). All experimental protocols were approved by the Animal Ethics Committee of Binzhou Medical University (No. 2022-353).

2.3. Establishment and treatments in a rat model

The SD rats were acclimated for 3 days prior to the experiments (24 ± 2°C and a 12/12 h light/dark cycle). The rats were randomly divided into four groups: (1) a control group, a model group, a positive group, and a polydatin group, with eight rats in each group. Potassium oxonate (300 mg/kg) and 10% fructose water were used to establish a hyperuricemic rat model (21). Potassium oxonate was resuspended in a 0.5% sodium carboxymethylcellulose (CMC-Na) solution and administered by gavage to rats in the model, positive, and polydatin groups at 8:00 every morning. After 1 h, the rats in the positive group were intragastrically administered 20 mg/kg benzbromarone, and the rats in the polydatin group were orally administered 50 mg/kg benzbromarone for 28 consecutive days. The doses of polydatin were determined based on previous reports (14, 22, 23). Rats in the control group were administered the same volume of 0.5% CMC-Na water by gavage. Benzbromarone and polydatin were dissolved in 0.5% CMC-Na. During the experiment, the rats in the positive and polydatin groups were fed 10% fructose water.

2.4. Sample collection and preparation

All rats were anesthetized by intraperitoneal injection of chloral hydrate (30 mg/kg) after fasting for 24 h. Abdominal aortic blood samples were collected and centrifuged at 3,500 rpm for 15 min at 4°C, and the supernatants were collected. Serum (200 μl) was

used to determine biochemical parameters using an automatic biochemical analyzer, and the remaining serum samples were stored at −80°C for metabolomics analysis.

Intact liver and kidney tissues were removed and washed with pre-cooled saline, followed by drying with filter paper. Fresh tissues were fixed in 4% paraformaldehyde for more than 24 h, trimmed, embedded in paraffin, routinely sectioned, dewaxed in xylene, dehydrated in gradient ethanol, stained with hematoxylin for 3–5 min, washed, stained with eosin for 5 min, washed, dehydrated in gradient ethanol, made transparent in xylene, and sealed with neutral glue (24). Finally, the pathological states of the liver and kidneys were observed under a light microscope.

2.5. Sample preparation for a metabolomic study

The serum sample was thawed at 4°C. Acetonitrile (400 μl) was added to 100 μl of a serum sample for protein precipitation. After vortexing for 1 min, the samples were centrifuged at 14,000 rpm for 10 min at 4°C. Subsequently, 150 μl of the supernatant was separated and evaporated to dryness with nitrogen at 27°C. The residue was dissolved in 100 μl of an 80% (v/v) acetonitrile aqueous solution and then injected for UHPLC-Q-Exactive Orbitrap MS analysis. Quality control (QC) samples were prepared in the same manner as described above and were mixed with all samples in equal volumes (10 μ l).

2.6. UHPLC-Q-Exactive Orbitrap MS analysis

Liquid chromatography was performed using a Q-Exactive Focus Orbitrap MS (Thermo Electron, Bremen, Germany) connected to a Thermo Scientific Dionex Ultimate 3000 RS (Thermo Fisher Scientific, CA, USA) equipped with an ACQUITY UPLC BEH C18 column (2.1 mm × 100 mm, 1.7 μm, Waters Corp., USA). The flow rate was 0.28 mL/min, and the column temperature was maintained at 45°C. The mobile phases were 0.1% formic acid in water (solvent C) and acetonitrile (solvent D). The gradient elution program was as follows: 0–1 min, 95% C; 1–5 min, 95–55% C; 5–10 min, 55–35% C; 10–15 min, 35–20% C; 15–15.1 min, 20–5% C; 15.1–17 min, 5% C; 17–17.1 min, 5–95% C; 17.1–20 min, 95% C. The injection volume was 2 μ l.

The electrospray ionization (ESI) source was operated in both positive and negative ion models for MS analysis. The following operating parameters were used: capillary voltage of 35 V; capillary temperature of 320°C; the tube lens voltage of 110 V; auxiliary gas flow rate of 10 arb. The m/z range was set at 100–1,000 Da.

2.7. Data analysis and identification of potential biomarkers

All data acquired from UHPLC-Q-Exactive Orbitrap MS were normalized using Compound Discover 3.0 (Thermo Fisher) software for pre-processing (peak identification, peak matching, data alignment, and experimental grouping design). Retention times and MS fragments were generated by analysis. Subsequently, the obtained data matrices were analyzed by principal component analysis (PCA) and orthogonal partial least squares discrimination analysis (OPLS-DA) using SIMCA-P 13.0 (Umetrics, Umeå, Sweden) (25–27). Metabolites with significant differences between different groups were screened based on variable importance in the projection (VIP) values (VIP > 1.0) and Student's *t*-test ($p < 0.05$). The structural identification of differential metabolites was conducted using the HMDB[1] (and PubChem databases (28–31).[2]

2.8. Pathway analysis

Metabolic pathway analysis was performed using MetaboAnalyst.[3] Biochemical interpretation of the metabolic pathways was performed using the KEGG database[4] and relevant references.

3. Results

3.1. Effects of polydatin on weight and serum biochemical indicators in hyperuricemic rats

An increased serum uric acid (SUA) level is considered a typical indicator of HUA. Blood urea nitrogen (BUN) and serum creatinine (Scr) are the final nitrogenous products of protein metabolism, and their levels indicate impaired or normal renal function. Alanine transaminase (ALT) and aspartate aminotransferase (AST) are valuable markers of liver function. As shown in **Figure 1A**, the changes in rats' body weight were insignificant, implying that the dose of polydatin used in the study was safe for HUA rats. Compared to the control group, at 28 days, the levels of SUA, Scr, AST, TG, and blood glucose were significantly higher, and the levels of BUN and ALT were significantly lower in the model group at 28 days ($p < 0.05$). After administering polydatin and benzbromarone as positive controls, there was a recovery trend in SUA, BUN, AST, TG, blood glucose, Scr, and ALT levels. This indicated that polydatin could have a urate-lowering effect in a rat model.

3.2. Effects of polydatin on liver and renal injury in hyperuricemic rats

Histopathological hallmarks of liver cells were vacuolar degeneration, local hepatocyte necrosis, and hepatic cords arranged less neatly in the liver of hyperuricemic rats compared with those

1 https://hmdb.ca/
2 https://pubchem.ncbi.nlm.nih.gov/
3 http://www.metaboanalyst.ca
4 http://www.kegg.com/

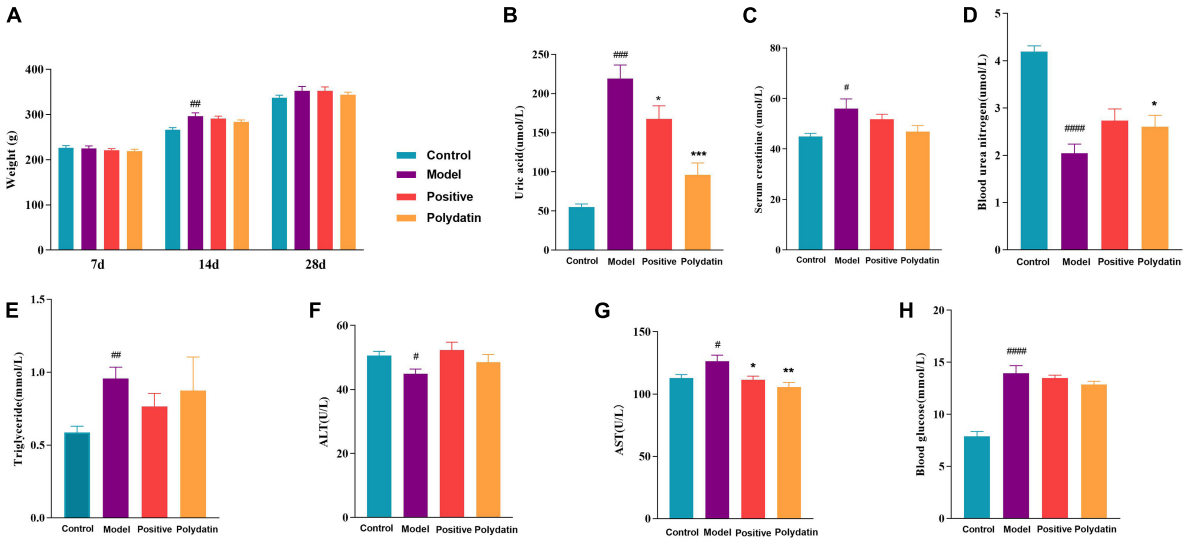

FIGURE 1
Effects of polydatin on biochemical indicators in serum from HUA rats. **(A)** Weight change of rats in 28 days. **(B)** Serum uric acid (SUA). **(C)** Serum creatinine (Scr). **(D)** Blood urea nitrogen (BUN). **(E)** Serum triglyceride (TG). **(F)** Alanine transaminase (ALT). **(G)** Aspartate aminotransferase (AST). **(H)** Blood glucose. Values are given as the mean ± SEM (n = 8) ($^{*}p < 0.05$, $^{**}p < 0.01$, $^{***}p < 0.001$, vs. model group; $^{\#}p < 0.05$, $^{\#\#}p < 0.01$, $^{\#\#\#}p < 0.001$, $^{\#\#\#\#}p < 0.0001$, vs. control group).

in normal rats. These pathological states were attenuated when treated with polydatin (Figure 2A). In addition, the histological analysis showed significant pathological changes in the kidneys of model rats. Noticeable pathological changes in renal tubular epithelial cells included atrophy of the glomerulus and vacuolar degeneration compared with the control group. As was observed for the pathological states in the liver, those in the kidneys were also ameliorated by treatment with polydatin (Figure 2B). The results indicated that the injuries induced by high UA levels were improved to varying degrees by polydatin. The histological results were in accordance with the levels of UA observed above in hyperuricemic rats.

3.3. Serum metabolic analysis

To systematically describe the underlying mechanisms of polydatin-ameliorating HUA, UHPLC-Q-Exactive Orbitrap MS was used to analyze serum samples from rats in positive and negative ion modes. Representative serum base peak ions (BPI) of serum samples from the control, model, positive, and polydatin groups were obtained (Supplementary Figure 1). All peaks in the serum samples from each group of rats were well separated at 20 min in both ESI^+ and ESI^- modes. The metabolic profiles of each group were different, indicating changes in the endogenous metabolic profiles between different groups.

Principal component analysis score plots were used to understand the differences in the serum metabolic profiles of rats in each group. We noticed a clear separation trend in the different groups in both ESI^+ and ESI^- mode experiments, suggesting that endogenous metabolites differed significantly among the control, model, positive, and polydatin groups, and the group difference was more evident than the individual difference (Figure 3). In addition, the QC samples aggregated significantly, indicating good repeatability and stability (Figures 3A, B).

3.4. Identification of potential biomarkers

To maximize class differentiation, supervised OPLS-DA was applied to differentiate among the control, model, positive, and polydatin groups to obtain potential biomarkers to evaluate the therapeutic effects of polydatin. As shown in Figures 4A, B, the control and model groups were clearly separated into different areas in both positive and negative ion modes, indicating significant metabolic changes in the HUA rat model. The R^2Y and Q^2 parameters were used to evaluate the OPLS-DA model. R^2Y and Q^2 were 0.986 and 0.982, respectively, in ESI^+ mode, and 0.998 and 0.987, respectively, in ESI^- mode (Supplementary Table 1). These values were close to 1, suggesting that the model was in good agreement with the experiment data. The model was validated by 200 rounds of permutation tests (Supplementary Figure 2A, B), and all R^2 or Q^2 values on the left were reliable and not over-fitted. To assess the urate-lowering effects of polydatin, the serum metabolic profiles of the positive and polydatin groups were compared with those of the model based on the OPLS-DA model (Figures 4C–F), and the scatter plots were significantly separated. Meanwhile, R^2Y and Q^2 (Supplementary Table 1) and permutation tests (Supplementary Figures 2C–F) confirmed that the models were successful. These results demonstrated that polydatin exhibits urate-lowering properties.

The S-plot (Supplementary Figure 3) was derived from the OPLS-DA, and each spot represented a substance that was used to screen endogenous biomarkers by detecting high contributions and correlations. Of all the metabolites, only those with VIP > 1 and $p < 0.05$ by t-test were identified as potential biomarkers between the control and model groups. The structural information of the

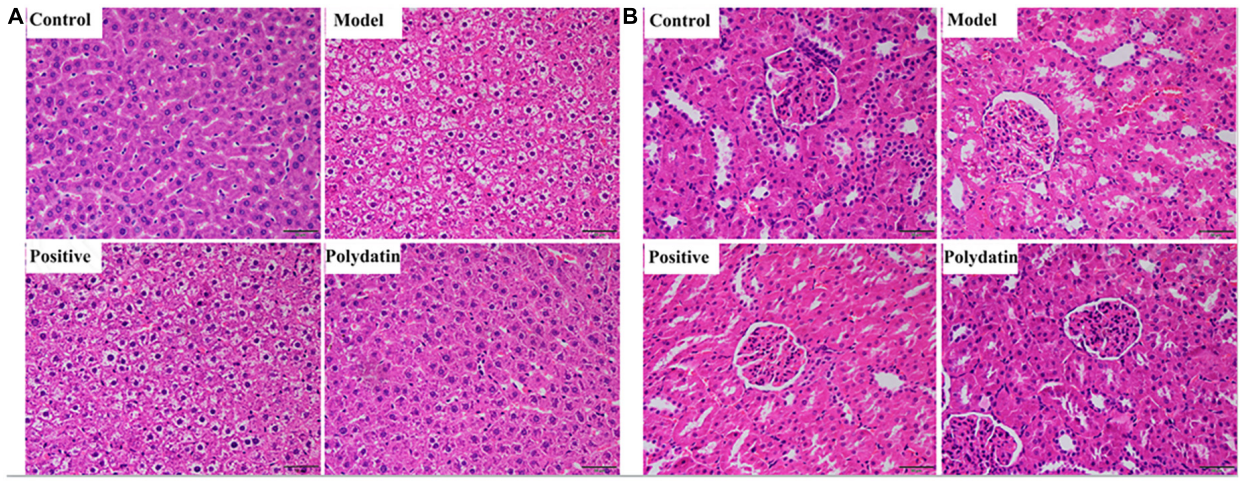

FIGURE 2
Histopathological evaluation of rat liver **(A)** and kidney **(B)** in different treatment groups. Scale bar = 100 μm.

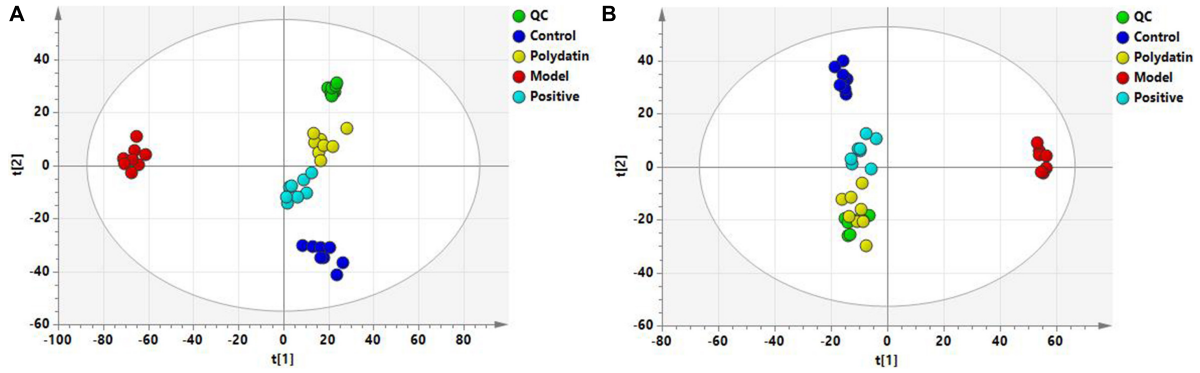

FIGURE 3
PCA score plots of QC and four groups based on serum metabolic profiles **(A)** ESI^+ mode; **(B)** ESI^- mode.

metabolites, such as molecular weight and MS/MS fragmentation, was confirmed using freely accessible public databases (HMDB and KEGG). According to the criteria above, potential biomarkers were chosen and identified between the control and model groups (Table 1). A total of 14 endogenous altered metabolites were identified in the serum of the model rats compared to that of the control group, related to lipid and amino acid metabolism and other metabolic pathways. The identified biomarkers are summarized in Table 1.

3.5. Metabolic pathway analysis of identified biomarkers

3.5.1. Alteration in metabolic pathways in hyperuricemic rats

As shown in Figures 5A–C, comparing the signal intensity of differential metabolites, 14 metabolites changed significantly in the model group compared to that in the control group. The levels of L-tyrosine, sphinganine, phytosphingosine, and valerenic acid increased in the model group, whereas the levels of alpha-methylstyrene, L-leucine, L-phenylalanine, 3-phenyl-2-propen-1-ol, nona-2,6-dienal, dihydroxyacetone phosphate, *O*-butanoylcarnitine, mono-(2-ethylhexyl) phthalate, 6-gingerol and 1,4-bis (2-ethylhexyl) sulfosuccinate were decreased in the model rats. To investigate the metabolic pathways in hyperuricemic rats, metabolites with apparent alterations were imported into MetaboAnalyst 5.0. The metabolic networks were mainly involved in phenylalanine, tyrosine, and tryptophan biosynthesis, phenylalanine metabolism, sphingolipid metabolism, aminoacyl-tRNA biosynthesis, and tyrosine metabolism in rats treated with potassium oxonate (Figure 6A).

3.5.2. Alteration in metabolic pathways in hyperuricemic rats treated with benzbromarone and polydatin

The heatmap (Figure 5D) represents the changes in 14 altered metabolites in the four groups. Figure 5D shows the information of metabolites as the ordinate and the information of groups as the abscissa. Each cell represents one metabolite, and deep red and deep blue represent upregulation and downregulation, respectively. The results showed that 14 metabolites varied significantly in the model

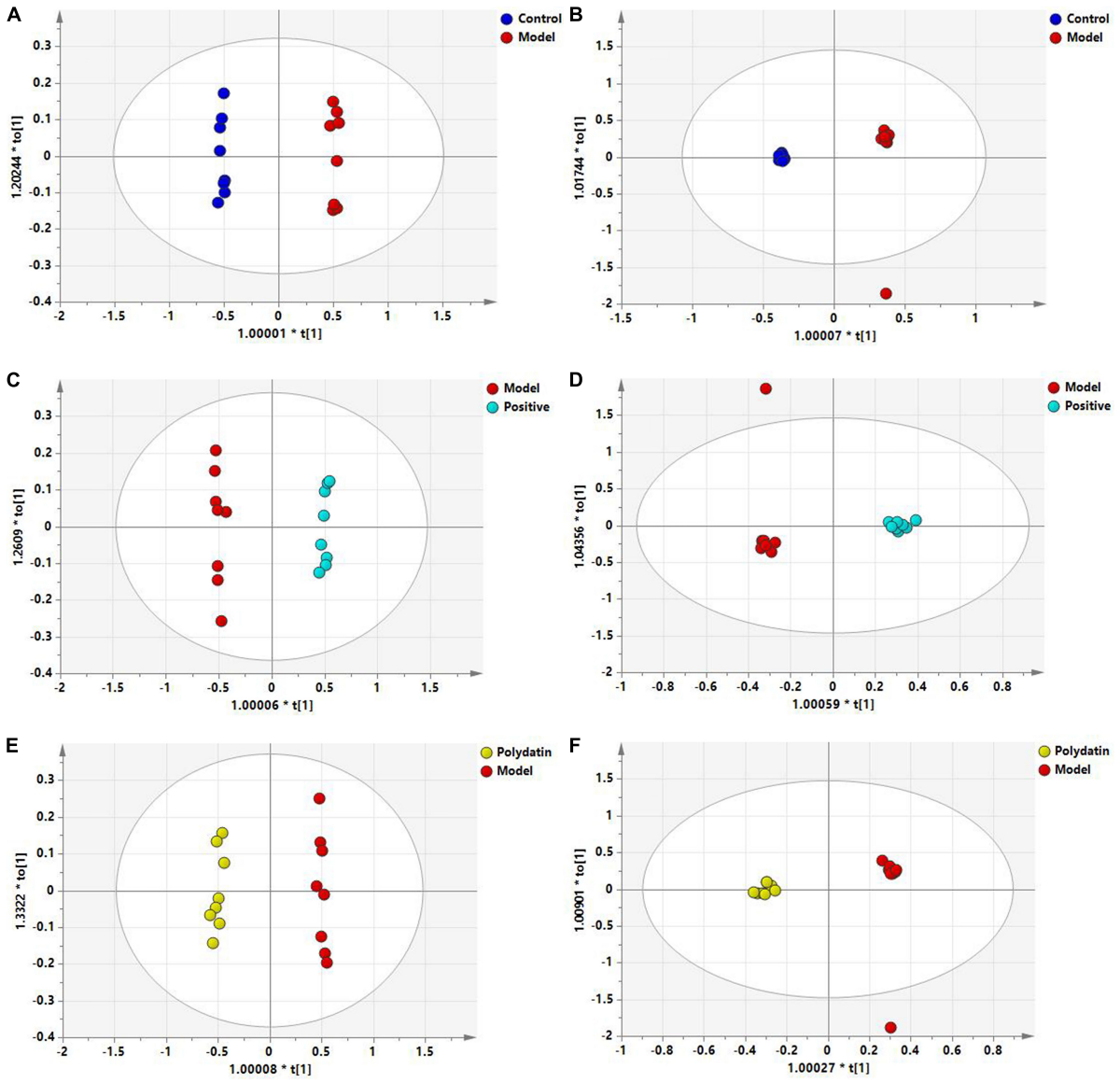

FIGURE 4
OPLS-DA score plots of serum samples in different groups. Control and model groups in ESI$^+$ mode **(A)** and ESI- mode **(B)**; positive and model groups in ESI$^+$ mode **(C)** and ESI$^-$ mode **(D)**; polydatin and model groups in ESI$^+$ mode **(E)** and ESI$^-$ mode **(F)**.

group, and the levels of the endogenous differential metabolites were reversed in hyperuricemic rats after the administration of benzbromarone and polydatin. Of all the differential metabolites, 12 metabolites associated with HUA were reversed significantly by polydatin and had a tendency to return to the levels of the normal group (Figures 5A–C). Furthermore, metabolic network analysis comprehensively demonstrated that polydatin interfered with pathways in the hyperuricemia group (Figure 6B). Taken together, the above results demonstrate that polydatin is an effective urate-lowering therapy.

4. Discussion

Sustaining high serum and UA levels can contribute to serious diseases. However, UA concentration is the only diagnostic indicator for HUA, and there are no satisfactory ways to reduce UA levels without harmful side effects. Polydatin (3,4,5-trihydroxystilbene-3-β-D-glucoside) is a natural resveratrol glucoside derived from plants. Containing three phenolic hydroxyl groups, it acts as an oxygen radical scavenger.

Polydatin is found in *Polygonum cuspidatum*, grapes, red wine, peanuts, and many other commonly consumed foods. Several studies have suggested that polydatin has many pharmacological activities, including effectively decreasing UA levels (10). In this study, we explored the interventional effects of polydatin in an HUA rat model using the UHPLC-Q-Exactive Orbitrap MS metabonomic approach, which provided a deep understanding of the urate-lowering effects of polydatin. We screened 14 metabolites related to HUA (Table 1). Analysis of the metabolites showed that they were mainly involved in amino acid, lipid, and energy metabolism.

TABLE 1 Identification of different metabolites and the change trends of metabolites in different groups.

No.	Metabolites	Formula	Rt (min)	ESI mode	Theoretical mass m/z	Experimental mass m/z	Error (ppm)	VIP score	MS^n	Trend		
										Model	Positive	Polydatin
1	Alpha-methylstyrene	C_9H_{10}	9.69	$[M+H]^+$	119.0853	119.0851	−3.58	2.29	103,92,78	$\downarrow^{\#\#\#\#}$	$\uparrow^{****}$	$\uparrow^{****}$
2	L-Leucine	$C_6H_{13}NO_2$	1.45	$[M+H]^+$	132.1017	132.1015	−2.91	3.51	87,86,56	$\downarrow^{\#\#\#}$	$\uparrow^{****}$	$\uparrow^{****}$
3	3-Phenyl-2-propen-1-ol	$C_9H_{10}O$	9.69	$[M+H]^+$	135.0800	135.0798	−4.60	1.30	108,54	$\downarrow^{\#\#\#\#}$	$\uparrow^{****}$	$\uparrow^{****}$
4	Nona-2,6-dienal	$C_9H_{14}O$	19.99	$[M+H]^+$	139.1114	139.1112	−3.39	1.35	83,69,56	$\downarrow^{\#\#\#\#}$	—	$\uparrow^{****}$
5	L-Phenylalanine	$C_9H_{11}NO_2$	2.07	$[M+H]^+$	166.0858	166.0856	−3.82	2.33	149,120,91	$\downarrow^{\#\#\#}$	$\uparrow^{****}$	$\uparrow^{****}$
6	Dihydroxyacetone phosphate	$C_3H_7O_6P$	19.12	$[M+H]^+$	171.0052	171.0050	−1.64	1.40	97,89,72	$\downarrow^{\#\#\#\#}$	$\uparrow^{****}$	$\uparrow^{****}$
7	L-Tyrosine	$C_9H_{11}NO_3$	1.16	$[M+H]^+$	182.0807	182.0805	−3.40	1.81	165,154,136	$\uparrow^{\#\#\#}$	—	—
8	O-Butanoylcarnitine	$C_{11}H_{21}NO_4$	3.28	$[M+H]^+$	232.1537	232.1534	−3.63	1.35	173,144,86,57	$\downarrow^{\#\#\#}$	$\uparrow^{**}$	$\uparrow^{****}$
9	Mono-(2-ethylhexyl)phthalate	$C_{16}H_{22}O_4$	19.99	$[M+H]^+$	279.1584	279.1580	−3.71	1.30	164,112,99,57	$\downarrow^{\#\#\#\#}$	$\uparrow^{****}$	$\uparrow^{****}$
10	Sphinganine	$C_{18}H_{39}NO_2$	10.09	$[M+H]^+$	302.3045	302.3041	−4.02	11.91	284,85,71,57	$\uparrow^{\#\#\#\#}$	$\downarrow^{****}$	$\downarrow^{****}$
11	Phytosphingosine	$C_{18}H_{39}NO_3$	8.53	$[M+H]^+$	318.2994	318.2990	−3.77	15.82	155,85,71,57	$\uparrow^{\#\#\#\#}$	$\downarrow^{****}$	$\downarrow^{****}$
12	Valerenic acid	$C_{15}H_{21}O_2$	11.61	$[M-H]^-$	233.1545	233.1545	1.48	1.18	193,165,121,110	$\uparrow^{\#\#\#}$	$\downarrow^{****}$	—
13	6-Gingerol	$C_{17}H_{26}O_4$	8.74	$[M-H]^-$	293.1762	293.1788	1.08	2.69	237,222,210,142	$\downarrow^{\#\#\#\#}$	$\uparrow^{****}$	$\uparrow^{****}$
14	1,4-Bis (2-ethylhexyl) sulfosuccinate	$C_{20}H_{37}O_7S$	13.73	$[M-H]^-$	421.2271	421.2272	1.54	1.95	283,227,80	$\downarrow^{\#\#\#\#}$	$\uparrow^{****}$	$\uparrow^{****}$

$^{**}p < 0.01$, $^{****}p < 0.0001$, compared with model group; $^{\#\#\#}p < 0.001$, $^{\#\#\#\#}p < 0.0001$, compared with control group. $^{-}$Denotes no statistically significant difference.

10.3389/fnut.2023.1117460

10.3389/fnut.2023.1117460

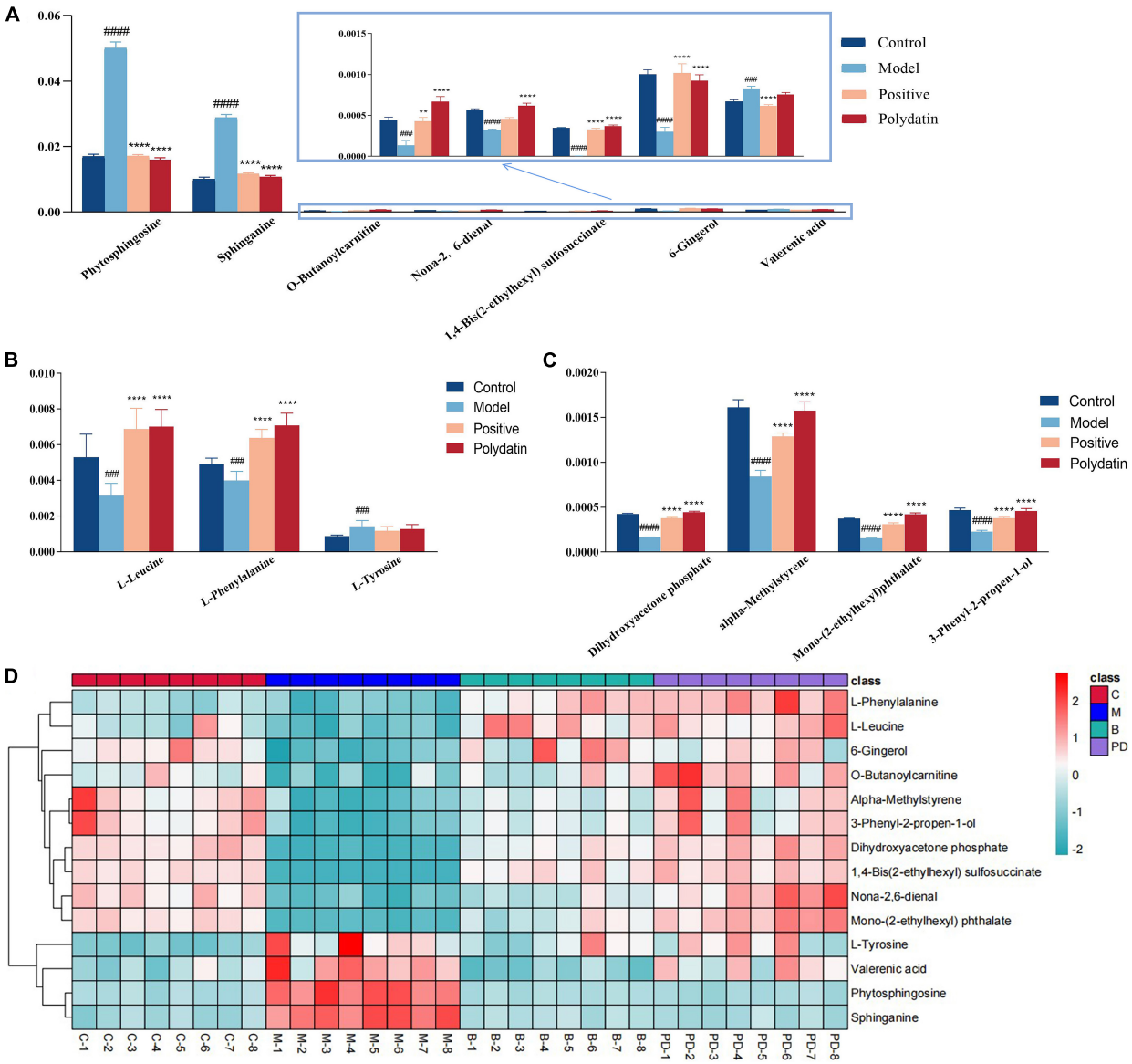

FIGURE 5
The relative levels of differential metabolites in serum from control group, model group, positive group and polydatin group. Comparison of signal intensity of significant metabolites related with lipid metabolism **(A)**, amino acid metabolism **(B)** and other metabolism **(C)** in different groups **(D)**. The hierarchical clustering heatmap of differential metabolites in serum from different groups. Deeper red represents up-regulation and deeper blue represents down-regulation, and each cell stands for one metabolite ($^{**}p < 0.01$, $^{****}p < 0.0001$, vs. model group; $^{###}p < 0.001$, $^{####}p < 0.0001$, vs. control group).

Moreover, these changes in hyperuricemic rats were reversed after oral administration of polydatin. Some possible mechanisms are summarized in Figure 7. The results indicated relevant metabolic pathways that were directly associated with HUA and proved that polydatin could ameliorate the related indicators, as discussed below.

(1) Hyperuricemia-induced changes in amino acid metabolism were reversed by polydatin.

Amino acids play important roles in vital activities, and amino acid metabolism regulates both protein and energy metabolism. The levels of L-leucine and L-phenylalanine decreased, whereas those of L-tyrosine significantly increased in HUA model rats (Figure 5B), indicating imbalances between protein and amino acid synthesis. These include phenylalanine, tyrosine, and tryptophan biosynthesis, phenylalanine metabolism, and aminoacyl-tRNA biosynthesis.

Leucine is a ketogenic amino acid that can be degraded to acetyl-CoA and acetoacetic acid in the body, entering glycolysis or other metabolic pathways through the tricarboxylic acid cycle, and participating in the regulation of the body's normal metabolic processes. It has been shown that leucine is associated with the PIK3 and protein kinase C signaling pathways, which regulate glucose uptake and utilization in the cell and are related to insulin resistance and the development of type 2 diabetes (32). Leucine, valine, and isoleucine are branched-chain amino acids (BCAAs). BCAAs and their catabolic

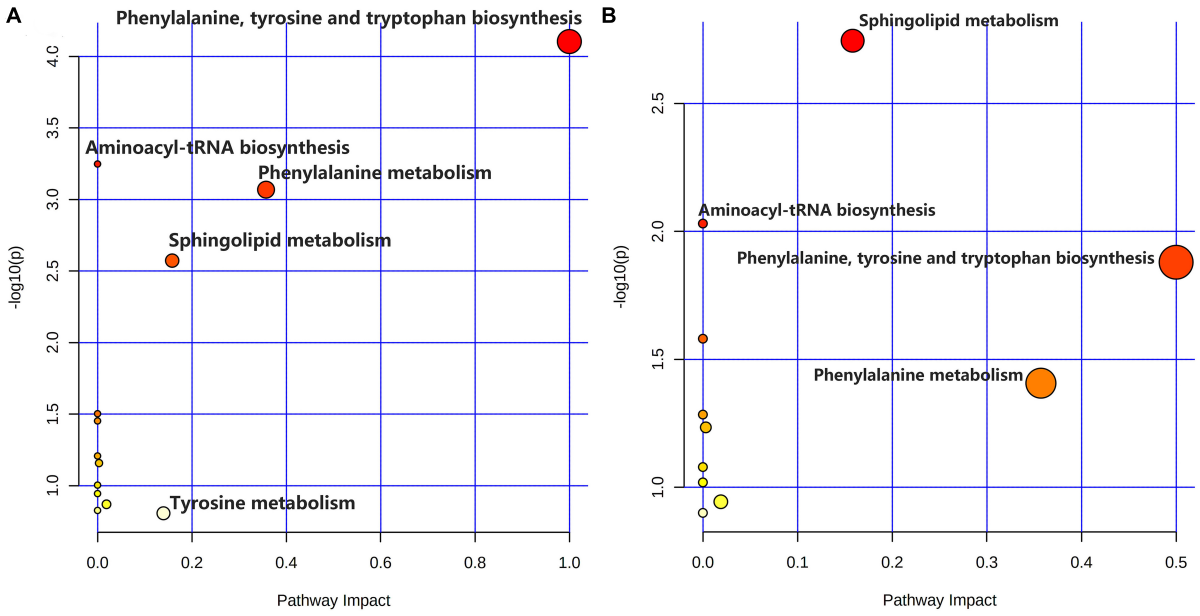

FIGURE 6
Summary of metabolic pathway analysis. **(A)** Control group vs. model group; **(B)** model group vs. polydatin group.

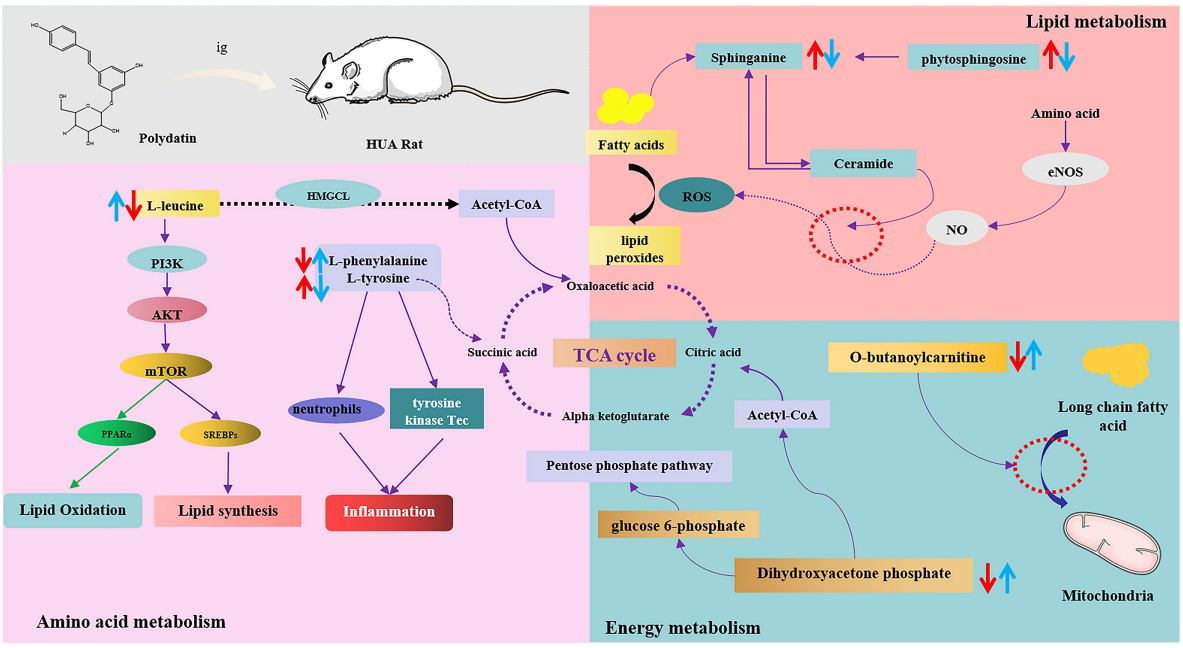

FIGURE 7
The intervention metabolisms of polydatin on HUA rats. The red arrow represents the changes of metabolites in hyperuricemic rats, and the blue arrow represents the changes of metabolites after oral administration of polydatin.

products participate in the regulation of numerous physiological processes in the body. Zhang et al. showed that leucine and isoleucine could be potential biomarkers for patients with HUA and gout (33). BCAAs are key factors in the development of metabolic diseases, and altered BCAAs may be indicators of type 2 diabetes mellitus (34, 35). However, since high UA levels are closely associated with the development of type 2 diabetes mellitus and other metabolic diseases, leucine may be a key indicator of HUA and other related diseases. In our study, after the administration of polydatin, the level of leucine reversed significantly compared with that of the untreated HUA group, implying that lowering UA by polydatin was related to the adjustment of background leucine levels.

The essential amino acids L-tyrosine and L-phenylalanine participate in phenylalanine, tyrosine, and tryptophan biosynthesis and phenylalanine metabolism. Phenylalanine can be hydroxylated

to produce tyrosine by phenylalanine hydroxylase, which is involved in synthesizing essential neurotransmitters and hormones related to glucose and lipid metabolism (36). Increased tyrosine stimulated by monosodium urate (MSU) is correlated with the activation of neutrophils and tyrosine kinase Tec, leading to the release of inflammatory factors such as IL-1β, IL-8, IL-1, and tyrosine. It is thought to be a potential biomarker for MSU-induced gout (37). A study also showed that the level of tyrosine increased in acute gout in hyperuricemic rats (38).

Moreover, high UA levels cause the accumulation of MSU in the body, leading to the development of gouty arthritis, indicating that high tyrosine levels may be associated with the development of gout. Elevated tyrosine levels in the body can affect the functions of enzymes, such as citrate synthase, malate dehydrogenase, and succinate dehydrogenase, in the tricarboxylic acid cycle, leading to disturbances in energy metabolism and oxidative stress in the mitochondria (39). In our experiments, the level of tyrosine was elevated, whereas that of phenylalanine decreased in the model group, suggesting that overproduction of UA disturbed phenylalanine, tyrosine, and tryptophan biosynthesis and phenylalanine metabolism by accelerating the conversion of phenylalanine to tyrosine. However, polydatin decreased and increased the levels of tyrosine and phenylalanine, respectively. Phenylalanine, tyrosine, and tryptophan biosynthesis and phenylalanine metabolism were also altered by polydatin treatment compared with those in the untreated HUA group (**Figure 6B**), indicating that the restoration of a low UA level by polydatin involved regulation of phenylalanine and tyrosine metabolic pathways.

Aminoacyl-tRNA biosynthesis plays a vital role in the synthesis of proteins by recognizing the correct amino acids with tRNAs, including the corresponding anticodon for mRNA in the ribosome (40). Zhang et al. found that aminoacyl-tRNA biosynthesis was abnormal in patients with HUA and gout (33). Furthermore, aminoacyl-tRNA synthetases (AARSs) play an important role in aminoacyl-tRNA biosynthesis and have been verified in various human diseases (41). High UA levels may disturb aminoacyl-tRNA biosynthesis by acting on AARSs. In our experiment, aminoacyl-tRNA biosynthesis was restored after the oral administration of polydatin, suggesting that the mechanisms of polydatin may be associated with inhibiting AARSs' activities. However, further studies are required to verify this hypothesis.

(2) Hyperuricemia-induced changes in lipid metabolism were reversed by polydatin.

Many researchers have reported that serum UA is associated with serum lipids in many diseases, such as HUA, gout, and cardiovascular and cerebrovascular diseases (33, 42). High serum TG levels were observed in a model of HUA (**Figure 1**). Moreover, a previous study showed that altered lipid metabolism is closely linked to HUA and gout (33). Our findings showed that lipid metabolism was disordered in hyperuricemic rats, which is consistent with the findings of previous studies, as discussed below.

Sphingolipids are amphiphilic lipids that include a sphingosine backbone and phospholipids, such as sphingol (Sph), ceramide (Cer), sphingomyelin (SM), gangliosides, and others. Intracellular sphingolipid metabolism plays a vital role in various metabolic diseases (43, 44). Sphinganine and phytosphingosine are involved in sphingolipid metabolism. Sphinganine can be converted into phytosphingosine by sphinganine C4-monooxygenase. Sphinganine and fatty acids of different chain lengths can form ceramides, which are central to sphingolipid synthesis and degradation. Studies have shown that ceramides mediate the conversion of NO to H_2O_2 in coronary microcirculation, thereby causing proinflammatory, prothrombotic, and atherogenic effects (45, 46). In this study, serum UA levels were elevated in HUA-model rats. The levels of sphinganine and phytosphingosine in the serum samples were elevated, which greatly promoted ceramide synthesis and caused abnormal sphingolipid metabolism *in vivo*. Therefore, abnormal sphingolipid metabolism may be the causative factor of cardiovascular disease caused by HUA. These trends were reversed compared to those found in normal rats after polydatin administration, indicating that polydatin might regulate sphingolipid metabolism to exert a UA-lowering effect.

(3) Hyperuricemia-induced changes in energy metabolism were reversed by polydatin.

Carnitine is essential for transporting long-chain fatty acids across the mitochondrial membrane. It also modulates the proportion of acyl-CoA/CoA and transfers some toxic acyl-CoA compounds. Derangement in the ability to transport long-chain fatty acids leads to the accumulation of harmful fatty acyl metabolites, which hinder gluconeogenesis and the citric acid cycle (47, 48). Therefore, carnitine is a powerful tool to identify whether energy metabolism is perturbed. Furthermore, carnitine transporters participate in the uptake and excretion of organic cations in the kidneys, and abnormal carnitine metabolism affects UA excretion in the kidneys (49). In this study, the level of *O*-butanoylcarnitine significantly decreased in the HUA model group. Treatment with polydatin resulted in a significant elevation in the levels of *O*-butanoylcarnitine, indicating that polydatin reversed the UA-induced disturbance of carnitine metabolism.

Dihydroxyacetone phosphate is an important component in gluconeogenesis and lipid metabolism. Dihydroxyacetone phosphate can be converted into glucose 6-phosphate and enter the gluconeogenic pathway. Moreover, dihydroxyacetone phosphate can be aerobically oxidized to produce acetyl CoA and enter the lipid metabolism pathway. The results showed that the level of dihydroxyacetone phosphate was decreased in hyperuricemic rats, indicating possible abnormalities in glucose and lipid metabolism. Aberrant dihydroxyacetone phosphate might be another important factor leading to changes in hyperuricemic rats' blood glucose and triglyceride levels. However, polydatin caused dihydroxyacetone phosphate to return to normal levels, demonstrating good regulation of energy metabolism.

5. Conclusion

Polydatin is a functional compound derived from mulberries and grapes, with multiple bioactivities, including lowering the level of UA in serum and tissues. In this study, a UHPLC-Q-Exactive Orbitrap MS-based metabolomics approach was applied to explore the potential molecular mechanisms underlying the urate-lowering of polydatin in hyperuricemic rats. A total of 14 differential metabolites were identified in response to the therapeutic effects of polydatin, which were associated with amino acid metabolism, lipid metabolism, and energy metabolism. After polydatin intervention, the results showed that differential metabolites and the metabolic

network were restored, approaching the levels observed in normal rats. This study has the potential to enhance our understanding of the mechanisms of HUA and demonstrate that polydatin is a promising adjuvant for lowering UA levels and alleviating HUA-related diseases.

Data availability statement

The datasets presented in this study can be found in online repositories. The names of the repository/repositories and accession number(s) can be found in the article/ **Supplementary material**.

Ethics statement

All experimental protocols were approved by the Animal Ethics Committee of Binzhou Medical University (No. 2022-353).

Author contributions

XG, XZ, and ZSh performed the experiments. PZ, KH, SZ, SH, YhW, YqW, and MZ analyzed the data. XL and ZSu wrote the manuscript. JZ conceived the project, designed the experiments, and revised the manuscript. All authors edited and approved the final version of the manuscript.

Funding

This study was financially supported by the General Program of the National Natural Science Foundation of China (82174039), the General Project of Shandong Natural Science Foundation (ZR2020MH371, ZR2021QH167, and ZR2021QH207), the Shandong Taishan Scholars Young Expert Project (tsqn202103110), the Shandong Province Youth Talents Introducing and Cultivating Program (10073004), the Binzhou Medical University Scientific Research Fund for High-Level Talents (50012304312), and Shandong College Students' Innovation and Entrepreneurship Training Program (S202110440054).

Conflict of interest

The authors declare that the research was conducted in the absence of any commercial or financial relationships that could be construed as a potential conflict of interest.

Publisher's note

All claims expressed in this article are solely those of the authors and do not necessarily represent those of their affiliated organizations, or those of the publisher, the editors and the reviewers. Any product that may be evaluated in this article, or claim that may be made by its manufacturer, is not guaranteed or endorsed by the publisher.

Supplementary material

The Supplementary Material for this article can be found online at: https://www.frontiersin.org/articles/10.3389/fnut.2023.1117460/full#supplementary-material

References

1. Bardin T, Richette P. Definition of hyperuricemia and gouty conditions. *Curr Opin Rheumatol.* (2014) 26:186–91. doi: 10.1097/BOR.0000000000000028

2. Ali N, Perveen R, Rahman S, Mahmood S, Rahman S, Islam S. Prevalence of hyperuricemia and the relationship between serum uric acid and obesity: a study on bangladeshi adults. *PLoS One.* (2018) 13:e0206850. doi: 10.1371/journal.pone.0206850

3. Yamanaka H. Gout and hyperuricemia in young people. *Curr Opin Rheumatol.* (2011) 23:156–60. doi: 10.1097/BOR.0b013e3283432d35

4. Li C, Li Z, Liu S, Wang C, Han L, Cui L. Genome-wide association analysis identifies three new risk loci for gout arthritis in han Chinese. *Nat Commun.* (2015) 6:7041. doi: 10.1038/ncomms8041

5. Yanai H, Adachi H, Hakoshima M, Katsuyama H. Molecular biological and clinical understanding of the pathophysiology and treatments of hyperuricemia and its association with metabolic syndrome, cardiovascular diseases and chronic kidney disease. *Int J Mol Sci.* (2021) 22:9221. doi: 10.3390/ijms22179221

6. Shao L, Wei L. Efficacry and safety of benbromarne and allopurinol for primary gout ULT: a meta-analysis. *Chin J of Evid-Based Med.* (2012) 12:722–6.

7. Imai S, Nasuhara Y, Momo K, Oki H, Kashiwagi H, Sato Y. Implementation status of liver function tests for monitoring benzbromarone-induced hepatotoxicity: an epidemiological survey using the Japanese claims database. *Biol Pharm Bull.* (2021) 44:1499–505. doi: 10.1248/bpb.b21-00393

8. Childs L, Dow C. Allopurinol-induced hepatomegaly. *BMJ Case Rep.* (2012) 2012:bcr2012007283. doi: 10.1136/bcr-2012-007283

9. Stone RB. Lifting the veil on traditional Chinese medicine. *Science.* (2008) 319:709–10. doi: 10.1126/science.319.5864.709

10. Du QH, Peng C, Zhang H. Polydatin: a review of pharmacology and pharmacokinetics. *Pharm Biol.* (2013) 51:1347–54. doi: 10.3109/13880209.2013.792849

11. Oliviero F, Zamudio-Cuevas Y, Belluzzi E, Andretto L, Scanu A. Polydatin and resveratrol inhibit the inflammatory process induced by urate and pyrophosphate crystals in THP-1 cells. *Foods.* (2019) 8:560. doi: 10.3390/foods8110560

12. Shi YW, Wang CP, Liu L, Liu YL, Wang X, Hong Y. Antihyperuricemic and nephroprotective effects of resveratrol and its analogues in hyperuricemic mice. *Mol Nutr Food Res.* (2012) 56:1433–44. doi: 10.1002/mnfr.201100828

13. Wu G, Wu HB, Jiang H. [Anti-hyperuricemia effect and mechanism of polydatin in mice]. *Yao Xue Xue Bao.* (2014) 49:1739–42.

14. Chen L, Lan Z. Polydatin attenuates potassium oxonate-induced hyperuricemia and kidney inflammation by inhibiting NF-κB/NLRP3 inflammasome activation via the AMPK/SIRT1 pathway. *Food Funct.* (2017) 8:1785–92. doi: 10.1039/C6FO01561A

15. Hisamatsu T, Okamoto S, Hashimoto M, Muramatsu T, Andou A, Uo M. Novel, objective, multivariate biomarkers composed of plasma amino acid profiles for the diagnosis and assessment of inflammatory bowel disease. *PLoS One.* (2012) 7:e31131. doi: 10.1371/journal.pone.0031131

16. Lu X, Xiong Z, Li J, Zheng S, Huo T, Li F. Metabonomic study on "kidney-yang deficiency syndrome" and intervention effects of rhizoma drynariae extracts in rats using ultra performance liquid chromatography coupled with mass spectrometry. *Talanta.* (2011) 83:700–8. doi: 10.1016/j.talanta.2010.09.026

17. Klassen A, Faccio AT, Canuto GA, da Cruz PL, Ribeiro HC, Tavares MF. Metabolomics: definitions and significance in systems biology. *Adv Exp Med Biol.* (2017) 965:3–17. doi: 10.1007/978-3-319-47656-8_1

18. Zhao DS, Jiang LL, Wang LL, Wu ZT, Li ZQ, Shi W. Integrated metabolomics and proteomics approach to identify metabolic abnormalities in rats with *Dioscorea bulbifera* rhizome-induced hepatotoxicity. *Chem Res Toxicol.* (2018) 31:843–51. doi: 10.1021/acs.chemrestox.8b00066

19. Souto-Carneiro M, Tóth L, Behnisch R, Urbach K, Klika KD, Carvalho R. Differences in the serum metabolome and lipidome identify potential biomarkers for seronegative rheumatoid arthritis versus psoriatic arthritis. *Ann Rheum Dis.* (2020) 79:499–506. doi: 10.1136/annrheumdis-2019-216374

20. Corona G, Polesel J, Fratino L, Miolo G, Rizzolio F, Crivellari D. Metabolomics biomarkers of frailty in elderly breast cancer patients. *J Cell Physiol.* (2014) 229:898–902. doi: 10.1002/jcp.24520

21. Wang Y, Liu Z, Wang S, Wang P, Dong F, Dai L. Effect of bidirectional fermentation system of paecilomyces cicadae/astragalus membranaceus in hyperuricemia models and its components. *Mod. Chin. Med.* (2020) 22:1638–43.

22. Han B, Gong M, Li Z, Qiu Y, Zou Z. NMR-based metabonomic study Reveals intervention effects of polydatin on potassium oxonate-induced hyperuricemia in rats. *Oxid Med Cell Longev.* (2020) 2020:6943860. doi: 10.1155/2020/6943860

23. Shi X, Zhuang L, Zhai Z, He Y, Sun E. Polydatin protects against gouty nephropathy by inhibiting renal tubular cell pyroptosis. *Int J Rheum Dis.* (2022) 2022:14463. doi: 10.1111/1756-185X.14463

24. Yang C, Wan J, Zheng D. Effects of qutan huoxue decotion on expressions of miR-27a, p38MAPKand AQP9 in nonalcoholic fatty liver disease rats. *Chin J Inf Tradit Chin Med.* (2021) 28:77–81.

25. Kusonmano K, Vongsangnak W, Chumnanpuen P. Informatics for metabolomics. *Adv Exp Med Biol.* (2016) 939:91–115. doi: 10.1007/978-981-10-1503-8_5

26. Kim YM, Heyman HM. Mass spectrometry-based metabolomics. *Methods Mol Biol.* (2018) 1775:107–18. doi: 10.1007/978-1-4939-7804-5_10

27. Jang C, Chen L, Rabinowitz JD. Metabolomics and isotope tracing. *Cell.* (2018) 173:822–37. doi: 10.1016/j.cell.2018.03.055

28. Chong J, Wishart DS, Xia J. Using metaboanalyst 4.0 for comprehensive and integrative metabolomics data analysis. *Curr Protoc Bioinformatics.* (2019) 68:e86. doi: 10.1002/cpbi.86

29. Pang Z, Chong J, Zhou G, de Lima Morais DA, Chang L. MetaboAnalyst 5.0: narrowing the gap between raw spectra and functional insights. *Nucleic Acids Res.* (2021) 49:W388–96. doi: 10.1093/nar/gkab382

30. Xia J, Wishart DS. Using metaboanalyst 3.0 for comprehensive metabolomics aata analysis. *Curr Protoc Bioinform.* (2016) 55: 14.10.1–14.10.91. doi: 10.1002/cpbi.11

31. Pang Z, Zhou G, Ewald J, Chang L, Hacariz O, Basu N. Using metaboanalyst 5.0 for LC-HRMS spectra processing, multi-omics integration and covariate adjustment of global metabolomics data. *Nat Protoc.* (2022) 17:1735–61. doi: 10.1038/s41596-022-00710-w

32. Yoon MS. The emerging role of branched-chain amino acids in insulin resistance and metabolism. *Nutrients.* (2016) 8:405. doi: 10.3390/nu8070405

33. Zhang Y, Zhang H, Chang D, Guo F, Pan H, Yang Y. Metabolomics approach by 1H NMR spectroscopy of serum reveals progression axes for asymptomatic hyperuricemia and gout. *Arthritis Res Ther.* (2018) 20:111. doi: 10.1186/s13075-018-1600-5

34. Wang SM, Yang RY, Wang M, Ji FS, Li HX, Tang YM. Identification of serum metabolites associated with obesity and traditional risk factors for metabolic disease in Chinese adults. *Nutr Metab Cardiovasc Dis.* (2018) 28:112–8. doi: 10.1016/j.numecd.2017.09.009

35. Wang TJ, Larson MG, Vasan RS, Cheng S, Rhee EP, McCabe E. Metabolite profiles and the risk of developing diabetes. *Nat Med.* (2011) 17:448–53. doi: 10.1038/nm.2307

36. Korner J, Cline GW, Slifstein M, Barba P, Rayat GR, Febres G. A role for foregut tyrosine metabolism in glucose tolerance. *Mol Metab.* (2019) 23:37–50. doi: 10.1016/j.molmet.2019.02.008

37. Popa-Nita O, Marois L, Paré G, Naccache PH. Crystal-induced neutrophil activation: X. proinflammatory role of the tyrosine kinase tec. *Arthr Rheum.* (2008) 58:1866–76. doi: 10.1002/art.23801

38. Chen W, Liu Y, Wei M, Shi L, Wu Y, Liu Z. Studies on effect of ginkgo biloba L. leaves in acute gout with hyperuricemia model rats by using UPLC-ESI-Q-TOF/MS metabolomic approach. *RSC Adv.* (2017) 7:42964–72. doi: 10.1039/C7RA08519B

39. Ferreira GK, Scaini G, Carvalho-Silva M, Gomes LM, Borges LS, Vieira JS. Effect of L-tyrosine in vitro and in vivo on energy metabolism parameters in brain and liver of young rats. *Neurotox Res.* (2013) 23:327–35. doi: 10.1007/s12640-012-9345-4

40. Ibba M, Soll D. Aminoacyl-tRNA synthesis. *Annu Rev Biochem.* (2000) 69:617–50. doi: 10.1146/annurev.biochem.69.1.617

41. Sissler M, González-Serrano LE, Westhof E. Recent advances in mitochondrial aminoacyl-tRNA synthetases and disease. *Trends Mol Med.* (2017) 23:693–708. doi: 10.1016/j.molmed.2017.06.002

42. Tsouli SG, Liberopoulos EN, Mikhailidis DP, Athyros VG, Elisaf MS. Elevated serum uric acid levels in metabolic syndrome: an active component or an innocent bystander? *Metabolism.* (2006) 55:1293–301. doi: 10.1016/j.metabol.2006.05.013

43. Jiang XC, Liu J. Sphingolipid metabolism and atherosclerosis. *Handb Exp Pharmacol.* (2013) 216:133–46. doi: 10.1007/978-3-7091-1511-4_7

44. Parveen F, Bender D, Law SH, Mishra VK, Chen CC, Ke LY. Role of ceramidases in sphingolipid metabolism and human diseases. *Cells.* (2019) 8:1573. doi: 10.3390/cells8121573

45. Freed JK, Beyer AM, LoGiudice JA, Hockenberry JC, Gutterman DD. Ceramide changes the mediator of flow-induced vasodilation from nitric oxide to hydrogen peroxide in the human microcirculation. *Circ Res.* (2014) 115:525–32. doi: 10.1161/CIRCRESAHA.115.303881

46. Yu Z, Peng Q, Li S, Hao H, Deng J, Meng L. Myriocin and d-PDMP ameliorate atherosclerosis in ApoE-/- mice via reducing lipid uptake and vascular inflammation. *Clin Sci.* (2020) 134:439–58. doi: 10.1042/CS20191028

47. Breningstall GN. Carnitine deficiency syndromes. *Pediatr Neurol.* (1990) 6:75–81. doi: 10.1016/0887-8994(90)90037-2

48. Evangeliou A, Vlassopoulos D. Carnitine metabolism and deficit–when supplementation is necessary? *Curr Pharm Biotechnol.* (2003) 4:211–9. doi: 10.2174/1389201033489829

49. Wang Y, Bi C, Pang W, Liu Y, Yuan Y, Zhao H. Plasma metabolic profiling analysis of gout party on acute gout arthritis rats based on UHPLC-Q-TOF/MS combined with multivariate statistical analysis. *Int J Mol Sci.* (2019) 20:5753. doi: 10.3390/ijms20225753

Frontiers in Nutrition

Explores what and how we eat in the context of health, sustainability and 21st century food science

A multidisciplinary journal that integrates research on dietary behavior, agronomy and 21st century food science with a focus on human health.

Discover the latest Research Topics

See more →

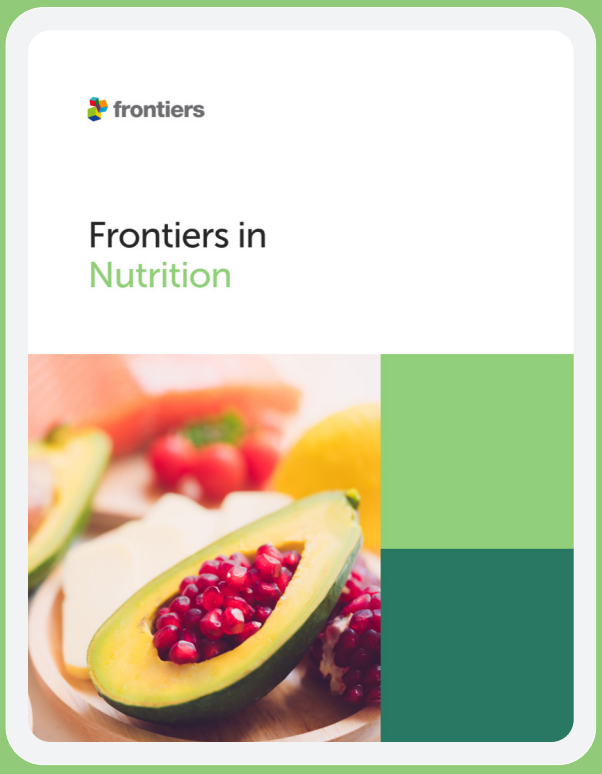

Frontiers

Avenue du Tribunal-Fédéral 34
1005 Lausanne, Switzerland
frontiersin.org

Contact us

+41 (0)21 510 17 00
frontiersin.org/about/contact